Limiting Fragmentation and Azimuthal Anisotropy of Photons in High Energy Collisions at RHIC Energies

Submitted in partial fulfillment of the requirements
degree of
Doctor of Philosophy

by

Dronika Solanki

Supervisor

Dr. Rashmi Raniwala

Department of Physics
University of Rajasthan, Jaipur, India

February 2014

I, a universe of atoms, an atom in the universe.

Richard P. Feynman

Dedicated to My Grandfather

Summary

According to the theory of strong interactions, Quantum Chromodynamics (QCD), quarks are almost non-interacting at short distances and the interactions become stronger as the distance increases between them. This leads to the confinement of quarks within colorless objects (hadrons) containing either qqq (baryons) or quark-antiquark (mesons). Lattice QCD calculations show that at high temperature and high density, quarks and gluons behave qualitatively different from that at normal nuclear matter. According to LQCD, at temperatures (T $\sim$ 200 MeV) and/or baryon density ($\sim$ 5 to 10 times normal nuclear matter density), the quarks and gluons are no longer confined inside hadrons but are free to roam over distance nuclear sizes; this new phase of matter is called Quark Gluon Plasma (QGP). The necessary conditions for phase transition of normal nuclear matter to QGP can be produced on earth by colliding two heavy nuclei at relativistic energies.

One of the primary goals of the heavy-ion experiments at Relativistic Heavy Ion Collider (RHIC) at Brookhaven National Laboratory (BNL), New York was to study the nuclear matter under extreme condition of temperature and density. The RHIC accelerated heavy-ions up to 100 AGeV, and based upon results in the first few years, RHIC later planned a Beam Energy Scan programme to accelerate heavy-ions at various energies (from 7.7 A GeV to 39 A GeV) to search for the critical point of the QCD phase diagram. The analysis in this pursuit is still continuing.

The present work is based on the data collected in one of the four experiments that were commissioned at RHIC, the Solenoidal Tracker at RHIC, more popularly known as the STAR experiment. Before discussing the data analysis and results, the STAR detector and its subsystems have been discussed in Chapter 2. In addition to various other measurements, the STAR experiment also probes the phenomena of multiparticle production by investigating a possible scaling with the number of participating nucleons or the number of nucleon-nucleon collisions in a heavy-ion collision. The evolution of the system is probed by measuring the coefficients of expansion in the azimuthally anisotropic distribution of the final

state particles. STAR has earlier reported results on observation of number of inclusive photons scaling with the number of participating nucleons and a centrality independent limiting fragmentation behaviour in pseudorapidity density measurements of photons. STAR has also reported results on elliptic flow measurements of identified particles, primarily in the midrapidity region.

The totally indigenous preshower Photon Multiplicity Detector (PMD) was designed to study the number and spatial distribution of inclusive photons produced at forward rapidities in heavy ion collisions in the STAR experiment. In addition to recording data at 62.4 and 200 A GeV, PMD took data during Beam Energy Scan at RHIC in the year 2010 and 2011 for Au+Au collisions at 39, 27 and 19.6 GeV. In the present work, the scaling of multiplicity and the limiting fragmentation is explored at the BES energies by measuring photons in the pseudorapidity region -3.7 $\leq \eta \leq -2.3$ of the PMD. The results presented in this thesis are preliminary results of STAR Collaboration.

The various procedures adopted for cleaning the raw data and for gain normalization have been discussed in Chapter 3. The more than 40 K channel in the PMD have varying response to the minimum ionising particles, requiring a proper gain normalisation of all the channels. Detailed procedures have been evolved to remove the malfunctioning channels and eventual normalisation to produce data in the form that is amenable to analysis. The actual photon yield and the pseudorapidity distributions are obtained from the raw measurements using corrections due to detector acceptance as well as photon reconstruction efficiency and purity of photon like sample. Detailed procedures for the same were carried out, and are discussed in Chapter 3, along with the final results on rapidity distributions and the systematic errors.

In Chapter 4, the photon multiplicity and rapidity density distributions for Au+Au collisions at 39, 27 and 19.6 GeV have been compared with data from HIJING and AMPT event generators. Earlier studies have shown that the number of photon produced per average number of participating nucleon pairs increases with the beam energy and is independent of the collision centrality. Earlier studies have also shown that the photon pesudorapidity distributions normalized by average number of participating nucleon pairs, plotted as a function of $\eta - y_{beam}$, are found

to follow a longitudinal scaling which is independent of centrality, collision energy and colliding ion species. At BES energies, the same investigation revealed that the scaled multiplicity is observed to increase with decreasing centrality. The cause for this excess is not currently not understood. The present work makes an attempt to understand this using a model independent parametrisation, using two free parameters which are determined from data. By using the same parametrised form, the photon production per unit rapidity, scaled by the proposed factor as a function of $\eta - y_{beam}$ also shows longitudinal scaling even beyond the beam rapidity.

In Chapter 5, the results on elliptic and triangular flow have been obtained using AMPT with string melting and default calculations. The primary purpose of these calculations is to provide a reference for measurements of the beam energy dependence of v_2 and v_3. The study showed that the data on multiplicity, v_2 and v_3 at RHIC and at LHC could be explained by turning off initial and final state radiation in HIJING (reducing the initial entropy) but keeping relatively large cross-sections in the QGP phase. In Chapter 6, the results of elliptic flow of photons using PMD for Au+Au collision at 39 GeV have been reported. The pseudorapidity dependence of v_2 have been studied for different centralities. The rapidity integrated v_2 results have been compared to the predictions from AMPT (string melting) and found to be in satisfactory agreement, while incorporating the systematic errors on v_2.

The thesis ends with conclusions and a short outlook for future.

Acknowledgements

Foremost, I would like to express my deepest gratitude to the Almighty God for giving me the strength and determination for making my studies a success. There are number of people whose constant support helped me during the whole journey of writing the thesis. I am greatly indebted to them for their inspiration and help during my graduation.

I would like to express my special appreciation and thanks to my advisor **Dr. Rashmi Raniwala** *and* **Dr. Sudhir Raniwala**. *They both have been tremendous mentors for me. Their wide knowledge and logical way of thinking have been a great value to me. I would like to thank them for encouraging my research and for allowing me to grow as a research scientist. Their advice on both research as well as on my career have been priceless. I have no words to express my gratitude and I know that their valuable guidance will always enlighten my path during journey of life. Thank you sir and mam and I owe my success to you.*

I would also like to give special thanks to Dr. Paul Sorenson for patiently helping me. I still remember the day when I went to his office and requested him to involve me also in some analysis work with him. He provided me the opportunity and we started analysis. Our initial results did not match the expectations and I was feeling hopeless. During that phase, Paul told me to do some magic. I considered myself as magician and got the desired results. Now I understood what that magic was. It was all about building up of self confidence, fighting spirit and problem solving attitude.

My sincere thanks also go to Dr. Tapan Kumar Nayak for his encouragement and support at various stages of my work. I always feel positive energy around him which always boost me up. His soft nature always allows me to ask my novice questions to him without any sort of hesitation.

There are friends around us who will continue to motivate us through the tough times, as well as the good. My friend Sumit Basu is one of them. He always made complex physics discussions much simpler due to his friendly talk. Thank you Bro.

I am grateful to Dr.Nu.Xu, the spokesperson of STAR experiment, for providing all the help and support at various stages. I would like to thank all the STAR collaborators for many useful discussions and help on my data analysis. It was a learning and memorable experience with them all.

I would like to express my sincere and heartfelt thanks to Dr. Frank Guerts for his continuous guidance, invaluable advice, untiring support and encouragement throughout my research period.

My grateful thanks are also due to Dr. Y P Viyogi, Dr. Subhasis Chatopadhyay, Dr. Bedanga Mohanty, Dr. Madan Aggarwal, Prof. Basanta Nandi, Prof. Raghav Verma, Prof. Anju Bhasin for their support, guidance and helpful suggestions. Their guidance has served me well and I owe them my heartfelt appreciation.

I would like to forward my sincere thanks to Prof. Kananbala Sharma, Head of Department of Physics, for providing necessary facilities in the department to carry out the present work. I extend my gratitude to Prof. Deepak Bhatnagar for their words of motivation, support and encouragement during my research work.

During my Ph.D., I have collaborated with many colleagues and seniors in PMD collaboration in India for whom I have great regards. I would like to extend my sincere thanks to my collaborators at IOP Bhubaneswar, NISER bhubaneswar, Jammu University, Panjab University, Chandigarh, and VECC Kolkata. I am really grateful and thank them all for their useful suggestions and encouragement. I have spent some very memorable time with them at various conferences, meetings, workshops etc. and during my stay at BNL. I wish to thank each and every member of the PMD collaboration for all their help and support.

I could not complete my work without invaluable friendly assistance of the participants of the STAR collaboration project. Bibhuti, Renu, Amal, Prithwish, Prabhat, Subikash, Arindam, Sabita, Nirbhay deserve my sincerest thanks. Their friendship and assistance has meant more to me than I could ever express.

I am also grateful to Department of Science and Technology of the Government of India for providing the financial support.

Most importantly a special thanks to my great superstar father and mother, for all of the sacrifices that you have made on my behalf. Without their love and support, this thesis would not have been possible. I am indebted to them for giving me the freedom to choose my carrier and for constantly providing me the much needed moral support at every stage. I am also thankful to my father in law and mother in law for providing constant love and blessings. Also, I am very thankful to my younger brothers Gajendra, Utsav, and younger sisters Vandana, Anshu, Usha for their fun loving support to me throughout the writing of this thesis. I am thankful to Puneet bhaiya to gave me so much love, affection and moral support during my entire research work.

At the end I would like to express appreciation to my beloved husband Anand who was always my support in the moments when there was no one to answer my queries. He has tolerated my anger, my sorrow, my excitements and all sorts of things that I have done. Thank you Anand for your unflinching support and loving companionship throughout all these days and forever.

Contents

List of Figures

List of Tables

Chapter 1

Introduction

The behaviour of matter under extreme conditions is governed by its equation of state. Equivalently, probing the matter in extreme conditions enables the determination of the equation of state. There is evidence of dense nuclear matter in the core of neutron star with density many times the density of normal nuclear matter [1]. The Big Bang Model of the creation of the Universe also assumes an evolution that includes a phase of dense nuclear matter of unconfined quarks and gluons. Thus, it is of interest to study nuclear matter under extreme conditions in controlled experiments. Such experiments can be done by colliding nuclear matter, heavy-ions, at extremely high energies in laboratories [2]. Measuring the final state particles and their distribution in the phase space can provide information about the different evolutionary stages of the collision, including the possible formation of dense nuclear matter. Quarks and gluons may be deconfined in this dense state of matter, producing a new phase of matter called the Quark-Gluon Plasma [3].

Earlier experiments on heavy-ion collisions were limited to exposing photographic emulsions to cosmic rays, and measuring the final state particles [4]. With the advent of technology to accelerate heavy ions at high energies, experiments could be conducted under controlled conditions. A systematic study of heavy-ion collisions started more than three decades ago. Such systematic study was conducted in fixed target experiments by accelerating heavy-ions at the Alternating Gradient Synchrotron at Brookhaven National Laboratory in New York [2, 5] and at the

Super Proton Synchrotron at the European Organisation for Nuclear Research in Geneva [6]. A wealth of data and results were obtained in fixed target experiments for collisions up to nucleon-nucleon centre of mass energies of about 19 GeV with nuclei as large as Lead (Pb) [7, 8].

The Relativistic Heavy Ion Collider (RHIC) at Brookhaven National Laboratory is the first heavy-ion collider, and has been in use since the year 2000 [9–11]. RHIC has provided nucleon-nucleon centre of mass energies of up to 200 GeV for nuclei as large as Gold (Au). Two beams of Au nuclei accelerated to 100 GeV per nucleon, are made to collide with each other, giving the total centre of mass energy of 200 GeV per nucleon. During the collisions, the nuclei may compress, pass through each other, create a violent collision converting the incident energy into particles of mass, form dense nuclear matter, or a combination of all of the above. Study of matter created in these collisions helps to understand the phase diagram [12, 13].

1.1 The Phase Diagram of Hadronic Matter

Quarks and leptons are the basic building blocks of matter. The quarks carry a colour charge, and their interactions with each other, and with the gluons, are described by the currently accepted theory of strong interactions, Quantum Chromodynamics (QCD). Due to colour confinement, free quarks and gluons can not be observed in nuclear matter under normal conditions. Lattice QCD predicts that quarks will be deconfined and a new state of matter called Quark-Gluon Plasma(QGP) will be created if the temperature is extremely high.

The QCD phase diagram is shown in Figure 1.1 [14]. The horizontal axis is the net baryon density, which is closely related to the baryochemical potential μ_b. Baryochemical potential is the amount of energy needed to add an additional baryon to the existing matter. Three different forms of nuclear matter are shown in this diagram.

- normal nuclear matter at low temperatures and density.
- quark-gluon plasma at high temperatures ,

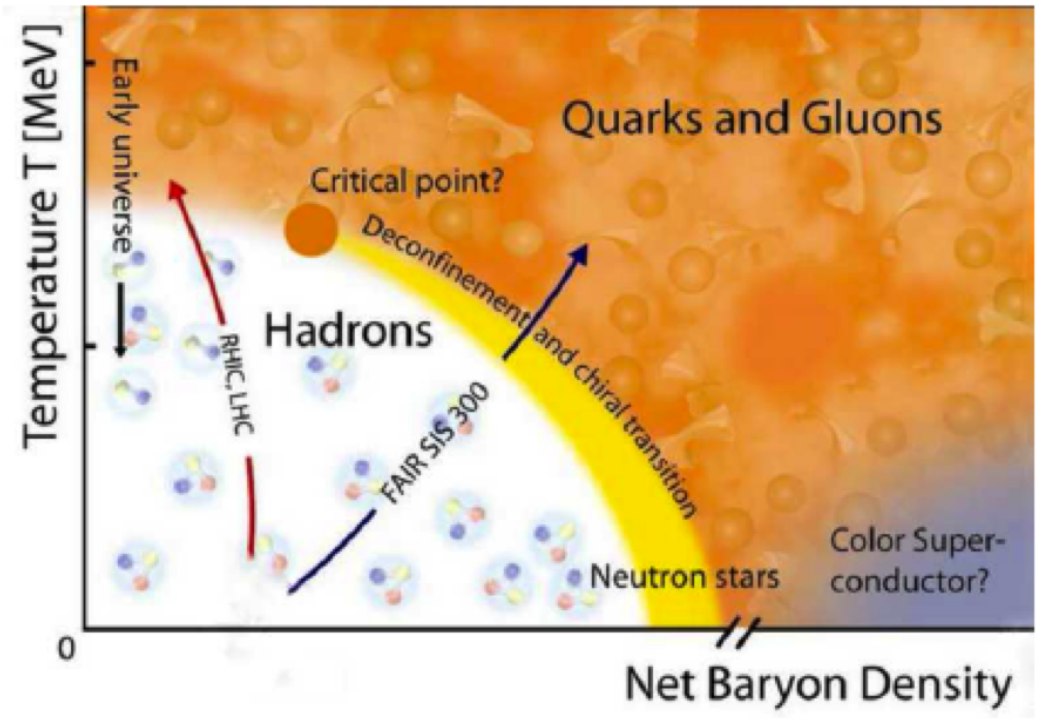

FIGURE 1.1: The QCD phase diagram

- color superconductor at low temperatures and high baryon density (e.g. neutron stars) [15].

Heavy-ion collisions lead to production of dense system which can reach energy densities and temperatures high enough for a phase transition to occur [16–18]. If μ_B is relatively small and temperature is high, a cross over to deconfined quark-gluon plasma phase is expected [19–21]. At higher μ_B, the phase transition is expected to be a first order transition. On the boundary of the hadronic and QGP phase, there is expected a critical point [22–24] where the phase transition would change from cross over to first order. However, due to the difficulty of lattice QCD calculations at finite μ_B, accurate predictions of the location of critical point in the phase diagram are still lacking.

The heavy-ion collisions at different colliding energies probe different regions of the QCD phase diagram. The main interest in theory and in experiments in high energy heavy-ion collision is to search for the QCD critical point and the effort to locate the QCD phase boundary in the phase diagram. At present, the experimental collaborations that are focusing on these exciting physics issues are STAR

(Solenoidal Tracker At RHIC) [12] and PHENIX (Pioneering High Energy Nuclear Interaction experiment) [25] at RHIC, and SHINE (SPS Heavy Ion and Neutrino Experiment) at SPS (the Super Proton Synchrotron) at CERN in Switzerland [26, 27]. The near future experiments which aim to search for a possible critical point are CBM (Compressed Baryonic Matter) [28] at FAIR (Facility for Antiproton and Ion Research) at Darmstadt in Germany, and NICA (Nuclotron-based Ion Collider facility) at Dubna in Russia [29]. All these experiments cover different regions of the phase diagram and hence complement each other. During the initial operation of the RHIC and at the Large Hadron Collider at CERN, the high temperature region is probed. To see the nature of the transition, and obtain the threshold conditions for the transition, it is important to study the collisions at varying energies. To meet this goal, the RHIC studied the collisions at a scan of beam energies from 39 A GeV to 7.7 A GeV, known as the Beam Energy Scan (BES) program.

1.2 High Energy Heavy-Ion Collisions

When two heavy nuclei approach each other at ultra-relativistic energies, they appear to be Lorentz contracted. The overlap region of the two nuclei depends upon impact parameter. The nucleons in the overlap region are called participants and those which are not participating are called spectators as shown in Figure 1.2.

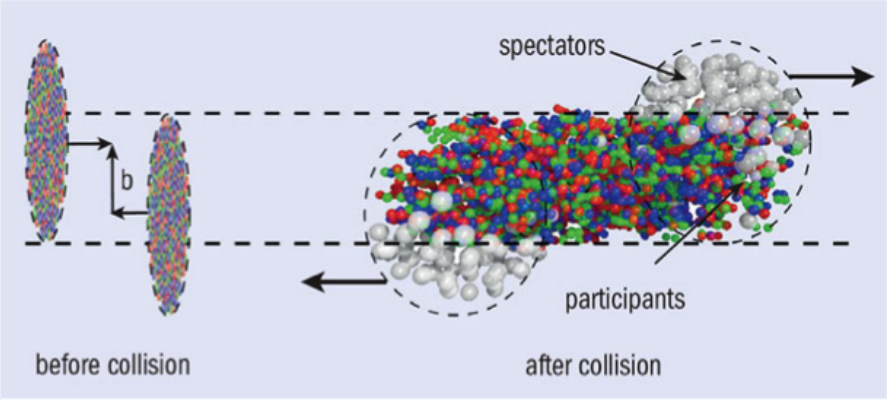

FIGURE 1.2: Schematic diagram showing collision of two nuclei with non zero impact parameter. The participants and the spectators are also shown.

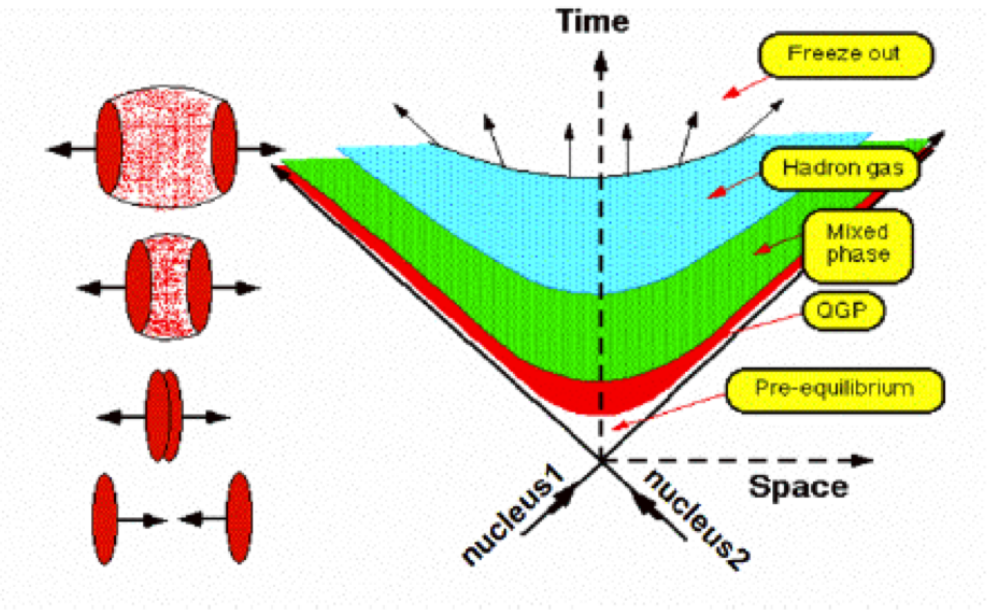

FIGURE 1.3: Space time diagram and different evolution stages of a relativistic heavy-ion collision.

When the impact parameter is small, the overlap is large, the collision is called a 'central' collisions. When the impact parameter is large, the overlap is small, the collision is called a 'peripheral' collision. For intermediate range of impact parameters, these are generally termed as semi-central collisions. The number of participating nucleons decreases as the impact parameter increases.

The dynamics of nucleus-nucleus collision can be viewed by space time diagram [30] with the longitudinal coordinate z (marked as space) and the time coordinate t as shown in Figure 1.3. The projectile and target nucleus both meet at z = 0 and t = 0. At very high energy, when a collision occurs, the large amount of energy is deposited in a small region of space for a short time, called the *fireball*. The energy deposited can produce a large number of quarks and gluons which, at sufficiently high temperature and particle density, can move freely over nuclear instead of nucleonic volumes. The quarks and gluons can interact strongly and may lead to a locally equilibrated state, quark gluon plasma,which is shown by the red band in Figure 1.3. The matter expands under its own strong internal pressure and cools down. When its temperature comes down to around T_c (critical temperature), the phase transition from QGP to hadronic matter occurs (hadronization). When the system cools further, below a certain temperature, there are no more elastic

or inelastic interactions. After this final freezeout, the particles stream through freely to the detector.

1.3 Evolution of Heavy-Ion Collisions

The heavy ions being extended objects, the geometry plays an important role in the evolution dynamics of the collision. Different stages of the collision can be probed using different measurements. The results of measurements reflect the initial geometry of the collision. The entire evolution of the collision can be described by an initial state governed by geometry, an expansion of matter depending upon its equation of state and the subsequent interactions, and the freezeout.

1.3.1 Initial Geometry and Characterisation

When two nuclei collide, the overlap region is decided by the impact parameter of the collision. The number of participating nucleons, N_{part}, in the collision affect the total energy deposited in the overlap region, and hence also the total number of particles produced. The measurement of the number of particles produced, to the first order, is a good estimate of the impact parameter of the collision, and of the energy density obtained in the system.

Various model calculations describe that with increasing collision energy, the produced particle multiplicity also increases. Measurments by PHENIX experiment at $\sqrt{s_{NN}} = 130$ GeV, reveal that collisions at RHIC generates $\sim$0.8 GeV of transverse energy per produced charge particle near midrapidity and independent of collision centrality. Under certain assumptions, suggested by Bjorken, the estimate of the initial spatial energy density [30] of the bulk matter is given by :

$$\epsilon_{Bj} = \frac{dE_T}{dy}\frac{1}{\tau_0 \pi R^2} \tag{1.1}$$

where τ_0 is the formation time and R is the initial radius of the expanding system. With reasonable estimates for these parameter values ($\tau_0 \approx 1 fm/c, R \approx 1.2A^{1/3}$), the energy density in Au+Au collisions at RHIC is $\sim$ 5 GeV/fm^3, which is well above the critical energy density $\sim$ 1 GeV/fm^3 expected from LQCD for the transition to the QGP phase.

The number of participating nucleons can be estimated on an average in a Glauber model approach [31]. Assuming a uniform density of the nuclei, the number of protons and neutrons can be estimated within a certain overlap region by using the nuclear thickness function. However, this approach provides only the mean number of participating nucleons. The distribution of the number of participating nucleons and the total (identified) particle multiplicity show a very similar characteristic behaviour, indicating a possible correspondence between multiplicity and impact parameter in minimum bias collisions. While the above may be correct on an average, fluctuations in particle production processes, and in the number of participating nucleons at a given impact parameter, inhibit a unique correspondence between the measured multiplicity and the impact parameter.

As a first approximation, it is tempting to consider nuclear collsions to be a superposition of nucleon nucleon collisions. Considering that there are two participants in a pp collision, it is interesting to study the multiplicity in a nucleus - nucleus collision, scaled by the number of participants, or scaled by the number of collisions. If the observed multiplicity demonstrates scaling with the number of participants, then the dominant process for particle production is 'soft', where the momentum transfer is small. However, if the multiplicity is seen to scale with the number of collisions, then the dominant process for particle production is 'hard', where the momentum transfer is large. Multiplicities and rapidity densities are characterised by estimates of N_{part} and N_{coll}. The initial shape of the colliding zone is decided by the positions of the nucleons. Both multiplicity and the initial shape are closely related to the expansion and subsequent freezeout of the nuclear matter.

PHOBOS experiment searched for a possible scaling of pseudorapidity density with N_{part} over a large pseudorapidity window [32]. The centrality dependence of charged particle density from PHOBOS experiment is shown in Figure 1.4. Panel (a) of Figure 1.4 shows the total charge particle multiplicity measured within the

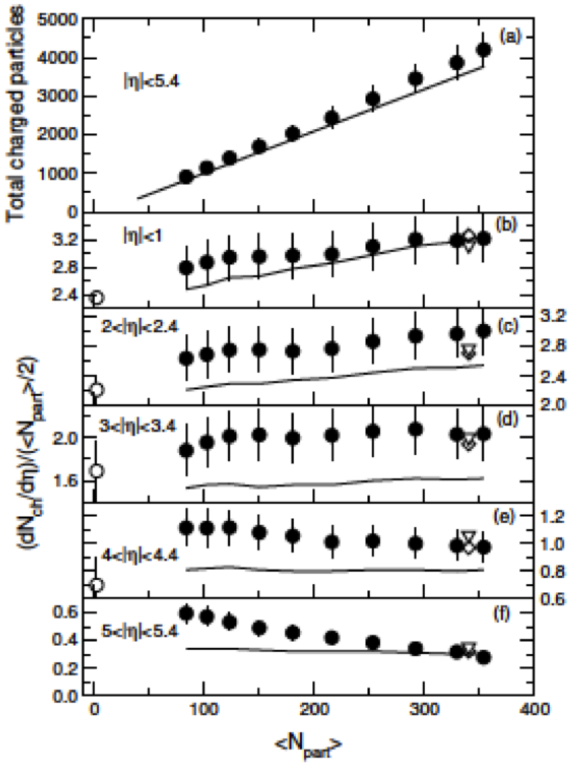

FIGURE 1.4: PHOBOS result on centrality dependence of $dN_{ch}/d\eta$ for different eta ranges in Au+Au collisions at $\sqrt{s_{NN}} = 200$ GeV [32].

range $|\eta| < 5.4$ for Au+Au collision a $\sqrt{s_{NN}} = 200$ GeV. Panel (b)-(f) shows the $< N_{part} >$ dependence of $dN_{ch}/d\eta$ per participant nucleon pair, plotted for five different eta bins. In all figures, PHOBOS has also shown predictions from an event generator HIJING as a solid line. Considering that the data shows behaviour that changes with the η region, the dependence on N_{part} is not the same everywhere. Further studies have attempted to explain the pseudorapidity density by considering a contribution that depends upon N_{part} and another that depends on N_{coll}.

Even in the case of symmetric nuclei, the overlap region is asymmetric because of density fluctuations inside nuclei. Many event generators that use the Glauber approach, generate positions of the nucleons in the nuclei using Monte Carlo methods, and assume a straight line trajectory for the nucleons. When two nucleons from different nuclei approach a distance less than the corresponding radius of a geometrical cross section of interaction, then the nucleons are considered to be

interacting, or participating. Such a simulation of nuclear positions and their approach towards each other is considered as one event in simulated data. Different event generators model the dynamics of collisions differently. By simulating a large number of events, the event generators can provide a distribution of the number of participants in a given impact parameter range. For each event, the information on the number of nucleons participating N_{part}, and the number of nucleon-nucleon collisions N_{coll} can be recorded. The same Monte Carlo event generators can provide an event-by-event position (spatial) map of the nucleons in the overlap region. The fluctuations in the number of nucleons, and in their positions, both contribute to the final state observables as will be discussed in the next section(s).

Further, features of particle production at different rapidities in collision of different beam energies may demonstrate the phenomena of 'limiting fragmentation' [33], and will be discussed in the next section(s).

1.3.2 Expansion of Matter and Freezeout

After the initial collision, the large energy deposited in the *fireball* materialises in thousands of partons interacting strongly. These interactions may lead to a thermal equilibrium. The expansion can be modeled using hydrodynamical evolution [34–36]. Any solution of hydrodynamical evolution requires an equation of state of the system, which along with the initial conditions, define the starting point of the system. Due to high parton density, the mean free path λ between the interactions is much smaller than the size of the *fireball*. This allows to assume that the system is in local thermodynamic equilibrium.

In addition to the radial flow of matter during the expansion, there is also an anisotropic flow caused due to the azimuthally anisotropic collision zone. The spatial anisotropy causes different pressure gradients in the direction along the impact parameter and perpendicular to it. Re-scattering processes amongst the produced particles transform this spatial deformation into momentum space with more matter flowing out along the reaction plane (i.e. in the plane defined by impact parameter and beam direction) than perpendicular to it. This causes the azimuthal distribution of particles to be anisotropic and correlated with the

reaction plane. This is termed as anisotropic flow [37–39]. As more particles push out along the event plane, the initial asymmetry of the fireball vanishes. This is called the self-quenching behaviour of flow. The anisotropic flow predominantly develops in the intitial stages, can be measured in the final state particles, and serves as a probe to study the initial stages of expansion in the evolution of heavy-ion collision.

Once the system expands, the hydrodynamic fluid is transformed to particles, a process modeled by the Cooper-Frye freezeout mechanism. These particles continue to interact inelastically until they cool down such that inelastic collisions do not occur. At this point, the hadron composition of the matter is frozen, the relative ratio of different hadron species are fixed, and this is referred to as the chemical freezeout. Subsequently, the particles continue to interact elastically until kinetic freezeout, beyond which the particles stream away freely. Since the particle ratios are fixed at the chemical freezeout, the measurement of their yields can provide information about the system during this stage [9].

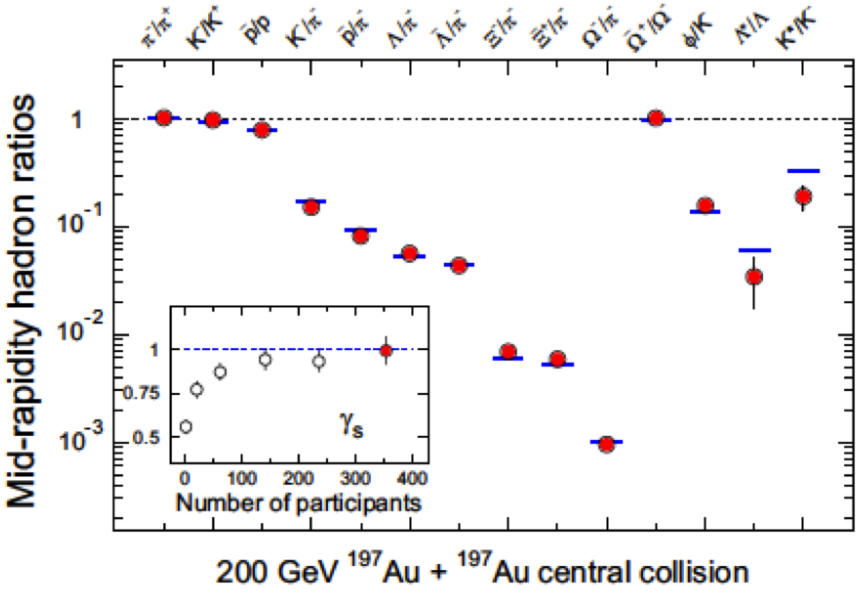

FIGURE 1.5: STAR results on ratios of p_T integrated mid-rapidity yields for different hadron species for central Au+Au collisions at $\sqrt{s_{NN}} = 200$ GeV. The horizontal bars represent statistical model fits to the measured yield ratios. The fit parameters are $T_{ch} = 163 \pm 4$ MeV, $\mu_B = 24 \pm 4$ MeV, $\gamma_s = 0.99 \pm 0.07$. The variation of γ_s with centrality is shown in the inset [9].

At chemical freezeout, the measured ratio can be used to constrain the system temperature and the baryonic chemical potential μ_B. The statistical model assumes that the system is in chemical and thermal equilibrium [40]. A comparison of the experimental p_T integrated hadron yield ratios measured by STAR experiment for central Au+Au collisions, with statistical model fits is given in Figure 1.5. The good fit obtained in describing the ratios by model calculations indicates that the light flavors have reached chemical equilibrium for central and semi-central collisions at temperature $T_{ch} = 163.5$ MeV [9].

Statistical model is able to explain the ratios of a large number of particle species using few parameters like baryon chemical potential, chemical freezeout temperature, and strangeness chemical potential. The strange particle ratios do not fit well, suggesting that these might freezeout at a different temperature. By including an additional factor, termed as the strangeness suppression factor γ_s, the statistical model is able to fit the strange particle ratios also. The variation of γ_s with centrality is shown in Figure 1.5. The value of γ_s reaches ~ 1 for most central collisions.

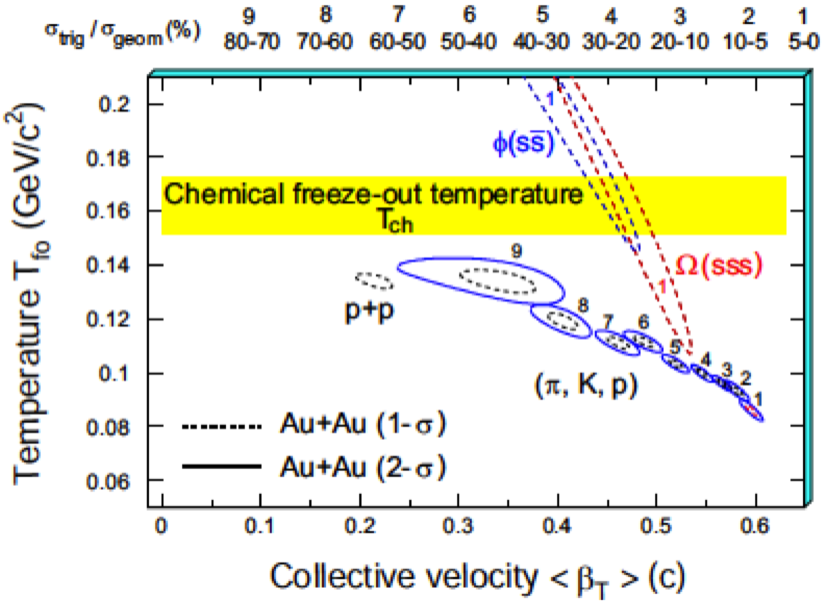

FIGURE 1.6: STAR results on the χ^2 contours for temperature T_{fo} and radial flow velocity β_T extracted from thermal and radial flow fits for hadrons produced in Au+Au collisions at 200 GeV. The centrality selection are indicated on the top of the plot [9].

Particles which are formed as a result of chemical freezeout, interact with each other and their space time evolution is modeled using hydrodynamics. The characteristics of the system at kinetic freezeout can be explored by studying the transverse momentum distributions for various hadron species [9]. The transverse momentum distribution of hadrons reflects the later conditions in the evolution as well as the integrated effect of expansion from the beginning of the collision. The result on spectra have shown that the details of the spectra are a combined effect of collective radial flow and a thermalised system yielding a temperature termed as the kinetic freezeout temperature T_{fo}. For each event centrality, the spectra of π, K, p were fit to a blast wave model using a single value of radial flow velocity $<\beta_T>$ and temperature T_{fo}, as can be seen in Figure 1.6 for Au+Au collisions at 200 GeV. It has been observed that the bulk of the system which consists of kaons, pions and protons become cooler at kinetic freezeout and develop a stronger collective flow.

1.4 Experimental Observables to Study Heavy-Ion Collisions

Systematic experimental studies and theoretical advances have provided a large number of experimental observables to discern the mechanism of heavy-ion collisions. Depending upon the various stages of collisions and evolution process, these signatures reveal insights about the collision processes and its different stages. The signals which are produced in the first stages of the collision are known as hard probes. There is a high momentum transfer between the colliding partons. This includes the signatures such as jet quenching and nuclear modification factor, direct photons and dileptons. The signals which are produced in the later stage of the collision are known as soft probes. These signals are affected primarily by the hadronization stage and may contain information about the properties of phase transition and the QGP. Results on particle multiplicities and their rapidity distributions provide information about particle production mechanism through scaling and limiting fragmentation. Initial state anisotropies determine the measurements of flow. Participant scaling and limiting fragmentation, and azimuthal anisotropy

are the two topics that are addressed in the present thesis using measurements of photons in the completely indigenous Photon Multiplicity Detector (PMD), and using data from event generators. These are discussed in greater detail in the following sub-sections. Some observables due to hard probes are also mentioned briefly.

1.4.1 Participant Scaling and Limiting Fragmentation

If the particle multiplicity scales with $< N_{part} >$, it shows that the particle production is due to soft processes whereas the scaling with $< N_{coll} >$ indicates that the particle production is due to hard processes. The results of PHENIX experiment showed that the charged particle production scales with a combination of $< N_{part} >$ and $< N_{coll} >$ at mid-rapidity, which indicates a significant contribution of hard processes in the particle production as shown in Figure 1.7 [41]. The data is fitted by a function $dN_{ch}/d\eta = A \times N_{part} + B \times N_{coll}$ and the details of obtaining the values of N_{part} and N_{coll} can be seen in [41] .

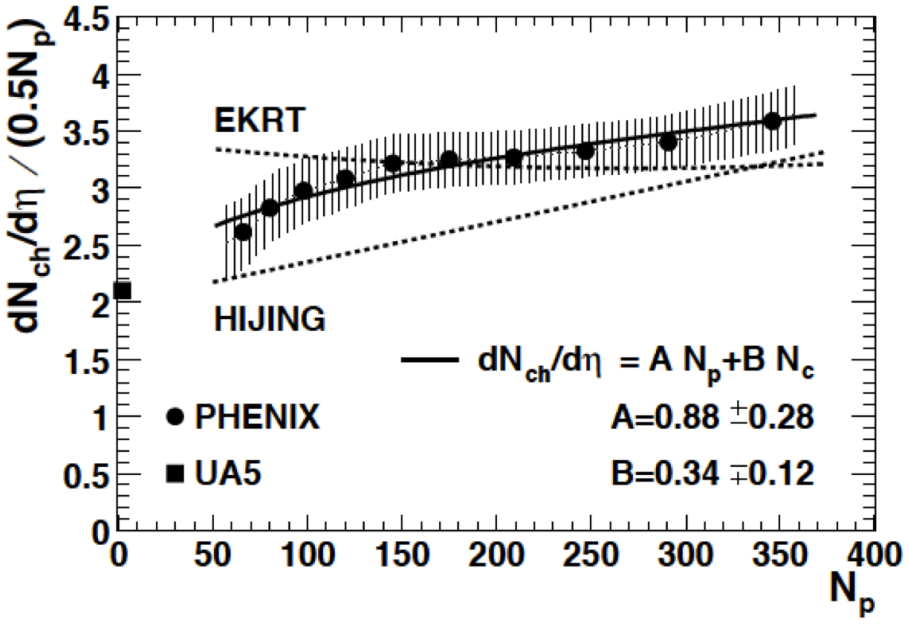

FIGURE 1.7: PHENIX results on charged-particle pseudorapidity density per participant pair vs. the number of participants. Predictions from model calculations are also shown. The shaded area represents the systematic errors on $dN_{ch}/d\eta$ and N_p. [41]

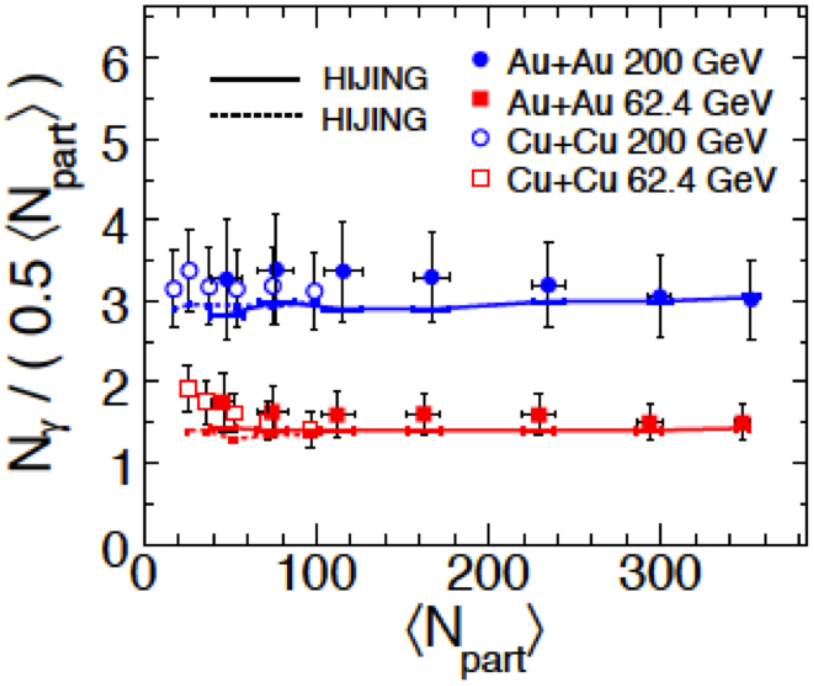

FIGURE 1.8: STAR results on the number of photons divided by $< N_{part}/2 >$ as a function of average number of participating nucleons for Au+Au and Cu+Cu at $\sqrt{s_{NN}}$ = 200 and 62.4 GeV. Results from HIJING are shown by solid line for Au+Au and dashed line for Cu+Cu [42, 43].

Figure 1.8 shows the variation of photon multiplicity per average number of participating nucleon pairs with $< N_{part} >$ for Au+Au and Cu+Cu at 200 and 62.4 GeV within eta range -3.7 $\leq \eta \leq$ -2.3 [42, 43]. Results from HIJING [44] are shown by solid line for Au+Au and dashed line for Cu+Cu collisions in the same figure. The photon multiplicity is seen to scale with $< N_{part} >$ at forward rapidity, which indicates that the photon production at forward rapidity is due to soft processes.

In relativistic heavy-ion collisions, large number of particles are produced. One convenient way to describe heavy-ion collisions is by measuring particle density in rapidity or pseudorapidity. The particle multiplicity contain information about the entropy of the system and the gluon density in the heavy-ion collisions. Photon pseudorapidity distribution are measured for Au+Au and Cu+Cu collisions at $\sqrt{s_{NN}}$ = 200 and 62.4 GeV [42, 43] for all centrality bins and are shown in Figure 1.9. The photon multiplicity is found to increase from peripheral to central collisions. The result have been compared to those obtained from HIJING event

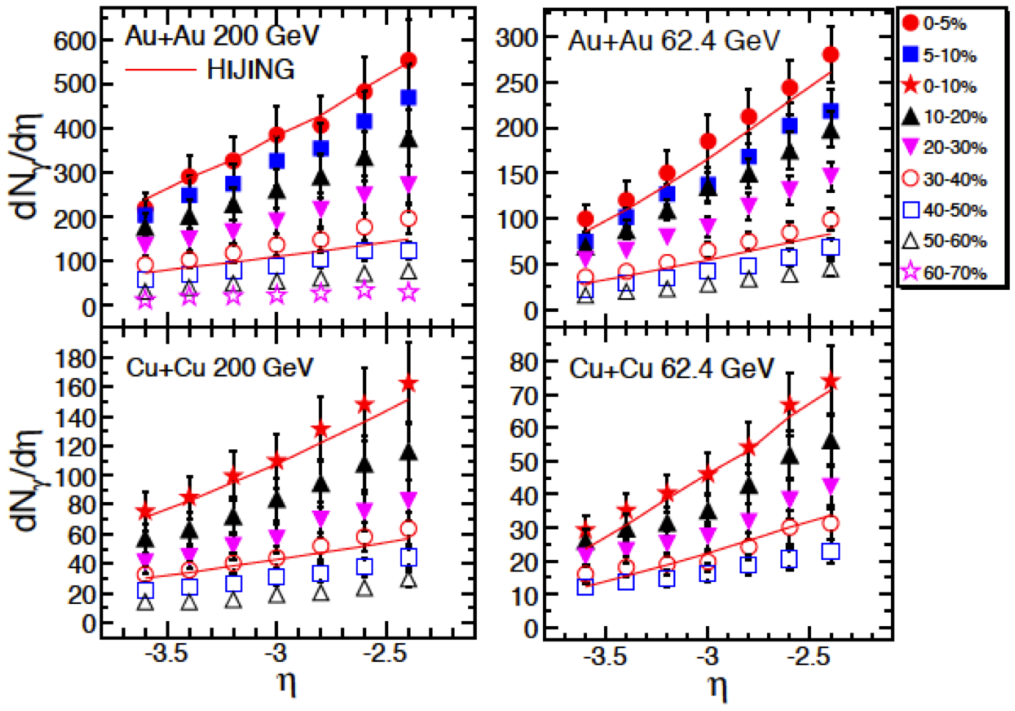

FIGURE 1.9: STAR results on photon pseudorapidity distributions for Au+Au and Cu+Cu at $\sqrt{s_{NN}}$ = 62.4 and 200 GeV. The solid lines are result from HIJING for central (0-5% for Au+Au and 0-10% for Cu+Cu) and 30-40% mid central collisions [42, 43].

generator for central (0-5% for Au+Au and 0-10% for Cu+Cu) and 30-40% mid-central collisions are also shown in the Figure 1.9 (solid curves). For both beam energies and colliding ion species the HIJING results are in reasonable agreement with the data.

With increase in the center of mass energy the rapidity distribution of all particles is expected and observed to become broader due to kinematics. To observe more interesting physics at forward rapidity, it was proposed that the rapidity distribution should be observed in the frame of reference of one of beam nuclei. This can be checked by shifting the distribution by beam rapidity and study it as a function of $\eta - y_{beam}$. Model predictions suggest that with increasing energy the rapidity distributions would reach a limiting value beyond which they will not grow any further. This behaviour is also called longitudinal scaling. This has been observed in a number of different experiments for different particle species and the physics phenomenon which is causing this is still being explored. In order to study

limiting fragmentation in different colliding systems, the rapidity distribution is scaled with the number of participant pairs. Normalizing with the number of participant pairs also allows us to study limiting fragmentation as a function of event centrality.

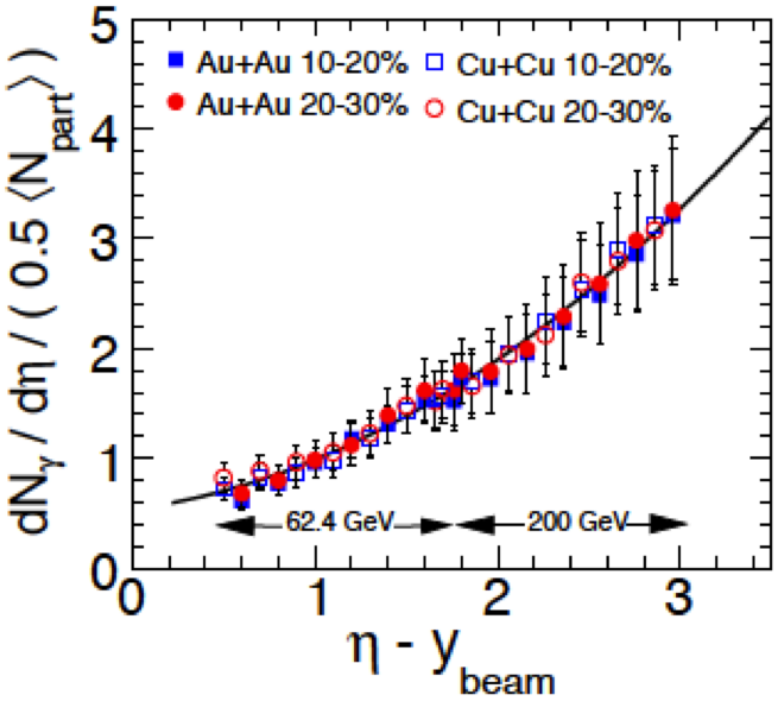

FIGURE 1.10: STAR results on photon pseudorapidity distributions normalized by the average number of participating nucleon pairs for different collision centralities are plotted as a function of pseudorapidity shifted by the beam rapidity for Au+Au and Cu+Cu collisions at $\sqrt{s_{NN}}$ = 62.4 and 200 GeV. The solid line is a second order polynomial fit to the data [42, 43].

Charged particles exhibit energy independent limiting fragmentation behaviour. This has been observed in central Au+Au collisions in BRAHMS [45, 46] and PHOBOS experiments [32, 47]. BRAHMS experiment reported that the longitudinal scaling is also independent of collision centrality, while PHOBOS observed a centrality dependent limiting fragmentation behaviour. When photon pseudorapidity density normalized by $< N_{part}/2 >$ are plotted as a function of $\eta - y_{beam}$ for Au+Au and Cu+Cu collision at $\sqrt{s_{NN}}$ = 200 and 62.4 GeV and show longitudinal scaling, independent of beam energy and collision centrality as shown in Figure 1.10. The solid line is a second order polynomial fit to the data. It was

also shown that the longitudinal scaling for produced photons is independent of colliding ion species.

These features of photon production are to be investigated at other energies, results of which will facilitate the complete understanding of the nuclear equation of state.

1.4.2 Azimuthal Anisotropy and Fluctuations

When two heavy nuclei collide the reaction volume is azimuthally asymmetric. Strong interaction in this volume convert this initial spatial anisotropy to momentum anisotropy as shown in Figure 1.11. As a result the distributions of particle in the azimuthal plane become anisotropic [37–39]. The anisotropy of the particle yield can be characterized by a Fourier expansion [48, 49]

$$\frac{dN}{d(\phi - \Psi_r)} \propto= 1 + 2\sum_n v_n cos[n(\phi - \Psi_R)] \tag{1.2}$$

where ϕ is the azimuthal angle of the particle, ψ_R is the reaction plane angle, where the reaction plane is the plane containing the impact parameter direction and the beam direction, v_n's are the n Fourier coefficients.

Measurement of the Fourier coefficients v_n for different hadrons provides information on the phase present in the initial stages of evolution of the collision and degree of thermalisation. These coefficients can be determined using different techniques, few of which are dicussed in Chapter 5. The first few coefficients are v_1 the directed flow, v_2 the elliptic and v_3 the triangular flow. Figure 1.12 gives the geometric representation of the origin of these three coefficients for a realistic positions of the nucleons.

Some of the important features of the observed elliptic flow at higher energy are:

(i) v_2 values measured for each centrality were observed to be large at RHIC energies and were found to be scale with the geometric eccentricity of the

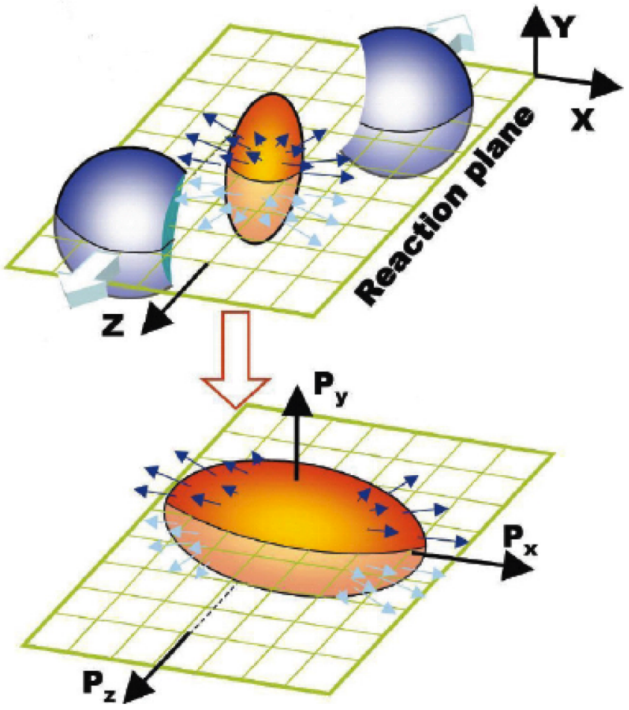

FIGURE 1.11: Schematic diagram showing event anisotropy in spatial and momentum space with respect to reaction plane

overlap volume. This established that v_2 is arising from the initial anisotropic conditions.

(ii) v_2 as a function of transverse momentum (p_T) for various particle species for $p_T < 1.0$ GeV/c showed mass ordering in Figure 1.13. At a given p_T,the hadron with higher mass has a lower value of v_2. This observation an be understood using hydrodynamical models [50].

(iii) For $p_T > 2.0$ GeV/c the v_2 values for all hadrons saturated, with mesons and baryons showing a clear split and saturating at different values as shown in Figure 1.14. This suggested a number of constituent quark (n_q) scaling (NCQ scaling) i.e when v_2/n_q was studied as a function of p_T/n_q all particles species showed exactly the same trend as shown in Figure 1.15. This is interpreted as a possibility that during the initial stages of evolution, when flow was developing, the system showed partonic degrees of freedom. During hadronization, three quarks coalesce to form baryons and a quark and anti-quark form a meson [50].

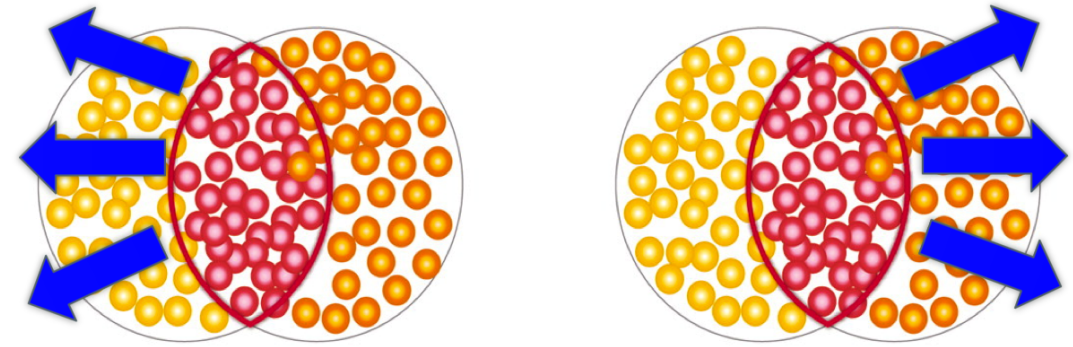

(a)

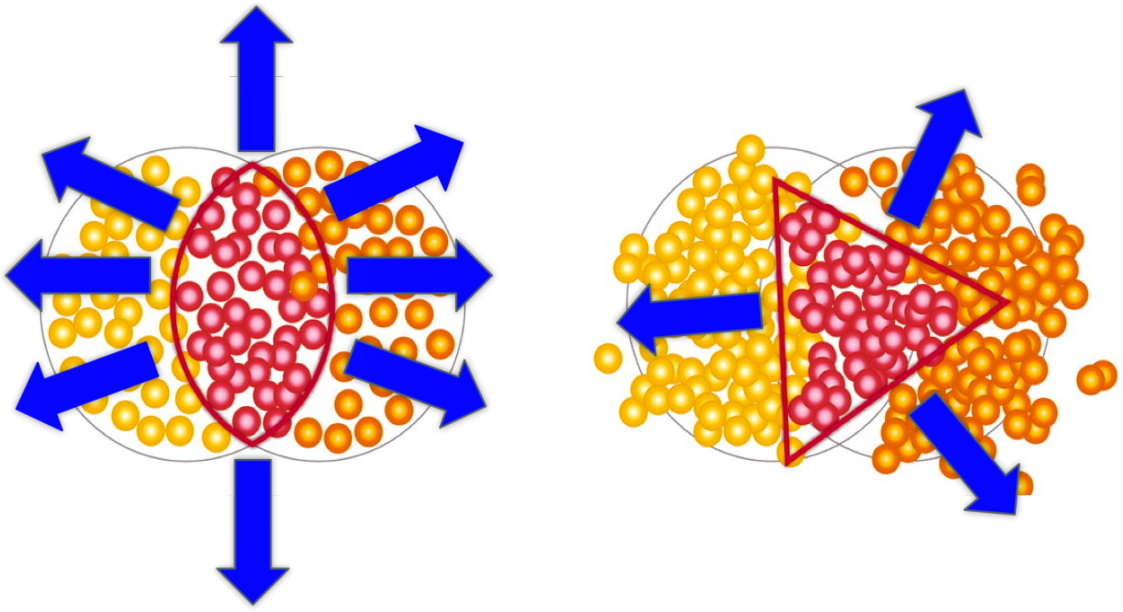

(b)

FIGURE 1.12: Schematic diagram showing (a) Directed flow negative (left) and positive (right) (b) geometric representation of elliptic flow (left) and for triangular flow (right).

It is expected that at lower energies, the NCQ scaling would disappear if the matter does not pass through the partonic phase. This was also observed by STAR Collaboration which studied elliptic flow of charged particles as well as identified particles at all the BES energies [51–53]. At the BES energies, v_2 of the particle and antiparticle were systematically studied and were found to be different, indicating a breakdown of NCQ scaling, providing a possibility of determining the threshold for production of the partonic medium.

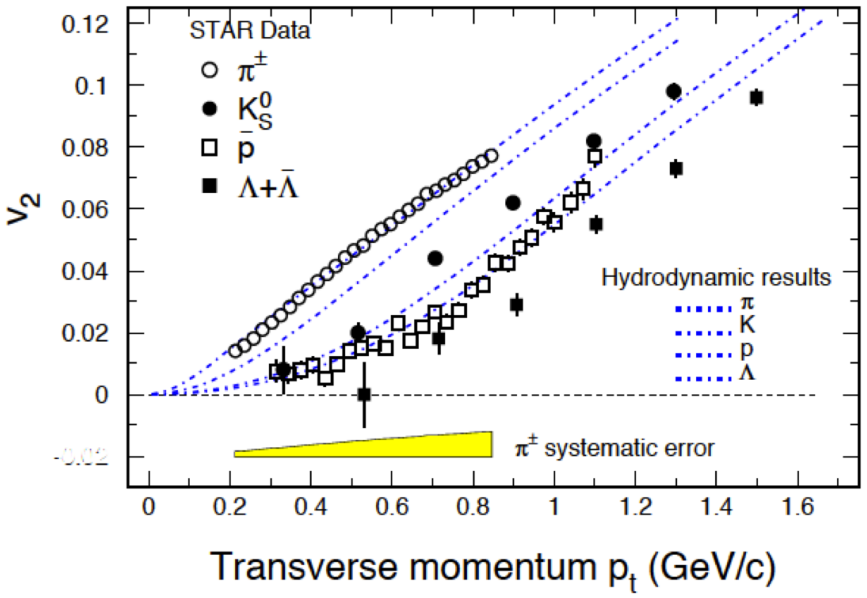

FIGURE 1.13: STAR results of the p_T dependence of the elliptic flow parameter v_2 in Au+Au collisions at 200 GeV. The hydrodynamic calculations are shown in dot-dashed lines. The figure is taken from [50]

.

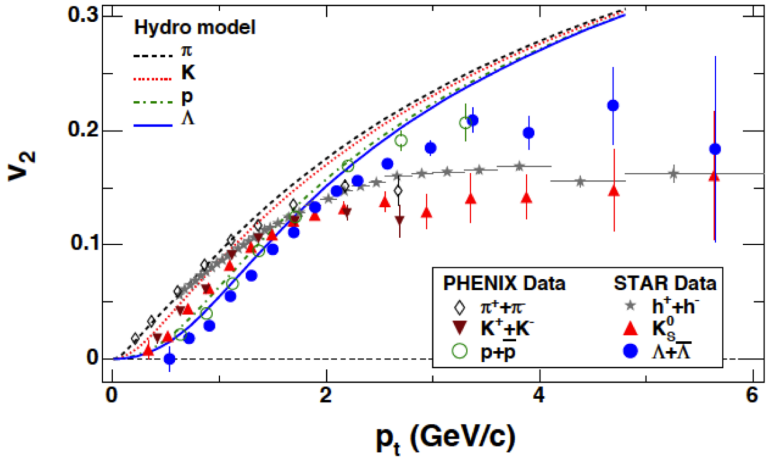

FIGURE 1.14: v_2 as a function of p_T for different hadrons in minimum bias Au+Au collsions at 200 GeV. Here hydrodynamical calculations are shown by solid and dotted curves. The figure is taken from [50]

1.4.3 Jet Quenching and Nuclear Modification Factor

In a heavy-ion colllision, hard scattering between two incoming partons can create a pair of energetic high p_T fast partons which move back to back in the centre of

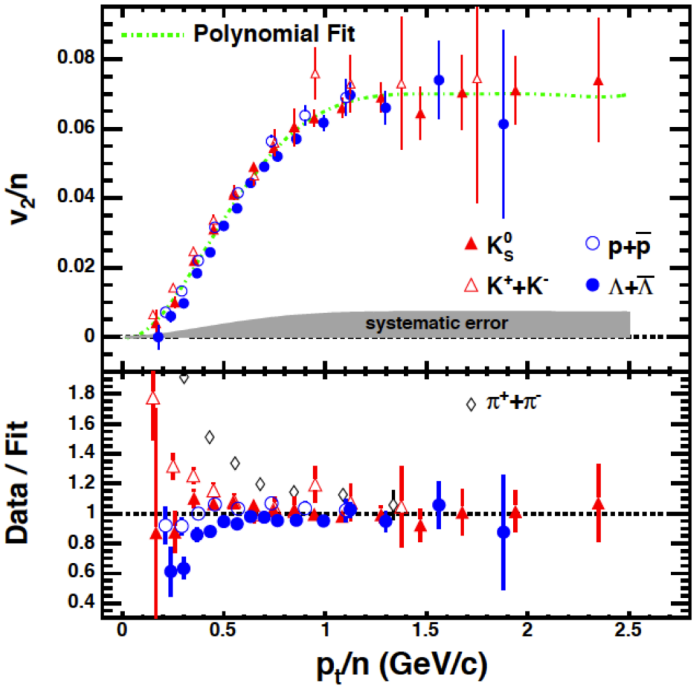

FIGURE 1.15: Upper panel : v_2/n vs. p_T/n for identified particles measured by the STAR exeriment. Here n is the number of constituent quarks. The dashed dotted line is the polynomial fit to the data. Lower panel : The data from the upper panel is divided by the polynomial fit as a function of p_T/n. The figure is taken from [50]

.

momentum (CM) Frame. Fragmentation of these partons leads to production of hadrons which are observed as a "jet" around the position of the initial parton. If a parton pair is produced in an AA collision, it is likely that one of the resulting jets passes through the dense medium formed in the interaction. If the medium making up the fireball is QGP the initially produced parton undergoes multiple interactions with the medium and looses its energy in the process. This partial or complete "disappearance" of jet is called as "jet quenching" [54, 55]. The degree of quenching of jet , therefore provides information on the properties of the medium and its interactions. Jet quenching has been studied extensively by RHIC experiments [56, 57]. To estimate the effect of medium on observables, the results are compared with corresponding results in pp collisions. The ratio of the two, normalised to the number of collisions in A+A, is termed as the nuclear modification factor R_{AA}. For cold nuclear matter, R_{AA} is expected to yield a value of 1. Smaller than 1 values of R_{AA} indicate the effect of medium on the observable.

It is now standard practice to estimate the medium effects using this method for all observables, including those mentioned in the following.

1.4.4 Strangeness Enhancement

The colliding nuclei are normal nuclear matter, and consist of protons and neutrons which in turn are made of up and down quarks. Strange quarks are only produced in the collision of partons. While s$\bar{s}$ pairs can be formed by collision of quarks (up and down) the dominant mode of production is through gluon gluon collisions (gg->s$\bar{s}$) which are present if the Quark-Gluon Plasma is formed [58]. This makes the abundance of strange quarks sensitive to the state of matter formed during the collision. Formation of a large number of ssbar pairs leads to a larger number of strange and multistrange hadrons. Strangeness enhancement is experimentally measured by comparing the yield in AA collisions per participant pair to the yield in pp collisions. Enhancement factors of 2-3 as compared to pp collisions have been reported in AuAu collisions at 200 GeV by STAR experiment. The enhancement is even larger 5-7 for multi-strange particles in central CuCu and AuAu collisions at200 GeV [59].

1.4.5 J/Ψ Suppression

J/Ψ is a bound state of charm and anticharm quark [60]. Like s$\bar{s}$, c$\bar{c}$ are also produced during a heavy-ion collision by gg->c$\bar{c}$. Interactions of J/Ψ with other hadrons during AA collision can cause them to breakup, leading to "normal" supression of their yield to a small extent. In a high density environment of QGP, the c and cbar are Debye screened from each other due to presence of other color charges. This is similar to screening of two charged particles in a di-electric medium due to polarization of the medium. As a result even though a large number of hadrons with single charm (or anticharm) are produced, the production of J/Ψ is suppressed and is termed as anomalous suppression. Features of anomalous suppression observed at SPS energies [61, 62] could not be explained by hadronic models. Anomalous suppression has also been confirmed at RHIC energies [62].

1.4.6 Fluctuations and Critical Phenomena

When a system approaches a critical point of continuous phase transformation the correlation length ξ diverges and microscopic details become irrelevant [22–24]. Such critical states of matter are highly correlated, and particularly sensitive to external perturbation.

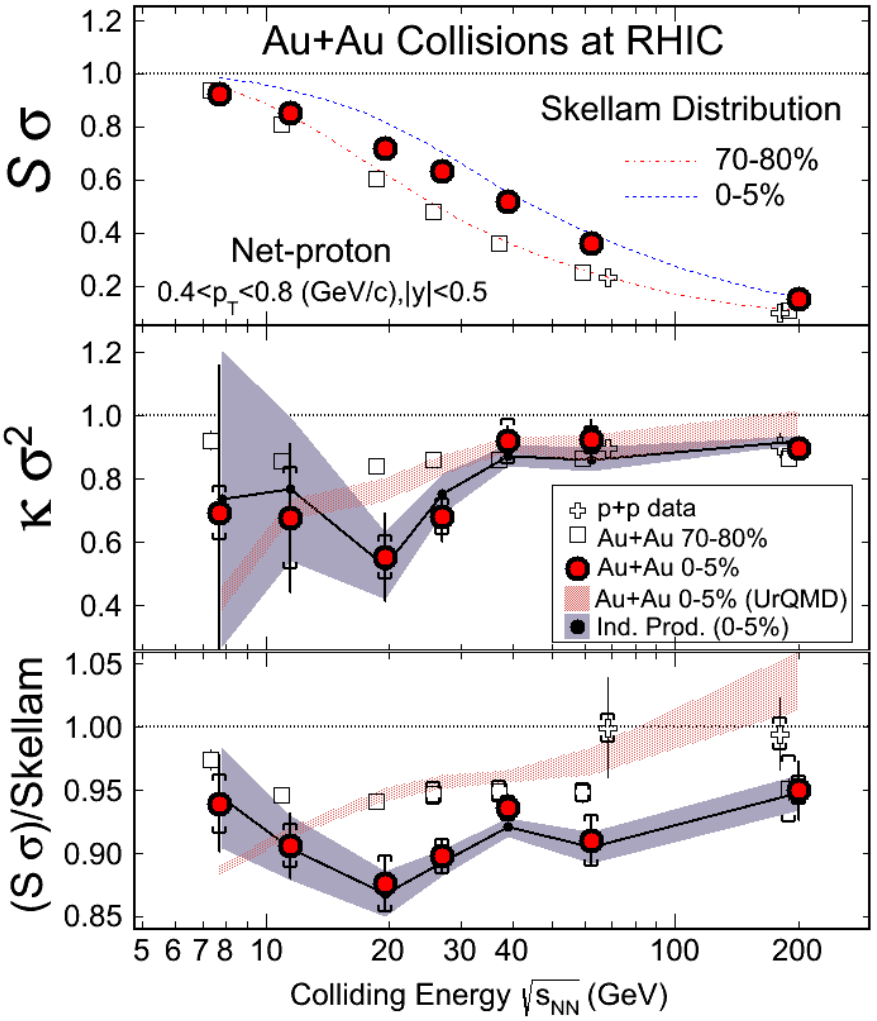

FIGURE 1.16: Collision energy and centrality depe ndence of the net-proton $S\sigma$ and $K\sigma^2$ from Au+Au and p+p collisions at RHIC. The width of the bands represents statistical u ncertainties. The hadron resonance gas model (HRG) values for $S\sigma$ and $K\sigma^2$/Skellam are unity. The error bars are sta- tistical and caps are systematic errors [63].

Any external perturbation is likely to cause large fluctuations. Experiments measure multiplicities N_π and N_p event by event. These quantities fluctuate event by event and their distribution is Gaussian. The fluctuations conform to a Gaussian

distribution. At critical point the fluctuations deviate from those expected from a Gaussian distribution. The correlation length is seen to affect the moments of the fluctuations, the second moment $< (\delta N)^2 > \sim \xi^2$. The higher moments have an even stronger dependence on ξ. Therefore study of the higher moments for various conserved quantities as a function energy of collision is a sensitive probe for locating the critical point on Hadron-QGP Phase transformation boundary. Experimentally, instead of moments of distributions of conserved quantities, it is easier to study ratios of the moments $\kappa\sigma^2$ and $S\sigma$, since the effects due to finite volume cancel out. One of the main goals of RHIC BES program was to search for the critical point. STAR experiment has studied the higher moments of net proton distributions [63] for a range of center of mass energy from 7.7 to 200 A GeV as shown in Figure 1.16. The measurements are carried out at mid-rapidity for various event centrality. The experimental observations are not reproduced by models that do not include a critical point in the phase diagram. More studies with higher statistics are underway for understanding the results. Fluctuations in net charge and net strangeness distributions are also being studied.

1.5 Beam Energy Scan (BES) at RHIC

The main goal of the beam energy scan at RHIC is to :

(i) To locate the existence of the critical point in the QCD phase diagram

(ii) To search of the evidence of the first order phase transition in the QCD phase diagram

(iii) To understand the properties of QGP

The BES phase-one recorded data successfully in 2010 (Run10) and in 2011 (Run11). STAR took data for Au+Au collision at $\sqrt{s_{NN}}$ = 7.7, 11.5 and 39 GeV in year 2010 and at $\sqrt{s_{NN}}$ = 19.6 and 27 GeV in year 2011. For these energies, the corresponding μ_B coverage is estimated from 112 to 410 MeV. This program provides a suitable access to most interesting region in QCD phase diagram to understand the bulk properties of the QGP. The measurements and the analyses in the present thesis correspond to data recorded as a part of the BES programme.

1.6 Organization of the Thesis

The work presented in the thesis deals with results of investigation of scaling and limiting fragmentation in photons in forward rapidity region in the BES energies. The thesis also investigates the ability of AMPT event generator to explain the published results on v_2 and v_3 of charged particles from BES energies to the energies at the Large Hadron Collider (2.76 A TeV). The elliptic flow, v_2, of photons has been measured at 39 A GeV and compared with AMPT predictions. To meet this aim, the data at BES energies from the Photon Multiplicity Detector in the STAR experiment is used. The results presented in this thesis are preliminary results of STAR Collaboration.

Chapter 2 contains a brief overview of the STAR detector and its subsystems which are connected with the analyses in the present work, and provides some details of working of PMD. Chapter 2 also contains the details of centrality selection for the various energies, as adopted by STAR, and the parameters characterising the centrality (N_{part}). In Chapter 3, the details of raw data, identification of bad channels and gain nornalization process has been provided. To correct the measured values of photon yield for efficiency and purity, simulations have been performed for different centralities, rapidity windows and the correction factors obtained for different occupancies in the detector. The procedure has been systematically shown in this chapter. The chapter also includes results on photon rapidity density distributions in Au+Au collisions at 39, 27 and 19.6 A GeV. Detailed estimates of systematic errors on rapidity densities are also included in this chapter. In Chapter 4, the results on photon multiplicity and rapidity density distributions for the three energies are compared with event generators, and the data investigated for possible scaling and limiting fragementation. Possible explanation for the observed deviation from limiting fragmentation at lower energies have been discussed, along with comparison with published data at higher energies. A new parametrisation for different contributions to the total yield of photons has been proposed, which describes the data at five energies using two free parameters. Chapter 5 deals with the results of AMPT model to describe the v_2 and v_3 of charged particles for a wide range of energies. The model parameters were tuned to reproduce multiplicity and the details are discussed here. In Chapter 6, the results on photon flow for

Au+Au collisions at 39 GeV are presented, along with comparison with AMPT data. The thesis ends with the conclusions in Chapter 7.

Chapter 2

The Experimental Facilities

The Relativistic Heavy Ion Collider (RHIC) complex at Brookhaven National Laboratory is a world-class scientific research facility designed to accelerate and collide the heavy-ion beams at relativistic speed to form and explore the matter which possibly existed in the early universe [64]. RHIC ring is 3.8 km in circumference and is at the ground level. The RHIC can accelerate a variety of heavy ions up to 100 A GeV and can also accelerate polarized protons up to 250 GeV. The aim of accelerating heavy ions is to conduct experiments to look for a new state of matter, the Quark-Gluon Plasma. The aim of polarized proton proton collisions is to study the spin structure of the nucleon.

The RHIC complex was designed to produce, accelerate and store the heavy-ion beams [65]. A schematic drawing of this complex is shown in Figure 2.1. It is composed of several accelerator facilities chained together to provide beams which are collided in detectors located around the RHIC ring. Before reaching RHIC, the particle accelerated at RHIC passes through several intermediate stages. Heavy ions are first accelerated to 1 MeV per nucleon in Tandem Van de Graff (shown by yellow color in Figure 2.1). Synchrotron further accelerates these partially stripped ions to 95 MeV per nucleon (shown by cyan color in Figure 2.1) which injects them into Alternating Gradient Synchrotron (AGS) (shown by bright green color in Figure 2.1), where the ions are stripped of the rest of their electrons and accelerated upto 8.9 GeV per nucleon and are then injected into RHIC at nearly 6 o'clock position on the Intersecting Storage Ring into two counter rotating rings.

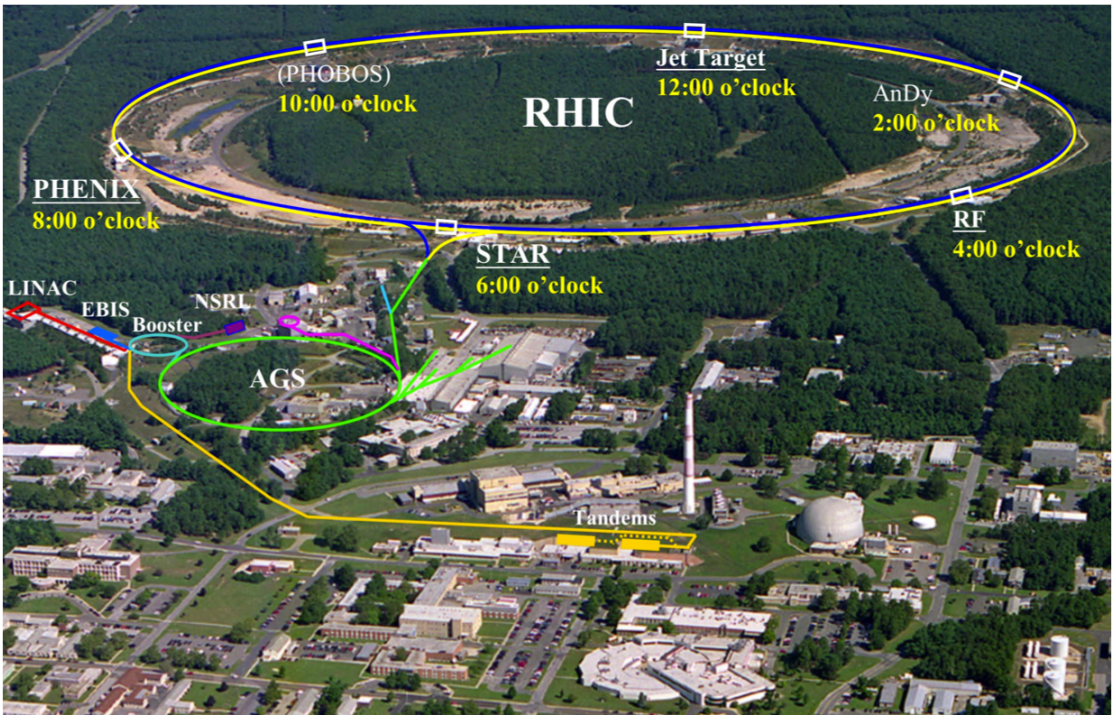

FIGURE 2.1: A picture of the Relativistic Heavy Ion Collider (RHIC) accelerator complex at Brookhaven National Laboratory.

The bunches of ions are accelerated to a maximum energy of 100 GeV/nucleon after the ions are injected to the two counter-rotating rings of RHIC. Clock-wise rotating beam is referred to as the blue ring and the ring with the anti-clock-wise rotating beam is referred to as the yellow ring.

Out of the six collision points, STAR [66] is at 6:00 o'clock, PHENIX [67] is at 8:00 o'clock, and PHOBOS [68] is at 10:00 o'clock position, respectively. Of these, PHOBOS have completed their operation while STAR and PHENIX are still active and will continue taking data in the coming years.

2.1 STAR Detector System

The Solenoidal Tracker at RHIC (STAR) is one of the major detector systems at RHIC [66]. The main motivation to build the STAR detector was to investigate the behavior of strongly interacting matter at high energy density through the simultaneous measurement of multiple observables. In order to achieve these goals,

STAR was constructed to measure hadron and photon production over a large acceptance. A schematic side view of the STAR detector is shown in Figure 2.2 .

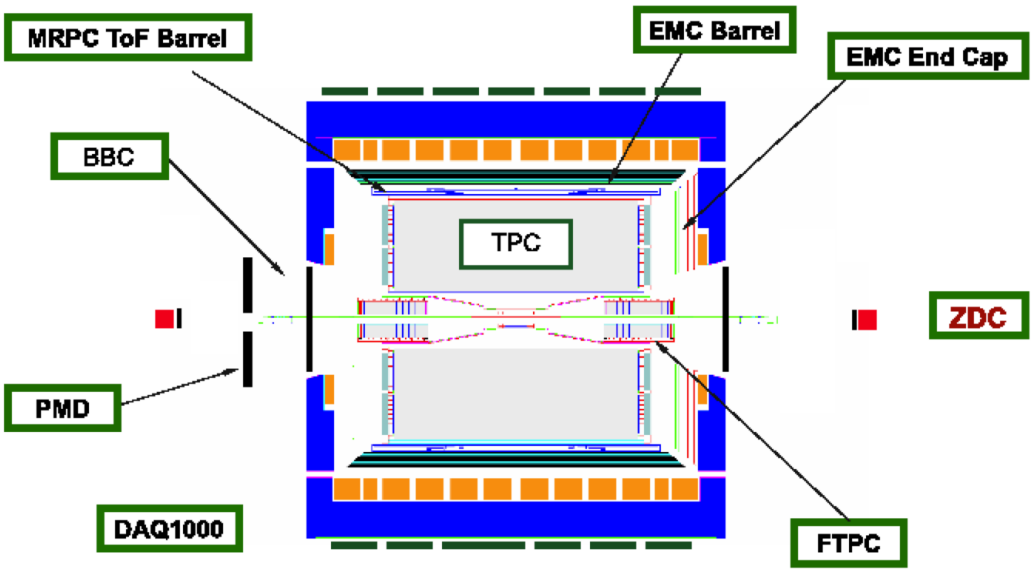

FIGURE 2.2: A schematic side view of STAR experiment.

The Solenoidal Tracker at RHIC (STAR) [66] is made of several sub-detectors, each specializing in detecting different types of particles or characterizing their motion. The main detector subsystems are: Time Projection Chamber (TPC) [69], Forward Time Projection Chamber (FTPC) [70], Time of Flight (TOF) [71], Photon Multiplicity Detector [72] (PMD), Barrel Electro-Magnetic Calorimeter (BEMC) [73], Endcap Electro-Magnetic Calorimeter (EEMC) [74], Beam-Beam Counters (BBC) [75] and Zero Degree Calorimeter (ZDC) [76]. The STAR magnet shown in the Figure 2.2 (in blue color) generates a field of ~ 0.5 Gauss over a large volume that houses most of the detectors of STAR. The magnet bends the charge particles, measuring the curvature of the tracks leads to the determination of transverse momentum of these particles.

When bunches of accelerated ions cross each other at the center of the STAR experiment, some of the ions collide with each other. It would be ideal to have one

collision per bunch crossing. The actual number of collisions in each bunch crossing depends on the bunch size, the spread, and the cross section. Each AA collision results in prouction of a number of particles, both charged and neutral which are detected by the various detectors of STAR. To recognise and choose the collisions of interest, STAR has a number of trigger detectors ZDC, BBC, BEMC, EEMC. On instructions from the trigger detectors, the other detectors save the information of the collision. The collision vertex is determined using TPC. TPC and TOF give information of the charge particles produced in the collision at midrapidity while FTPC measures the charged particles at forward rapidity. BEMC and EEMC measure the energy of the particles which are interacting through electromagnetic interaction. PMD is a photon mulitplicity detector which measures the multiplicity of photons at forward rapidity. The pseudorapidity range of the PMD overlaps with that of FTPC which facilitates study of charge to neutral fluctuations.

In this chapter, we will briefly mention the trigger detectors, and the detectors which have been used in the analysis in the present work. The analysis presented in the thesis is based on the data collected using PMD, which is described in detail at the end of this chapter.

2.2 Trigger Detectors

In STAR, some of the slow detector subsystems like TPC, FTPC, TOF, etc., can only operate at rates of ∼100 Hz. The interaction rates at RHIC for the highest luminosity beams can even approach ∼10 MHz. This requires the fast detectors to provide a means to choose events of interest. STAR detector consists of some fast detectors, which are employed to provide trigger for the slow detectors in order to record the data. The main triggering detectors for STAR are: Zero Degree Calorimeter (ZDC), Beam Beam Counter (BBC), and Electro Magnetic Calorimeters (BEMC and EEMC) [75].

2.2.1 Zero Degree Calorimeter

To provide some universal characterization of heavy-ion collisions, all four experiments at RHIC use a pair of Zero Degree Calorimeter (ZDC) as a common tool for monitoring interactions at each interaction point. The STAR ZDCs are hadron calorimeters used for detecting primarily neutrons [76]. The ZDCs are located ±18 m away, on either side of the interaction point.

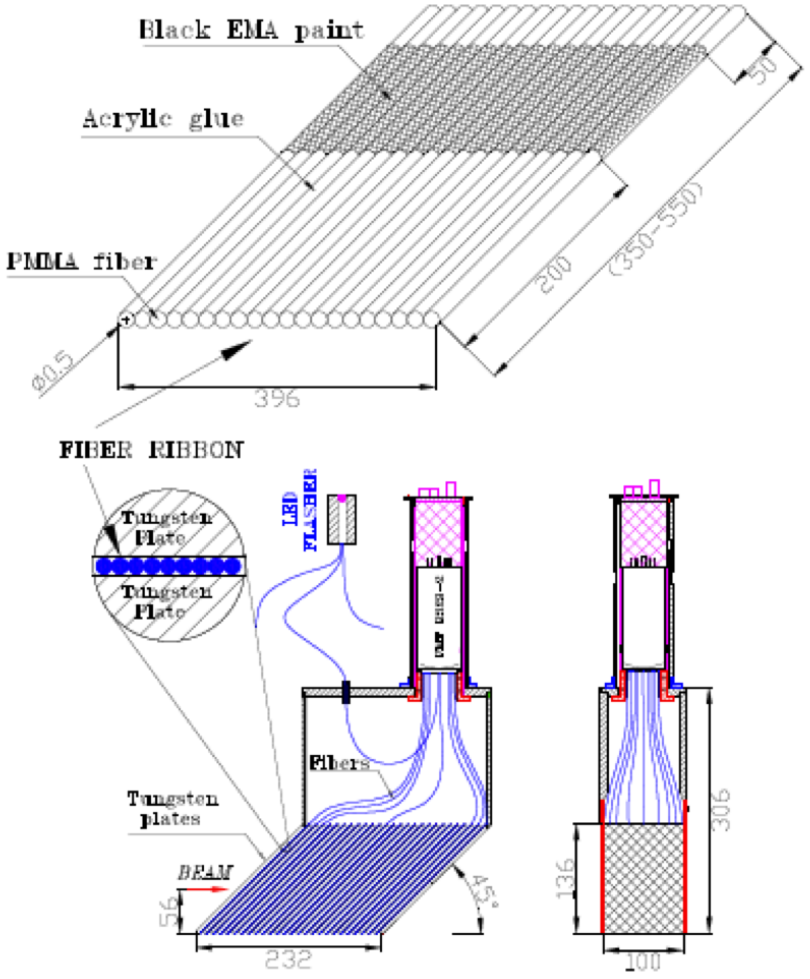

FIGURE 2.3: Schematic layout of the ZDC detector module [76].

Each ZDC consists of three modules made from alternating layers of tungsten absorber and Cerenkov fiber ribbons placed at an angle 45 degree relative to the incident beam as shown in Figure 2.3. In an AA interaction, the spectator fragments of the colliding ions move practically along the same path as the original

beam. Magnets bend all the charged fragments as well as the non interacting ions away from ZDC. The neutral particles, mostly neutrons, reach the ZDC.

In order to study the spatial distribution of the neutron hits on the transverse plane of the ZDCs, a Shower Maximun Detector (SMD) was installed between the first and second ZDC module. The ZDCs are also used to locate the interaction vertex by using the time delay between the coincidences. This information helps in determining the centrality of the event. In effect, ZDCs are very useful for the beam monitoring, triggering, and locating interaction vertices.

2.2.2 Beam-Beam Counter

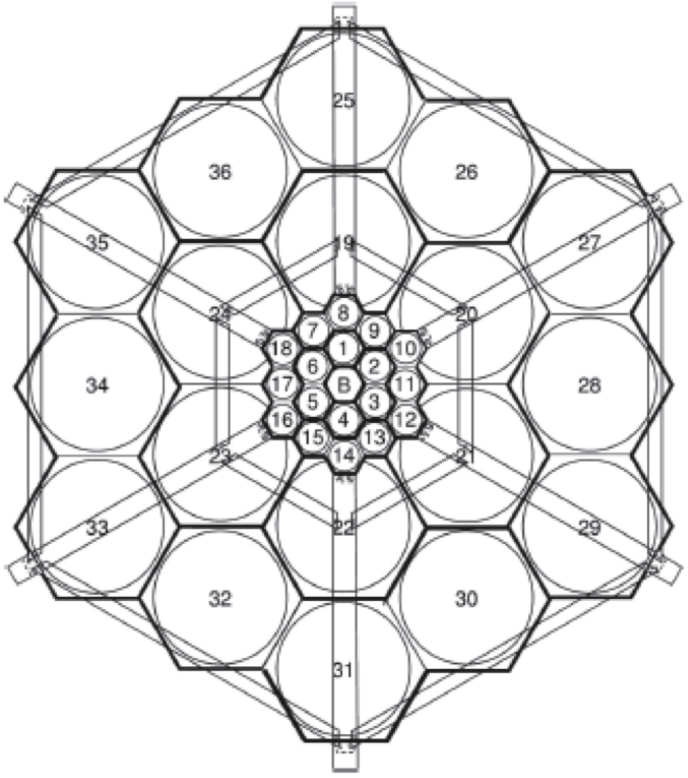

FIGURE 2.4: Schematic layout of the BBC detector tiles [75].

The Beam-Beam Counters (BBCs) are mounted around beam pipe beyond the east and west pole-tip of the STAR magnet at about 3.7 m from the interaction point [75]. Each BBC consists of 2 sets of 18 small and 18 large, 1 cm thick,

hexagonal plastic scintillator tiles. Being a scintillator detector, the response is very fast which makes it useful for providing the necessary triggers. It covers pseudorapidity region of $3.4 < |\eta| < 5.0$. The small tiles make up an outer radius of 48 cm while the larger tiles make up an outer radius of 193 cm as shown in Figure 2.4. Each scintillator tile has four wavelength shifting (WLS) optical fibers inserted into circular groves inscribed within the hexagonal scintillator to collect scintillation light. The primary vertex can be determined from the measured time difference between the two BBC detector signals in a beam-collision event and known locations of the detector planes.

2.2.3 Electromagnetic Calorimeters (EMC)

The EMC is utilized to trigger on and study rare, high p_T processes like jets, leading hadrons, direct photons and heavy quarks. Other applications include general event characterization in heavy-ion collisions including ultra peripheral collisions. In order to achieve these physics goals STAR has installed two electromagnetic calorimeters which are briefly discussed below.

2.2.3.1 Barrel Electromagnetic Calorimeters

The Barrel Electromagnetic Calorimeter (BEMC) is a projective lead scintillator calorimeter positioned inside the aluminium coil of the STAR solenoid [73]. It measures the electromagnetic energy deposits associated with jets, leading hadrons, direct photons, and electrons produced in large pT processes. It covers the pseudorapidity region $|\eta| < 1$ with full azimuthal angle. This is shown schematically in Figure 2.5.

It is 586 cm long with an inner and outer radius of 223 cm and 263 cm. It has 20 layers of lead plates and 21 layers of scintillator. The BEMC consists of 120 calorimeter modules, each covering 6° ($\sim$0.1 radian) in $\Delta\phi$ and 1.0 unit in $\Delta\eta$. Each module is further segmented into 40 towers, 2 in ϕ and 20 in η, with each tower having a granularity of 0.05 in both $\Delta\phi$ and $\Delta\eta$. Each of the module consists of a lead scintillator stack and a set of Shower MaximumDetector (SMD), situated

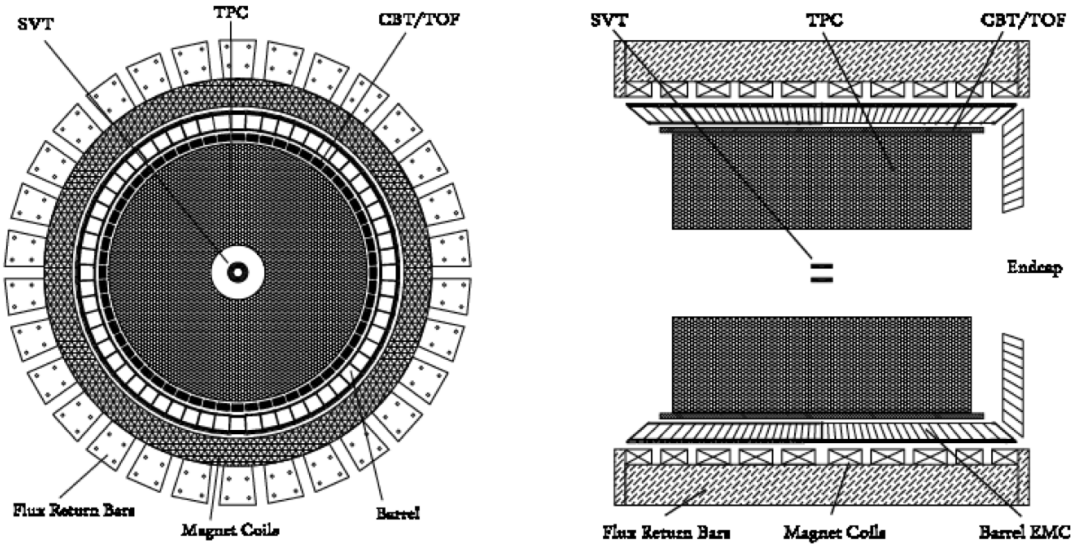

FIGURE 2.5: (Left side) X-Y view of STAR Barrel electromagnetic calorimeter (Right side) Y-Z view of STAR Barrel electromagnetic calorimeter [73].

approximately 5.6 radiation length (X_0) away from the front of the stack. The SMD is used to provide fine spatial resolution in a calorimeter.

2.2.3.2 Endcap Electromagnetic Calorimeters

The Endcap Electro-magnetic Calorimeter (EEMC) is positioned at the west pole-tip of the STAR detector [74]. It covers the pseudorapidity region $1 \leq \eta \leq 2$ with full azimuthal range, supporting the barrel EMC (BEMC). This is shown schematically in Figure 2.6.

The construction of EEMC includes a SMD optimized to discriminate between photons and π^0 or η mesons over the energy region 10 - 40 GeV. The triggering capabilities and its coverage are crucial for the spin physics program in polarized p+p collisions. It has the capability to detect photons and electromagnetically decaying mesons (π^0, η). It consists of preshower and postshower layers used to discriminate between electrons and hadrons.

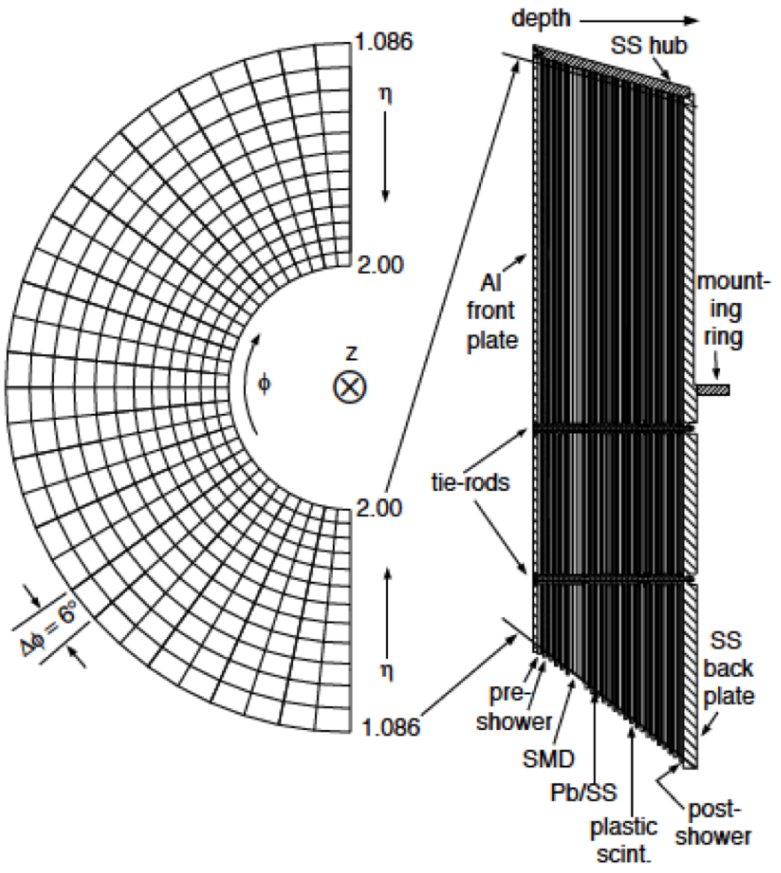

FIGURE 2.6: A schematic diagram of STAR endcap electromagnetic calorimeter [74].

2.3 Time Projection Chamber

The main tracking detector in STAR is the Time Projection Chamber. It is a gas detector capable of recording tracks of particles, measuring particle momentum, and performing particle identification by measuring ionization energy loss (dE/dx) combined with the measurement of the magnetic rigidity [69]. The TPC covers a pseudorapidity region $|\eta| < 1.8$ with full azimuthal coverage. The TPC is the primary tracking detector and effectively records tracks of all produced charged particles. It can measure their momenta in the range 100 MeV/c to 30 GeV/c and can identify particles in the range 100 MeV/c to ∼1 GeV/c by measuring their ionization energy loss (dE/dx). Figure 2.7 shows the schematic view of STAR TPC.

It is a 4 meter long cylinder surrounding the beam pipe with inner radius 50

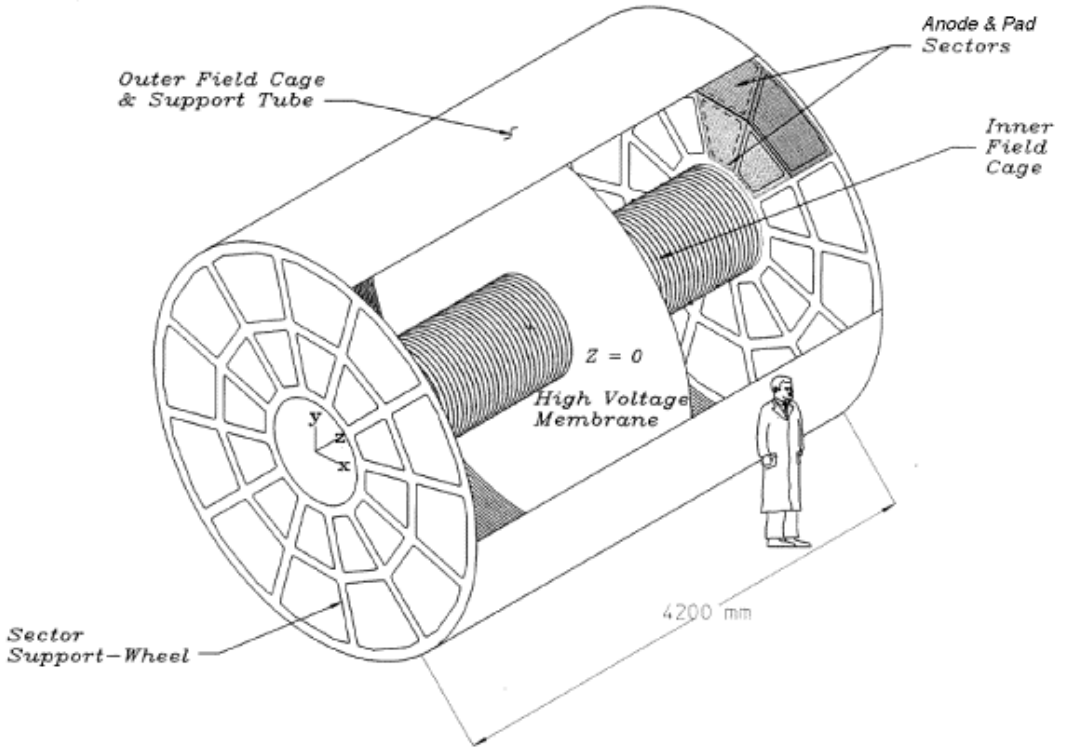

FIGURE 2.7: A schematic view of the Time Projection Chamber [69].

cm and outer radius 200 cm. The detector volume is filled with P10 gas (10% methane, 90% argon) held at 2 mbar above atmospheric pressure. This slight over-pressure is designed to ensure that air does not contaminate the P10 in the detection volume. The P10 gas has an advantage of fast drift velocity which peaks at a low electric field.

The TPC is essentially a large cylindrical gas filled detector with a uniform electric field of ∼135 V/cm. As primary ionizing particles pass through the gas in the detector, their paths are reconstructed via the secondary electrons they release. The secondary electrons drift in the electric field (defined by the thin conductive Control Membrane (CM) at the center of the TPC) to the readout endcaps at the end of the chamber. At both ends of the TPC, the readout system is based on the Multi Wire Proportional Chambers (MWPC) with readout pads.

Particle Identification using dE/dx

When a charge particle passes through TPC, it loses energy through ionization.

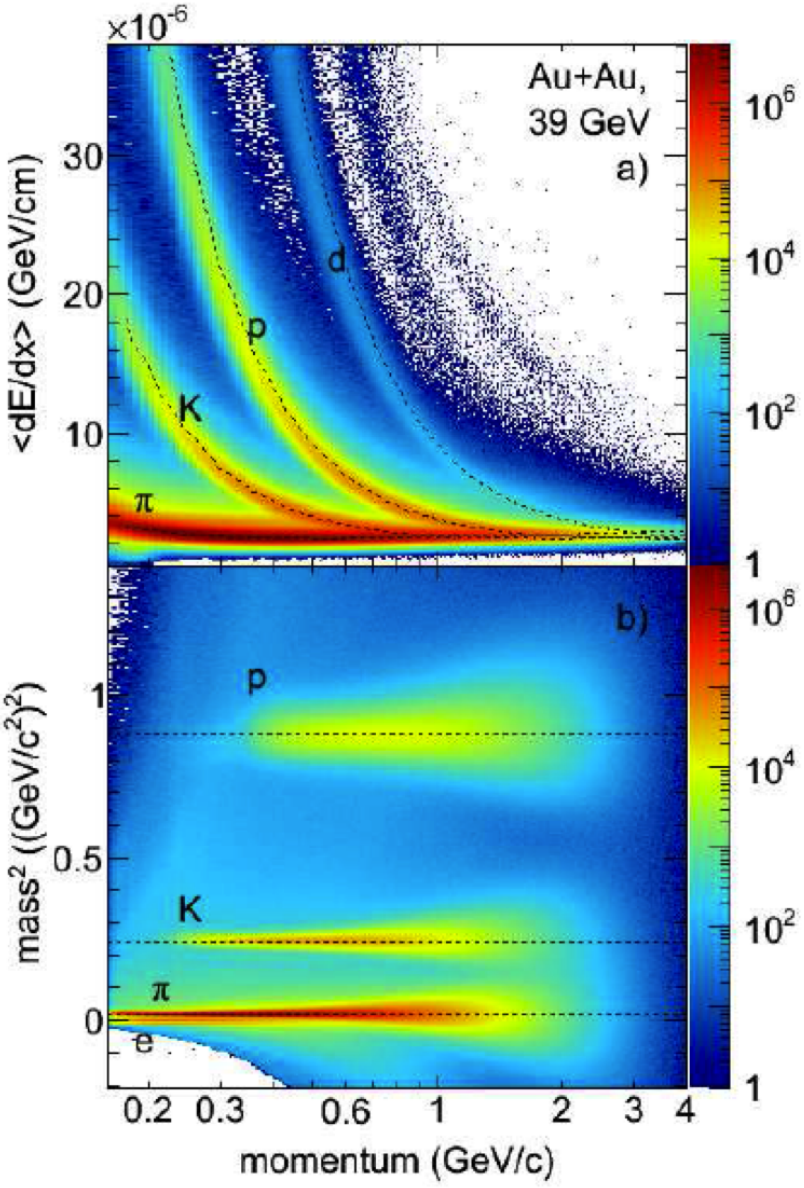

FIGURE 2.8: The mean specific energy loss, <dE/dx>, of reconstructed tracks within a pseudorapidity range of $|\eta| < 1$ in the TPC (a), and the mass-squared, m^2, as a function of momentum (b). The Bichsel functions used to determine the nÏČparticle values are shown in (a) as the dashed curves. The horizontal dashed lines in (b) correspond to the nominal particle masses of π, K and p

For a particle, which passing through a medium with density ρ, and speed β= v/c, the mean energy loss is given by:

$$-\frac{dE}{dx} = Kz^2\frac{Z}{A}\frac{1}{\beta^2}\left(\frac{1}{2}ln\left[\frac{2m_ec^2\beta^2\gamma^2T_{max}}{I} - \beta^2 - \frac{\delta}{2}\right]\right) \tag{2.1}$$

Here z is the charge of particle, Z is the atomic number of absorber, A is the atomic mass of absorber, K is the constant ($0.307 MeV g^{-1} cm^2$) c is the speed of light, m_e is the electron mass, I is the average ionization energy of absorber, T_{max} is the maximum kinetic energy that can given to a free electron in an interaction, δ is the density correction and β, γ are relativistic variables. Figure 2.8 shows energy loss as a function of particle momentum in TPC for Au+Au collisions at 39 A GeV. In this figure the lines show the theoretical predictions from Bichsel function for different particle species and the band around the lines represents measured value of dE/dx in data. The Bichsel functions for pions and kaons are well separated upto 0.75 GeV/c and hence they can be distinguished up to momentum 0.75 GeV/c. Similarly protons and anti-protons are well separated upto 1.1 GeV/c and can be identified up to momentum 1.1 GeV/c.

2.4 Time-Of-Flight Detector

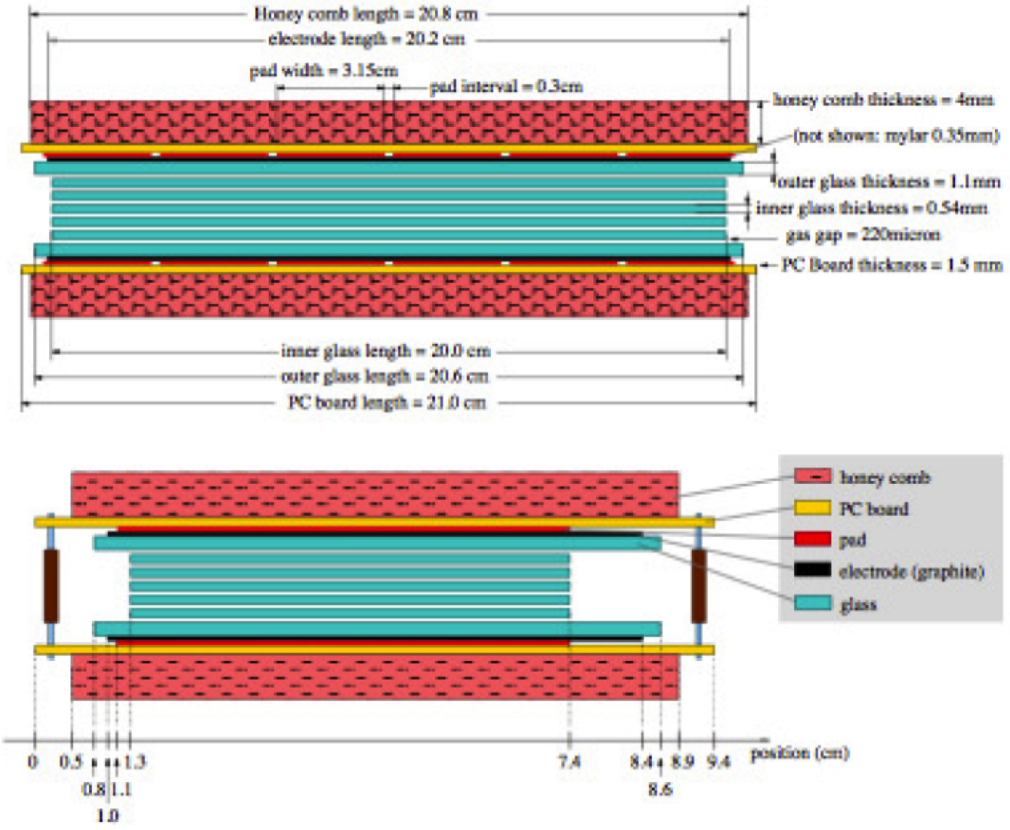

FIGURE 2.9: A side view of the short edge of a MRPC module of TOF [71].

The STAR Time-Of-Flight (TOF) is located just outside the TPC, covering $|\eta| < 1$ in pseudorapidity and 2π in azimuth [71]. It extends the direct particle identification (PID) capabilities of STAR to higher momenta. The intrinsic time resolution is less than one hundred picoseconds and it has a high detection efficiency (> 95 %) for minimum ionizing particles. It identifies π, κ and p up to the momentum $\sim$1.8 GeV/c and can separate p from π and κ up to momentum $\sim$3 GeV/c. It also identifies electrons above the transverse momentum (p_T) 0.2 GeV/c. The active detector in the TOF system is a Multigap Resistive Plate Chamber (MRPC) and these MRPC modules are mounted inside trays as shown in Figure 2.9. The basic idea of the TOF detector system is to precisely measure the flight time of a charged particle when traveling between two space points. The start time is determined by two upgraded pseudo-vertex position detectors (upVPD) and the stop time is determined by TOF barrel itself. Each upVPD has 19 detector channels of photomultiplier tubes (PMT) with scintillators and is mounted close to the beam pipe.

The lower panel of Figure 2.8 shows the m^2 vs momentum (measured in TPC) for charged hadrons emerging from Au+Au collision at 39 A GeV. In this figure the pion, kaon and proton bands are clearly visible at low momentum. At higher values of momentum they start to merge. TOF extends the momentum range in which the particles can be precisely identified.

2.5 Forward Time Projection Chamber

The Forward Time Projection Chambers (FTPC) were designed to extend the phase space coverage for detecting charged particles in the STAR experiment [70]. The increased acceptance improves the event characterization at forward pseudorapidity region. They cover the pseudorapidity range of $2.5 < |\eta| < 4.0$ on both sides of the TPC.

The two FTPCs are situated on both sides of STAR along the beam pipe. The full two component system measures momenta and production rates of positively and negatively charged particles as well as neutral strange particles. Each of the FTPCs is a 120 cm cylindrical structure, 75 cm in diameter with a radial drift field.

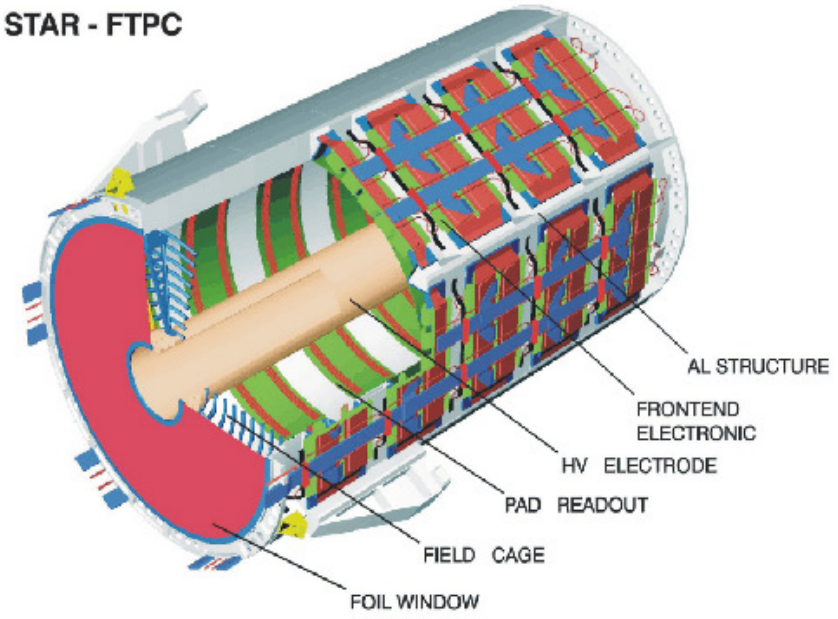

FIGURE 2.10: A schematic diagram of FTPC for the STAR experiment [70].

It has readout chambers located in five rings on the outer cylindrical surface. The radial drift configuration was chosen to improve the two-track separation in the region close to the beam pipe where the particle density is highest. The Front End Electronics (FEE) boards are mounted on the back of the readout chambers. The ionization electrons drift to the anode sensor wires. The induced signals on the adjacent cathode surface are read-out by 9600 pads. The FTPC uses a mixture of Ar and CO2 with a ratio of 50% : 50% by volume. The track points are calculated from the charge distribution measured by read-out electronics. These track points are grouped into tracks which together with magnetic field maps, can be used to get the particle momenta.

2.6 Photon Multiplicity Detector

The Photon Multiplicity Detector (PMD) is installed on east wall of the wide angle hall in the STAR experiment at distance of 540 cm from the center of the

TPC [72]. PMD was completely designed and manufactured in India and was also installed and maintained by the teams from Indian Universities and Institutes.

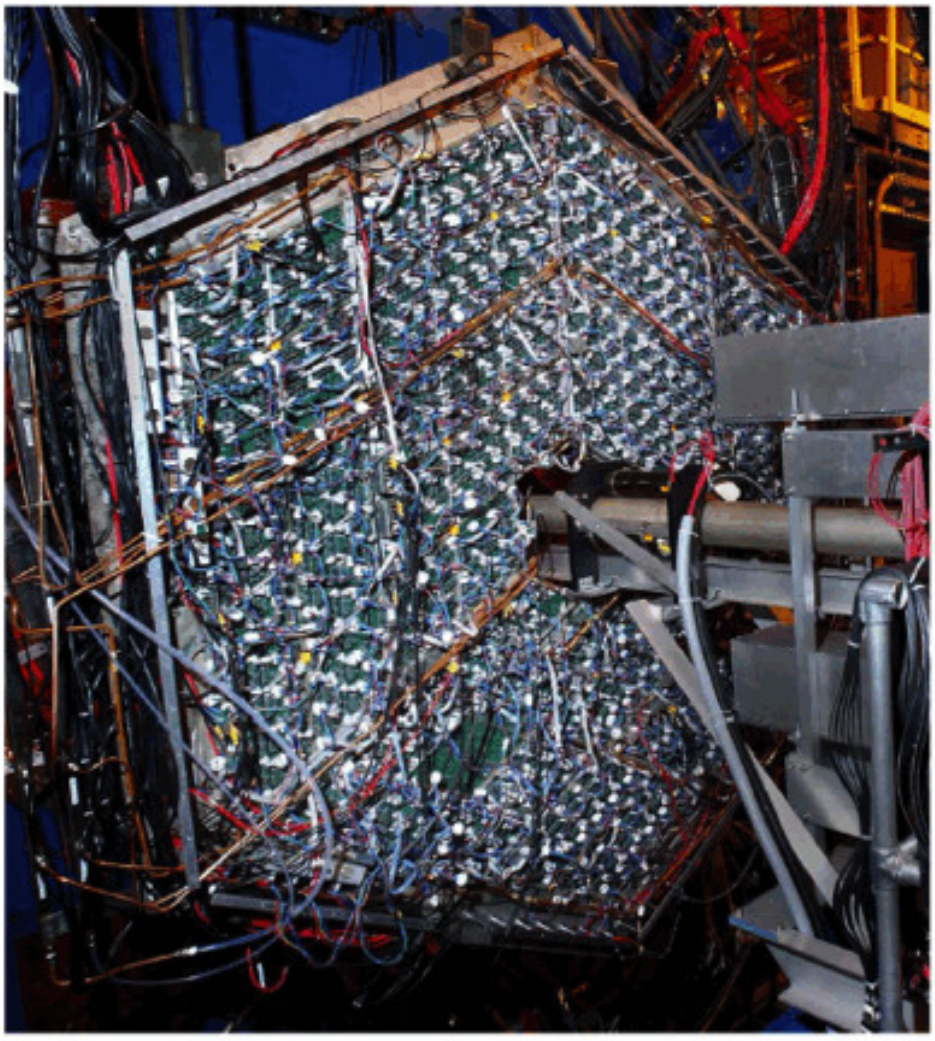

FIGURE 2.11: A picture of PMD in STAR experiment

The PMD was designed to measure photon multiplicity in the forward rapidity region, where the calorimeters are not efficient due to high particle density. It covers a pseudorapidity region -3.7 $\leq \eta \leq$ -2.3 with full azimuthal angle. It can detect photons with p_T as low as 20 MeV/c. This region has been selected to minimize the effect of upstream materials and to maximize the overlap with the coverage of the FTPC. The PMD is a highly segmented preshower detector placed behind a lead converter plate of 3 radiation length thickness. The detector is based on a proportional counter design using $Ar + CO_2$ gas mixture in ratio 70:30 by weight. The choice of this gas mixture is due to its insensitivity to neutrons.

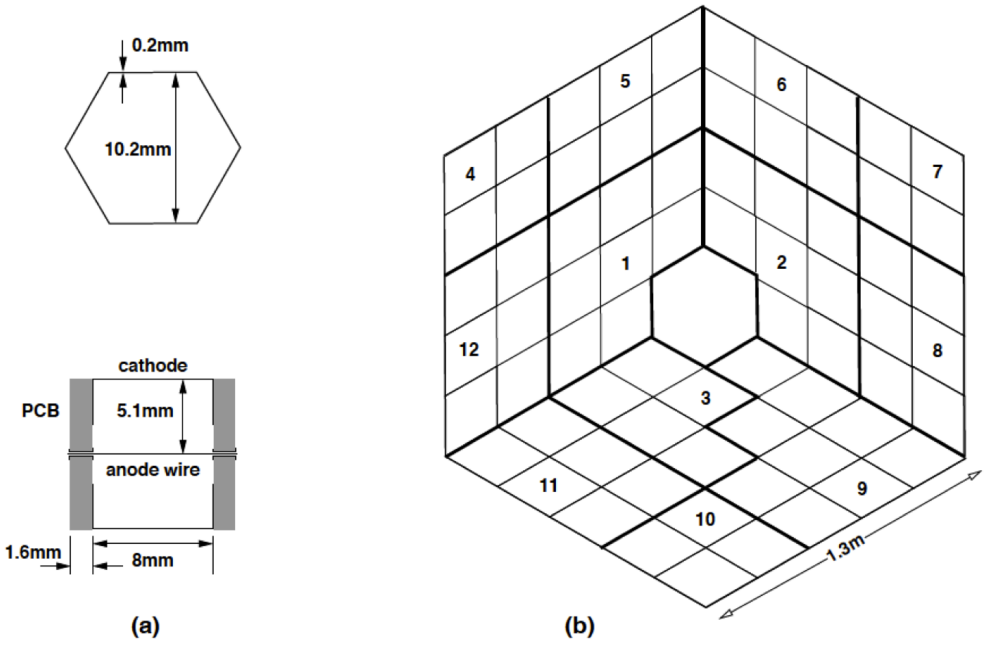

FIGURE 2.12: (a) Schematic diagrams of a unit cell showing the cross-section (upper) and other dimensions and the cathode extension (lower). (b) Layout of STAR PMD. Thick lines show supermodule boundaries. The thin lines show the unit module boundaries [72].

The PMD consists of an array of hexagonal cells. A schematic diagram of unit cell is shown in Figure 2.12 (a). A unit module is formed by honeycomb of 24×24 cells. The schematic of a unit module is shown in Figure 2.13. The shape of unit module is rhombus of side ∼254 mm having identical boundaries on all four sides. The walls of cell at the boundary of module are kept half as thick as those inside so that adjacent unit modules join seamlessly. A set of unit modules are enclosed in a gas tight chamber called supermodules. Each plane of PMD consists of 12 super modules arranged in the form of a hexagon and has 41,472 hexagonal honeycomb cells as shown in Figure 2.12. Each cell of PMD is $\sim 1 cm^2$ in area. The cell wall is kept at -1350V while the readout is through the central anode wire. The extended cathode cell wall (Figure 2.12(a))ensures a good efficiency of collection of the ions produced by the electrons and positrons produced by the photon in the convertor plane. The highly segmented design of PMD is to contain the delta rays produced by the electrons and positrons , thus reducing the spread of the electro-magnetic shower.

Two Au plated printed circuit boards (PCB) with metalized inner surfaces, having

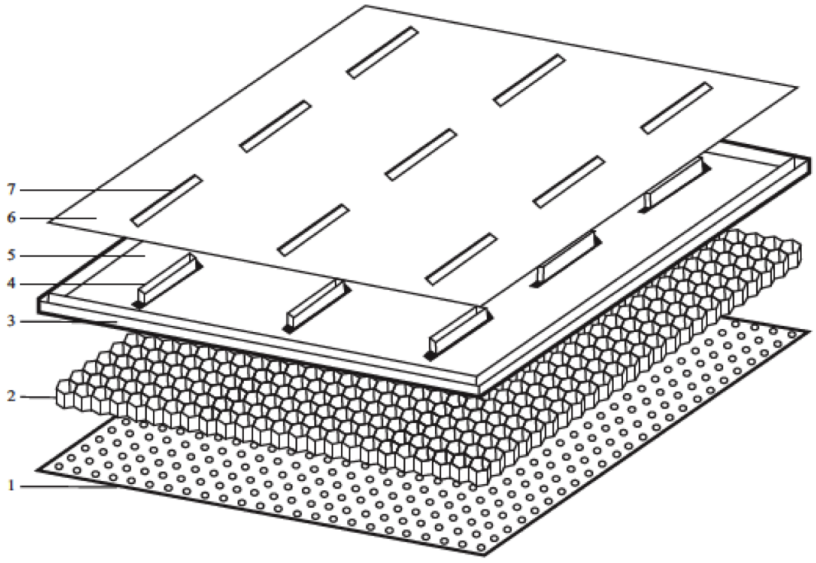

FIGURE 2.13: A schematic view of components of a unit module: (1) bottom PCB, (2) honeycomb cathode, (3) moulded frame, (4) SAMTEC connectors, (5) top PCB, (6) shielding PCB with (7) slot for connector [72].

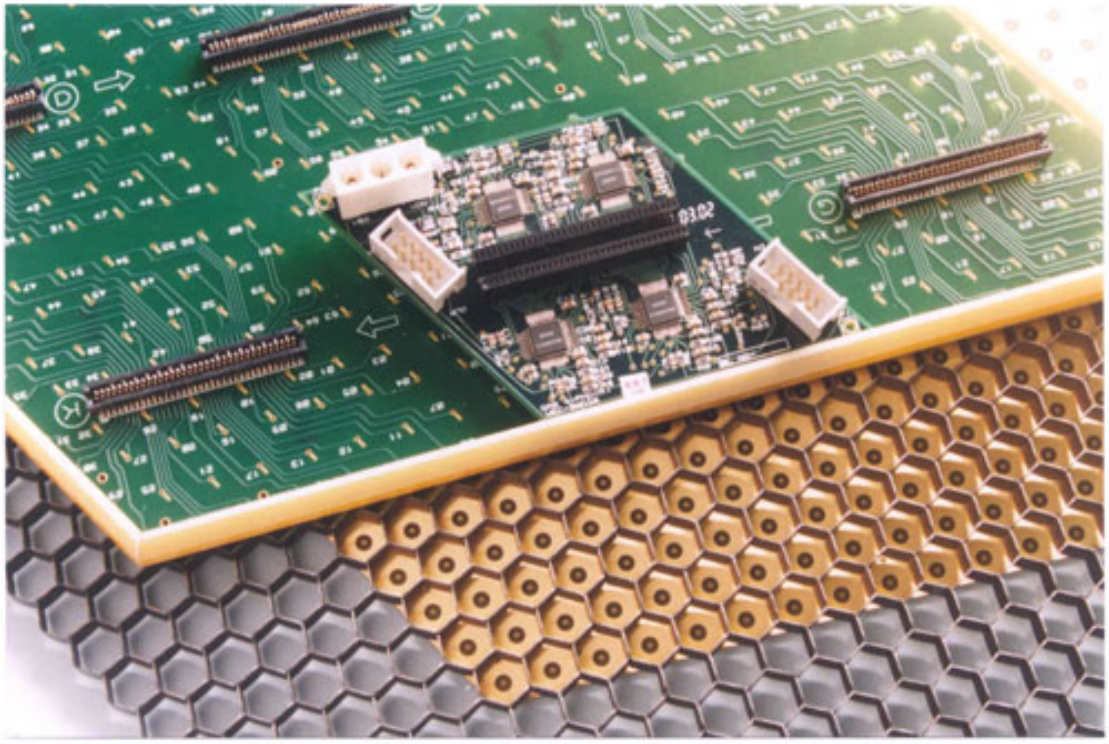

FIGURE 2.14: A picture of unit module components with electronics board mounted on the connector [72].

insulation circles of 4 mm diameter formed the front and the back surfaces of the unit modules. For fixing the anode wire, each of the solder islands, at the

center of the insulated circles, has a Au plated through hole . There are nine sets of signal tracks on the top PCB, each set corresponding to 64 cells. These are grouped to be connected to a 70-pin connector (TFM-135- 01-S-D SAMTEC) as shown in Figure 2.14. For fixing the anode wire, the PCB on the bottom side has only soldering island . Each pair of PCBs for a given UM are provided with 24 alignment holes for fixing alignment studs during assembly. A honeycomb is sandwiched between the two PCBs, properly aligned using 24 Cu studs which protrude only 0.5 mm above the PCB surface. The stud heads were then covered with polyamide pads to provide insulation.

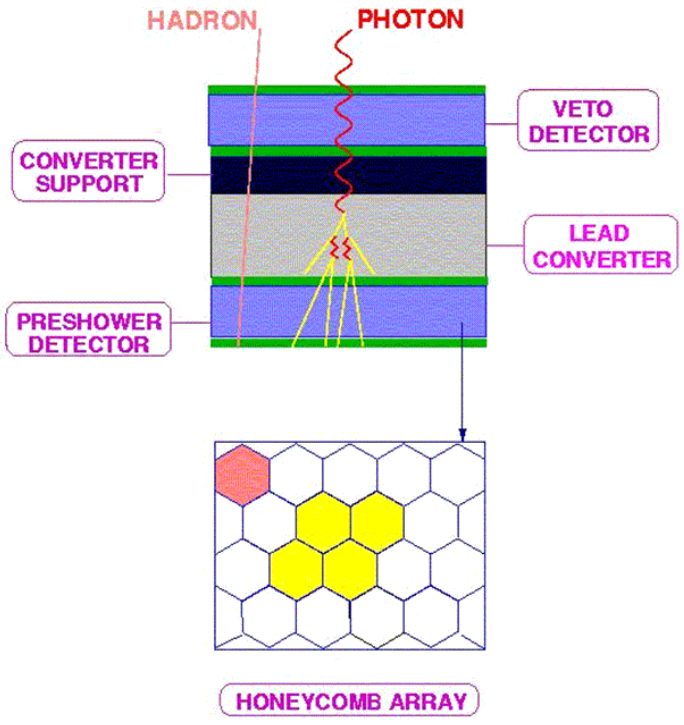

FIGURE 2.15: A schematic diagram showing the working principle of PMD. (top) An x-z section of PMD showing the convertor and sensitive layers of PMD. (bottom) An x-y schematic diagram showing the hit cells on preshower due to a hadon and a photon [72].

Figure 2.15 shows the schematic diagram on the working principle of the PMD. A photon passing through the converter produces an electromagnetic shower. These shower particles produce signals in several cells of the sensitive volume of the detector. The charged hadrons usually affect only one cell and produce a signal which resembles that from Minimum Ionizing Particles (MIPs). The thickness of

converter is optimized such that the conversion probability of photons is high and transverse shower spread is small to minimize shower overlap in high multiplicity environment.

In this thesis, we have studied the multiplicity and pseudorapidity distribution of photons and also measured azimuthal anisotropy of photons with respect to the event plane determined using charge particles in TPC.

2.7 STAR and PMD Software

A multi-detector experimental system like STAR requires elaborate software for its functioning. The STAR software environment StRoot, is based on ROOT with STAR specific libraries added to it. StRoot consists of multiple *Makers* which are chained together to make an Analysis, Simulation or Reconstruction chain. The libraries for each have been written by various STAR users and are present within STAR environment. The libraries are modified or added to as per the requirements of the experiment and so STAR periodically releases different versions of libraries. For the present work we have used P10ik and P11id libraries. Each Subsystem of STAR has its own *Makers* which are written by the users of that subsystem but are available to all STAR collaborators. STAR also maintains a database to store the constant details of each subsystem e.g. pedestal files, calibration constants required during reconstruction of data or hardware details required for simulating the events in STAR environments. PMD has the following utility Classes and Makers, listed below with their main functions. StPmdHit, StPmdCluster, StPmdGeom are utility Classes. StPmdReadMaker, StPmdClusterMaker are part of the STAR Reconstruction Chain. StPmdSimulator along with StPmdReadMaker and StPmdClusterMaker are also part of STAR Simulation Chain, this ensures that the software for simulated data reconstruction is same as that of real data. Besides these there are a number of other Makers specific to PMD. Some of the important STAR-PMD Library routines are briefly described below:

(1) **StPmdHit:** This is a utility class to contain the position and ADC of the hit along with details about the detector plane, channel number, row, column,

chain and SuperModule Number of the channel. The gain normalization constants are also stored for each channel.

(2) **StPmdCluster:** This is a utility class to contain the following information of a cluster on PMD: cluster position (x,y), η, ϕ, SuperModule and Particle Id (for simulated events). It also contains the addresses of all the StPmdHits that make up the cluster along with the total Cluster Size as well as Cluster ADC.

(3) **StPmdGeom:** This is a utility class which contains information of the geometry of the chains of PMD along with the working and non-working boards on each chain. This class facilitates conversion from channel number to channel position and vice-versa. It also contains the routines to obtain the η, ϕ of a hit/cluster from the position and vice-versa.

(4) **StPmdReadMaker:** This is a part of the reconstruction chain of STAR. It reads the real data from the raw data files written during the readout of the detector after subtraction of pedestal. This can also read data from the *.fzd* files produced by the STAR Simulator chain. This constructs StPmdHits from the information which is put in StPmdCollection for further use by other Makers of PMD.

(5) **StPmdClusterMaker:** This receives the StPmdHits from StPmdReadMaker and applies the calibration constants on them before clustering them to make StPmdClusters. The calibration constants are received from the STAR Database. The StPmdClusters are also stored in the StPmdCollection and are added to the STAR root files for further use.

(6) **StPmdSimulator:** This class is a part of STAR Simulation chain that constructs simulated signal on PMD according to the geometry of the PMD detector.

(7) **StPmdAssociationMaker:** It is used to make association between the tracks in simulated data and the clusters detected after reconstruction. This Maker helps to understand the PMD signal by determining the efficiency and purity of PMD signal and understanding of the background.

(8) **StPmdMuAnalysis:** It is used to reduce the full STAR root files to smaller files by selecting the quantities of interest for specific analysis.

(9) **StPmdFlowMaker:** It is used in conjunction with StFlowMaker for flow analysis. The event plane is calculated in StFlowMaker using either TPC or FTPC and the azimuthal anisotropy in photons is studied with respect to this event plane.

Besides the Classes mentioned above, a number of other STAR Library Classes have been used e.g. StRefMultCor that is used to determine the centrality of event after correcting for different efficiency of TPC for different vertex positions. A large number of PMD Specific classes and routines have been used for cleaning PMD data and for determination of gains of each channel. StPmdMuAnalysis was designed to make nano-dst files to contain the necessary data for multiplicity and flow analysis. Most of the analysis on PMD Multiplicity and flow has been performed locally using these nano-dst files.

2.8 Details of Data

The Photon Multiplicity Detector took data during Beam Energy Scan Program at RHIC during its operation in 2010 and 2011, referred to as Run 10 and Run 11 respectively, for Au+Au collisions at $\sqrt{s_{NN}}$ = 39, 27, 19.6, 11.5 and 7.7 GeV. In this thesis, we have analysed data for $\sqrt{s_{NN}}$ = 39, 27 and 19.6 GeV.

The Production Id, Trigger Id and Production library which has been used to processed the data used in our analysis is shown in Table 1.

Trigger Name	Production Id	Vertex Cut	Trigger Id	No. of Events
AuAu39_Production	P10ik	$\mid Vz \mid < 30$ cm	280002	$\sim$ 1M
AuAu27_Production	P11id	$\mid Vz \mid < 50$ cm	360002 || 2	$\sim$ 1M
AuAu19_Production	P11id	$\mid Vz \mid < 50$ cm	340002 || 340022 || 340012	$\sim$ 1M

TABLE 2.1: Details of data sets being used for analysis in this thesis

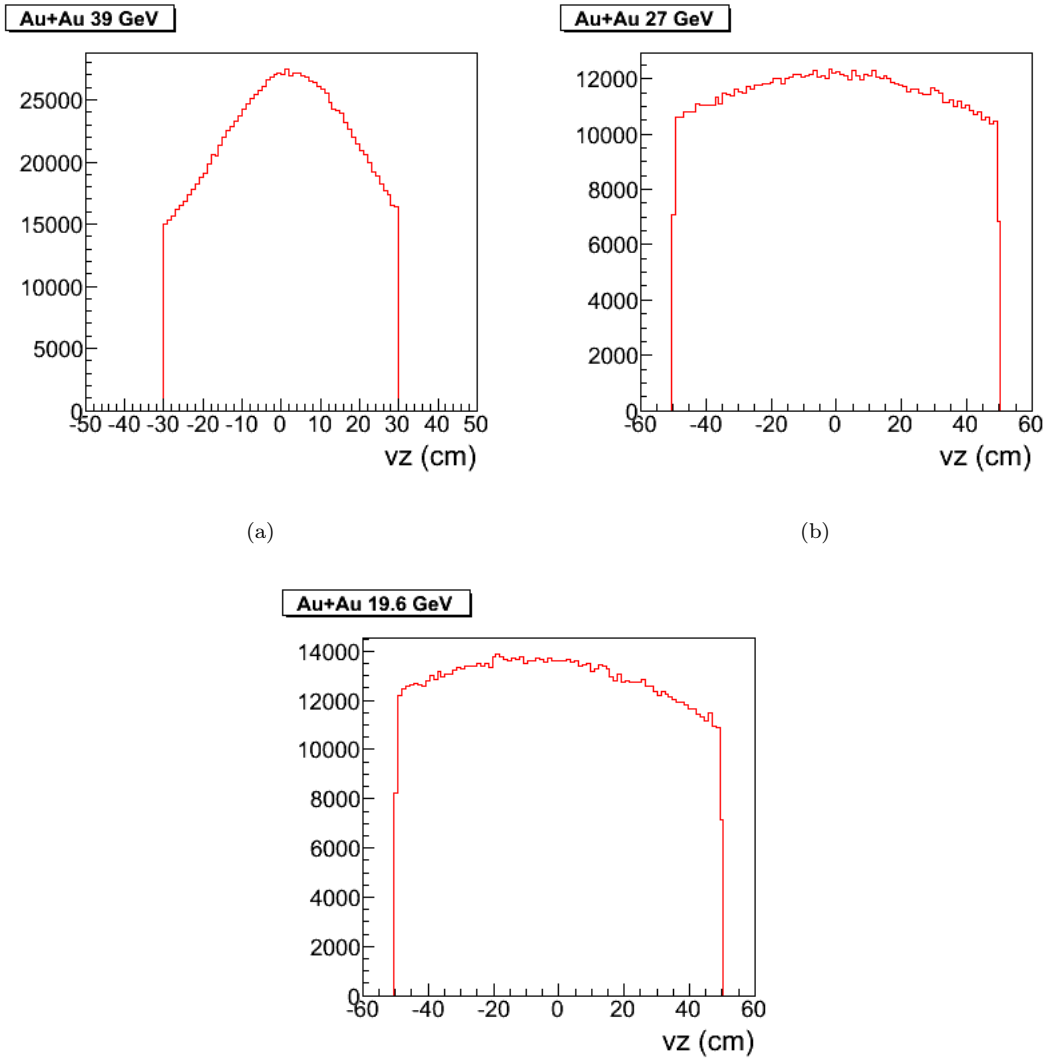

(a) (b)

(c)

FIGURE 2.16: Distribution of z position of the vertex of selected events for Au+Au collisions at 39, 27 and 19.6 A GeV. The y axis shows the number of events

2.8.1 Vertex Selection

For present analysis only those events are selected whose collision vertex position is within a limited range of the center of STAR. The allowed range for v_z is chosen to be ± 30 cm for Au+ Au 39 A GeV and ± 50 cm for Au + Au 27 and 19.6 A GeV from the center of STAR along the beam axis. v_x and v_y are chosen to be within 1 cm of the center of STAR. Figure 2.16 shows the vertex distribution of the selected events. These event selection criteria were used keeping in mind the

ability of the central STAR detectors for determining the event vertex and event centrality.

2.8.2 Centrality Determination

In the STAR experiment, centrality of an event was decided on the basis of uncorrected charged particle multiplicity measured in the TPC [69] within $\mid \eta \mid \leq 0.5$. For present analysis we have used StRefMultCor class of STAR software library, for deciding the centrality of the events. A small variation was observed in RefMult with the z position of the vertex (v_z) which is taken care of in StRefMultCor class. The same centrality criteria can be applied for all events irrespective of their (v_z) position. Figure 2.17 shows the reference multiplicity distribution for the data samples used at the three energies.

These raw charge particle distributions are compared to Monte Carlo Glauber simulations. A two-component model [77] is used to calculate the simulated multiplicity and is given by :

$$\frac{dN}{d\eta} = n_{pp}\left[(1-x)\frac{N_{part}}{2} + xN_{coll}\right] \tag{2.2}$$

where N_{part} is the number of participating nucleons and N_{coll} is the number of binary collisions. N_{part} and N_{coll} are obtained in the simulations using Glauber Model. The fitting parameter n_{pp} is the average multiplicity per unit of pseudorapidity in minimum-bias pp collisions. The parameter x is determined experimentally and its value is fixed at 0.12 $\pm$ 0.02 based on linear interpolation of the PHOBOS results at $\sqrt{s_{NN}}$ = 19.6 and 200 GeV [78]. The inelastic nucleon-nucleon cross section σ_{NN}^{inel} used in the model calculations is extracted from fitting the results of available experimental data for total and elastic pp cross sections from the Particle Data Group. Table 2.2 shows the value of parameters in the two-component model and σ_{NN}^{inel} in the MC Glauber simulations. Values of other Glauber Model parameters used are: Radius of Au nucleus= 6.38 fm, Skin depth = 0.535 fm.

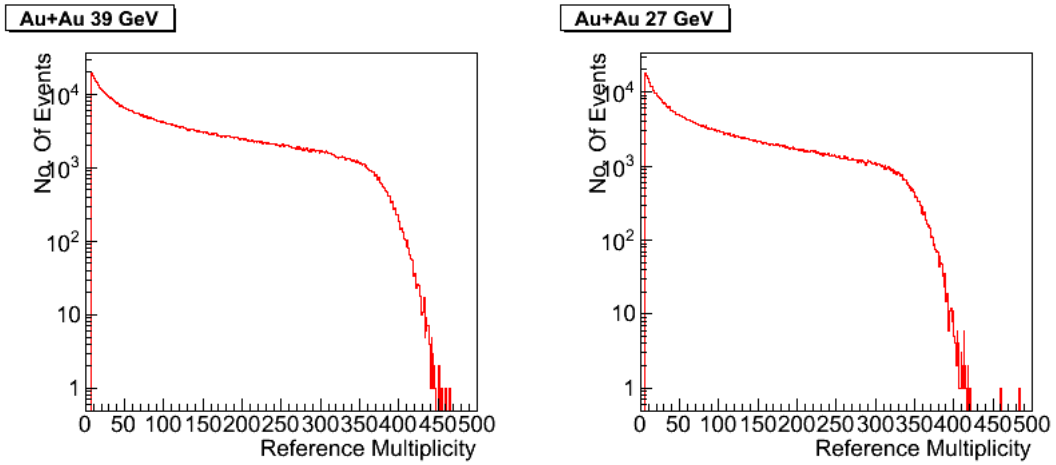

(a) (b)

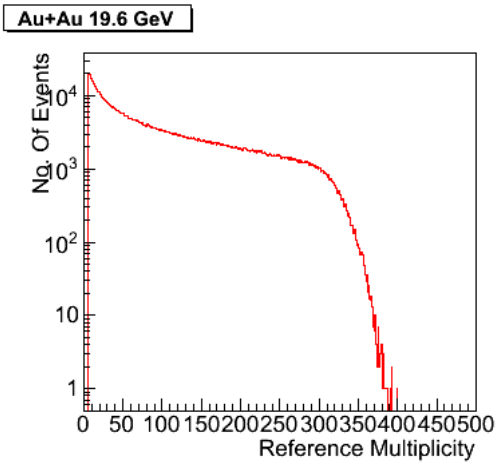

(c)

FIGURE 2.17: Distribution of Raw multiplicity in TPC (RefMult) of events selected for analysis

Fit parameters	Au+Au 39 GeV	Au+Au 27 GeV	Au+Au 19.6 GeV
n_{pp}	1.52 ± 0.08	1.385 ± 0.06	1.29 ± 0.05
σ_{NN}^{inel}	34.0 ± 1.0	33.0 ± 1.0	32.0 ± 1.0

TABLE 2.2: Summary of n_{pp} and σ_{NN}^{inel} with systematic uncertainties for Au+Au collisions at 39, 27 and 19.6 A GeV

The event-by-event multiplicity fluctuations have been included using the negative binomial distributions [79]. The centrality classes are defined by the fractions of geometrical cross section from the simulated multiplicity distributions. For each centrality bin, the average quantities are calculated in the Monte Carlo Glauber

% cross section	$< N_{part}^{AuAu} >$ 39 GeV	$< N_{part}^{AuAu} >$ 27 GeV	$< N_{part}^{AuAu} >$ 19.6 GeV
0 - 5	341.65 ± 2.18	343.26 ± 2.00	338.04 ± 2.29
0 - 10	293.87 ± 6.41	299.26 ± 6.19	289.21 ± 5.99
10 - 20	229.77 ± 8.72	233.64 ± 8.98	224.91 ± 8.61
20 - 30	162.37 ± 10.19	165.51 ± 10.71	158.10 ± 10.47
30 - 40	111.43 ± 10.82	114.03 ± 11.27	108.04 ± 10.64
40 - 50	73.52 ± 10.43	74.97 ± 10.33	70.84 ± 10.08
50 - 60	45.51 ± 8.92	46.67 ± 9.19	43.87 ± 8.70
60 - 70	26.32 ± 6.98	26.77 ± 7.57	25.46 ± 6.78
70 - 80	14.05 ± 5.18	13.76 ± 5.83	13.84 ± 4.98

TABLE 2.3: Average number of participating nucleons for various collision centralities for Au+Au collisions at 39, 27 and 19.6 GeV

simulations for $<N_{part}>$ and $<N_{coll}>$. The $< N_{part} >$ values corressponding to various percentages of the cross section for Au+Au collisions at 39, 27 and 19.6 GeV are given in Table 2.3.

2.9 Summary

This chapter contains a description of the experimental facilities which were used to obtain data for the analysis presented in this thesis. It contains an overview of the RHIC accelerator facility. The STAR detector system is also briefly decribed. A short description of some of the STAR detectors which have been used in the present analysis is also included. The present work is based on data from Photon Multiplicity Detector. The working principle and layout of PMD has been discussed in detail. An overview of the STAR software system has been presented with the details of PMD software packages which have been used for the present analysis. The Photon Multiplicity Detector took data during Run 10 and in Run 11 at Au+Au collision at 39, 27, 19.6, 11.5 and 7.7 A GeV. For the analysis presented in this thesis, data from Au+Au collisions at 39, 27 and 19.6 A GeV have been used. The libraries, triggers for each dataset have been stated. The chapter also contains some details of the method of the centrality selection of events and the centrality classes used for analysis. N_{part}, the mean number of participant nucleons for each centrality interval is an important parameter which has been

used at various places in this thesis. The mean N_{part} values, calculated for each centrality interval, have been tabulated for each of the three energies.

Chapter 3

PMD Data Cleanup, Gain Normalization, Efficiency and Purity

The preshower Photon Multiplicity Detector(PMD) [72] was designed to measure inclusive photon multiplicity in the STAR experiment at forward region $-3.7 \leq \eta \leq -2.3$. PMD is a highly segmented preshower detector placed behind a lead plate and a stainless steel (SS) converter plate of combined thickness 3 radiation length. The lead and SS plates act as a photon converter producing an electromagnetic shower. This shower produces a signal spread over several cells of the PMD. A charged hadron is also detected by the PMD, but most of the time it affects only one cell. The signal of a charged particle on PMD resembles that due to a Minimum Ionizing Particle (MIP). The converter thickness is optimized such that

(i) the conversion probability for photons is high.

(ii) the shower spread is low so that in a high multiplicity environment, the overlap between showers of different photons is minimum.

(iii) the interaction probability of hadrons is small.

Since both hadrons and photons give a signal on PMD, it is important to discriminate between their signals in order to reject hadrons. For achieving better hadron rejection capability, another plane of identical dimension as that of the

preshower, was placed before the lead plate, which could serve as veto for charged particles (CPV). For present analysis the CPV was not used for hadron veto. For Au+Au collisions at 39 A GeV, the CPV data was used to identify bad events. The discrimination between a hadron and a photon using only the preshower plane of PMD was done by the amount and distribution of energy deposited by the particles. Since a photon passing through the converter produces an electromagnetic shower in the preshower plane, the signal is spread over several cells. The signal due to a charged particle is mostly confined to one cell. Therefore, for the present analysis, photons have been discriminated from hadrons on the basis of energy deposited (cluster ADC) and the number of cells affected (cluster size).

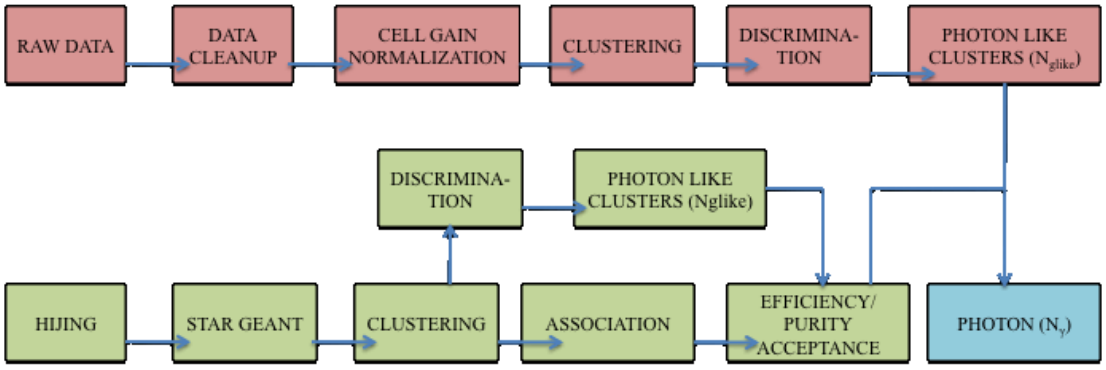

FIGURE 3.1: Flow chart for obtaining the photon multiplicity from PMD data and from simulated data

The steps followed for the reconstruction of photon signal are shown in Figure 3.1. The top row (in red online) shows the procedure for reconstruction of photons in data. The second and third rows show the simulation chain which is used to determine the efficiency and purity of the sample detected in PMD. This information is used to obtain the number of photons from the measured photon like clusters in data. Each step and its details are discussed in the next few sections.

3.1 Raw Data

The Photon Multiplicity Detector took data during Beam Energy Scan Program at RHIC during its operation in 2010 and 2011, referred to as Run 10 and Run 11 respectively, for Au+Au collisions at $\sqrt{s_{NN}}$ = 39, 27, 19.6, 11.5 and 7.7 GeV.

In the present work, analyses and results at $\sqrt{s_{_{NN}}}$ = 39, 27 and 19.6 GeV are presented.

In each Au + Au collision recorded in STAR, both charge particles and photons (mostly decayed from π^0) are incident on PMD. The primary charge particles as well as the showers produced by photons in Pb+SS layer cause ionization in the volume of the cell. The electrons thus produced in the gas are collected by the central anode wire. When PMD recieves the trigger signal, each channel of PMD is readout sequentially, its signal is digitized and the ADC values are recorded for further processing. If the trigger is not recieved, the collected charge is flushed out and the detector is reset to take the next event.

Intermittently, PMD recorded special sets of data to estimate the electronic noise of all its channels; these are called the Pedestal Runs. These Runs are taken without the RHIC trigger. In these Runs, the signal in the PMD is only due to electronic noise and not due to presence of actual signal. The information of the mean and sigma of the pedestal signal of each channel was calculated and stored. The pedestal ADC (mean + 3*RMS) for each channel was subtracted from the ADC recorded by that channel in any event, to give the actual ADC count of that channel to the signal. The pedestal subtracted signal has been called the ADC of a channel in the text hereafter. Since each cell of PMD is readout separately, i.e. is an independent channel, the word cell and channel are used interchangeably here.

3.1.1 Run Selection for Analysis

During data taking, the data recorded in one continuous time interval without any break is referred to as a data Run or just Run. Parts of PMD malfunctioned during certain periods. Sometimes one (or more) readout chains of PMD tripped during a Run. The next few Runs might have been taken while the tripped chain was being recovered. As a result the data from this chain would be missing in the next few Runs. The information of all the working chains as well their respective high voltages (HV) for each Run was recorded in the Run log for later reference.

Information on each Run regarding beam status, detectors taking data, magnet conditions and other qualifiers is recorded in the STAR Online log book. The information in the log book facilitiated the selection of good Runs which were then included for cleanup and gain normalization. Sometimes during a Run PMD malfunctioned causing multiple chains to trip. Such Runs were also not used for the present analysis.

3.2 Data Cleanup

It is essential to ensure that out of multiple channels of PMD which recorded data, only the channels which are giving good data are used for analysis. During the whole data taking period some chains of PMD were not able to hold high voltage up to the required value and tripped due to high leakage current. Some channels of PMD were giving signal all the time, even in absence of any charge particle passing through them. These channels are called hot channels. Some channels of PMD were not giving any signal even when charged particles may be incident on them, and are called cold channels. During tests, some channels were sparking and causing the whole chain to trip. These channels were termed as dead channels, and their signals were not even read out.

These problems may be caused due to presence of impurity in cells, broken or loose anode wires or due to faults in the electronics like burning out of some boards or chips. During the data taking, all the chains of PMD were constantly monitored. If any chain had a problem and tripped multiple times or was unable to hold required voltage, it was switched off.

Due to all the above mentioned features, some PMD cells were not giving reliable signal. Further, there was lack of uniformity in the response of different cells. For the purpose of normalization of response of all channels, roughly one Run for every 5-6 hours of data taking was selected for pre-production. Data from these selected Runs was used to identify and remove bad channels and normalization of performance of different channels. For each chain, the following histograms were drawn in order to identify bad channels as shown in Figure 3.2 :

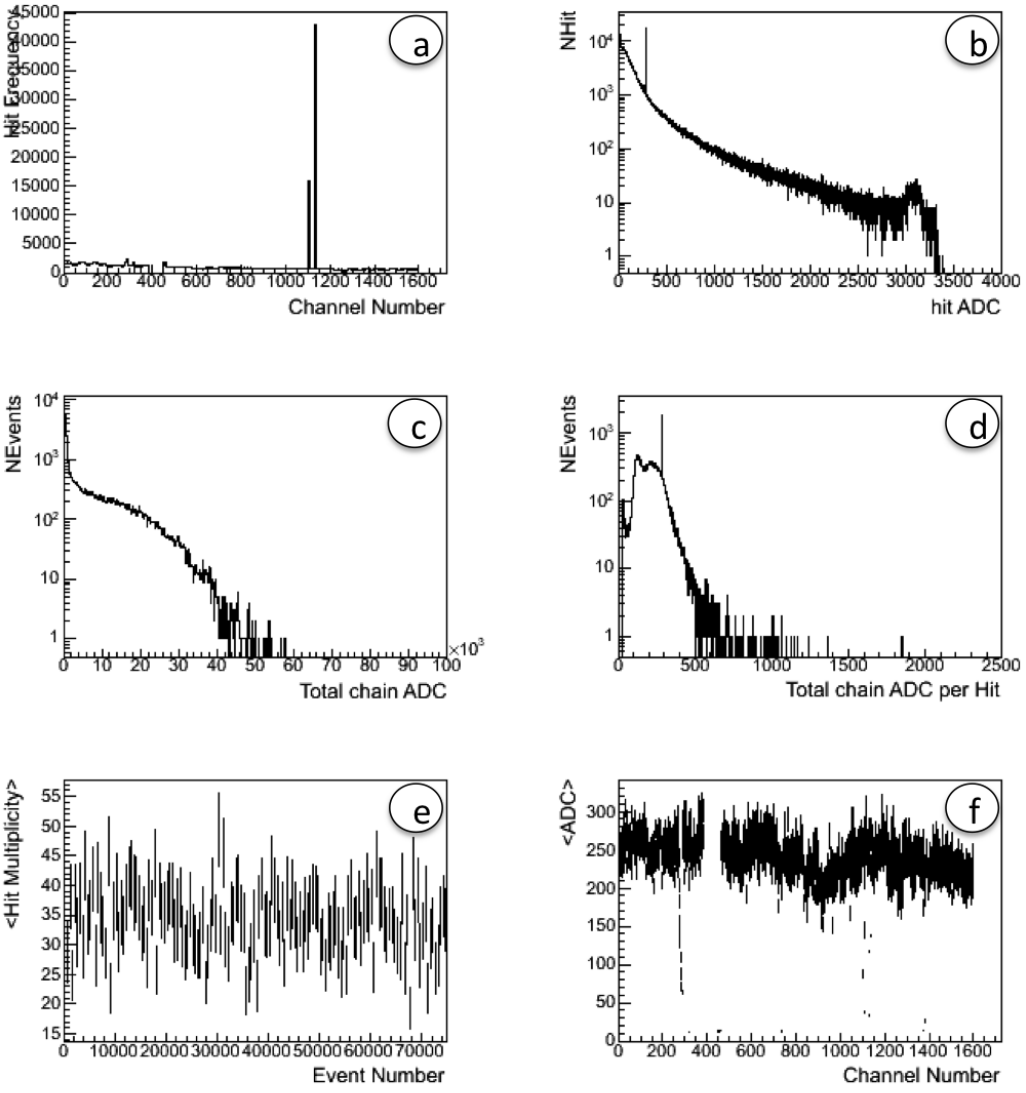

FIGURE 3.2: Quality histograms for a chain of a Run to obtain hot/bad/cold channels (details in text).

(i) **Hit frequency of each channel of the chain:** The overactive(hot), underactive (cold) or nonactive (dead) channels are removed by studying the hit frequency distribution. All the cells of a chain of PMD are continous, and nearly in the same physical location, covering approximately the same phase space. Therefore one expects little variation in the number of times each cell is hit. Figure 3.2(a) shows the hit frequency of all the channels of a chain. The x-axis is the channel number assigned to the cell, and the y-axis shows the hit frequency. A higher hit-frequency on any channel may indicate that the channel may be tripping. To identify these channels, the

mean and RMS of channel hit frequency is calculated for each Run (after removing the channel in question). If the channel hit frequency is beyond the mean ± 5*RMS of all other channels. The procedure is repeated again and this time only channels with hit frequency within ± 3 RMS of the mean hit frequency are used for further analysis. This process removed outliers and retained good channels.

(**ii**) **ADC spectra of hit cells:** The physics signal recieved by each cell may differ from event to event. For the same physics signal, the ADC count may be different for different cells. The distribution of ADC of all cells of all the events for a Run has been shown in Figure 3.2(b). The figure shows some spikes at certain values of ADC. This is due to the presence of sparking cells which give a low ADC signal with a frequency higher than that of normal cells. It is expected that after removal of hot channels, the spike would vanish and the ADC spectra would show a smooth behaviour. The spectra shows a higher frequency of occurrance (a bump) for ADC around 3000. This is due to saturation of response of electronics due to limitation of word size for storing data at this value. A small spread observed at 3000 ADC is due to spread in the pedestal of each cell (already subtracted from this data).

(**iii**) **Distribution of total ADC of the chain in an event:** The total ADC of the chain is the total ADC deposited in an event by all the photons as well as charge particles. This is expected to show a shape similar to the multiplicity distribution of produced particles, and is shown for a particular chain in Figure 3.2(c). If one or multiple boards of a chain are faulty, the shape gets modified or shifted. This helps to identify presence of bad boards and remove the corresponding data. (Data with chains including malfunctioning boards are not shown here).

(**iv**) **Distribution of total ADC of the chain per hit:** Since the total ADC is proportional to the total number of particles, the total ADC divided by the total number of hit cells is expected to be constant with small statistical variations. Different parts of the chain might have slightly different gains and hence the actual distribution might be an overlap of more than one Gaussian. Presence of bad events/ channels results in spikes in the distribution of total

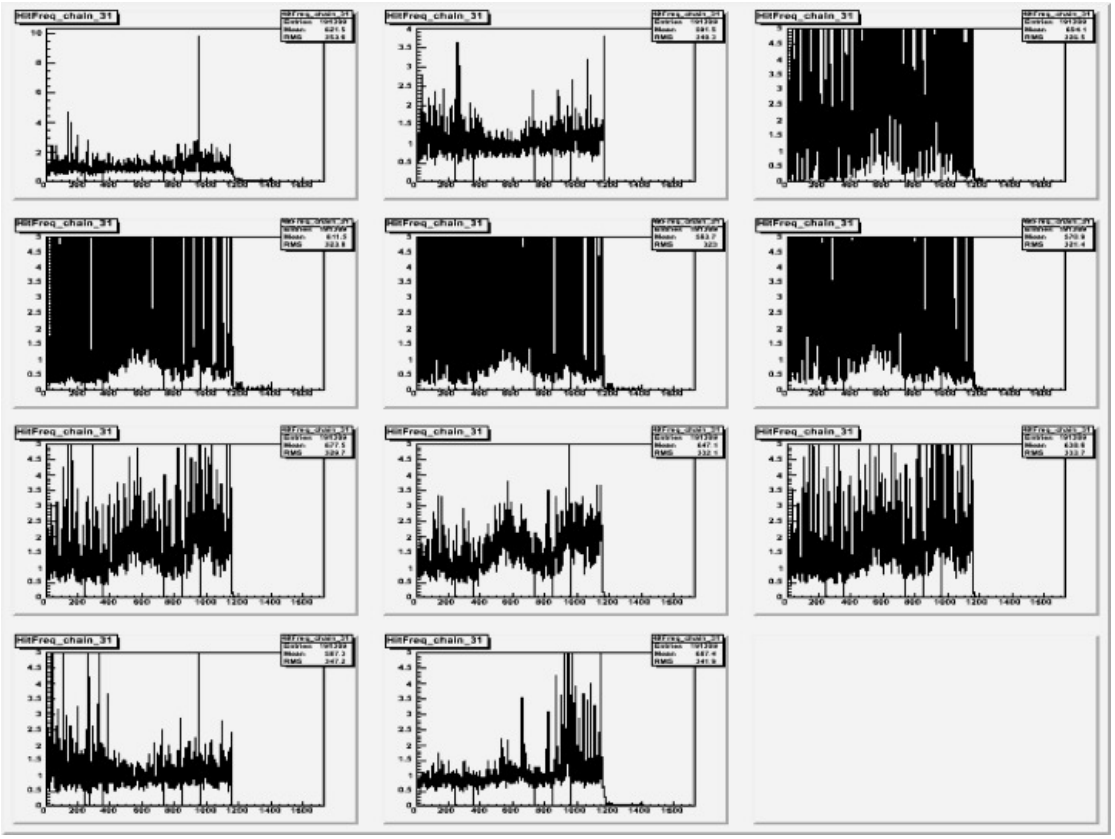

FIGURE 3.3: An example of hit frequency ratio plot for a bad chain

ADC per hit, as can be seen in the Figure 3.2(d). The ADC per hit is shown on the x-axis.

(v) **Distribution of hit multiplicity of the chain in an event:** The mean hit multiplicity averaged over 500 events is expected to be constant. Some times all channels of the PMD started firing. This state was referred to as PMD busy state, and was observed during data taking at 200 A GeV. Such a situation would show up in this plot as a sudden increase in the mean hit multiplicity. The actual mean multiplicity is also expected to change with trigger used for analysis. No such state was observed for this chain, as can be seen in Figure 3.2(e).

(vi) **Mean ADC for each channel:** To identify bad channels in each readout chain, the mean value of ADC is obtained in each cell, averaged over all events. The mean ADC is plotted in in Figure 3.2(f). The x-axis shows the channel numbers. The vertical spread on the mean ADC are the RMS of that channel. Such a plot helps to identify the bad channels which correspond

to a mean ADC much lower than the remaining. As mentioned above, the sparking contributes to the large frequency for the channel yielding a low value of ADC. A small systematic variation in mean ADC is observed due to topology of the chain and depends on actual multiplicity as well as occupancy in that part of the detector.

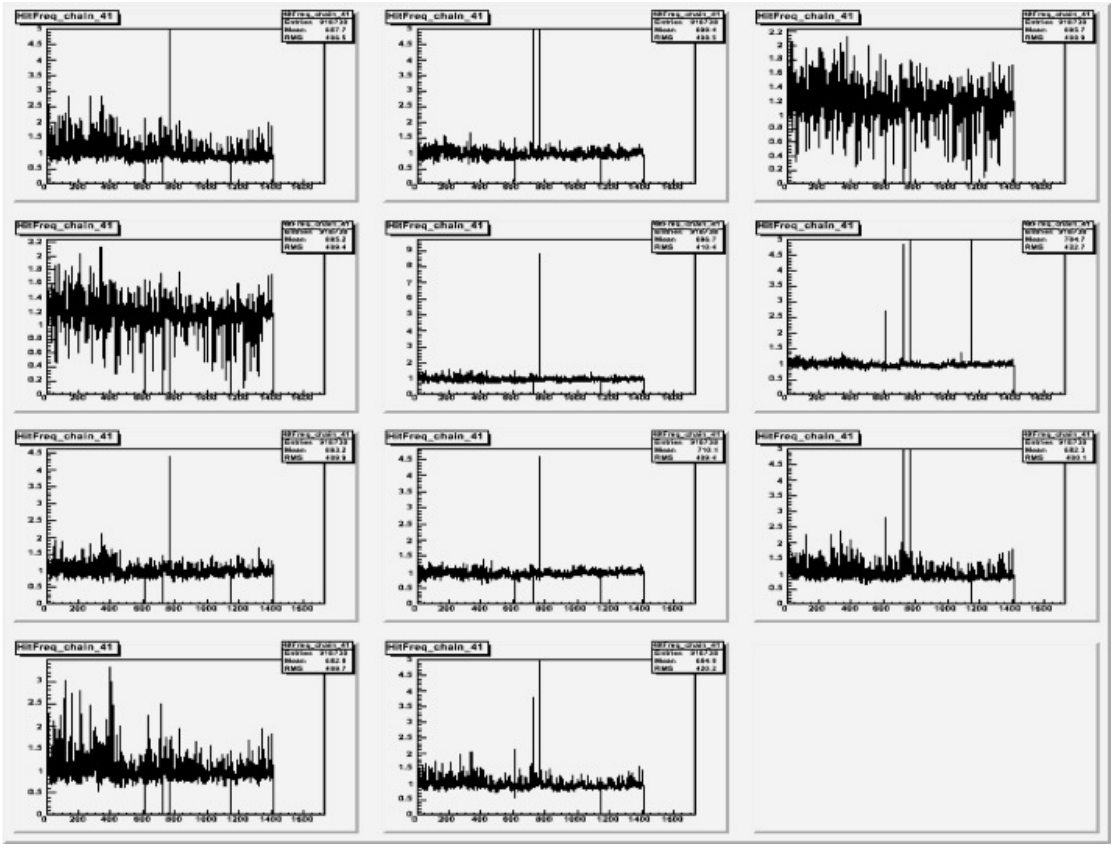

FIGURE 3.4: An example of hit frequency ratio plot for a good chain

(**vii**) **Chain Stability:** After removal of hot, cold and dead channels, the stability of the response of the channels is checked. The hit-frequency of each channel is compared from different Runs. If a channel is unstable then its behaviour would be changing over different Runs. Different Runs correspond to different number of events. To compare the hit frequency of a channel in different runs, it is important to normalise with the number of events in each Run. Out of the large number of Runs used, a good Run was selected as a reference Run. For this Run, the hit frequency of each channel was obtained normalised to total number of events. The same quantity is obtained for different Runs. If the performance of a channel remains same over all Runs,

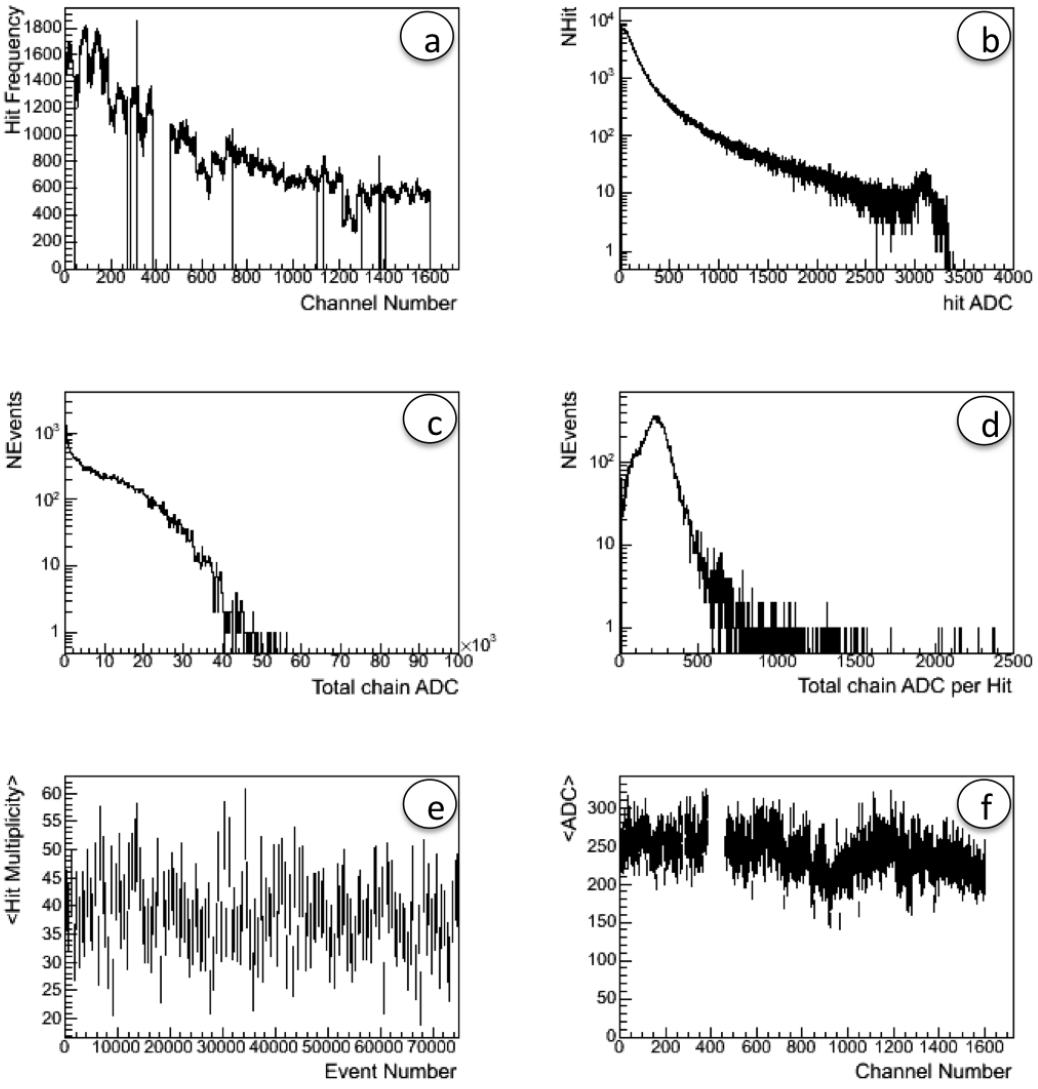

FIGURE 3.5: Quality histograms after cleanup

then the ratio of normalised hit-frequency of any Run with the normalised hit-frequency of the reference Run is expected to be distributed around 1. Figure 3.3 shows the ratio for all channels of a bad chain in 11 different Runs. The x-axis shows the channel numbers. If the ratio is ~ 1 for all the channels, the chain performance can said to be stable. The same ratio for a good chain is shown in Figure 3.4 also for 11 Runs. The few channels which show unstable behaviour are identified at this stage and removed from the data. If most of the channels of the chain are unstable, the chain is dropped from analysis. In a few Runs it was observed that many chains, that were

normally giving good data, were showing unstable behaviour. This analysis was carried out for each chain in each Run. A detail log of stable and unstable chains were prepared so that only stable and clean chains from good Runs are used for further analysis.

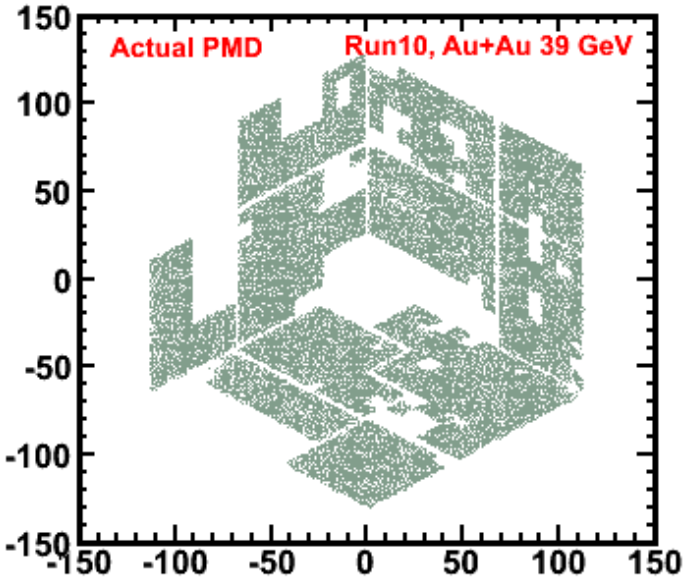

FIGURE 3.6: XY distribution of hits on PMD for Au+Au collisions at 39 A GeV.

The process of cleaning described above is executed for each of the selected Runs. The bad chains, boards, channels are identified and this information is stored in STAR database. The bad channels are not included in event reconstruction and analysis. Figure 3.5 shows the data obtained after cleaning up as defined above. This should be compared with plot in Figure 3.2, which included spikes due to bad channels before the data was cleaned up. An XY plot showing all the live channels of PMD after clean up, is given in Figure 3.6. This figure is for the data of Au + Au 39 A GeV collisions. Similar figures were obtained for data at all collision energies.

3.3 Gain Normalization of PMD

The incident charged particles and photons give signal on the various cells of the PMD, giving a finite ADC signal above the pedestal cut off. If a cell gives a signal above the pedestal, it is called a hit-cell or a hit. The magnitude of the signal due to a minimum ionising particle depends on the intrinsic *gain* of the cell.

The hits are grouped together to make clusters to reconstruct the position of the original photon and charge particles. Since the ADC of a group of cells (cluster) is used for discriminating between the clusters due to photons and the clusters due to hadrons later, it is essential that the response of each cell be normalized with respect to each other. This is obtained by studying the ADC spectra of each cell, when all six neighbouring cells have zero ADC as shown in Figure 3.7. This is referred to as isolated hit ADC spectra of that cell. This isolated hit is most likely due to a Minimum Ionising Particle (MIP). The MIP spectra is plotted in Figure 3.8, along with a fit to Landau distribution. Isolated hits were collected for each channel over many events and their mean ADC, calculated in the ADC range 10 to 500, is used for relative gain normalization.

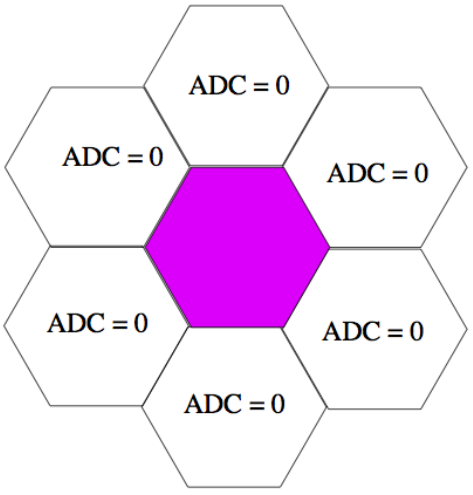

FIGURE 3.7: Schematic diagram of an isolated cell in PMD

Many factors influence total gain of a channel. The differences in gains of different channels may be due to differences in fabrication, both mechanical and electronic hardware, high voltage, temperature and gas flow. Some factors like differences in fabrication and electronic hardware remain constant over the whole period of data

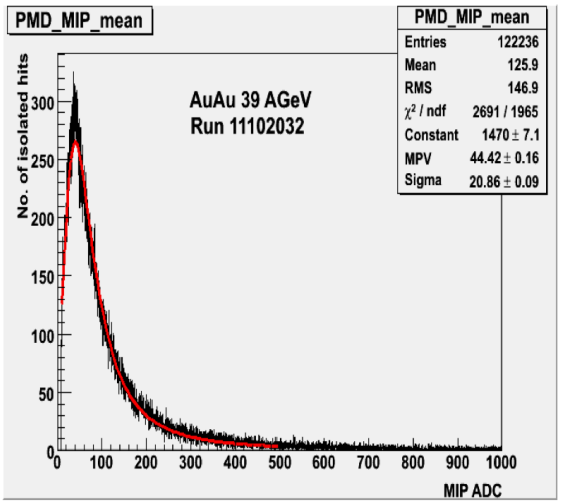

FIGURE 3.8: MIP distribution for all the cells of PMD fitted by Landau distribution (red color)

taking, unless the hardware is changed. Operating factors like voltage, gas conditions and temperature are vulnerable to change within a shorter time duration. resulting in change in gain over short periods.

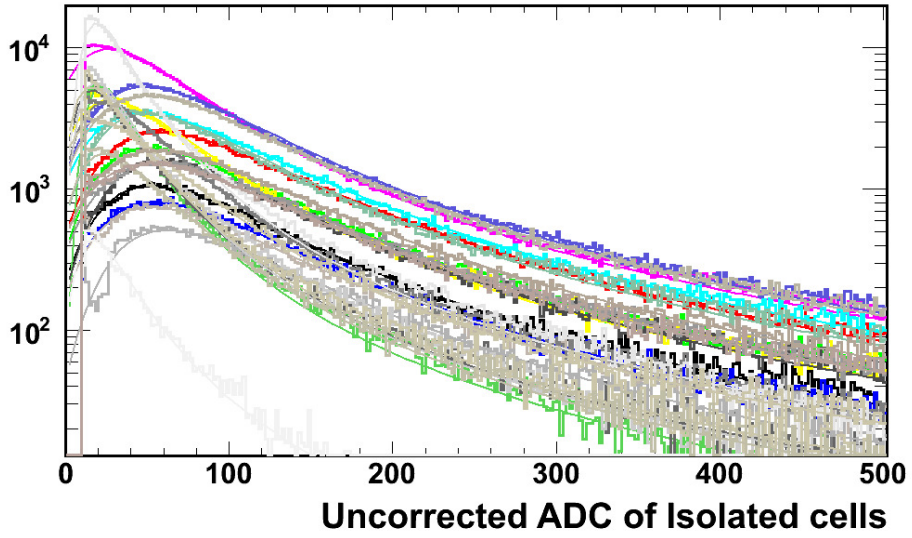

FIGURE 3.9: Isolated cell ADC distribution for all the cells before gain normalization. Each color represents a different SMChain

Each super module consists of separate gas supply and independent high voltage supply. Each readout chain has an independent low voltage supply. Variations in HV affects all the cells of a supermodule, while variations in LV affect all the

cells in a particular chain. Since, a chain may span cells over more than one super module, each super module chain combination (SMChain) is considered as a unit for gain normalization. Figure 3.9 shows isolated cell ADC distribution before gain normalization. Each SMChain is shown in a different color and combines the data for all cells within that SMChain. The dispersion in the positions of the peaks of the distribution can be seen, underlining the need for gain normalisation.

The total gain normalization factor (GNF) for a channel can be factorised as :

$$Total\_GNF = Cell\_GNF * SMChain\_GNF \tag{3.1}$$

Here $Cell\_GNF$ is the relative gain of each cell within one SMChain with respect to the average gain of all cells in the same SMChain. The $Cell\_GNF$ has been obtained for each cell of each SMChain. Applying $Cell\_GNF$ normalizes gains of all cells within an SMChain. Different SMChains have to be normalised with respect to reach other. For each SMChain, the mean gain of all cells is obtained by averaging over the gain of each cell. This is obtained for each SMChain. The $SMChain\_GNF$ is obtained by normalising the mean gain of that SMChain with respect to average of mean gain of all other SMChains, weighted with the number of live cells in each SMChain.

Since relative conditions of the cells within a SMChain do not vary with time, the $Cell\_GNF$ is likely to remain constant over a long period. The voltage (HV and LV) and gas conditions may vary over short time period and these affect different SMChains differently. Therefore the $SMChain\_GNF$ for different chains are likely to vary over a short time period. Due to these reasons the $Cell\_GNF$ is determined once for a period of 4-5 days and $SMChain\_GNF$ once for every six hours of data taking.

3.3.1 $Cell\_GNF$

To determine the $Cell\_GNF$, the mean of the ADC distribution of isolated cells is used.

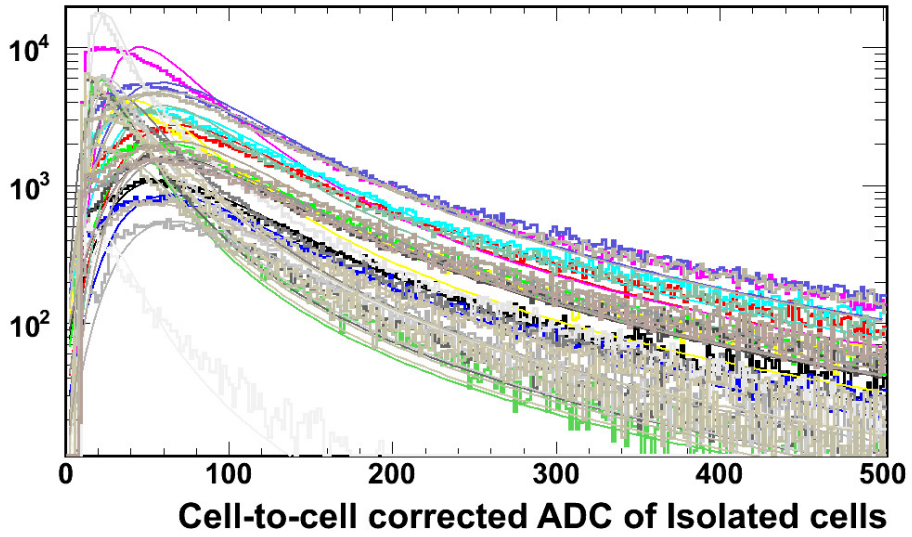

FIGURE 3.10: MIP distribution for all the cells after cell to cell gain normalization. Each color represents a different SMChain

$$Cell\_GNF = \frac{mean\ ADC\ of\ the\ isolated\ cell}{< mean\ ADC\ of\ all\ isolated\ cell >} \tag{3.2}$$

where the average (denoted by angular brackets) is over all the cells within the SMChain to which the cell belongs. Figure 3.10 shows the MIP distribution for all the cells of each SMChain after cell to cell gain normalization. The distributions for different SMChains is shown in different colours (online).

3.3.2 $SMChain\_GNF$

All the cells of an SMChain are relatively normalized by applying the $Cell\_GNF$ obtained by methods as described in the previous subsection. The ADC distribution of isolated hits for all the cells, after cell to cell gain normalization, are then combined to yield an isolated hit ADC distribution for each SMChain. The mean of this distribution for an SMChain is used as a parameter to normalise gains of different SMChains. The relative gain of each SMChain is then determined by:

$$SMChain\_GNF = \frac{mean\ ADC\ of\ the\ isolated\ hits\ of\ a\ SMChain}{< mean\ ADC\ of\ the\ isolated\ hits\ of\ SMChains >} \tag{3.3}$$

The mean ADC of each SMChain is used to determine the average in the denominator.

3.3.3 Gain Normalized Data

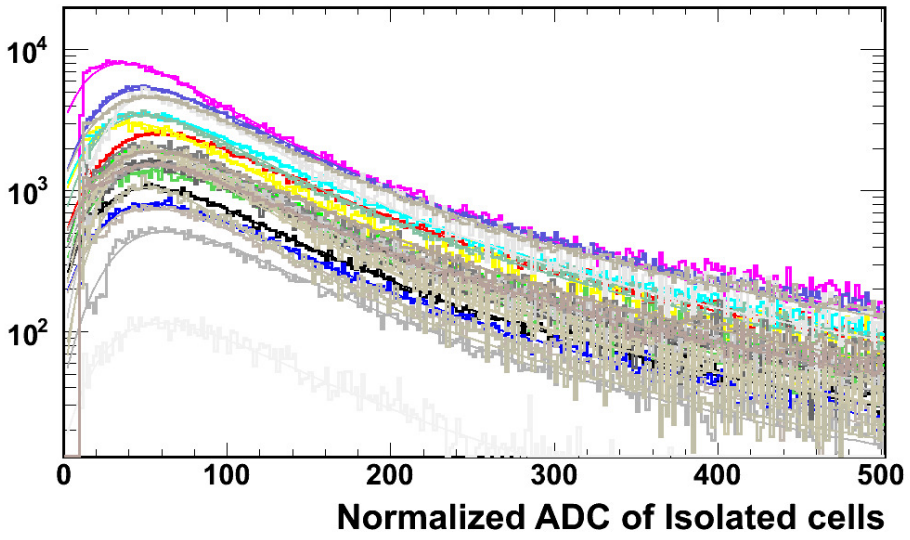

FIGURE 3.11: MIP distribution for all the cells after normalization. Each color represents a different SMChain

One set of $Cell\_GNF$ are determined for each batch of data (one batch comprises of a few days of data taking) and stored in the STAR database with appropriate date and time stamp. One set of $SMChain\_GNF$ are determined for every 6 hours of data taking and these are also stored in a database with appropriate date and time stamp.

When processing data of a Run, the total Gain Normalization factor is generated for each cell by multiplying $Cell\_GNF$ of that batch with $SMChain\_GNF$ closest to the date and time of that Run. The total gain normalization is then applied

to the ADC of that cell in each event. Figure 3.11 shows the MIP distribution for all the cells after gain normalization. The scale on the y-axis is in absolute units. The spread of the various spectra in the y-direction is because of different number of active cells in different SMChains.

3.4 Clustering

The main class of STAR PMD software where the cleanup and gain normalization information is applied is StPmdReadMaker. After applying the gain normalization factors on ADC values of hits from all good cells, all StPmdHits (the parameters of hits as defined earlier) are sent to StPmdClusterMaker for clustering. The details of data sets and the centrality selection criteria were discussed in Chapter 2.

A photon incident on the PMD is expected to give a signal spread over a number of cells. The 3 radiation length of material limit the radial spread of the photon shower. The number of cells affected by the shower depends upon this radial spread. All continuous hits (having at least one common boundary with other hits) are grouped together to form a cluster of hits (called cluster for brevity). Each cluster is then characterized by the number of constituent hits (cluster- size) and their total ADC (sum of ADC of all its constituent hits). The (η, ϕ) of each cluster can be determined from the ADC weighted centroid of its hits. The same routine (StPmdClusterMaker) is used for clustering real data as well as simulated data. In simulated data cluster ADC is replaced by energy deposited in KeV i.e. E_{dep}.

The first step for clustering is to collect all the continuous cells having non-zero ADC. This group of cells is referred to as a supercluster. Thus the superclusters are separated from each other by cells having zero ADC (E_{dep}) unless part of their boundary coincides with the SM boundary. Superclusters are constructed starting from the cell with largest ADC (E_{dep}) and forming a cluster of continuous cells, all with finite ADC (E_{dep}). For making the subsequent superclusters we search for the next largest ADC (E_{dep}) cell and follow the same procedure of collecting continuous non-zero ADC (E_{dep}) cells. This process is repeated till all the non-zero ADC (E_{dep}) cells in a SM are incorporated.

In a higher multiplicity environment of Au+Au collisions at 200 A GeV, a supercluster might get contribution from more than one incident particle (2 photons or 2 charged particles or a photon and a charged particle). In such a case, a method of resolving a supercluster having more than 2 hit cells, into its constituent clusters was evolved. This routine was called refined clustering. But it was observed that this procedure can sometimes cause a supercluster due to a single photon to be broken into two clusters (referred to as split clusters). It was observed that even for Au + Au collisions at 200 A GeV, using refined clustering did not increase the efficiency appreciably and increased the instances of split clusters. The analysis at this energy was carried out using superclusters defined in the above paragraph. At collision energy 39 A GeV and lower energies, the photon multiplicity is lower and hence probability of overlapping clusters is also lower than at 200 and 62.4 A GeV. Therefore, analyses at lower energies also uses superclusters, as defined above. In simulated data, the superclusters themselves are directly associated with the incident particles (photons or charged particles) falling on the detector. This helps to obtain the efficiency and purity of the clusters identified in simulated data.

3.5 Analysis Specific QA

The gain normalisations are obtained only from a subset of data of a given period, as described above, and then applied on the entire data sample for that period. A Quality Assessment (QA) analysis of the data is performed before using it for further analysis. The correlation plots of PMD Multiplicity with Time Projection Chamber (TPC) , Forward Time Projection Chamber (FTPC) and Barrel Time of Flight Detector (BTOF) multiplicity are shown in the three panels of Figure 3.12. Here PMD Multiplicity refers to the number of clusters on PMD which clear threshold conditions, also called $N_{\gamma-like}$. The threshold conditions are discussed in detail in section 1.9.2. Figure 3.12 shows the event by event correlation plot of PMD multiplicity with RefMult (The uncorrected TPC track Multiplicity within ($\mid \eta \mid < 0.5 units$). Two bands are observed in this plot. The same extra band persists when PMD $N_{\gamma-like}$ is plotted with FTPC (East / West) multiplicity as well as BTOF multiplicity, confirming that the origin of the double band is due to the PMD data.

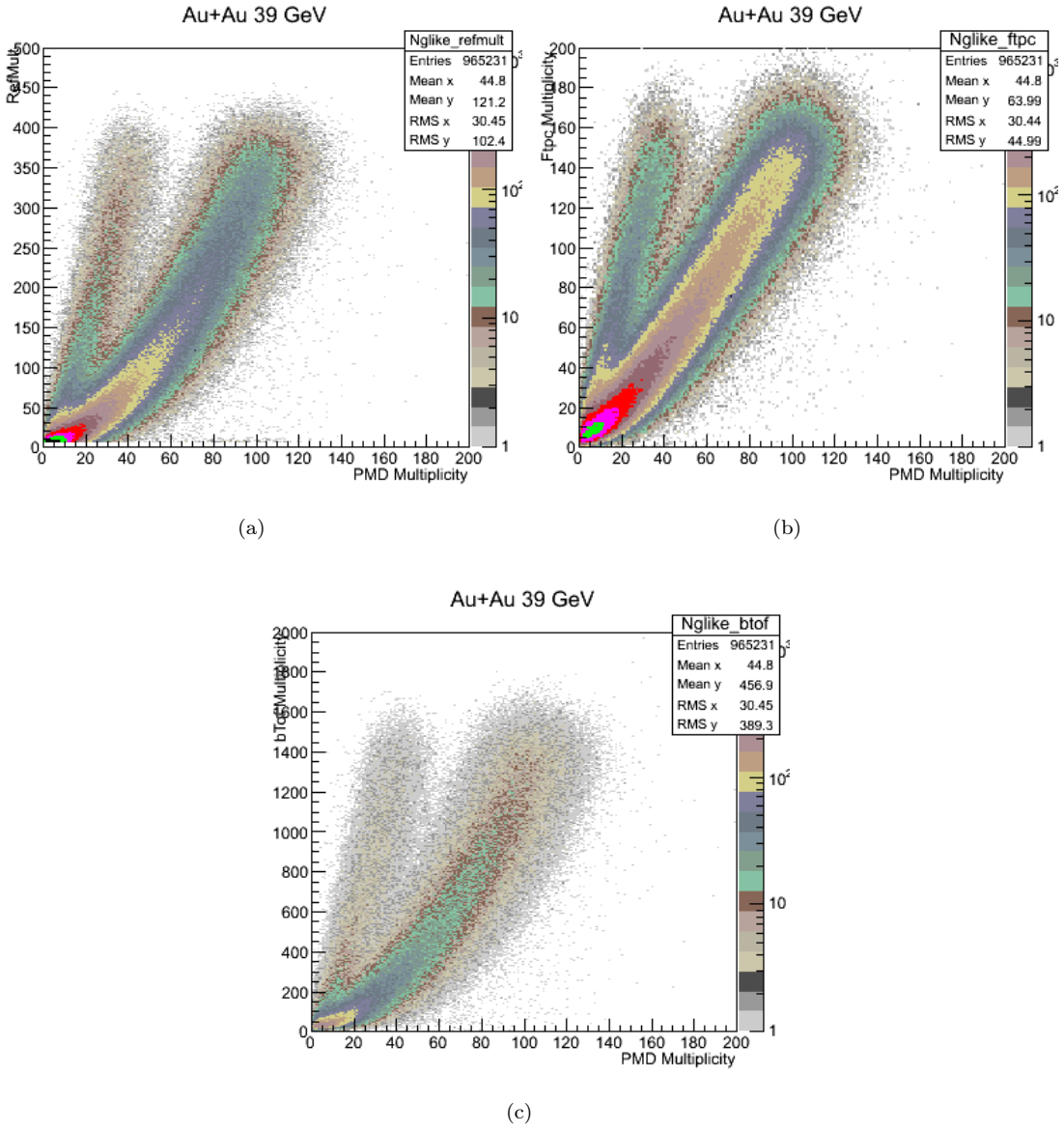

FIGURE 3.12: Correlation plots between (a) Uncorrected charge particle multiplicity in TPC and PMD multiplicity (b) FTPC multiplicity and PMD multiplicity (c) BTOF multiplicity and PMD multiplicity for 39 A GeV Au+Au collisions

After some investigations, it was found that these bands were due to the data corresponding to few Runs in which PMD was probably not behaving well. To remove this band without biasing the data, the following process was adopted.

(a) The mean cluster ADC in CPV plane (before the photon converter) averaged for each event v/s Mean ADC of $N_{\gamma-like}$ averaged for each event in Preshower plane (after the photon convertor) is plotted in Figure 3.13. A separate cluster was observed for some events, which showed smaller values of mean

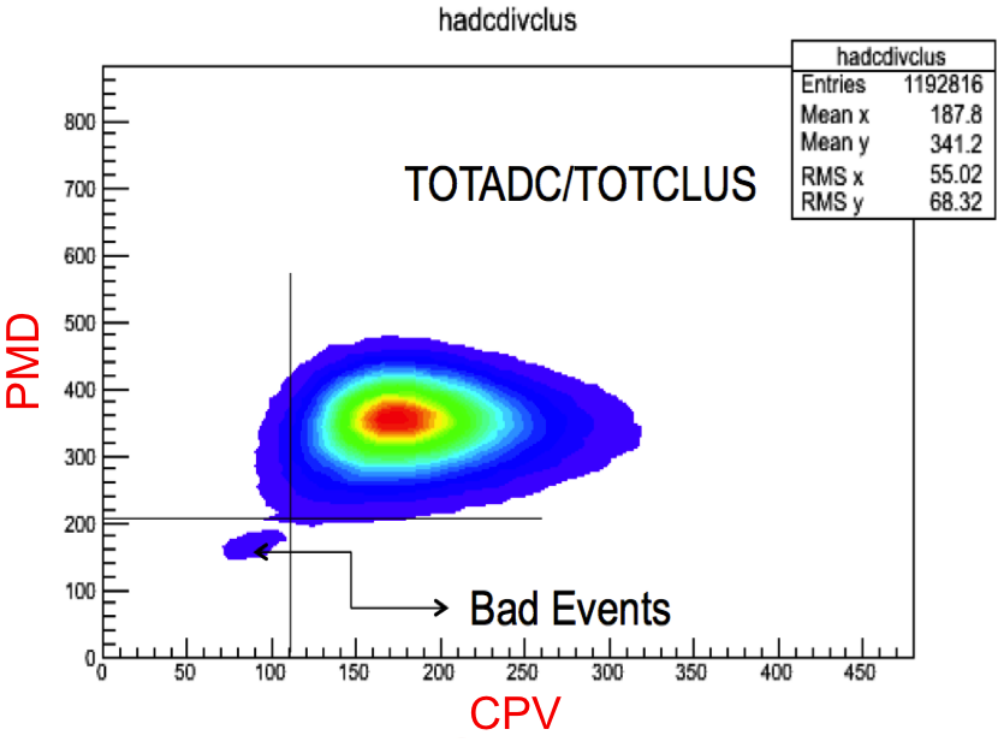

FIGURE 3.13: Ratio of total ADC of the cluster and total number of cluster for both CPV and pre-shower plane of PMD

ADC for CPV and PMD. Since data from CPV plane is not being used in the analysis, a cut was applied on the mean ADC in CPV to remove bad events without biasing the data.

(b) The mean of multiplicity in TPC for each Run, $< RefMult >$, is plotted against the mean of $< N_{\gamma-like} >$, also obtained over events of the same Run, and is shown in Figure 3.14. A scatter plot of $< RefMult >$ and $< N_{\gamma-like} >$ for each Run is shown in Figure 3.14(a). While $< N_{\gamma-like} >$ for most Runs were scattered around a certain value, its values for some Runs was much lower. When $< N_{\gamma-like} >$ is plotted for each Run as shown in Figure 3.14(b), the Runs corresponding to low $< N_{\gamma-like} >$ show up clearly and have not been used for analysis. Figure 3.14(c) is a distribution of ratio of PMD multiplicity and TPC multiplicity. The runs in which PMD is underperforming show up clearly outside the main Gaussian, and were removed by using the criteria that these were more than 3 sigma away from the mean of the Gaussian. Similarly, Figure 3.14(d) is a distribution of mean multiplicity of PMD over all the runs. The runs where the PMD is

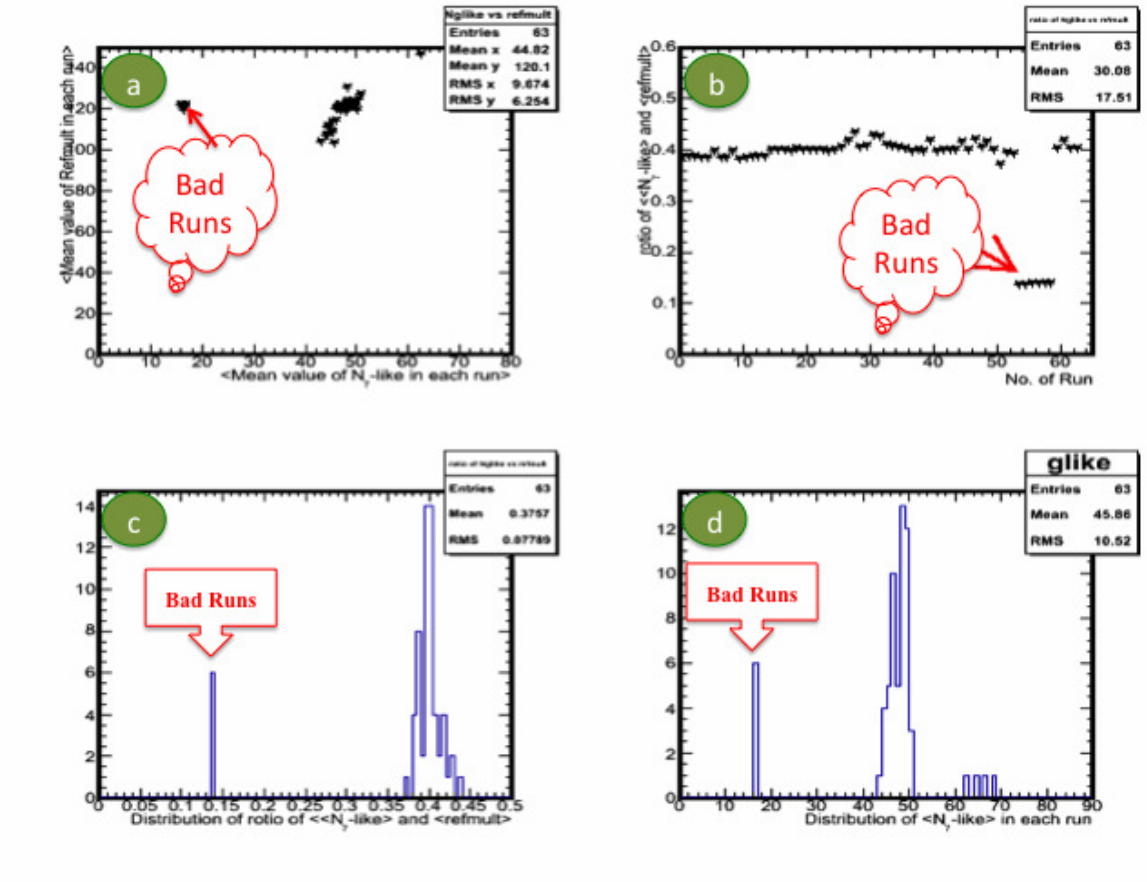

FIGURE 3.14: (a) A scatter plot of $< RefMult >$ and $< N_{\gamma-like} >$ (b) $< N_{\gamma-like} >$ for different Runs (c) Distribution of ratio of $< N_{\gamma-like} >$ to $< RefMult >$ (d) Distribution of $< N_{\gamma-like} >$.

underperforming are identified again by their occurring outside the main Gaussian.

The bad Runs identified by the above two studies were most likely a few Runs in which part of PMD was not working and hence gave a much lower PMD multiplicity. These Runs were not used for further analysis.

3.5.1 Correlation Between Multiplicity in PMD and Other Detectors

After removing bad Runs, scatter plots between $N_{\gamma-like}$ multiplicity in PMD [72] and charged particle multiplicity in TPC [69] in Au+Au collisions are shown in

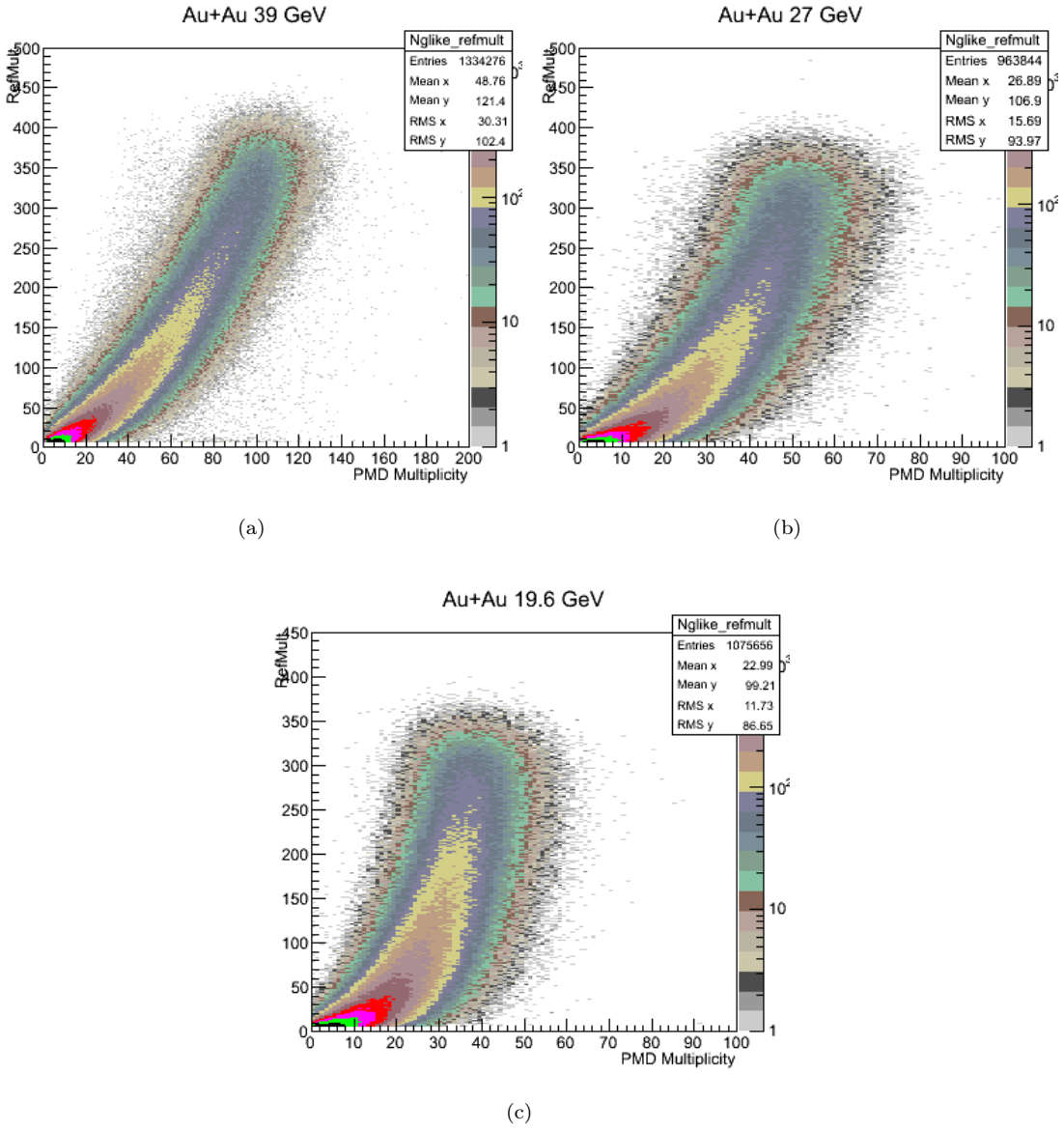

FIGURE 3.15: Correlation between uncorrected charge particle multiplicity in TPC and PMD multiplicity in Au + Au collisions at 39, 27 and 19.6 A GeV

Figure 3.15. The three panels show the figure for the three different energies, 39, 27 and 19.6 A GeV. A single correlation band is observed between both multiplicities. The correlation band is almost linear for 39 A GeV but shows a clear *bending* for 27 A GeV. For 19.6 A GeV the *bend* is much more pronounced.

The bending in these plots can be qualitatively understood by realising that with decreasing collision energy, the beam rapidity decreases and gets closer to the acceptance range of PMD. Possible differences between the particle production at mid rapidity and forward rapidity may lead to other phenomena that may give an extra yield on the PMD even for peripheral collisions. Such extra yield may result

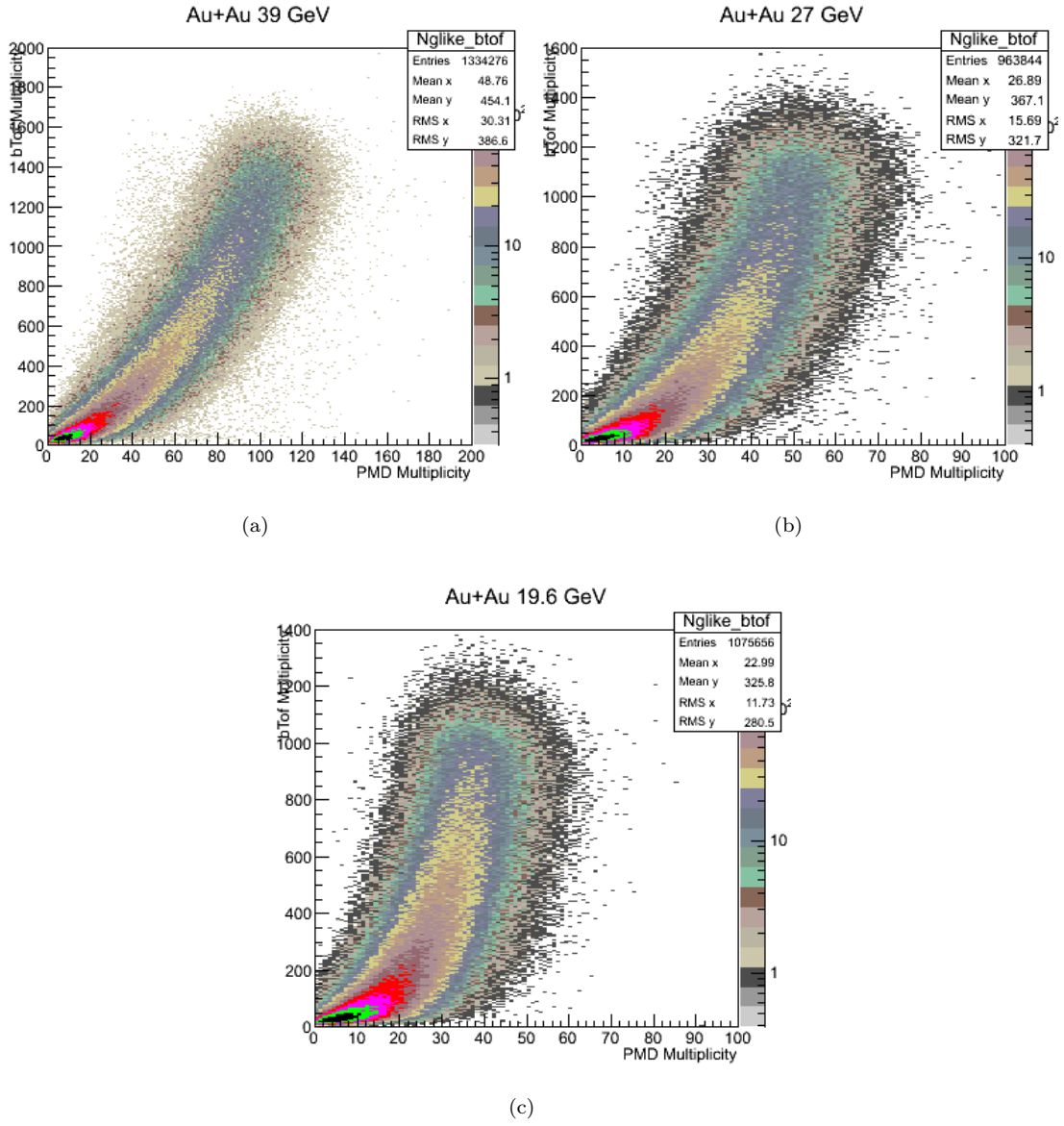

FIGURE 3.16: Correlation between charge particle multiplicity (measured in ToF) and PMD multiplicity in Au + Au collisions at 39, 27 and 19.6 A GeV

into the observed correlation plots. The increased bending of the correlation band between RefMult (from TPC) and PMD Multiplicity observed for 19.6 A GeV events as compared to 39 A GeV events seems to indicate a source of particles identified on PMD, which may depend upon the spectator size. The effect becomes more prominent with increasing overlap between PMD rapidity coverage and the beam rapidity.

In line with this argument, one can expect a similar bending to be observed when studying the correlation between PMD Multiplicity with the BTOF Multiplicity, as can be seen in Figure 3.16. FTPC detector is also at forward rapidity; its

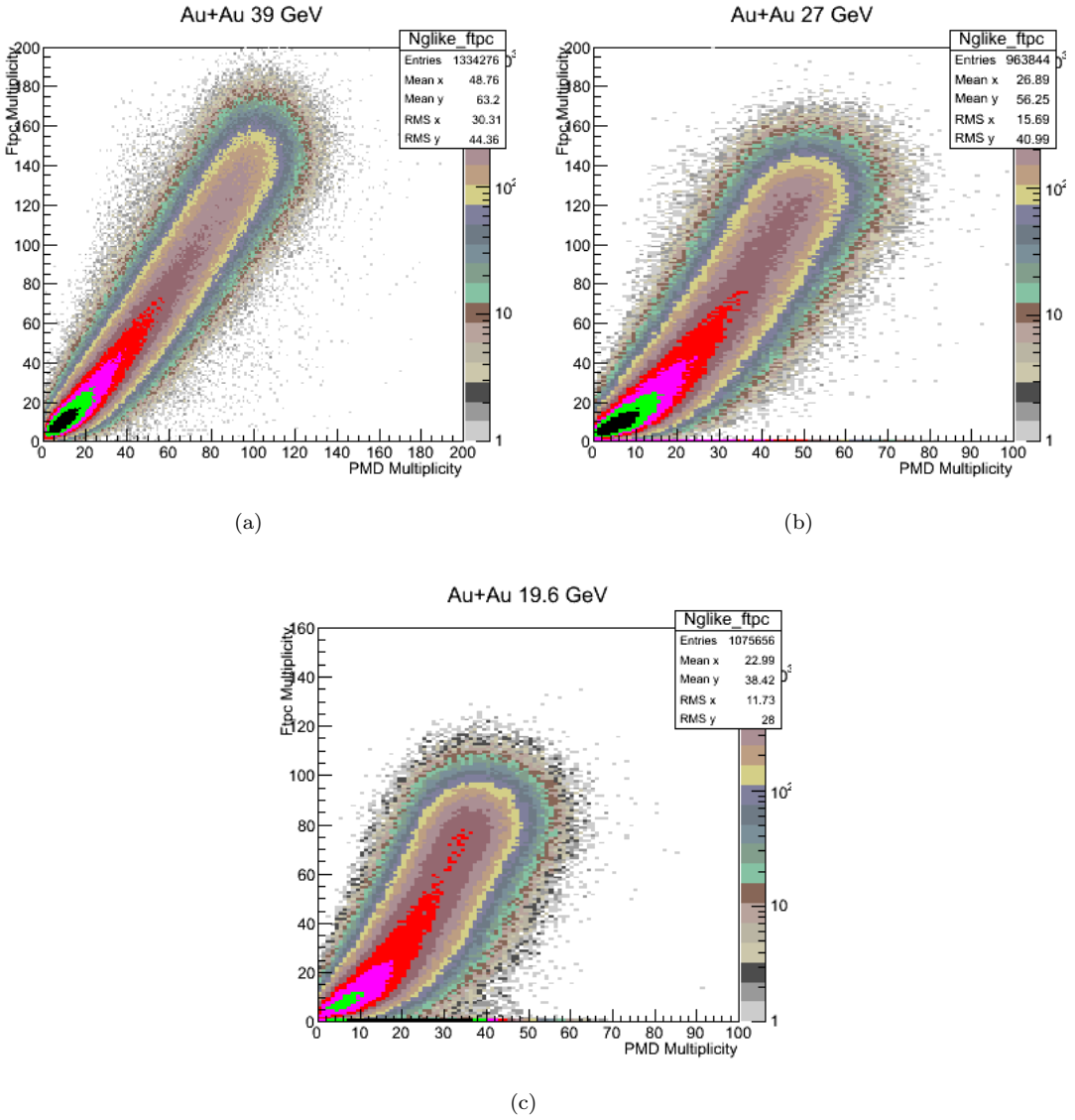

FIGURE 3.17: Correlation between charge particle multiplicity (measured in FTPC) and PMD multiplicity in Au + Au collisions at 39, 27 and 19.6 A GeV

rapidity acceptance range is 2.5 to 4.0. So we expect a much smaller bending of the correlation band between FTPC Multiplicity [70] and PMD Multiplicity. This is seen in Figure 3.17 .

3.5.2 $N_{\gamma-like}$ Distributions

The Photon Multiplicity Detector gets a signal both from incident charged particles and photons, forming clusters. The clusters of continuous cells are identified with two parameters, the total ADC count (ClusterADC) and the number of cells

(ClusterSize) in the cluster. Clusters above the threshold as defined in Chapter 2, are referred to as $\gamma - like$. Their number is corrected for efficiency and purity to estimate the photon multiplicities.

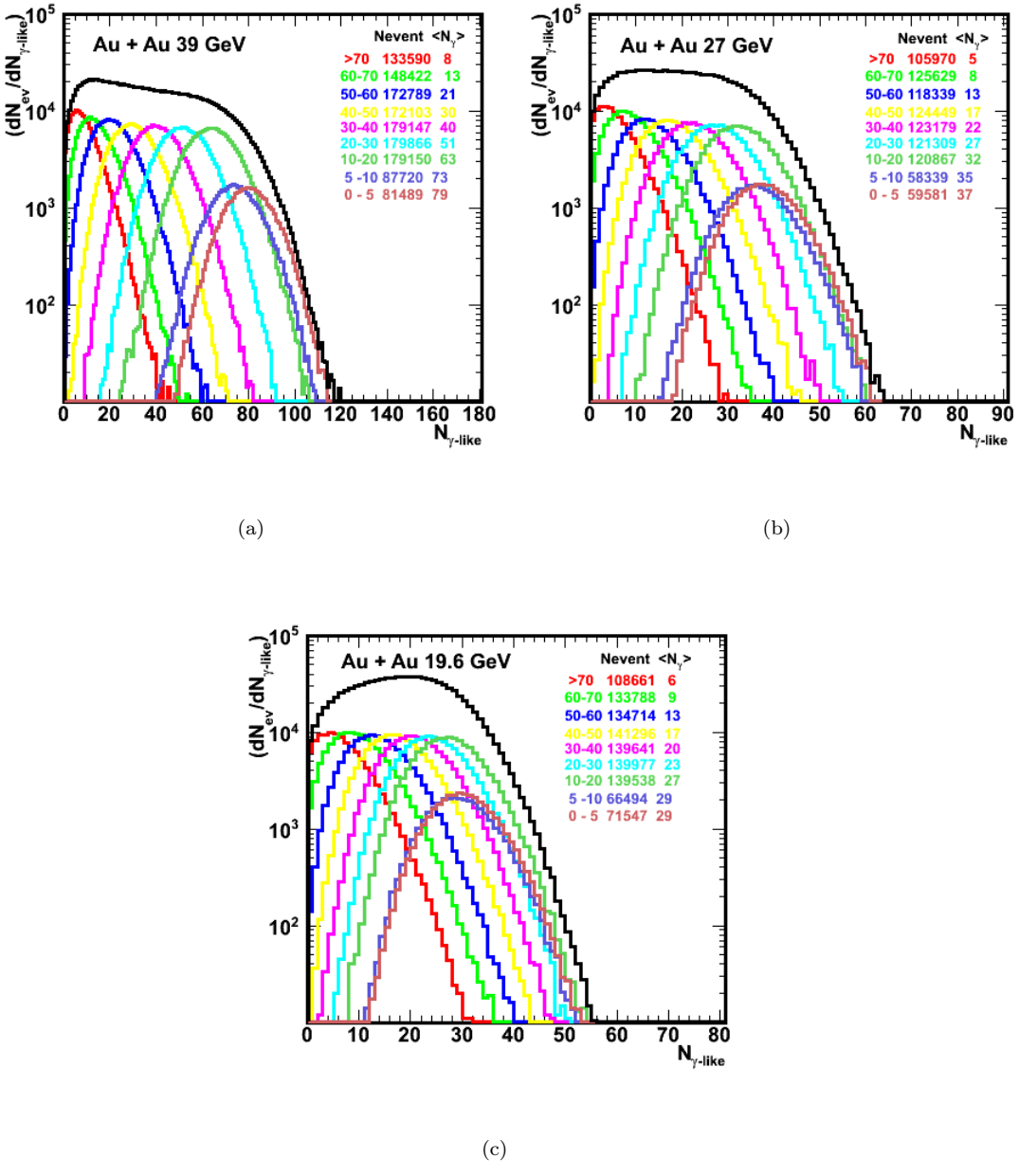

(a) (b)

(c)

FIGURE 3.18: Uncorrected photon multiplicity distributions for minimum bias Au + Au collisions at 39, 27 and 19.6 A GeV.

After cleanup, the distributions of $N_{\gamma-like}$, are plotted in Figure 3.18 for each energy. At each energy, the figure shows the $N_{\gamma-like}$ distributions for each centrality separately, where the centrality has been obtained by methods detailed in Chapter 2. The actual number of events, for each centrality, are also mentioned

on the figure. The min-bias distribution is also plotted for centrality 0-80% for Au + Au collisions at each energy. These distributions have to be corrected for acceptance, efficiency and purity in order to obtain the actual photon multiplicity. The method used for acceptance, efficiency and purity determination is described in the next two sections.

3.6 PMD Acceptance

The acceptance of PMD within pseudorapidity -3.7 to -2.3 is limited due to inactive cells and dead area (e.g. boundaries of the supermodules). Therefore, to estimate the correct $N_{\gamma-like}$ from the measured number we need a correction due to finite acceptance. Since PMD is planar, the acceptance of the detector is defined as the ratio of *active area* of the detector with the *actual area* in the same region.

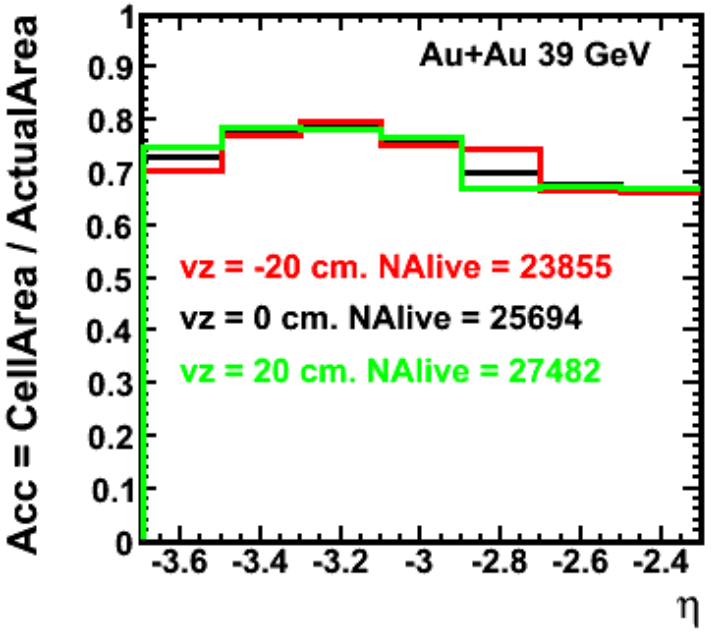

FIGURE 3.19: Acceptance of PMD in three different Vz bins.

The z position of the vertex of an accepted Au + Au collision at 39 A GeV can vary from -30 to +30 cm of the STAR center. The radial distance (r_η) of a particle of rapidity η, on PMD plane, is given by

$$r_\eta = z * tan^{-1}[2tan^{-1}(e^{-\eta})] \tag{3.4}$$

Here z = 540 $cm + v_z(cm)$. This implies that the actual part of PMD which is contributing to the detection of photons for a particular rapidity range changes with the vertex position. This requires that correction factors for acceptance are calculated for different vertex positions. The total v_z range used for analysis was divided into 5 cm. bins and acceptance of PMD was calculated with respect to the center of each v_z bin as follows:

$$Acceptance\ in\ an\ \eta\ bin = \frac{No.\ of\ active\ cells\ within\ that\ \eta\ bin}{\pi(r^2_{\eta_{max}} - r^2_{\eta_{min}})} * cell - area \tag{3.5}$$

This acceptance was applied to all events with v_z within that bin. The Figure 3.19 shows the acceptance of PMD for three different v_z bin. The number of active cells of PMD have also been marked on the Figure 3.19 for three different vertex positions. The area of the cell, used as cell-area in the above equation, is 0.966 cm^2.

3.7 Efficiency and Purity

To estimate the photon multiplicity from the $N_{\gamma-like}$ clusters, the photon reconstruction efficiency and purity of the sample of $N_{\gamma-like}$ is to be estimated. This has been achieved by simulating HIJING events [44] with STAR GEANT for Au + Au at 39, 27, 19.6 A GeV. These data have been produced including all the detectors of STAR which were present during Run10 and Run11. About 200 K simulated events for 39 A GeV, 180 K for 27 A GeV and 120 K for 19.6 A GeV Au + Au collisions have been used to obtain efficiency and purity.

The data of simulated events is also processed using the same software chain as was used on the actual data. The clusters are then processed in StPmdAssociationMaker class which associates all clusters to the incident particles. Using the

E_{dep} distribution of isolated clusters (single cell clusters), we determine the mean E_{dep} of the minimum ionising particle. In addition to cluster size, the mean E_{dep} is used in simulated data to define the threshold for gamma-like clusters. As discussed in Chapter 2, this threshold for a cluster has been chosen as clustersize $>$ 1 and $E_{dep} > 3$ times the E_{dep} of a MIP. The same criteria is used in experimental data where ADC is measured instead of E_{dep}.

While the energy deposited in most of the clusters is due to a single particle, some are formed by more than one particle. In such cases the cluster is associated to the particle contributing maximum energy to it. Sometimes a photon contributes to two clusters and both clusters clear the threshold for selection of gamma-like clusters. In such a case the clusters to which the photon has contributed higher amount of energy is called the (primary) photon cluster while the second cluster is called the split cluster. Thus all the clusters which clear the threshold conditions are classified as photon clusters or hadron clusters or split clusters.

The photon counting efficiency ϵ_γ and the fractional purity f_p of the photon sample [42, 43] are defined by the following relations:

$$\epsilon_\gamma = N_{cls}^{\gamma,th}/N_{inc}^{\gamma} \tag{3.6}$$

$$f_p = N_{cls}^{\gamma,th}/N_{\gamma-like} \tag{3.7}$$

where, N_{inc}^{γ} is the number of photons incident within the PMD acceptance range, which is known from the HIJING event generator, $N_{cls}^{\gamma,th}$ is number of photon clusters above the hadron rejection threshold. $N_{\gamma-like}$ is the total number of clusters detected on PMD above the hadron rejection threshold. These include clusters due to photons, hadrons as well as split clusters. Using the estimated values of ϵ_γ and f_p as defined above, one can estimate the number of incident photons (N_γ) as:

$$N_\gamma = N_{\gamma-like} \times f_p/\epsilon_\gamma \tag{3.8}$$

The efficiency as defined above includes detection efficiency (conversion probability and subsequent discrimination) and effect due to acceptance. The acceptance has been calculated in section 3.8 and can be factored out. Hereafter, for brevity, the detection efficiency has been called as efficiency.

3.7.1 Effect of Finite Acceptance

The simulated data was produced with both ideal PMD (all cells are used) and actual PMD (cells rejected in data are not used). Efficiency and purity was determined for each case. For both cases, efficiency (detection efficiency) is plotted as a function of η is shown in Figure 3.20 (a) .

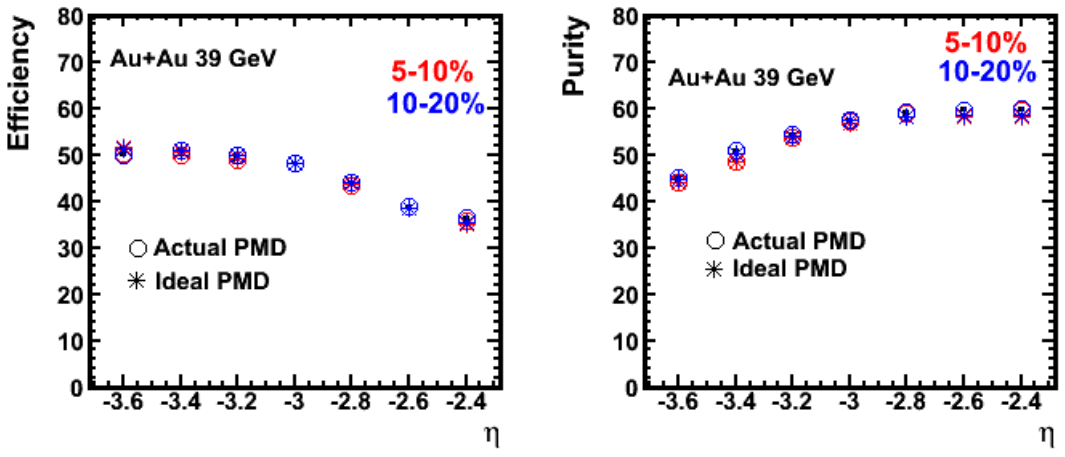

(a) (b)

FIGURE 3.20: (a) Efficiency as a function of η corrected by the acceptance for both ideal and actual PMD (b) Purity as a function of η for both ideal and actual PMD

Since these two efficiencies match, more detailed studies of efficiency and purity have been conducted using simulated data for ideal PMD. To obtain the values of N_γ, the $N_{\gamma-like}$ is corrected for efficiency and purity and also by the acceptance of the detector. Purity from the two cases can also be observed in Figure 3.20 (b). The purity of the signal remains unaffected by the acceptance of the detector, as expected.

3.7.2 Effect of Different Event Generators

To estimate any possible effect of details of event generator, efficiency and purity values have been obtained using both HIJING [44] and AMPT [80].

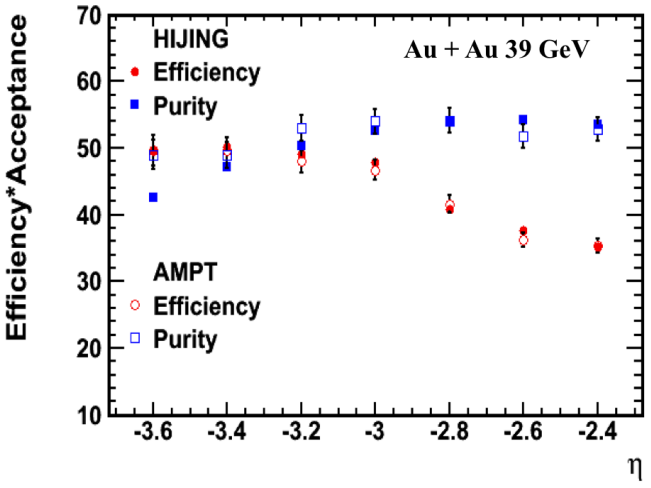

FIGURE 3.21: Efficiency and purity as a function of η from two different event generators HIJING and AMPT.

Figure 3.21 shows the efficiency and purity as determined by both AMPT and HIJING. The efficiency and purity from both event generators show agreement. For all analyses presented here, detailed estimates of efficiency and purity for all cases have been obtained using HIJING events.

3.7.3 Photon Hadron Discrimination

In order to discriminate between clusters due to a hadron track or due to a photon track, we need to understand the properties of photon clusters and charged hadron clusters [81].

A threshold condition has to be chosen to eliminate majority of clusters due to charged hadrons, while maximising efficiency of photon detection. The variation of photon counting efficiency and purity for various threshold cuts decides the photon-hadron discrimination criteria. Figure 3.22 shows the efficiency of photon counting and purity of photon sample as a function of threshold E_{dep} (ADC in

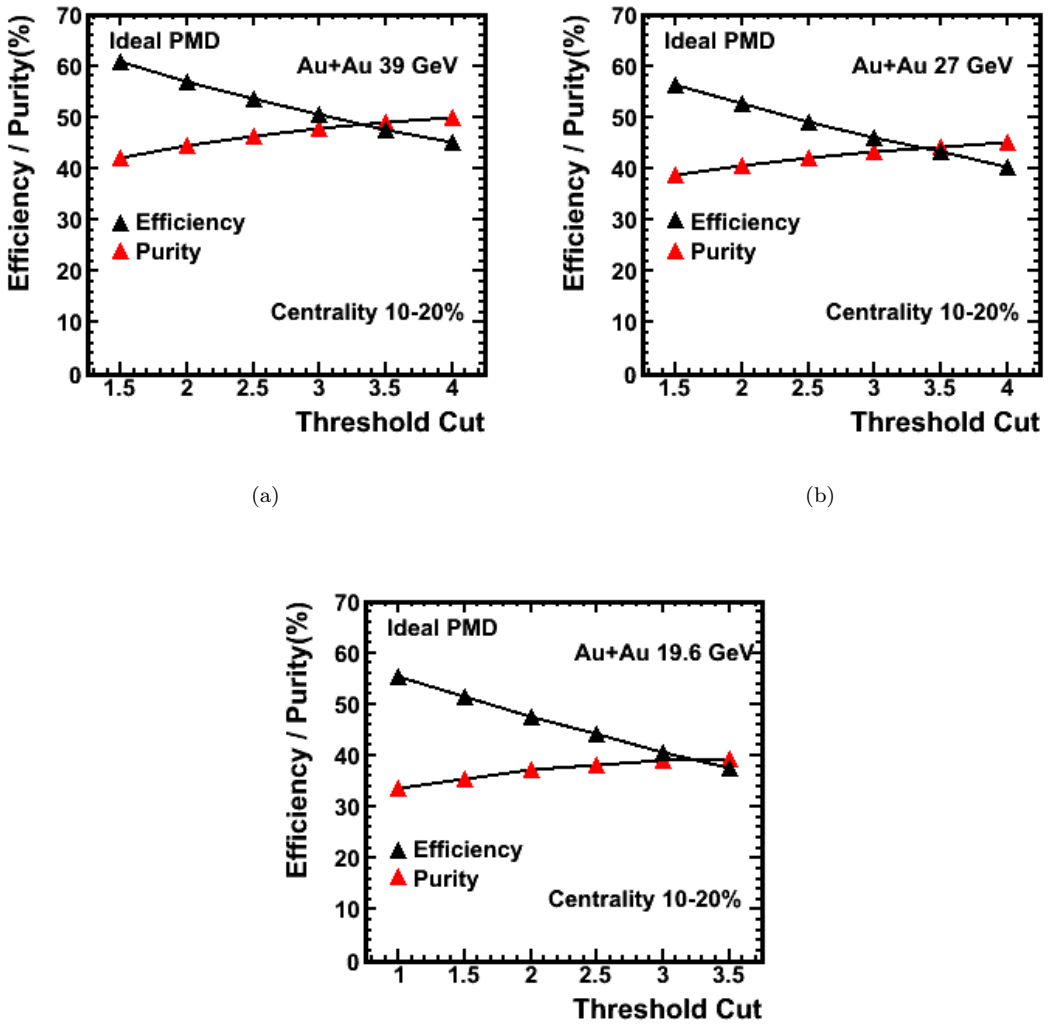

FIGURE 3.22: Efficiency and purity of photon counting for different threshold cuts in units of E_{dep} of the MIP at 39, 27 and 19.6 A GeV. E_{dep} of MIP obtained in simulation is $\sim$ 2.5 keV.

data) given in units of E_{dep} of MIP (single cell clusters). With increasing threshold ADC, the hadron contribution to the $N_{\gamma-like}$ would decrease, though in the process some photon clusters are also lost. So with increasing threshold ADC, the purity of sample increases but the efficiency decreases. With decreasing collision energy both purity and efficiency decrease by a few percent at all threshold cuts. For selection of $N_{\gamma-like}$ in 39 and 27 A GeV, a threshold cut of 3 times the MIP ADC was used. For 19.6 A GeV in order to keep a higher efficiency, a threshold cut on ADC of 2.5 times MIP ADC was used.

3.7.4 Occupancy

Occupancy of a certain region of PMD is defined as the ratio of total number of cells with a finite signal above noise threshold (a hit) to the total number of active cells in that region of PMD. Figure 3.23(a) shows the occupancy as a function of η for two different event centralities in data for Au+Au collision at $\sqrt{s_{NN}}$= 39 GeV.

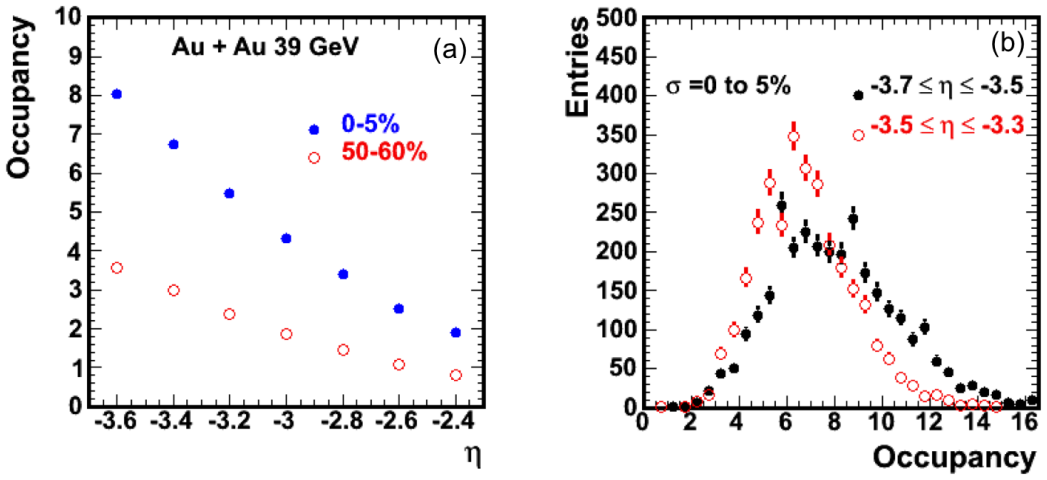

FIGURE 3.23: (a) Mean occupancy as a function of η for 0 to 5% central and 50 to 60% peripheral Au+Au collisions at $\sqrt{s_{NN}}$= 39 GeV. (b) The occupancy in different rapidity intervals for most central events.

Since the particle density is higher in central collisions, the occupancy is also higher as compared to corresponding values in peripheral collisions. Figure 3.23(a), shows the occupancy of PMD in events from top centrality bin 0-5% (central collisions) and from centrality bin 50-60% (peripheral collisions). It is observed from Figure 3.23(b) that the occupancy increases even though the number of photons are expected to decrease as we move from $\eta \sim$ -2.3 to $\eta \sim$ -3.7. This is because of the planar design of PMD and can be understood.

Different pseudorapidity intervals can be imagined on PMD as annular rings. The rapidity intervals -3.7 to -3.5 corresponds to a much narrower ring shaped area on PMD as compared to rapidity interval -2.5 to -2.3. Since the cell size is uniform for all regions of PMD, the number of cells within equal size rapidity intervals decreases rapidly towards forward pseudorapidity. The ratio of number of particles falling on the PMD to the number of cells is higher at η equal to -3.6 region as

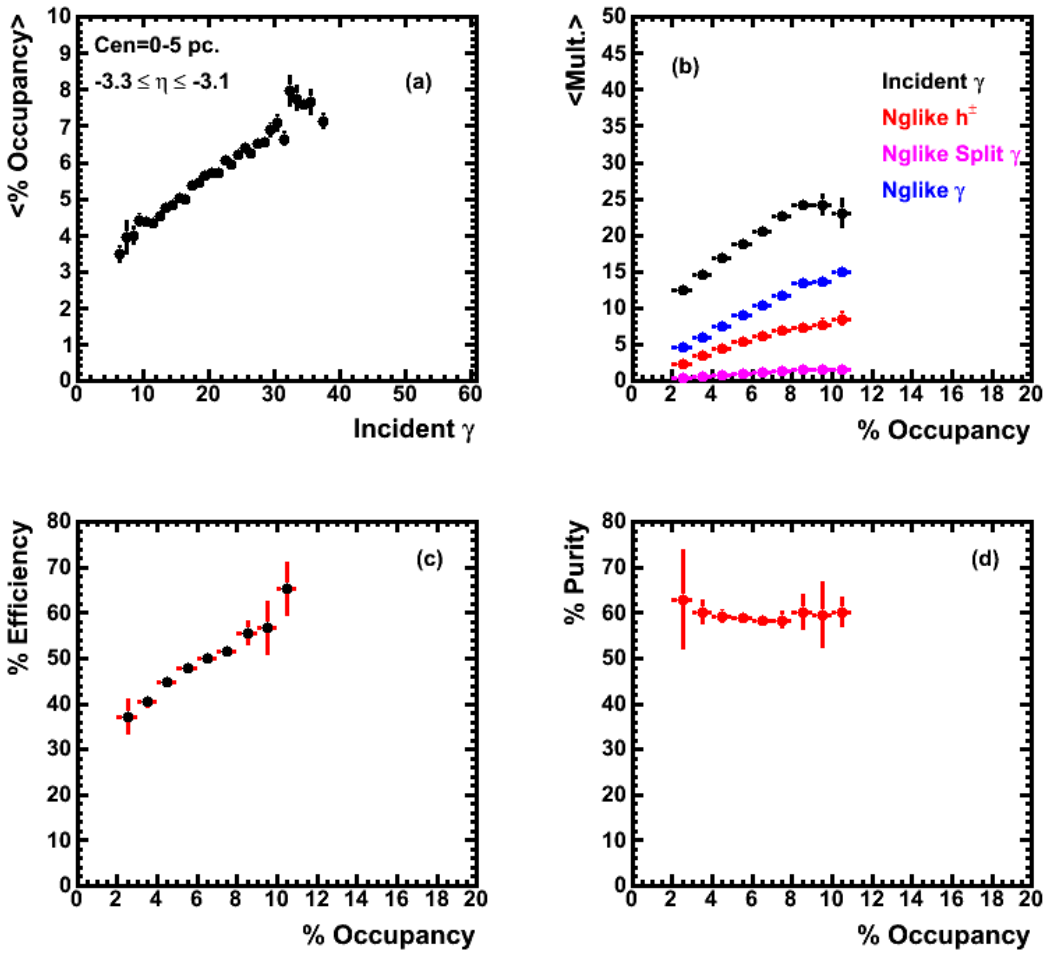

FIGURE 3.24: (a) Mean occupancy as a function of number of incident photons for centrality bin 0 - 5 % and for η bin -3.3 to -3.1. (b) Mean multiplicity as a function of occupancy. (c) Efficiency as a function of occupancy. (d) Purity as a function of occupancy.

compared to corresponding number at η equal to -2.4, resulting into higher value of occupancy.

Both efficiency and purity of the photon signal are expected to depend on the occupancy in PMD. A photon is more likely to give a bigger cluster on PMD which would result in higher occupancy values. To understand this, the occupancy has been obtained as a function of number of incident photons. For each value of occupancy, the average contribution of charged particles, photons and split clusters to the total $N_{\gamma-like}$ is also obtained. In Figure 3.24(a) the percentage occupancy as a function of the number of photons incident on PMD is shown. The plot is for most central events (0-5%) and for eta bin -3.3 to -3.1. It shows a clear

increase in occupancy with incident photon multiplicity. A similar behaviour is observed for all centralities and rapidity bins. Figure 3.24(b) shows the $N_{\gamma-like}$ clusters (clusters clearing the threshold condition) formed (i) by photons tracks (in blue) (ii) by hadron tracks (in red) and (iii) by split clusters (one photon making more than one clusters) in pink as a function of detector occupancy. The figure also shows the incident number of photons as a function of occupancy. The ratio of $N_{\gamma-like}$ due to photons (detected photons) to the incident multiplicity of photons (i.e. efficiency) shows a clear increase with occupancy as shown in Figure 3.24 (c). The ratio of $N_{\gamma-like}$ due to photons to the total $N_{\gamma-like}$ is purity and shows weak variation as shown in Figure 3.24 (d). Efficiency and purity for different values of occupancy in each eta window for each centrality have been obtained. The centrality bins in simulated data were chosen such that the mean occupancy matches that in data for the corresponding centrality bin. The mean occupancy in data and simulation are shown in Figure 3.25 for the most central events. Figure 3.25(a) shows the mean occupancy as a function of rapidity interval for data and simulated data for a centrality and Figure 3.25(b) shows their ratio in each rapidity interval.

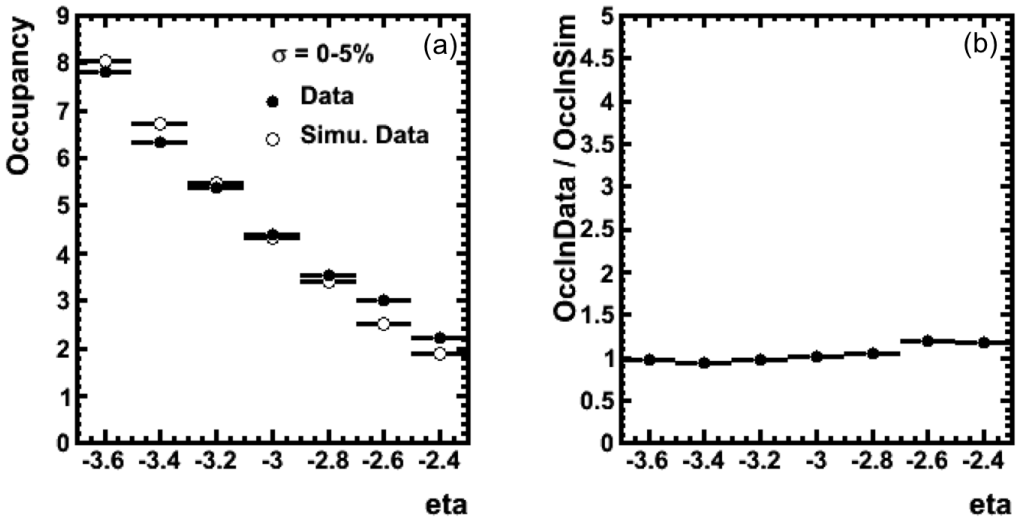

FIGURE 3.25: (a)Mean occupancy as a function of pseudorapidity interval for data (filled circles) and simulated data (open circles) for centrality bin 0-5 %.(b) The ratio of occupancy in data to simulated data

3.7.5 Efficiency Variation with Occupancy

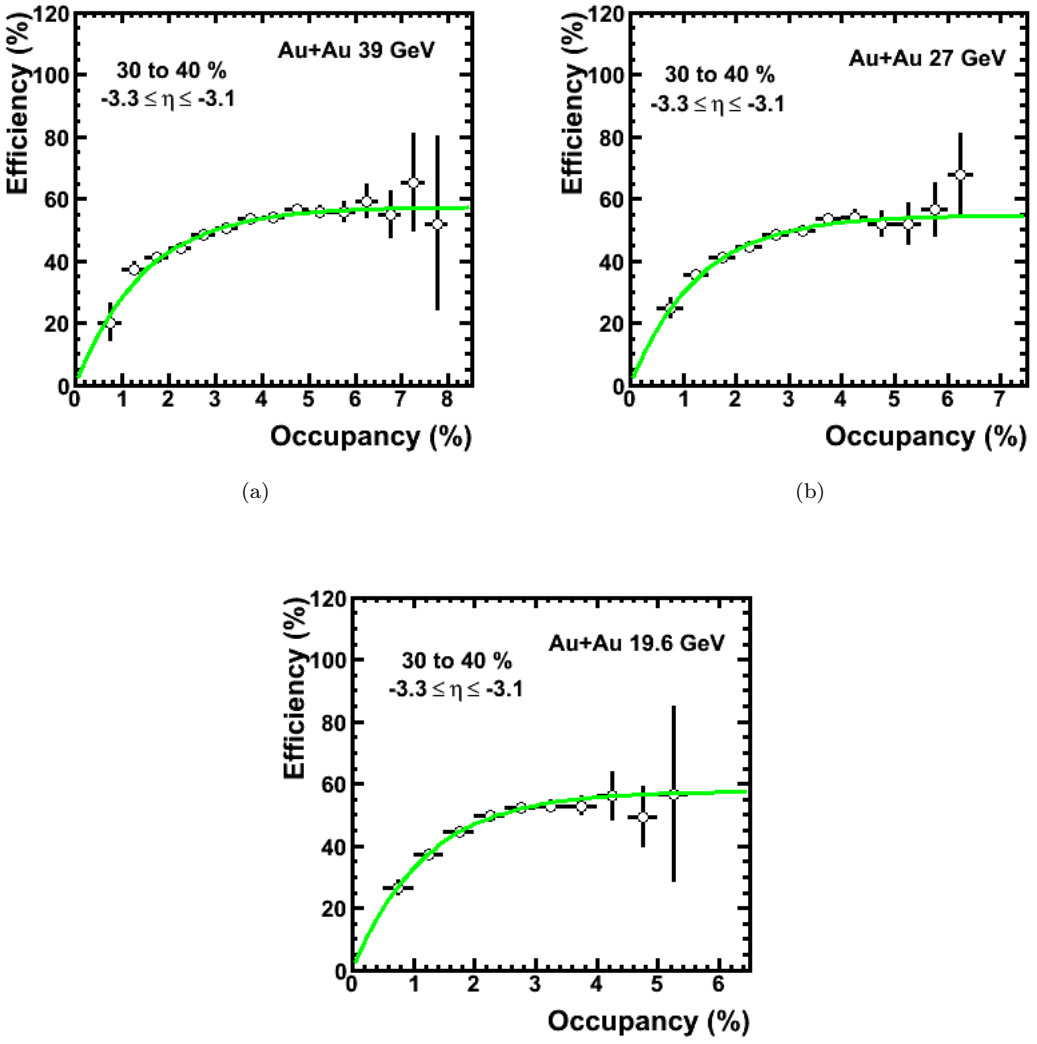

(a) (b)

(c)

FIGURE 3.26: Efficiency of photon sample as a function of occupancy at $\sqrt{s_{NN}}$ = 39, 27 and 19.6 GeV. The figures shown are for event centrality 30-40% and rapidity interval -3.3 to -3.1. Similar graphs were obtained for each rapidity interval for each event centrality

Efficiency has been obtained for different values of occupancy for each eta window and for each event centrality. Figure 3.26 shows the percentage efficiency as a function of occupancy for 30-40 % centrality and pseudorapidity bin -3.3 to -3.1 for Au + Au 39, 27 and 19.6 A GeV. Similar plots were obtained for each value of centrality and for each pseudorapidity bin. A function (given below) was fitted to efficiency for each eta window for each centrality. A small factor of 0.0005 was added to occupancy for ease of fitting; since the binsize for occupancy is 0.5%,

the factor does not affect our results. These fit functions are used to obtain the efficiency in data according to the observed occupancy.

$$Efficiency = A[1 - \exp^{-(\frac{Occ+0.0005}{B})}] \tag{3.9}$$

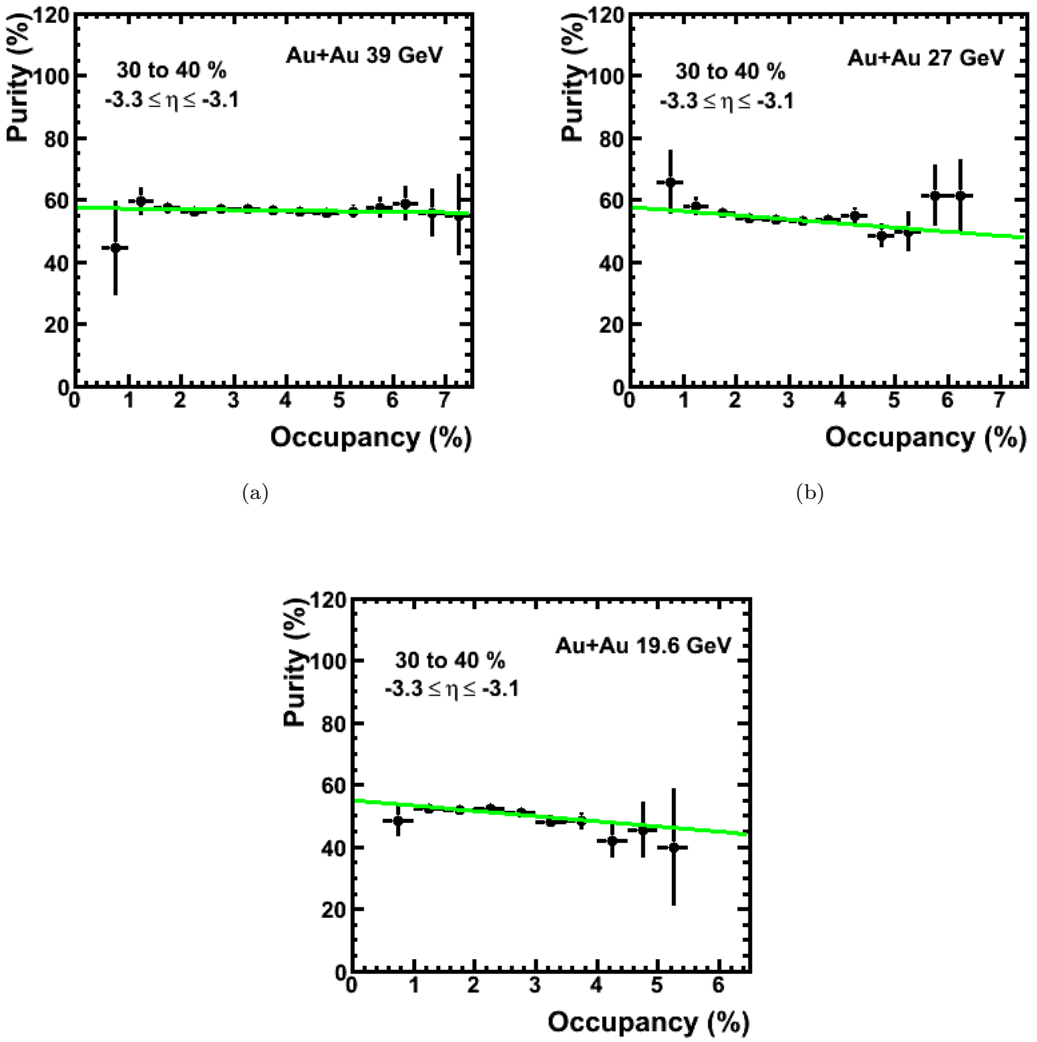

(a) (b)

(c)

FIGURE 3.27: Purity of photon sample as a function of occupancy for Au+Au collisions at $\sqrt{s_{NN}}$ = 39, 27 and 19.6 GeV. The figures shown are for event centrality 30-40% and rapidity interval -3.3 to -3.1. Similar graphs were obtained for each rapidity interval for each event centrality

3.7.6 Purity Variation with Occupancy

Purity of the photon sample has been obtained for different values of occupancy for each eta bin and for each centrality bin. Figure 3.27 shows the percentage purity as a function of occupancy for 30-40 % centrality and eta bin -3.3 to -3.1 for Au + Au 39, 27 and 19.6 A GeV. Similar plots were obtained for each value of centrality and for each eta bin. A polynomial of order 1 for each centrality bin and for each eta window was fitted. These fit functions are used to obtain the purity in data according to the observed occupancy. It is clear that purity depends weakly on occupancy. A study of events of different centralities in different rapidity windows shows that purity has a weak dependence on event centrality and rapidity also.

3.8 Systematic Errors

The systematic errors on photon multiplicity and rapidity distributions ($dN_\gamma/d\eta$) have been determined for [42, 43]:

- Uncertainty in estimates of efficiency and purity values
- Variation in the choice of photon-hadron discrimination threshold condition
- Non-uniformity of the detector response

3.8.1 Uncertainty in Efficiency and Purity

The errors on the parameters of the fit functions obtained for efficiency and purity reflect the uncertainty in the determination of their values. Figure 3.28 shows the functions for efficiency and purity using their best fit values (black line) and also the maximum (red line: upper edge of the hatched red band) and minimum (blue line: lower edge of the hatched red band) possible fit functions as given by the errors on fitted parameters. For a given centrality and rapidity window, these three functions give the uncertainty in the estimated values of efficiency and purity at a given occupancy. We used the function giving highest values of

purity along with the function giving lowest values of efficiency and reobtained the $dN_\gamma/d\eta$ distributions. This is repeated with lowest values of purity coupled with the highest values of efficiency. The difference in the $dN_\gamma/d\eta$ distributions as compared to the the best fit cases, gives the systematic error due to uncertainty in effciency and purity values. The difference in the estimates of $dN_\gamma/d\eta$ is included in the results as the systematic error due to uncertainty in efficiency and purity values. For each energy, the difference in estimates of $dN_\gamma/d\eta$ can be seen in Figure 3.29 for Au+Au 39 A GeV, Figure 3.30 for Au+Au 27 A GeV, Figure 3.31 for Au+Au 19.6 GeV. In each figure the different blocks corresponds to different event centrality. For 39 A GeV it can be observed from the Figure 3.29 that the systematic error due to uncertainty in efficiency and purity is about 15% for most central events.

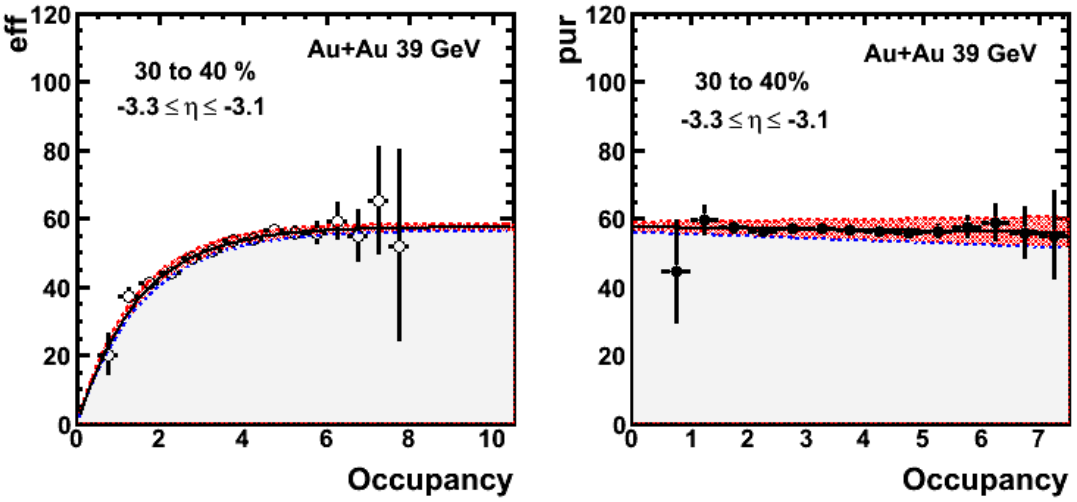

(a) (b)

FIGURE 3.28: Efficiency and purity for different occupancies. See text for details.

3.8.2 Variation in Discrimination Threshold

The threshold conditions used for photon-hadron discriminiation are as follows:

- Cluster Size $>$ 1 cell.

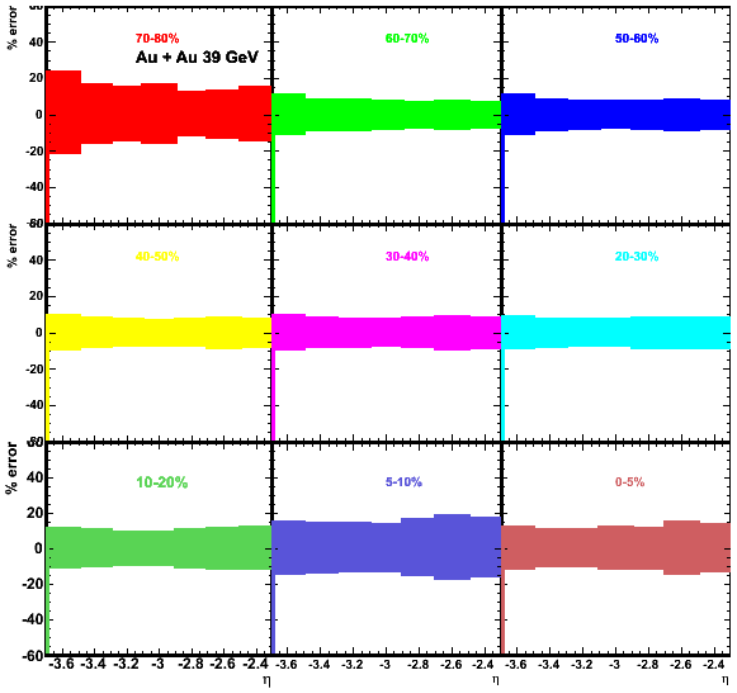

FIGURE 3.29: Systematic error due to uncertainty in estimates of efficiency and purity values at Au + Au 39 A GeV.

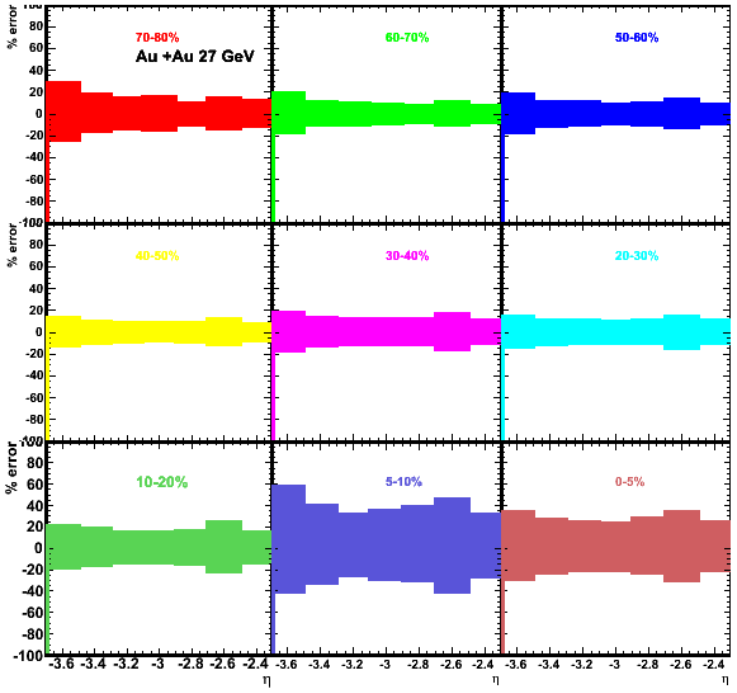

FIGURE 3.30: Systematic error due to uncertainty in estimates of efficiency and purity values at Au + Au 27 A GeV.

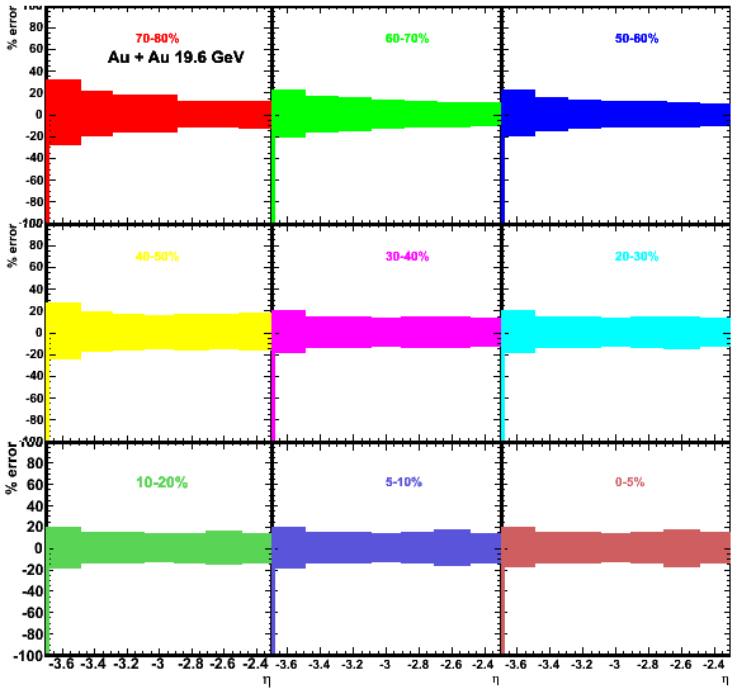

FIGURE 3.31: Systematic error due to uncertainty in estimates of efficiency and purity values at Au + Au 19.6 A GeV.

- ClusterADC $> 3 \times MIP - ADC$ cell for Au + Au collisions at 39 A GeV and 27 A GeV. ClusterADC $> 2.5 \times MIP - ADC$ for 19.6 A GeV collisions.

The same conditions are applied in simulated data to obtain efficiency and purity. The threshold conditions were varied both in simulated data and in actual data to study the variation in the N_γ distributions. Different threshold cuts were used for ClusterADC. In particular, the cuts were set at 2 times MIP-ADC and 4 times MIP-ADC for the case when the cut used was 3 times MIP-ADC, and were set at 1.5 times MIP-ADC and 3.5 times MIP-ADC for the case when the cut used was 2.5 times MIP-ADC. The efficiency and purity were recalculated for these cuts. The N_γ distributions were re-obtained after applying the corresponding efficiency and purity corrections. The difference in rapidity density due to using different thresholds is included in our result as systematic error due to threshold cut variation. This is shown in Figures 3.32, 3.33 and 3.34 for 39, 27 and 19.6 A GeV respectively. It can be seen that while the error is small for central events, the peripheral events show a much larger variation, up to 15%, for low occupancy

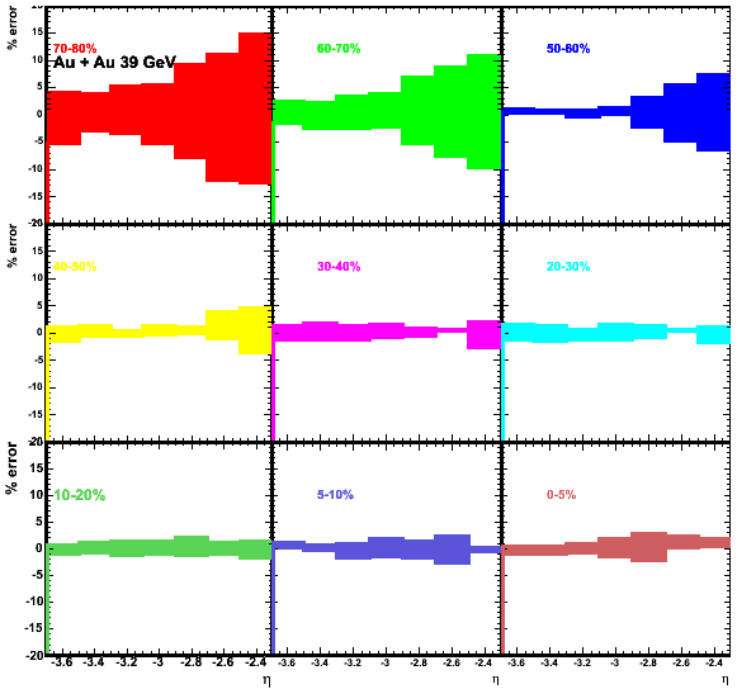

FIGURE 3.32: Systematic error in N_γ multiplicity due to variation in discrimination threshold condition for Au + Au collisions at 39 A GeV.

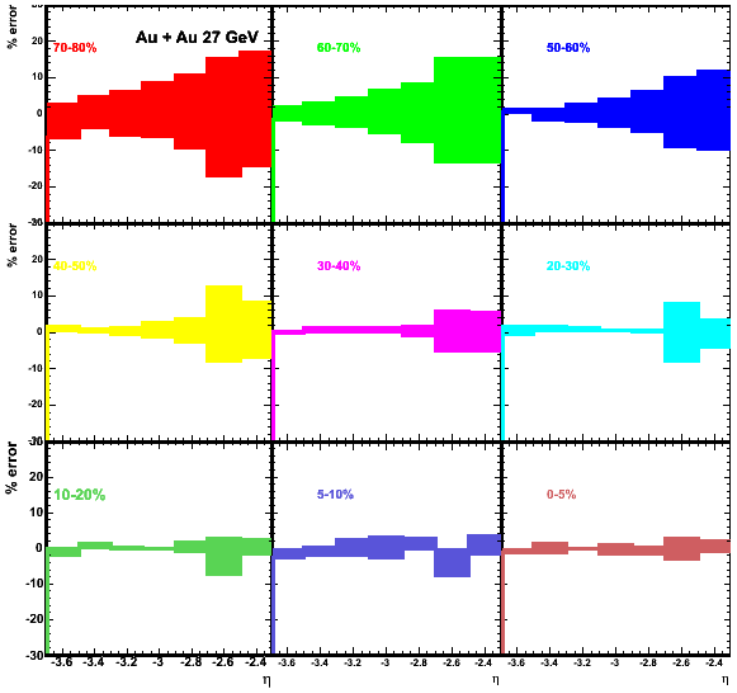

FIGURE 3.33: Systematic error in N_γ multiplicity due to variation in discrimination threshold condition for Au + Au collisions at 27 A GeV.

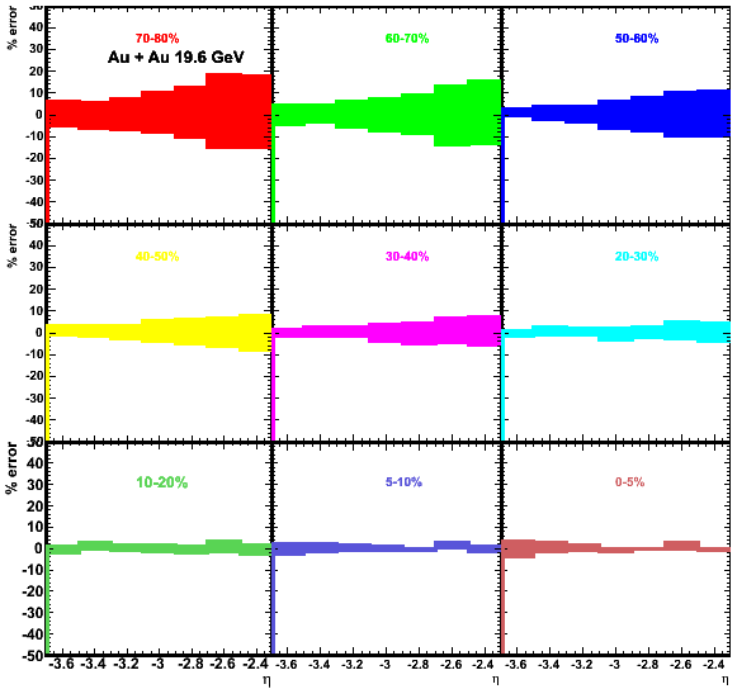

FIGURE 3.34: Systematic error in N_γ multiplicity due to variation in discrimination threshold condition for Au + Au collisions at 19.6 A GeV.

rapidity bins. This is probably due to larger variations in efficiency with occupancy for low occupancy regions.

3.8.3 Azimuthal Non-Uniformity

In each eta bin, after acceptance correction, the azimuthal distribution of the clusters passing the threshold, $N_{\gamma-like}$ is expected to be uniform. The phi distribution of $N_{\gamma-like}$ was studied in each eta bin and found to deviate from the expected uniformity. To understand this observation, the $N_{\gamma-like}$ for each SMChain were obtained in each eta bin and were normalized with the number of active cells for that SMChain and eta bin i.e.

$$\overline{N_{\gamma-like}^{SMChain,\eta}} = \frac{< N_{\gamma-like}\ for\ an\ SMChain\ and\ \eta\ bin >}{(Number\ of\ active\ cells\ for\ same\ SMChain\ in\ that\ \eta\ bin)} \tag{3.10}$$

SM No.	Chain No.	$< adc >$ of cells	Hit Loss Correction Factor
14	26	119.4	1.0
14	28	125.9	1.0
15	29	119.9	1.0
15	33	124.5	1.2
16	30	90.5	1.1
16	31	96.0	1.1
16	33	118.8	1.0
17	34	53.8	3.5
18	35	119.2	1.0
18	36	116.7	1.0
19	36	121.6	1.0
19	37	124.8	1.0
20	38	57.9	1.45
20	40	75.7	1.2
21	39	127.2	1.0
21	41	130.4	1.0
22	42	60.1	3.2
22	44	56.8	3.2
22	45	55.2	1.0
23	41	80.1	1.3
23	43	57.4	1.45
23	45	75.5	1.3
24	46	119.7	1.0
24	47	125.3	1.0
24	48	123.5	1.0

TABLE 3.1: Mean ADC and hit loss correction factor (HLCF) for SMChains.

For most SMChains, $\overline{N_{\gamma-like}^{SMChain,\eta}}$ was nearly the same within the same eta window, but for some SMChains it was much smaller than others. The result is understandable as due to low gain of such chains which results in a large no. of hits (and hence clusters) being lost when we applied the noise threshold cut of 15% of Mean ADC of MIP. This hit/cluster loss cannot be compensated by gain normalisation. To obtain a uniform azimuthal distribution of these clusters, a Hit-Loss-Correction-Factor(HLCF) is obtained for each SMChain and applied to obtain a relatively uniform azimuthal distribution in all eta bins.

Table 3.2 shows mean ADC for each SMChain. This mean is over all cells of the particular SMChain before normalization. The hit loss correction factor for all SMChains is also given. The table shows that the HLCF factor is large for low

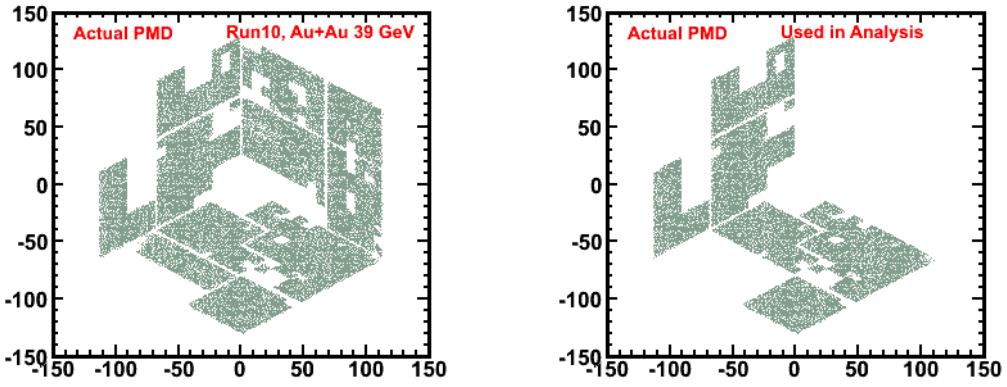

(a) (b)

FIGURE 3.35: XY distribution of hits on PMD in Run 10 (a) All good SMChains (b) All SMChains used for analysis

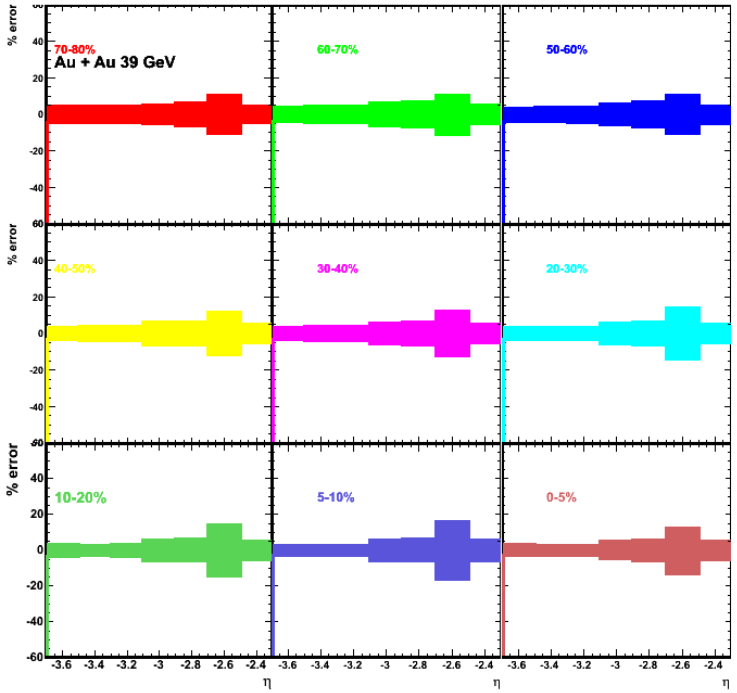

FIGURE 3.36: Systematic error variation in N_γ multiplicity due to non-uniformity in PMD response at Au + Au collisions at 39 A GeV.

gain chains (grey rows).

All the SMChains with low gain and hence high HLCF were located in one sector of PMD which constituted 1/3 of PMD. The high HLCF factors were causing large systematic errors and hence it was decided to drop that whole sector of

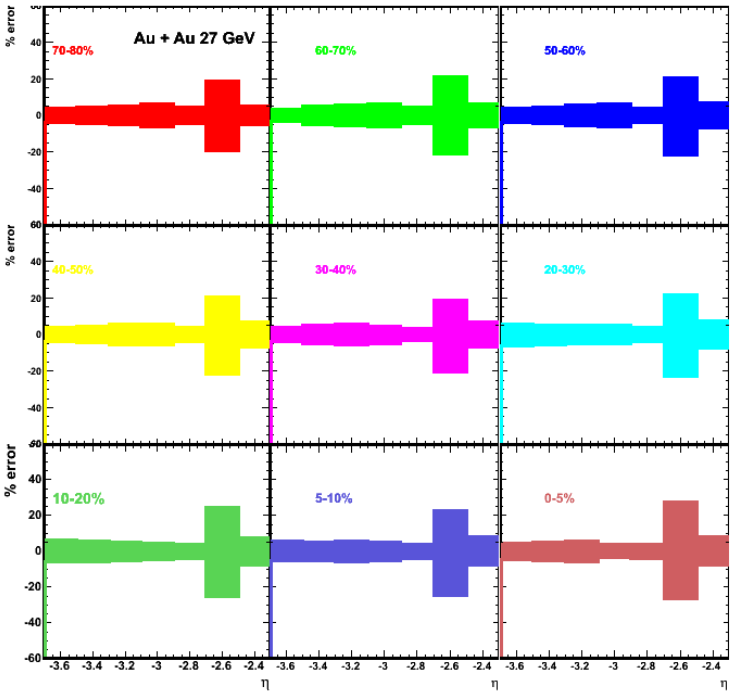

FIGURE 3.37: Systematic error variation in N_γ multiplicity due to non-uniformity in PMD response at Au + Au collisions at 27 A GeV.

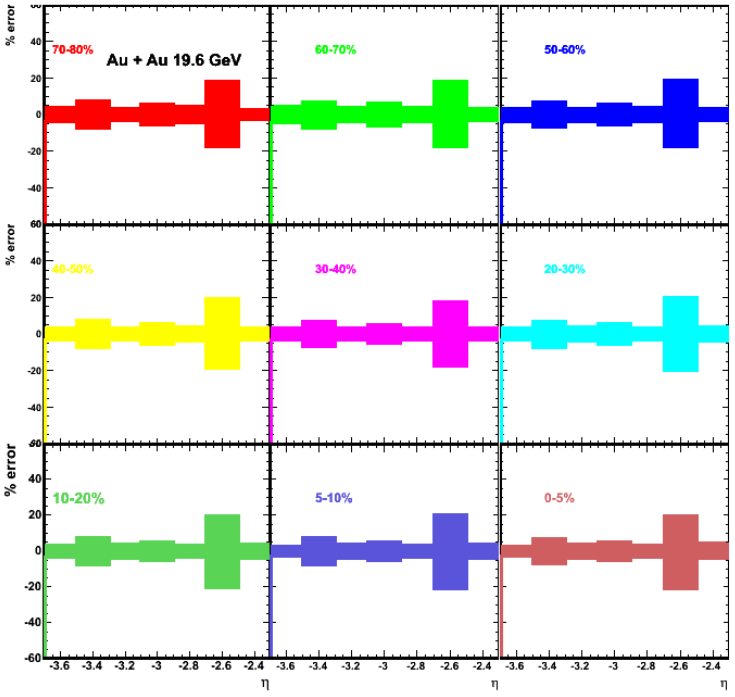

FIGURE 3.38: Systematic error variation in N_γ multiplicity due to non-uniformity in PMD response at Au + Au collisions at 19.6 A GeV.

PMD from analysis at 39 A GeV. While this loss of data contributes to increased statistical error, the overall uncertainties on multiplicity due to systematic effects were smaller. The XY distribution of PMD in Au + Au collisions at 39 A GeV is shown in Figure 3.35(a). Figure 3.35(b) shows the XY distribution of PMD after removing the sector as described above, and corresponds to the data used in the analysis. At 27 A GeV and 19.6 A GeV the acceptance in the eta ring -2.7 to -2.5 was low, some chains from that sector were used in analysis (chain 39 and 41 from SM 21).

The azimuthal distributions of photons from the remaining SMChains were studied, after application of HLCF, for each centrality and eta bin. The mean of the $N_{\gamma-like}$ and RMS of the $N_{\gamma-like}$ over different azimuthal bins was calculated for each eta and centrality bin. The RMS value indicate the uncertainty in the estimate of the mean $N_{\gamma-like}$.

In order to obtain the corresponding uncertainty in N_γ we proceeded as follows.

$$N_\gamma(UpperLimit) = (\langle N_{\gamma-like}\rangle + RMS_{\gamma-like}) * \frac{Efficiency}{Purity} \tag{3.11}$$

$$N_\gamma(LowerLimit) = (\langle N_{\gamma-like}\rangle - RMS_{\gamma-like}) * \frac{Efficiency}{Purity} \tag{3.12}$$

Values of efficiency and purity used in the above equations corresponded to occupancy values increased/decreased by a fraction equal to $RMS_{\gamma-like}/< N_{\gamma-like} >$. This yields two values of N_γ for each eta bin for each centrality. This spread is the systematic error due to azimuthal non-uniformity within an eta bin, and is shown in figure 3.36 for Au+Au 39 A GeV, Figure 3.37 for Au+Au 27 A GeV, Figure 3.38 for Au+Au 19.6 GeV. The large errors for the eta bin = -2.7 to -2.5 bin is because of the small acceptance in this bin.

The three systematic errors were added in quadrature to obtain the total systematic error on the photon multiplicities in different rapidity windows.

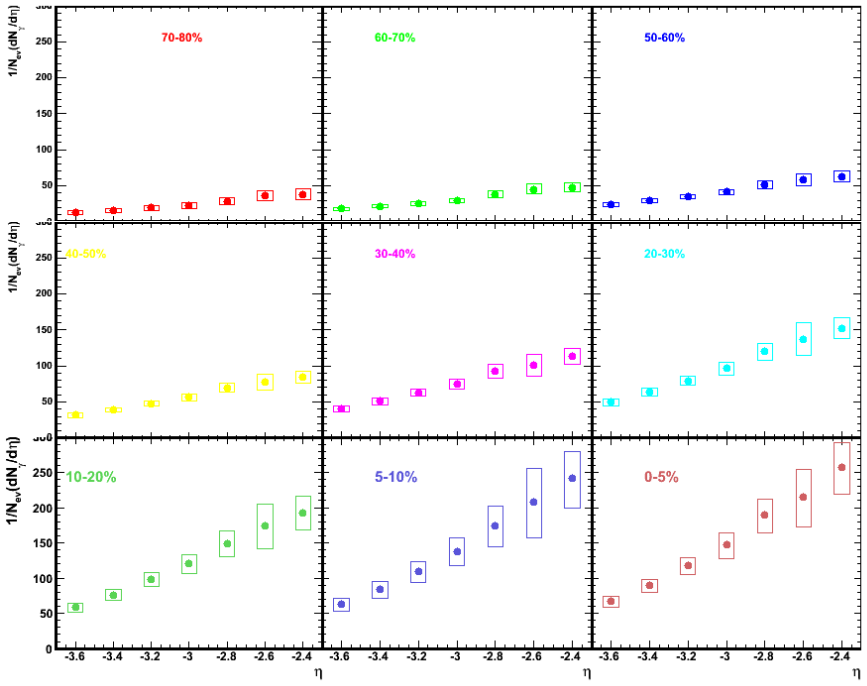

FIGURE 3.39: Inclusive photon pseudorapidity distributions for Au + Au collisions at 39 A GeV for different centralities.

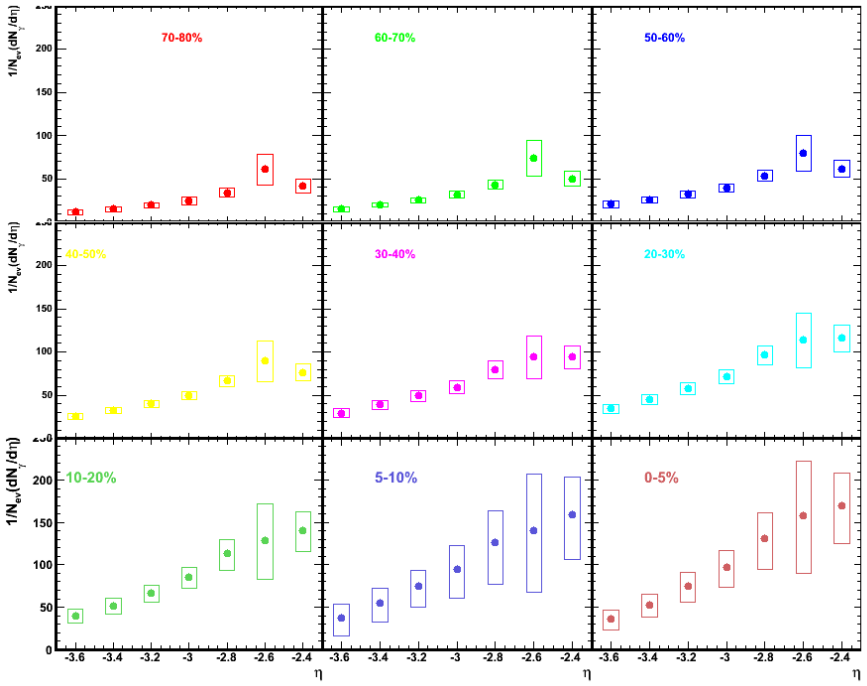

FIGURE 3.40: Inclusive photon pseudorapidity distributions for Au + Au collisions at 27 A GeV for different centralities.

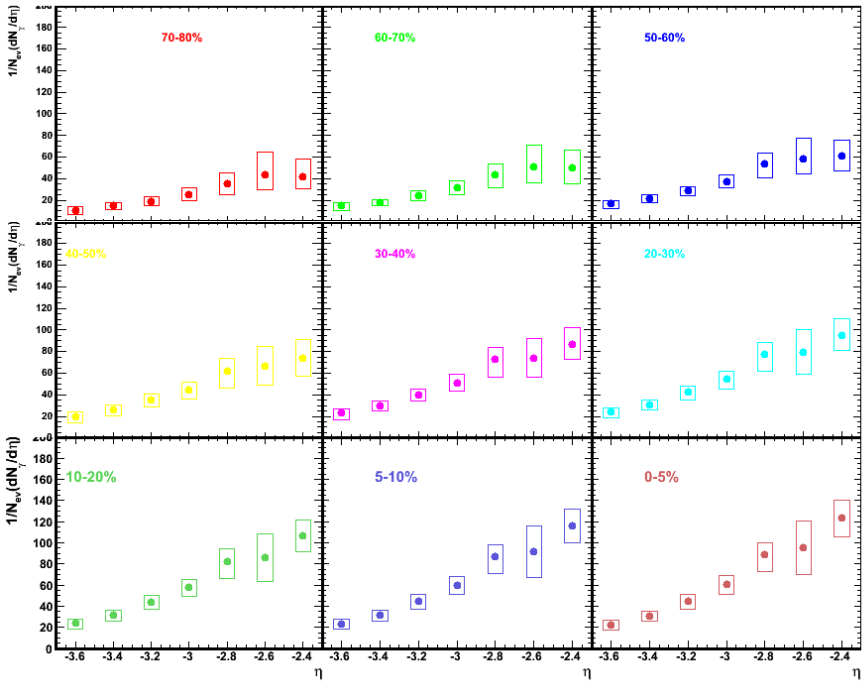

FIGURE 3.41: Inclusive photon pseudorapidity distributions for Au + Au collisions at 27 A GeV for different centralities.

The final results of photon mulitplicity and rapidity distributions for nine different centralities for the three energies are shown in Figure 3.39, 3.40 and 3.41, alongwith the systematic errors estimates, as detailed above. Their comparisons with data from event generators, and possible scaling with number of participants and other behaviour is discussed in the next chapter.

3.9 Summary

Starting from the raw data recorded by the PMD in the STAR experiment, the process of cleanup, normalisation and calibration of the detectors cells was described in this chapter. The process was independently repeated for data at all energies. Some bad Runs were identified and removed, without introducing a bias in the data. Quality of the data was assessed by studying the correlation plots between the multiplicity measured in the PMD and other STAR detectors, both in the barrel region and in the forward region. The distributions for number of clusters above the threshold, $N_{\gamma-like}$ were obtained for each centrality, at each

energy. The correction factors for acceptance, efficiency and purity were also estimated. The latter two were obtained for different centralities and different eta windows and different occupancies. Uncertainties in these correction factors were also estimated, and will contribute to the final systematic error on the multiplicity and rapidity distributions. The detailed systematic study has allowed us complete checks on systematic errors. The results on rapidity distributions and possible scaling and limiting fragmentation will be explored in the next chapter.

Chapter 4

Photon Multiplicity and Limiting Fragmentation

The measurements of particle multiplicity in high-energy heavy-ion collisions provide information on particle production mechanisms [9, 10, 82, 83]. The width of the pseudorapidity distributions is found to be sensitive to longtitudinal flow, the velocity of sound in medium and rescattering of particles [84]. Identified particle multiplicity as a function of collision centrality can shed light on relative contribution of soft and hard processes in particle production [41]. In the following sections, the results from the inclusive photon multiplicity measurments at forward rapidity in Au + Au collisions at $\sqrt{s_{NN}}$ = 39, 27 and 19.6 GeV will be discussed. Measuring N_γ at different energies enable to study the systematic dependence on energy. To explore the nature of photon production processes N_γ scaled by number of participant pairs has been studied at all these energies for different event centralities, and compared with data at high energies. Limiting fragmentation has been observed for both photons and charged particles at higher energy at RHIC, and this property of particle production at BES energies is explored.

4.1 Multiplicity Distributions

The photon multiplicity distributions have been measured for different centralities in Au+Au collisions at $\sqrt{s_{NN}}$ = 39, 27 and 19.6 GeV. Figure 4.1 shows photon

multiplicity distributions for minimum bias (0-80%) Au+Au collsions at the three energies. These measurements enable investigation of participant scaling and limiting fragmentation behaviour.

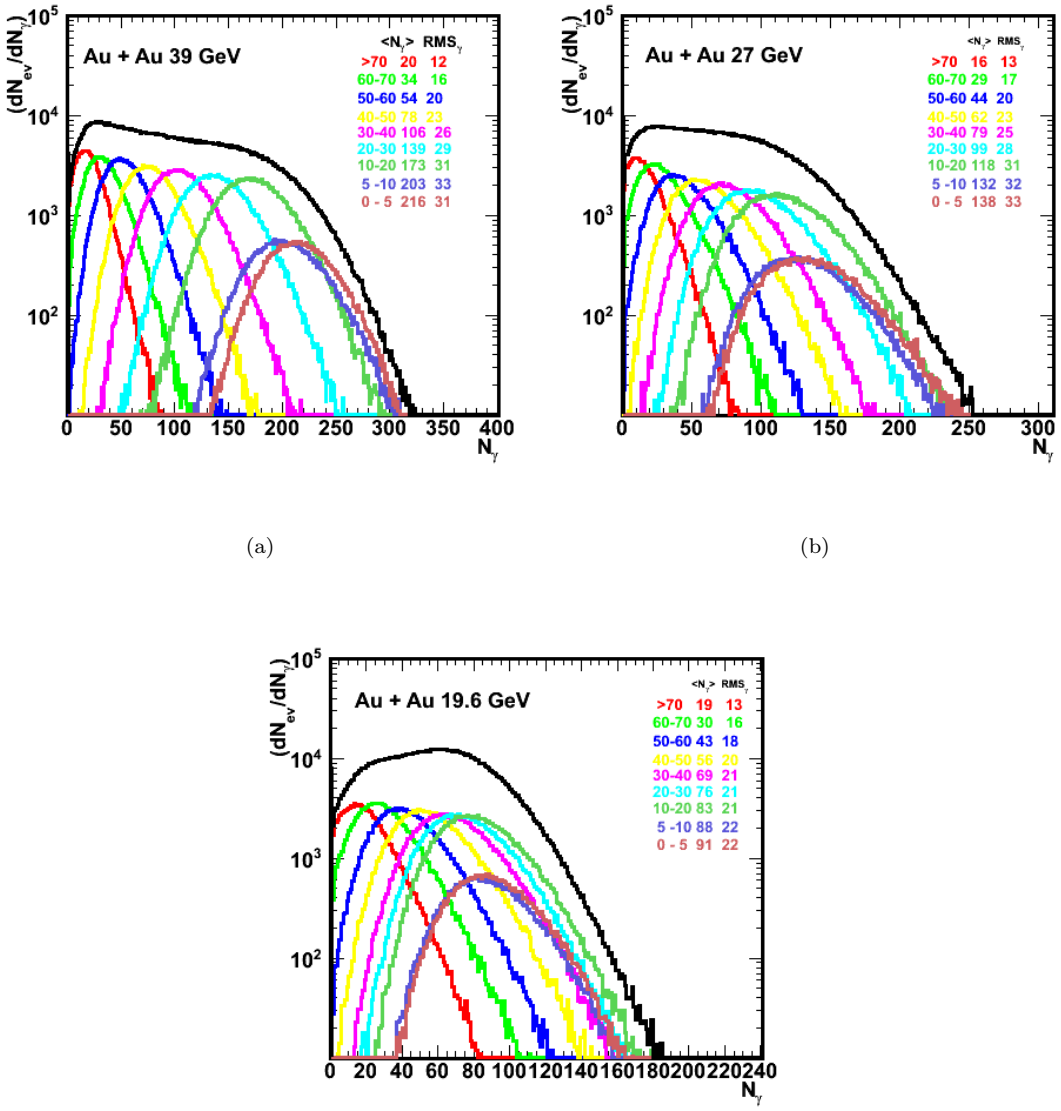

FIGURE 4.1: Photon multiplicity distributions for minimum bias Au + Au collisions at 39, 27 and 19.6 A GeV for different centrality bins.

For each centrality at each energy, the multiplicity distributions are shown in Figure 4.1. It is observed that the multiplicity distribution of photons for each centrality exhibits Gaussian-like distributions. This is true at all energies. However, for the most central collisions, the distribution extends to large values of the multiplicity, making it a little asymmetric, particularly at the lowest energy.

This can also be deduced from the correlation plots between refmult and PMD multiplcity, as seen in the chapter 3.

The distribution of N_{part} and N_{coll} can be obtained from Glauber model, or event generators, for minimum bias collisions. The gross shape of the minimum bias multiplicity distributions is similar to the shape of these distributions. The participant nucleon distribution has a steep rise for peripheral collisions followed by a near plateau region which corresponds to mid central events and a fall-off region which corresponds to the most central events. The mimimum bias photon multiplicity distribution at each energy shows the well defined plateau and the fall-off region. The steep rise correponding to the very peripheral events is not observed since only events with 0-80% centrality are included.

4.2 Inclusive Photon Pseudorapidity Distributions

The pseudorapidity distributions of photons measured in the PMD for various collision centralities in Au+Au collisions at $\sqrt{s_{NN}}$ = = 39, 27 and 19.6 A GeV are shown in Figure 4.2, Figure 4.3 and Figure 4.4 respectively. The errors shown on the data points are systematic errors. The estimates of systematic errors are as detailed in chapter 3. Statistical errors are within the size of the symbol at all energies.

It can be observed from the photon pseudorapidity distributions that for a given event centrality, the photon yield is higher towards more central rapidity. The inclusive photon multiplicity is found to increase from peripheral to central collisions. These results can be directly compared with different models in order to understand the mechanism of particle production in relativistic heavy-ion collisions at forward rapidity. Inclusive photon pseudorapidity distributions have been obtained using HIJING and AMPT event generator for each centrality bin and these are also shown in the figures as a solid line for HIJING and a dashed line for AMPT. HIJING is based on perturbative QCD processes which lead to multiple jet production and jet interactions in matter. The data is also compared with results from A Multi-Phase Transport model (AMPT). The AMPT event generator [80] includes both initial partonic and final hadronic interations. For most

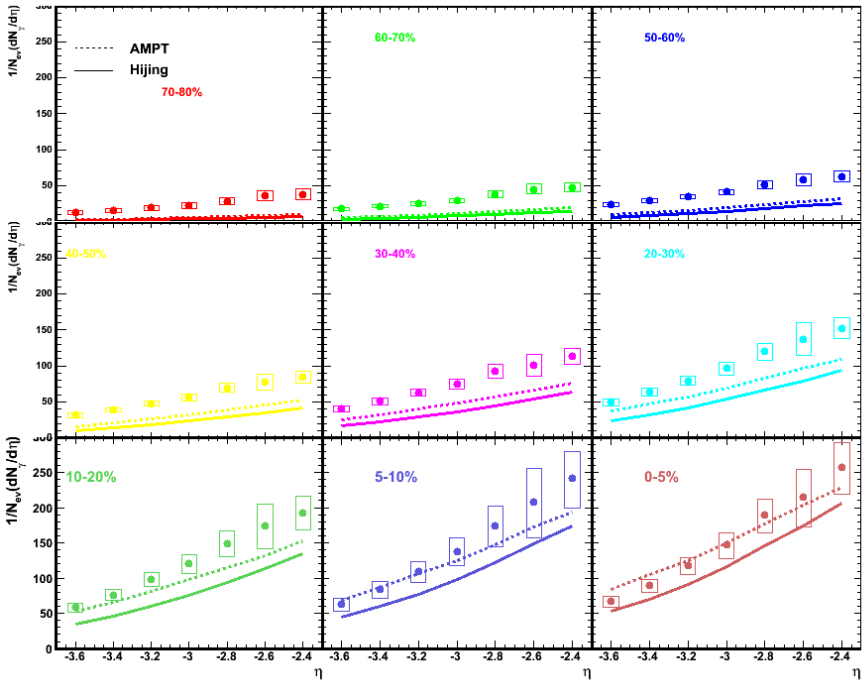

FIGURE 4.2: Inclusive photon pseudorapidity distributions for Au + Au collisions at 39 A GeV for different centralities.

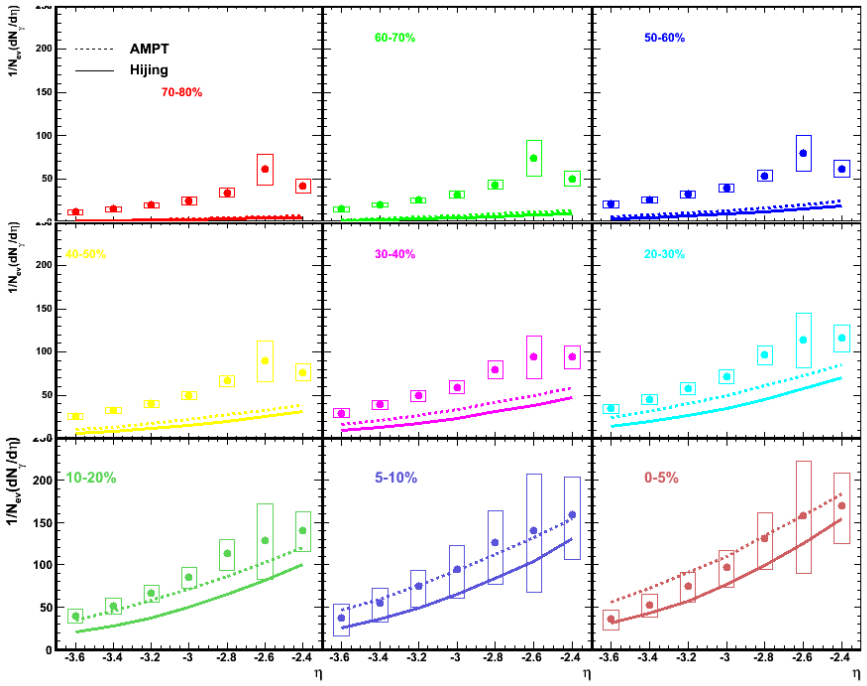

FIGURE 4.3: Inclusive photon pseudorapidity distributions for Au + Au collisions at 27 A GeV for different centralities.

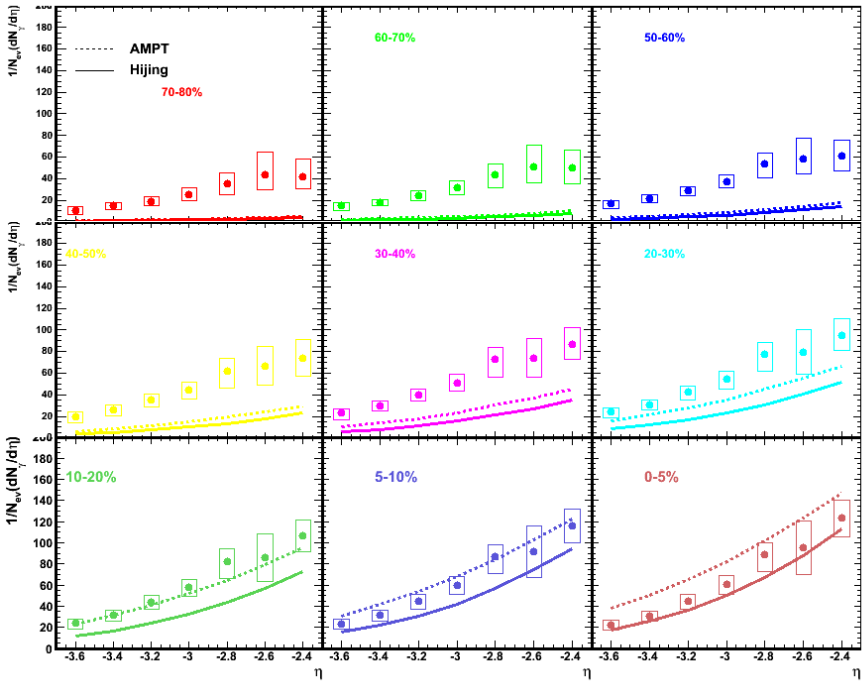

FIGURE 4.4: Inclusive photon pseudorapidity distributions for Au + Au collisions at 19.6 A GeV for different centralities.

central Au+Au collisions at 19.6 A GeV, the data agrees with HIJING predictions, where as it is systematically lower than AMPT predictions. At 39 A GeV, the data shows a greater yield than HIJING, and agrees with predictions from AMPT. At 27 A GeV both AMPT and HIJING describe the data within systematic errors. For mid-central and peripheral collisions, one observes that the data lies significantly above the predictions from both HIJING and AMPT. It is worth noting that for Au+Au collisions at 200 A GeV and 62.4 A GeV, HIJING reproduced the pseudorapidity distributions for both central and peripheral collisions within the systematic errors [42, 43]. At forward rapidities in peripheral collisions, PMD observes an excess of photons as compared to model predictions. Some possiblities are qualitatively discussed in section 4.5. It is worth noting that the PHOBOS experiment also observed excess of charge particles at forward rapidity which became more prominent for peripheral collisions at lower collision energy (Au + Au at 19.6 A GeV) [47].

4.3 Scaling of Photon Multiplicities

The total photon multiplicity per participant pair is obtained for different centralities to look for scaling with $< N_{part} >$. Centralities are measured using the multiplicity in the TPC, and using a Glauber model prescription as detailed in Chapter 2, $< N_{part} >$ is obtained at each centrality for each energy. Different centralities are shown on the x-axis as different values of $< N_{part} >$. If the particle multiplicity scales with $< N_{part} >$, it shows that the particle production is due to soft processes; scaling with $< N_{coll} >$ indicates that the particle production is due to hard processes [41].

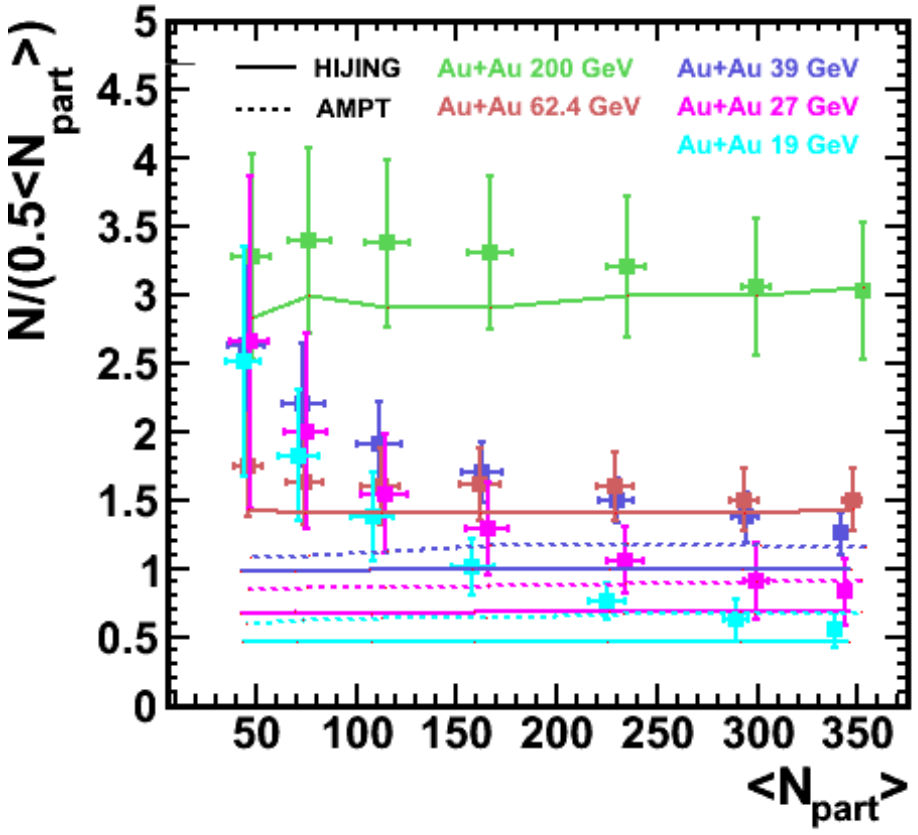

FIGURE 4.5: The number of photons per participating nucleon pair as a function of average number of participating nucleons for Au+Au collisions at $\sqrt{s_{NN}}$ = 200, 62.4, 39, 27 and 19.6 A GeV within $3.7 \leq \eta \leq 2.3$. The Errors shown are systematic errors. The statistical errors for each point are within the symbol size.

It was observed in the PHENIX experiment, that at mid-rapidity, the charged particle production scales with a combination of $< N_{part} >$ and $< N_{coll} >$, which indicates a significant contribution of hard processes in particle production [41]. PHOBOS experiment studied the scaling over a large pseudorapidity window and showed that such a scaling has a pseudorapidity dependence [32, 47]. STAR experiment also showed that, for Au+Au and Cu+Cu collisions at 200 and 62.4 A GeV, photon production scales with $< N_{part} >$, in the rapidity region -3.7 to -2.3, which indicates that the photon production is dominantly due to soft processes at forward rapidity [42, 43]. The charge particle multiplicity measured by STAR in Forward Time Projection Chamber does not scale with the number of participants.

Considering that the identified particles (photons) showed $< N_{part} >$ scaling and charged particles did not, the difference was understood due to the presence of protons in the sample of charged particles. These protons may have a source, or a mechanism of production, that is different from the majority charged particles.

Figure 4.5 shows the variation of photon multiplicity per average number of participating nucleon pair with N_{part} for Au + Au collisions 200, 62.4, 39, 27 and 19.6 A GeV. Data of Au+Au collisions at 200 and 62.4 A GeV is taken from reference [42, 43] and shows that the photon multiplicity scaled with number of participant pairs is independent of event centrality. At lower energies the data shows a deviation from such a scaling, the deviation systematically increasing from central to peripheral collisions. For central collisions the scaled multiplicity matches quite well with the predictions from AMPT and HIJING. Event generators (HIJING and AMPT) predict N_{part} scaling of photon multiplicity at lower energies also and hence expect a constant value for N_γ normalized by number of participant pair (also shown in Figure 4.5). The deviation from this scaling seems to increase with decreasing $\sqrt{(}s)$. Possible reasons for this deviation are discussed in section 4.5.

4.4 Longitudinal Scaling

For Au+Au and Cu+Cu collisions at 200 A GeV and 62.4 A GeV, it was observed that the longitudinal scaling is independent of beam energy for both charged particles [32, 45, 47] and photons. [42, 43]. It was also observed that the longitudinal

scaling was centrality dependent for charged particles but was centrality independent for photons. This was explored in detail for identified charged particles and it was found that the mesons exhibit longitudinal scaling but the baryons do not. The presence of baryons in the inclusive charge particle data caused the observed centrality dependence.

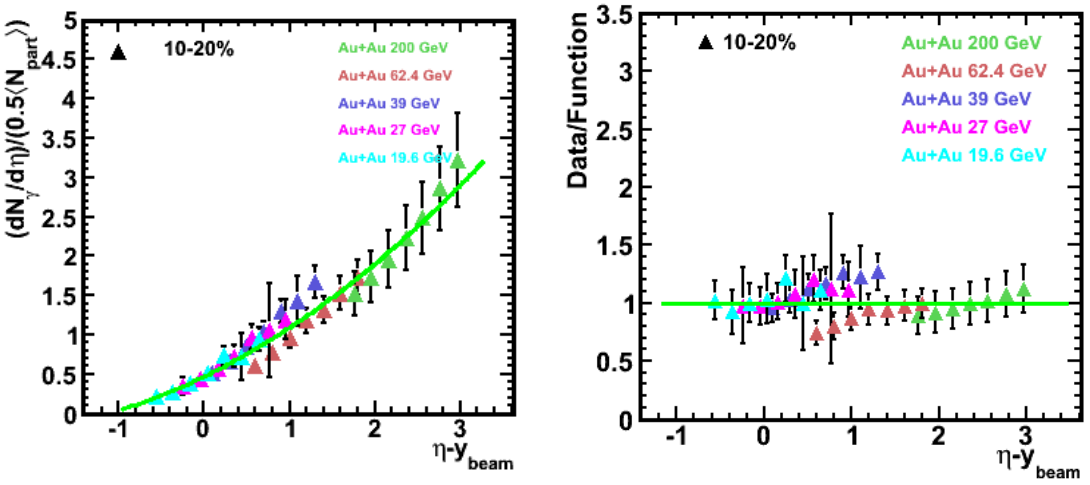

(a) (b)

FIGURE 4.6: (a) Photon pseudorapidity distributions per participant pair for 10-20% collision centrality as a function of pseudorapidity shifted by the beam rapidity for Au+Au collisions at $\sqrt{s_{NN}}$ = 200, 62.4, 39, 27, and 19.6 GeV. Errors are systematic only, statistical errors are negligible in comparison. The solid line is a second order polynomial fit to the data points. (b) Ratio of the data points to fit function with N_{part} scaling

Figure 4.6 (a) shows the photon pseudorapidity density normalized by the average number of participating nucleon pairs as a function of $\eta - y_{beam}$ for 10-20% centrality bin for Au + Au collisions at 200, 62.4, 39, 27 and 19.6 A GeV, where y_{beam} is the beam rapidity. This scaled pseudorapidity distributions for all energies show similar values. This indicates that at these energies photon data shows energy independent limiting fragmentation behavior for central collisions. The solid line is a second order polynomial of the form $0.507 + 0.534(\eta - y_{beam}) + 0.088(\eta - y_{beam})^2$ fitted to all data points. The ratio of data to fit function is close to 1 for all values of $(\eta - y_{beam})$ as can be seen in Figure 4.6 (b).

The photon pseudorapidity density normalized by the average number of participating nucleon pairs as a function of $\eta - y_{beam}$ for 10-20% and for 20-30% centrality

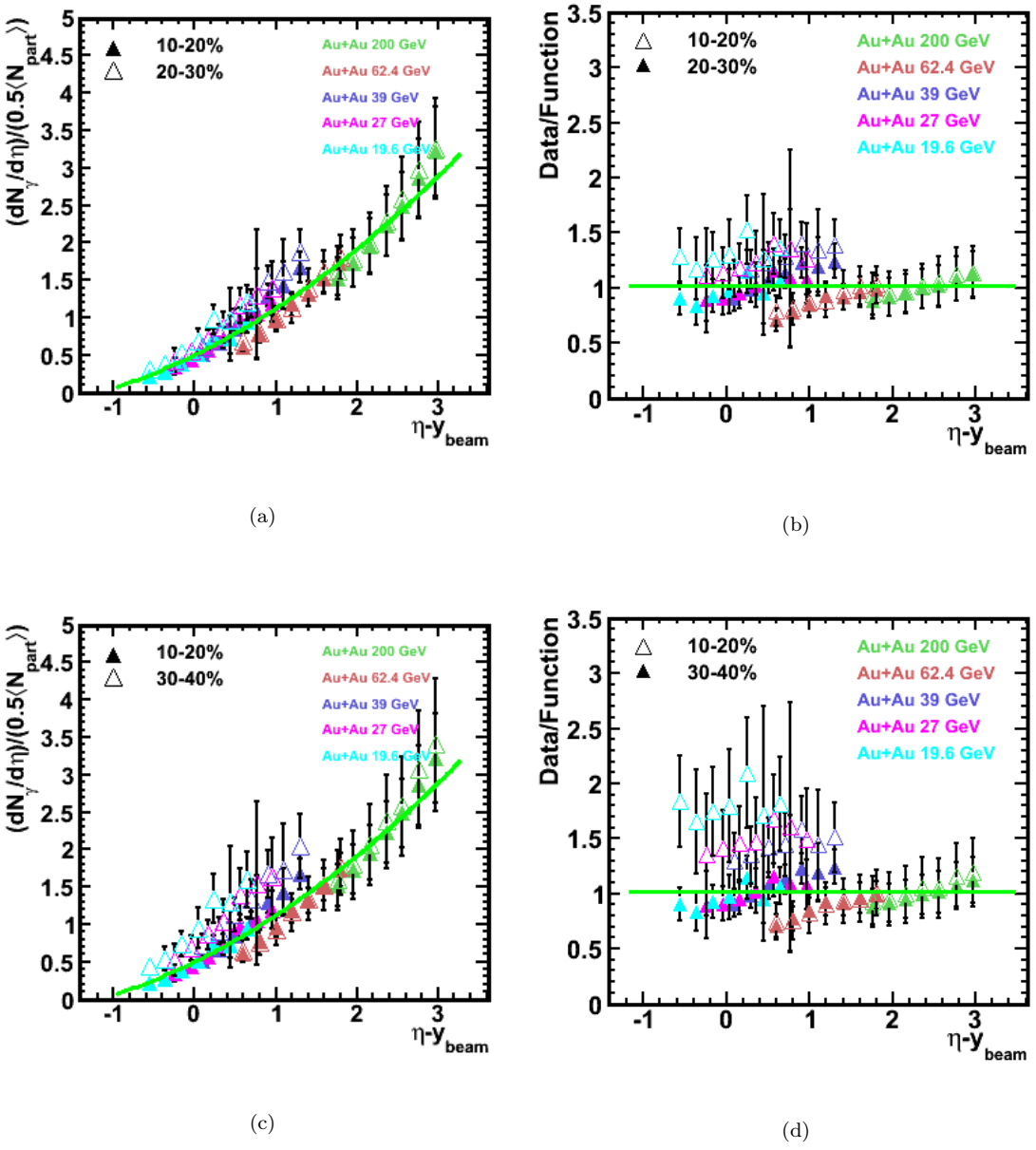

FIGURE 4.7: Photon pseudorapidity distributions per participant pair as a function of pseudorapidity shifted by the beam rapidity for Au+Au collisions at $\sqrt{s_{NN}}$ = 200, 62.4, 39, 27, and 19.6 GeV for (a) 10-20% and 20-30% centralities. (b) Ratio of the data points in (a) to fit function with N_{part} scaling. (c) 10-20% and 30-40% centralities. (d) Ratio of the data points in (c) to fit function with N_{part} scaling.

bin for Au + Au collisions at 200, 62.4, 39, 27 and 19.6 A GeV is shown in Figure 4.7 (a). The same for 30-40% centrality is shown in Figure 4.7 (c). The data points of 20-30% and 30-40% centrality show a larger spread about the fit function which can be clearly seen in the plot of ratio of data to fit function 4.7 (b) and

(d). It can be seen that the centrality independence that was observed at Au+Au 200 and 62.4 A GeV is not valid at lower energies.

At 200 and 62.4 GeV, the rapidity density for different event centralities (20-30% and 30-40%) scaled with N_{part}, showed remarkable similarity leading to the conclusion that longitudinal scaling is independent of event centrality for photons. While for different event centralities, the data at 39 A GeV shows little difference, the data at 19.6 GeV shows much greater difference. This indicates that the pseudorapity density distribution of photons at 39, 27 and 19.6 A GeV do not show centrality independent limiting fragmentation behavior; the difference between data at various centralities increases with decreasing energies.

4.5 Possible Explanations for Scaling Deviations

The data for Au+Au collisions at 39, 27 and 19.6 A GeV show that there is excess of photons in peripheral collisions as compared to central collisions. This is most evident when N_{part} normalized multiplicity of photons for central and semi-central collisions are compared. The observation is true at all three energies, as seen in Figure 4.8.

Figure 4.8 shows the ratio of the N_{part} normalized rapidity distribution of photons in semi-central (30-40%) collisions with that in central collisions (0-5%) as a function of rapidity in the beam frame of reference i.e. $\eta - y_{beam}$, for Au+Au collision at 200, 62.4, 39, 27 and 19.6 A GeV. The ratio increases from its value $\sim$1.0 in 200 A GeV collisions to $\sim$3.0 at 19.6 A GeV collisions. This result is similar to PHOBOS result in [47] where a ratio of $dN_{ch}/d\eta$ for non-central collision (35-40%) with $dN_{ch}/d\eta$ for central collision (0-6%) has been plotted as a function of $\eta^{'} = \eta - y_{beam}$ for Au+Au collisions at 200,130 and 19.6 A GeV as can be seen in Figure 4.9. One possibility of these excess charged particles in PHOBOS as well as photons in PMD is the presence of spectator nucleons, as mentioned in Ref. [85].

None of event generators used in the present analysis include spectator fragmentation. Lacking such a model inhibits a comparison of data with event generator

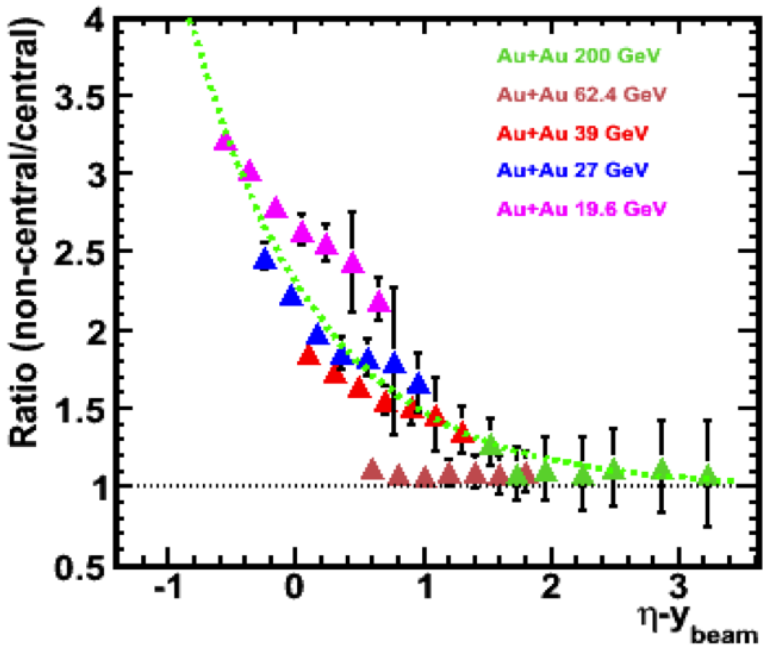

FIGURE 4.8: The ratio for $dN_\gamma/d\eta$ per participant nucleon pair of non-central (30-40%) to central (0-5%) data plotted for $\sqrt{s_{NN}}$ = 200, 62.4, 39, 27, and 19.6 GeV. Only systematic errors are shown. The dashed line is only to guide the eye.)

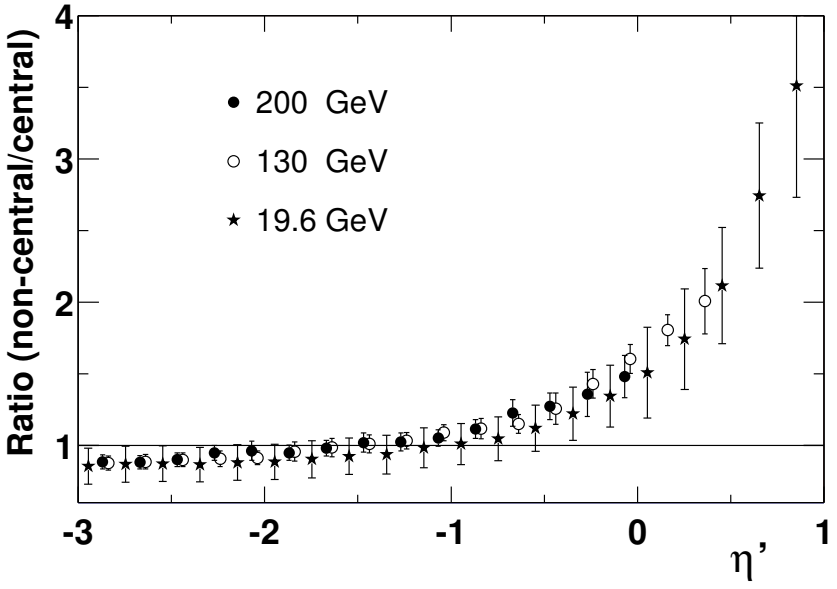

FIGURE 4.9: The ratio of $dN_{ch}/d\eta$ per participant nucleon pair between non-central (35-40%) and central (0-6%) data plotted for $\sqrt{s_{NN}}$ = 200, 130, and 19.6 GeV as measured by PHOBOS detector [47].)

or model. The data from event generators conform to N_{part} scaling in the region that is studied in the present work. That the discrepancy between the model and the data is increasing with the decreasing event centrality suggests a source which is getting stronger with decreasing centrality. A number of possiblities have been speculated upon in Ref [85] and are briefly discussed below.

(i) For central and semi-central collisions the spectators are completely disintegrated into protons and neutrons that continue with the original beam velocity [85]. For larger impact parameters, the spectator region disintegrates into smaller nuclei and nucleons. These nuclei are in an excited state due to breaking of short range correlations and possibly due to absorption of a few nucleons from the participant region. These excited spectator fragments can emit photons.

It was possible to check if the photons emitted by the spectator fragments may fall within PMD acceptance. A photon emitted at 90 degrees in the beam frame of reference is Lorentz boosted and would be observed at an angle $1/\gamma$ in the lab frame. Assuming an isotropic distribution, half of the photons emitted in the forward direction in the beam frame are expected within an angle $1/\gamma$ in the lab frame. This gives a good order of magnitude estimate of the spread of the photons and the beam fragments. The $1/\gamma$ factor for each energy can be seen in Table 4.1. The PMD coverage starts from 55 milli-radian hence might get a signal from the photons resulting from spectator fragments. Photons emitted in the spectator rest frame may have energies of the order of nuclear energy levels, and would be Lorentz boosted to higher energies in the laboratory frame. Such photons will be detected in the PMD, the detector being sensitive to very low energy photons.

Beam Energy (A GeV)	Beam rapidity	$1/\gamma$ (in mrad)
Au + Au 200	-5.36	9.38
Au + Au 62.4	-4.19	30.06
Au + Au 39	-3.73	48.10
Au + Au 27	-3.36	69.48
Au + Au 19.6	-3.04	95.71

TABLE 4.1: Beam rapidity and $1/\gamma$ for each energy.

(ii) In the three radiation length thickness of the converter, the charged particles also interact. While the probability of pion to interact is lower, that of protons and neutrons is considerably greater. Nucleons may produce pions in this interaction or, exchange charge for a proton to produce a shower and give a $N_{\gamma-like}$ signal on PMD. Detailed estimates of the yield due to this will require the energy dependence of interaction length, and is beyond the scope of the present work.

(iii) The conventional Monte Carlo models for heavy-ion collision are HIJING and AMPT. Private communication with the authors of both the event generators has confirmed that these models do not treat spectator fragments. In absence of any model calculations, a small parameterization was used to understand the excess. The parametrisation is based on simple assumptions given below.

  (a) The source of excess $N_{\gamma-like}$ are the spectator nucleons.

  (b) The yield from the spectator is distributed isotropically in the beam frame of reference and hence their distribution in lab frame can be well described by a Gaussian. The width of the Gaussian, σ, is a free parameter and will be determined by the data. This parameter is assumed to be same at all energies considered in this study.

  (c) The equation 4.3 is used to estimate the number of spectators that might be contributing to $N_{\gamma-like}$ in the acceptance range of PMD.

  (d) Number of photons per spectator might not be the same as the number of photons produced by a participant source. To accommodate this a factor C is included, and is a free parameter which will be determined from data.

PMD measures photons in a fixed rapidity window -3.7 to -2.3, therefore with decreasing beam energy, PMD acceptance range gets closer to beam rapidity as shown in Table 4.1 and can also be seen in Figure 4.10. Considering the overlap between acceptance of PMD in η and the beam rapidity, it is possible that PMD gets contributions from sources which exist due to spectators of the colliding nuclei.

The above assumption suggest that the number of photon sources can be written as nsource($N^{'}$):

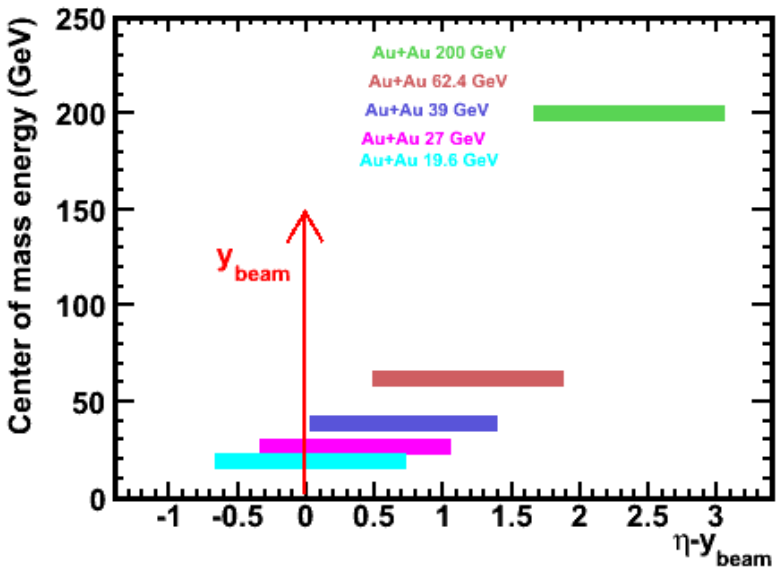

FIGURE 4.10: PMD acceptance range with respect to the $\eta - y_{beam}$

$$N' = 0.5 * N_{part} + X * N_{spect} \tag{4.1}$$

Where $N_{spect} = 197 - 0.5 * N_{part}$ is the number of spectator nucleons which are moving in the negative z-direction of STAR experiment. The PMD is also on the negative z-direction. The other half of spectator nucleons move in the opposite direction. X is expected to depend on the rapidity coverage of PMD with respect to the beam rapidity, as well as relative contribution of photons from a spectator as compared to photons from a participant, and is parametrised by:

$$X = C\frac{2}{\sqrt{\pi}}[\int_{x_1}^{x_2} e^{-t^2} dt] \tag{4.2}$$

where $x_1 = \eta_{min} - y_{beam}$ and $x_2 = \eta_{max} - y_{beam}$ and

Beam Energy (A GeV)	X value
Au + Au 200	0.00
Au + Au 62.4	0.03
Au + Au 39	0.18
Au + Au 27	0.323
Au + Au 19.6	0.37

TABLE 4.2: Values of X for each energy as detailed in text.

$$t = \frac{\eta - y_{beam}}{\sigma\sqrt{2}} \tag{4.3}$$

Since the PMD rapidity coverage with respect to the beam rapidity changes with beam energies, the limits in the integral in equation 4.3 also change, giving different values of X at different energies.

The above relation for X is only indicative of the yield on the PMD due to spectators. The total photon multiplicity as well as photon rapidity distribution has been scaled by the number of "effective number of photon sources" as given by N'. A future course of work might be to construct a more evolved model which can comment on both the total multiplicity as well as rapidity distribution of photons due to spectator fragments. The present work essentially highlights the necessity of developing models for spectator fragments which will be very useful in the upcoming of fixed target physics experiments at lower beam energy at FAIR accelerator.

Values of X at 62.4 A GeV and at 39 A GeV, $X_{62.4}$ and X_{39} respectively, were estimated by inspection of data to be 0.03 and 0.18 respectively. Using $X_{62.4}$ and X_{39}, the proportionality constant C and the σ of the Gaussian are estimated to be 0.193 and 0.345 respectively. The same values of C and σ were used to estimate X_{27} and $X_{19.6}$ and applied to data to obtain N' for these energies. The values of X are given in table 4.2.

Figure 4.11 shows N_γ scaled with N' for different colliding energies and different event centralities. The photon multiplicity, within PMD acceptance, scales well

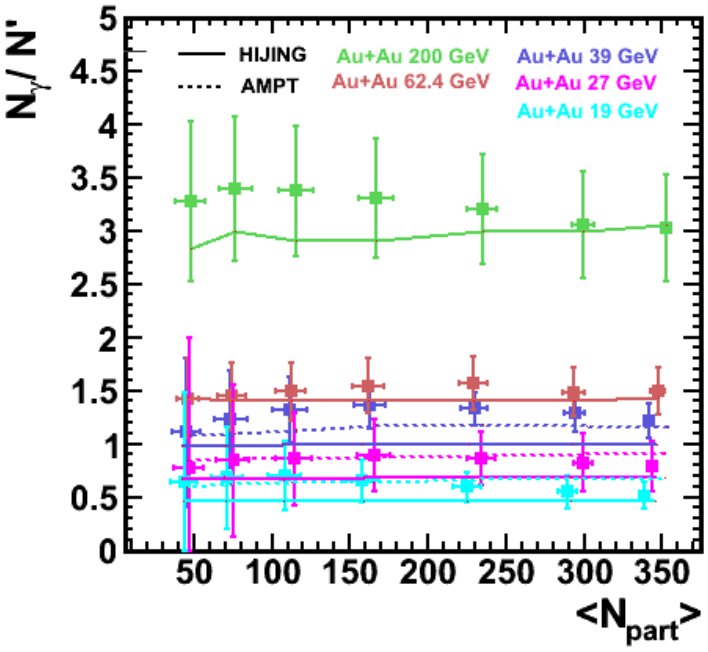

FIGURE 4.11: The number of photons scaled with N' as a function of average number of participating nucleons for Au+Au collisions at $\sqrt{s_{NN}}$ = 200, 62.4, 39, 27 and 19.6 GeV within $3.7 \leq \eta \leq 2.3$. Errors shown are systematic errors.

with N' for all event centralities and for all colliding energies. The observed scaled photon multiplicity also gives a good agreement with the model calculations for all collision centralities. Scaled by N', no excess is seen in peripheral collisions as were seen when the yield was scaled by N_{part}. Note that since the event generators do not include any contribution from the spectators, N' for them reduces to 0.5*Npart, and hence show the same result as earlier.

The same parametrisation has been applied to the rapidity distribution of photons. The rapidity distribution of photons scaled by N' for all energies from 19.6 to 200 A GeV are shown for 10-20% and 20-30% centrality in Figure 4.12 (a). All data points seem to fall on the same line, showing a nice scaling. The same distribution has been observed for 30-40% and 40-50%, as shown in Figure 4.12 (b). The solid curve in both the figures is a second order polynomial of the form $0.407+0.497*(\eta - y_{beam})+0.128*(\eta - y_{beam})^2$ fitted to the data. The ratio plot shows smaller spread with N' scaling as shown in Figure 4.13. The wide spread observed when pseudorapidity density is scaled with $0.5 \times N_{part}$ disappeares when

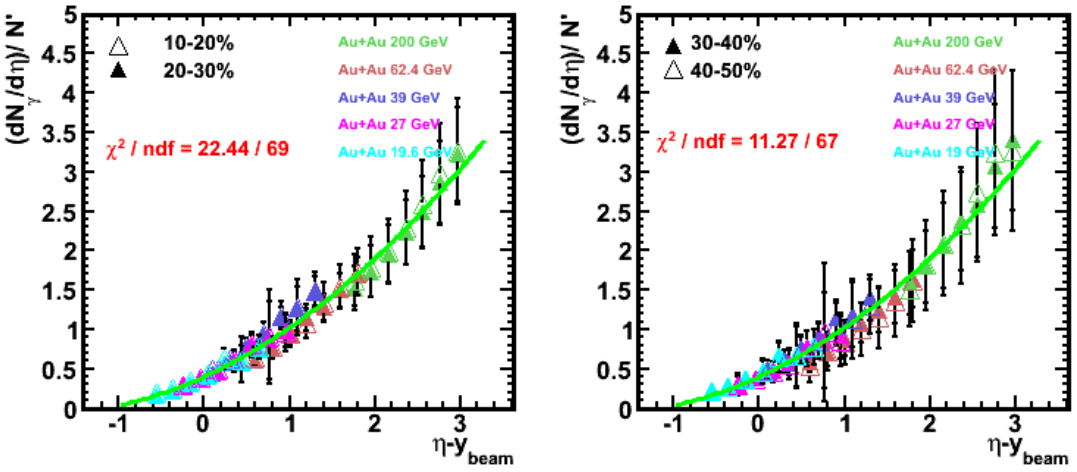

(a) (b)

FIGURE 4.12: Photon pseudorapidity distributions normalized by the proposed factor N' as a function of pseudorapidity shifted by the beam rapidity for Au+Au collisions at $\sqrt{s_{NN}}$ = 200, 62.4, 39, 27, and 19.6 A GeV for (a) 10-20% and 20-30% centrality and (b) 30-40% and 40-50% centrality. Only systematic errors are shown, statistical errors are negligible. The solid line is a second order polynomial fit to the data points.

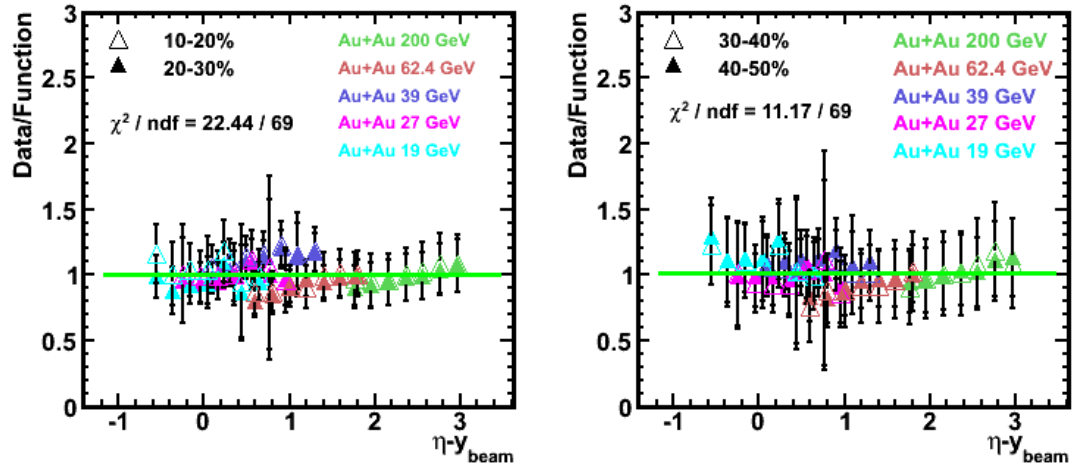

(a) (b)

FIGURE 4.13: (a) Ratio of the data points to fit function shown in Figure 4.12 for centrality bin 10-20% and 20-30% (b) for centrality bin 30-40% and 40-50%

pseudprapidity density is scaled with $N^{'}$. The results for 0-5% and 5-10% as well as 50-60% and 60-70% are also shown for BES energies in Figure 4.14 (a) and (b) respectively. The results demonstrate that the photon production per unit

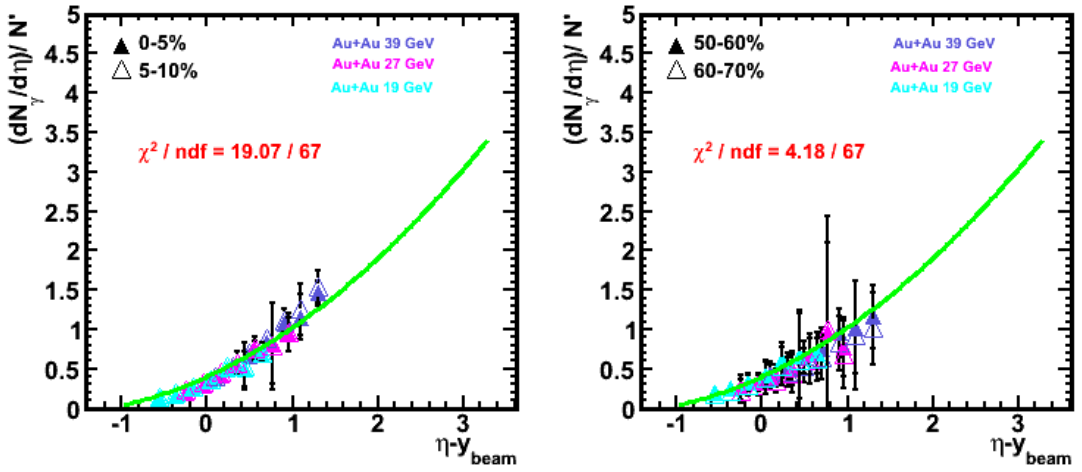

(a) (b)

FIGURE 4.14: Photon pseudorapidity distributions normalized by the proposed factor N' as a function of pseudorapidity shifted by the beam rapidity for Au+Au collisions at $\sqrt{s_{NN}}$ = 39, 27, and 19.6 A GeV for (a) 0-5% and 5-10% centrality and (b) 50-60% and 60-70% centrality. Only systematic errors are shown, statistical errors are negligible. The solid line shown is same as that in Figure 4.12

rapidity, scaled by the proposed term, as a function of $\eta - y_{beam}$ shows longitudinal scaling even beyond the beam rapidity. The data reconfirms that such scaling for photons is independent of beam energy and collision centrality as reported earlier in [42, 43].

4.6 Summary

In this chapter, the photon multiplcity and rapidity distributions have been shown for different centralities at three different energies of the STAR Beam Energy Scan program. The rapidity distributions have been compared to results from HIJING and AMPT event generators for each energy and centrality. The multiplicity of the photons was scaled with N_{part}, both for data and for the event generators. Data from both event generators exhibit N_{part} scaling. The data from PMD shows deviations from N_{part} scaling for smaller values of N_{part} corresponding to the peripheral collisions. This deviation is seen to increase with decreasing energy. This deviation has been explained by assuming another source of signal on the PMD. The yield

from this source contributing to the photon multiplicity has been parametrised using two constants and the known rapidity acceptance of the detector and the beam rapidity. The values of the two constants have been obtained using data at 62.4 and 39 A GeV. The same values of the constants are able to successfully describe the yield at lower energies.

The total yield on PMD divided by a modified term which includes N_{part}, and a measure of spectator size is seen to scale with event centrality, as measured by N_{part}.

The PMD yield in the central collisions showed limiting fragmentation in the energy range 19.6 to 200 A GeV. While for 62.4 and 200 A GeV collisions, the data showed centrality independent limiting fragmentation, the same was not observed at BES energies. This conclusion was drawn by looking at data corresponding to collisions of 10-20% centrality and 20-30% centrality. When the same data was scaled by the modified term, centrality independent limiting fragmentation was observed at all energies for centrality ranging from 10% to 50% in different bins.

Chapter 5

Elliptic and Triangular Flow with AMPT Model

The motivation for colliding heavy ions at facilities like the Relativistic Heavy Ion Collider (RHIC) at Brookhaven National Laboratory and the Large Hadron Collider (LHC) at CERN is to study nuclear matter at extreme conditions and study the properties of deconfined matter called the Quark-Gluon Plasma (QGP) [86]. Each of these collisions can create a region so hot and dense that quarks and gluons become the relevant degrees of freedom instead of hadrons [20]. Studying the conversion of coordinate space anisotropies into momentum space anisotropies gives insight into the nature of the matter created in these collisions [87]. For decades, elliptic flow ($v_2 = \langle \cos 2(\phi - \Psi_{\mathrm{RP}}) \rangle$) has been studied to probe the conversion of the elliptic shape of the initial overlap zone into azimuthal anisotropy in momentum space [50] over a broad range of colliding beam energies. Measuring the strength of that conversion as a function of beam energy to search for evidence of the onset of deconfinement or a softening of the equation-of-state is one of the goals of the RHIC Beam Energy Scan program. Using a generalization of participant eccentricity ($\varepsilon_{n,\mathrm{part}}$) to arbitrary values of n as in Ref. [88], it was shown that within the AMPT model, the final momentum space anisotropy for v_3 was proportional to the initial $\varepsilon_{3,\mathrm{part}}$ [89]. This explained the previous observation that the AMPT model produced correlations similar to those seen in the data (albeit with smaller amplitudes) [90]. Later studies showed that with changes to the input parameters, AMPT could quantitatively describe the centrality dependence of v_2 and v_3 at 200

GeV and 2.76 TeV [91]. In this chapter the AMPT model is used to study the beam energy dependence of v_2 and v_3. Results have been obtained for collisions ranging from $\sqrt{s_{_{NN}}}$ = 7.7 GeV to 2.76 TeV as published in [92].

5.1 Flow Analysis Methodology

The methods used to calculate the flow harmonics in the present work are discussed in this section. The harmonics have been obtained by using the event plane method and the Q cumulant method.

5.1.1 Event Plane Method

The flow is calculated by estimating the reaction plane angle ψ_{RP} in the event plane method. For each harmonic of the anisotropic flow, the event plane can be determined independently. The event flow vector Q_n and the event plane angle ψ_n from the n-th harmonic of the distribution are defined as [48] :

$$Q_n cos(n\Psi_n) = X_n = \sum_i w_i cos(n\phi_i) \tag{5.1}$$

$$Q_n sin(n\Psi_n) = Y_n = \sum_i w_i sin(n\phi_i) \tag{5.2}$$

$$\Psi_n = tan^{-1}\left(\frac{\sum_i w_i sin(n\phi_i)}{\sum_i w_i cos(n\phi_i)}\right)/n \tag{5.3}$$

where ϕ_i is the azimuthal angle of the i^{th} particle in an event and the w_i are the weights. Usually the weights are used to optimize the event plane resolution. This method needs acceptance corrections for the non-uniform azimuthal coverage.

There are several methods available to flatten the azimuthal distribution of event plane. The most commonly used methods for flattening are phi-weighting, re-centering and shifting.

The phi-weighting can be done by weighting each track with inverse of the azimuthal distribution of the particle average over many events,

$$w_i = \frac{1}{< N(\phi_i) >} \tag{5.4}$$

Re-centering is acheived by subtracting Q-vector averaged over large number of events from the Q-vector of each event. After this the shifting can be done by fitting the non-flat azimuthal distribution of Q-vector angles with Fourier expansion and calculating the shift necessary to force a flat distribution. The n^{th} flow harmonic of the azimuthal distribution of the particles with respect to the measured event plane can be written as;

$$v_n^{obs} =< cos(n(\phi - \psi_n)) > \tag{5.5}$$

Since the event plane angle obtained this way fluctuates about the actual reaction plane, the v_n^{obs} values have to be corrected for this fluctuation. This is done by obtaining the event plane resolution as follows:

$$v_n = \frac{v_n^{obs}}{< cos(n(\psi_n - \psi_{RP})) >} \tag{5.6}$$

The event plane resolution factor can be calculated by dividing the event into two subevents and calculating the resolution for subevent. The full event plane resolution can be estimated by the $< cos[n(\psi_n^a - \psi_n^b)] >$ of the event planes of

independent subevent ψ^a and ψ^b. The subevent plane resolution factor is given as:

$$< cos[n(\Psi_n^a - \Psi_{RP})] >= \sqrt{< cos[n(\Psi_n^a - \Psi_n^b)] >} \tag{5.7}$$

and the full event plane resolution can be calculated by using the event plane resolution of the subevents taking into account that the multiplicity of the full event is twice the multiplicity of the subevent,

$$< cos[n(\Psi_n - \Psi_{RP})] > \leq \sqrt{2} < cos[n(\Psi_n^a - \Psi_{RP})] > \tag{5.8}$$

The main drawback of this method is the fact that the event plane resolution is affected by correlations which do not stem from genuine correlation of all particles with the true reaction plane. This causes a a bias in the flow estimates. Multi particle correlation help to minimize those correlations and measure the correlation with the reaction plane alone.

5.1.2 Multiparticle Correlations

In this subsection mostly 2- and 4-particle azimuthal correlations will be discussed. Their generalization to azimuthal correlations involving more particles is straightforward. All the correlations are obtained by first averaging over all particles in a given event and then averaging over all events.For this, single-event average 2- and 4-particle azimuthal correlations is defined in the following way [93]:

$$< 2 >=< e^{in(\phi_1 - \phi_2)} >= \frac{1}{\binom{M}{2} 2!} \sum_{i,j=1,(i \neq j)}^{M} e^{in(\phi_i - \phi_j)} \tag{5.9}$$

$$< 4 >=< e^{in(\phi_1+\phi_2-\phi_3-\phi_4)} >= \frac{1}{\binom{M}{4}4!} \sum_{i,j,k,l=1,(i\neq j\neq k\neq l)}^{M} e^{in(\phi_i+\phi_j-\phi_k-\phi_l)} \tag{5.10}$$

Where ϕ_i is the azimuthle angle of the i^{th} particle. To avoid trivial and strong contribution coming from autocorrelations constraints have been enforced in both equations.

The second step involves averaging over all events.

$$\langle\langle 2\rangle\rangle = \left\langle\left\langle e^{in(\phi_1-\phi_2)}\right\rangle\right\rangle = \frac{\sum_{i=1}^{N}(W_{\langle 2\rangle})_i(\langle 2\rangle)_i}{\sum_{i=1}^{N}(W_{\langle 2\rangle})_i} \tag{5.11}$$

$$\langle\langle 4\rangle\rangle = \left\langle\left\langle e^{in(\phi_1+\phi_2-\phi_3-\phi_4)}\right\rangle\right\rangle = \frac{\sum_{i=1}^{N}(W_{\langle 4\rangle})_i(\langle 4\rangle)_i}{\sum_{i=1}^{N}(W_{\langle 4\rangle})_i} \tag{5.12}$$

Where N is the number of events and double bracket denotes an average first over all particles, and then over all events. $W_{<2>}$ and $W_{<4>}$ are the event weights, which are used to minimize the effect of multiplicity variations in the event sample.

$$W_{<2>} = M(M-1) \tag{5.13}$$

$$W_{<2>} = M(M-1)(M-2)(M-3) \tag{5.14}$$

Multi particle azimuthal correlations as presented above are observables which can be used to calculate flow harmonics v_n without requiring the information about reaction plane Ψ_n

5.1.2.1 Cumulants

Consider two random variables x and y and their joint probability distribution function f(x, y). If x and y are statistically independent the joint probability distribution function can be written as:

$$f(x,y) = f(x)f(y) \tag{5.15}$$

In case if x and y both are not statistically independent, then the 2- particle correlation is understood by the following decomposition:

$$f(x,y) = f(x)f(y) + f_c(x,y) \tag{5.16}$$

The second term on the right side, $f_c(x,y)$, is by definition the 2- particle cumulant. This can be written in the form of expectation values as follows:

$$E[x,y] = E[x]E[y] + E_c(x,y) \tag{5.17}$$

The procedure can be generalized to any number of variables.

5.1.2.2 Cumulants in Flow Analysis

The general formalism of cumulants was introduced into flow analysis by Borghini and Ollitrault [93–95]. For two random variables x and y they used

$$x = e^{in\phi_1} \tag{5.18}$$

$$y = e^{-in\phi_2} \tag{5.19}$$

Here ϕ_1 and ϕ_2 are the azimuthal angle of two particles. The equation 5.1.2.1 can be written as:

$$E[e^{in(\phi_1-\phi_2)}] = E[e^{in\phi_1}]E[e^{-in\phi_1}] + E_c[e^{in(\phi_1-\phi_2)}] \tag{5.20}$$

where $E_c[e^{in(\phi_1-\phi_2)}]$ is by definition the 2- particle cumulant. To understand the meaning of this quantity, consider that for a detector with uniform azimuthal acceptance, $E[e^{in\phi_1}]$ and $E[e^{-in\phi_2}]$ vanishes by symmetry.

$$E[e^{in(\phi_1-\phi_2)}] = E_c[e^{in(\phi_1-\phi_2)}] \tag{5.21}$$

The 2^{nd} order cumulant, $c_n\{2\}$, is an average of 2- particle correlation defined in equation 5.1.2.

$$c_n\{2\} = \langle\langle 2\rangle\rangle \tag{5.22}$$

Similarly the higher order harmonics can be written as:

$$c_n\{4\} = \langle\langle 4\rangle\rangle - 2 * \langle\langle 2\rangle\rangle^2 \tag{5.23}$$

$$c_n\{6\} = \langle\langle 6\rangle\rangle - 9 * \langle\langle 2\rangle\rangle \langle\langle 4\rangle\rangle + 12 * \langle\langle 2\rangle\rangle^3 \tag{5.24}$$

These equations are applicable only for detector with uniform azimuthal acceptance. Different order cumulants provide independent estimates for the same reference harmonics.

$$v_n\{2\} = \sqrt{c_n\{2\}} \tag{5.25}$$

$$v_n\{4\} = \sqrt[4]{-c_n\{4\}} \tag{5.26}$$

$$v_n\{6\} = \sqrt[6]{\frac{1}{4}c_n\{4\}} \tag{5.27}$$

5.2 Eccentricity and Participant Plane

To calculate flow harmonics in AMPT model, the notations for the various observables used is as per reference [89]. The eccentricity is defined as a measure of deformation with respect to the azimuthally symmetric conditions in the transverse plane. It must be distinguished between two sources of eccentricity, the asymmetry of the nuclear overlap and the one arising from fluctuations. In the non-central collision, elliptic eccentricity arises due to asymmetry of the nuclear overlap in the transverse plane. The participant eccentricity is defined as :

$$\epsilon_2 = \frac{\sqrt{(\sigma_y^2 - \sigma_x^2)^2 + 4(\sigma_{xy})^2}}{\sigma_y^2 + \sigma_x^2} \tag{5.28}$$

where σ_x^2, σ_y^2 and σ_{xy} are the event-by-event covariances of the participant nucleon distributions along the transverse directions x and y. If the coordinate system is shifted to the center of mass of the participating nucleons such that $< x >=< y >=0$, the eccentricity can be written as

$$\epsilon_n^{part} = \frac{\sqrt{< r^n cos(n\phi_{part}) >^2 + < r^n sin(n\phi_{part}) >^2}}{< r^n >} \tag{5.29}$$

where r and ϕ_{part} are the polar coordinate positions of the participating nucleons in the AMPT model. Higher order eccentricity in the most central collisions is dominated by fluctuations in the initial energy density distribution. The minor axis of the ellipse defined by this region is given by :

$$\psi_2 = \frac{atan2(< r^2 sin(2\phi_{part}) >, < r^2 cos(2\phi_{part}) >) + \pi}{2} \tag{5.30}$$

The 2^{nd} Fourier coefficient v_2 of the particle distribution with respect to ψ_2 is given by

$$v_2 =< cos(2(\phi - \psi_2)) > \tag{5.31}$$

The triangular flow coefficient v_3 are defined as

$$v_3 =< cos(3(\phi - \psi_3)) > \tag{5.32}$$

where ψ_3 is the minor axis of participant triangularity and is given by

$$\psi_3 = \frac{atan2(< r^2 sin(3\phi_{part}) >, < r^2 cos(3\phi_{part}) >) + \pi}{3} \tag{5.33}$$

5.3 AMPT Model

In AMPT, the program initially generates the collisions utilizing the HIJING model, but in addition, it also simulates the transport of the produced particles from the collision point to the detectors. In the event loop of AMPT, the event number, multiplicity, impact parameter, the number of projectiles and targets, and the corresponding number of targets and projectiles undergoing elastic and inelastic collisions respectively are generated. In the track loop, for each event, the particle ID, components of the momentum along the X, Y and Z axes, the mass of the particle, and the space-time coordinates of the produced particles are obtained.

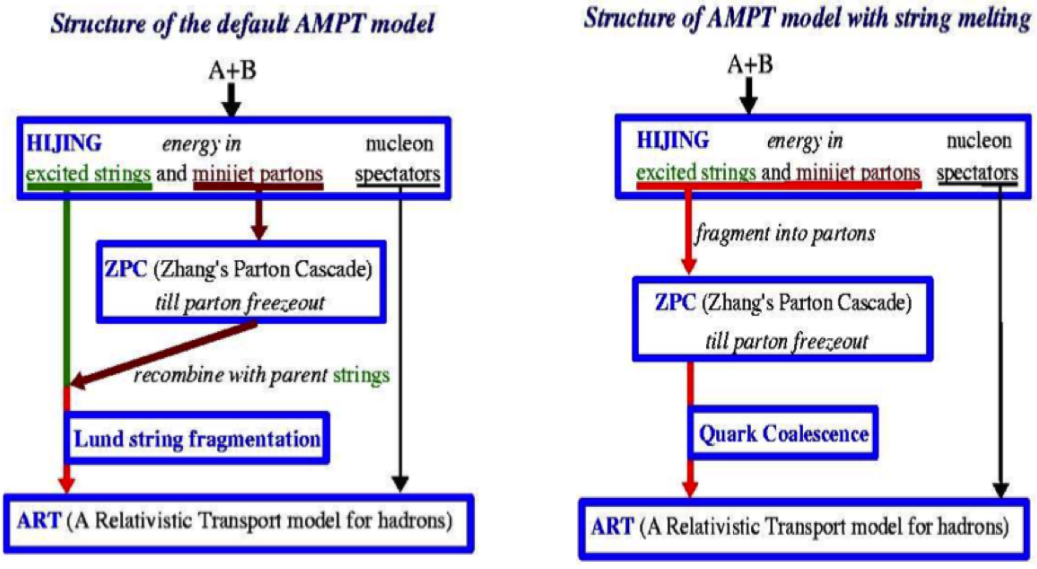

(a) (b)

FIGURE 5.1: (a) Structure of the default AMPT model (b) Structure of the AMPT model with string melting

The AMPT model provides two modes: Default and String Melting [80]. In both the cases these two modes take the initial conditions from HIJING with Lund string fragmentation function [44] as shown in Figure 5.1. AMPT, in the default

mode, is essentially a string and minijets model where initial strings and mini- jets are produced with the HIJING event generator. The interactions of the minijet partons are then calculated using ZhangâĂŹs Parton Cascade (ZPC), before the strings and partons are recombined, and the strings are fragmented via Lund string fragmentation again. ART (A Relativistic Transport model for hadrons) is used to describe how the produced hadrons will interact. In the String Melting mode, the strings produced from HIJING are decomposed into partons which are fed into the parton cascade along with the minijet partons. The partonic matter is then turned into hadrons through coalescence and the hadronic inter-actions are subsequently modeled using ART. Here the main idea is that beyond a critical value of energy density 1 GeV/fm^3 coexistence of string and partons are not possible, and hence strings are melted into partons. So while the Default mode describes the collision evolution in terms of strings and minijets followed by string fragmentation, the String Melting mode includes a fully partonic QGP phase that hadronizes through quark coalescence. The model therefore provides a convenient way to investigate expectations for a variety of observables, with and without a QGP phase.

5.4 Tuning AMPT Parameters to Multiplicity

Several parameters need to be specified in the model. This includes some parameters required for Lund string fragmentation (referred here as 'a' and 'b'), the QCD coupling constant α_s (which the model treats as a constant), and the screening mass for gluons in the QGP phase μ. A recent study found that a good description of the multiplicity density, v_2 and v_3 could be achieved with the parameters set as: a=0.5, b=0.9 (GeV^{-2}), α_s=0.33 and μ=3.2 (fm^{-1}) [91]. In this study, it was possible to acheive a good desciption of the charged particle multiplicity density at all energies from $\sqrt{s_{NN}}$= 7.7 GeV to 2.76 TeV by using parameter set: a=2.2, b=0.5 (GeV^{-2}), α_s=0.47 and μ=1.8 (fm^{-1}), and turning off initial and final state radiation in HIJING. In this case, the initial cutoff for minijets (termed as p_0) does not need to be adjusted with $\sqrt{s}$ in order to match the LHC multiplicity densities [97]. The value of p_0 and all other parameters are kept fixed for all energies in the present study. Figure 5.2 shows the charged particle multiplicity density scaled by $N_{\mathrm{part}}/2$ for 0-5% central Au+Au or Pb+Pb collisions from AMPT String

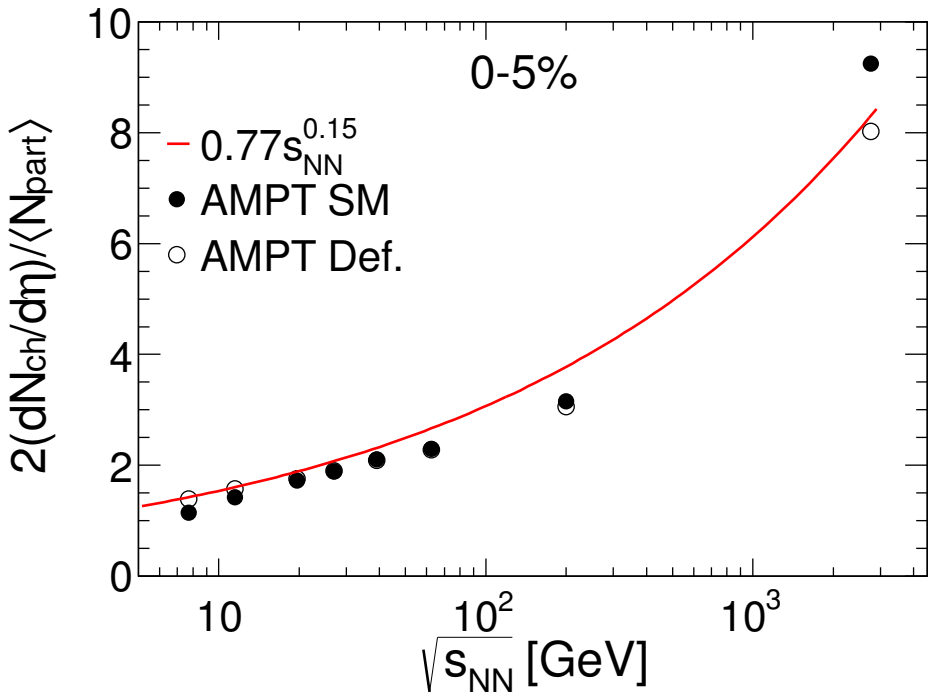

FIGURE 5.2: The charged particle multiplicity density scaled by $N_{\text{part}}/2$ in the AMPT model for String Melting and Default modes. The red line shows the parameterization of experimental data presented in Ref [96].

Melting and Default vs $\sqrt{s_{NN}}$. The line shows the parameterization of the experimental data from Ref. [96]. Both the SM and Default calculations are in good agreement with the experimental data throughout the energy range.

5.5 Comparison of v_2: AMPT and Data

In Figure 5.3, the AMPT model results are compared to experimental data of charged particles at mid-rapidity at $\sqrt{s_{NN}}$ =62.4 GeV, 200 GeV, and 2.76 TeV. For the SM calculations, the following are obtained:

1. (i) v_2 relative to the participant plane ($v_2\{PP\}$) calculated from the initial conditions of AMPT and

2. (ii) the two-particle cumulant results $v_2\{2\}$.

While $v_2\{2\} = \sqrt{\langle v_2^2 \rangle} + \delta$ where δ is a term to account for correlations not related to the participant plane (non-flow), $v_2\{PP\}$ is the true mean v_2 relative to the participant plane. The difference between those results therefore reflects both the effect of fluctuations $\sqrt{\langle v_2^2 \rangle - \langle v_2 \rangle^2}$ and non-flow correlations present in the model. All the model calculations have a similar centrality dependence but the Default results are well below the SM results. The data generally agree well with the SM calculations. The fact that the experimental $v_2\{4\}$ results are slightly below the model results calculated with respect to the participant plane does not therefore signify a discrepancy between data and model. The agreement between the model and the data is considered to be satisfactory.

STAR has shown that for $p_T < 1$ GeV, $v_2\{4\}(p_T)$ increases with $\sqrt{s_{NN}}$ and for $p_T > 1$ GeV $v_2\{4\}(p_T)$ is observed to be roughly independent of collision energy in the range 7.7 GeV to 2.76 TeV [98]. It is surprising for a measurement that is supposed to be sensitive to viscosity and collective effects in the expansion to not depend on $\sqrt{s_{NN}}$ over such a wide range of energies where the initial conditions and properties of the fireball should be changing quite significantly.

Given this surprising experimental result, it is interesting to see if the same trend is reproduced in the AMPT model. In Figure 5.4, $v_2(p_T)$ calculated with respect to the reaction plane for collisions with center of mass energies ranging from 7.7 GeV to 2.76 TeV is shown. Although the statistics in the present study were not sufficient to calculate $v_2\{4\}(p_T)$, it has been shown that as long as v_2 fluctuations are dominated by eccentricity fluctuations and those eccentricity fluctuations are Gaussian distributed along the x and y axis, then $v_2\{4\}$ is equivalent to $v_2\{\text{RP}\}$ [99]. It is worth investigating the independence of $v_2\{\text{RP}\}(p_T)$ on $\sqrt{s_{NN}}$ for $p_T > 1$ GeV in the AMPT model. It is observed that the variation of $v_2\{\text{RP}\}$ is not large in AMPT throughout the energy range studied. For $p_T < 1$ GeV, $v_2\{\text{RP}\}$ varies by about 5% from 7.7 GeV up to 200 GeV. Going from 200 GeV to 2.76 TeV, $v_2\{\text{RP}\}$ increases by 20%, independent of p_T. In the RHIC range, the AMPT $v_2\{\text{RP}\}$ results for $p_T > 1$ GeV are actually increasing as the energy is decreased with $v_2\{\text{RP}\}$ at $p_T = 1.5$ GeV for 7.7 GeV being 20% larger than for 200 GeV. This likely reflects the softening of the spectrum which allows flow effects that push low momentum particles to higher momentum, to have a larger influence at intermediate p_T. The same trends hold when studying $v_2\{\text{PP}\}(p_T)$

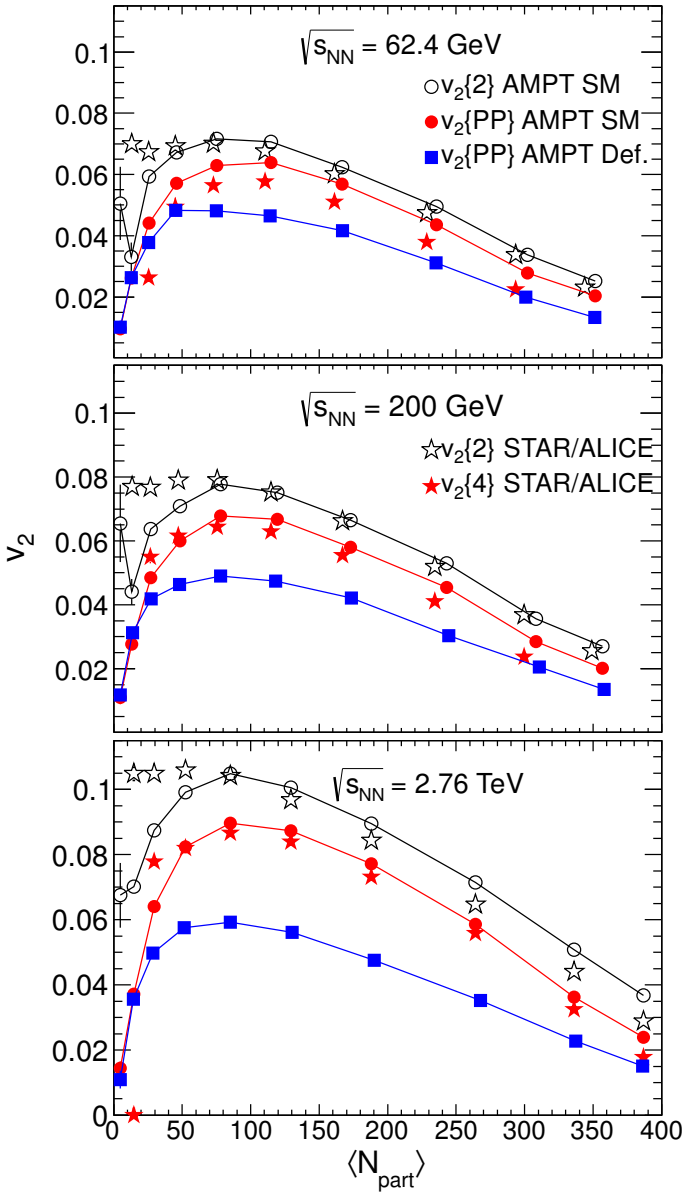

FIGURE 5.3: Elliptic flow data from AMPT and experiments at $\sqrt{s_{NN}}$=62.4 GeV, 200 GeV [STAR], and 2.76 TeV [ALICE]. For the String Melting calculation v_2 calculated relative to the participant plane $v_2\{\mathrm{PP}\}$ defined by the positions of the nucleons and using the two particle cumulant $v_2\{2\} = \langle \cos 2(\phi_i - \phi_j)\rangle$. Experimental results are shown for the two-particle $v_2\{2\}$ and four-particle $v_2\{4\}$ cumulants.

(not shown). Although there are differences between the trends seen in AMPT and in the data, one can conclude that even in the AMPT model, the changes in $v_2\{\mathrm{RP}\}(p_T)$ or $v_2\{\mathrm{PP}\}(p_T)$ when increasing $\sqrt{s_{NN}}$ from 7.7 GeV to 2.76 TeV are not large. In this case, it is not necessarily surprising that the data also does not

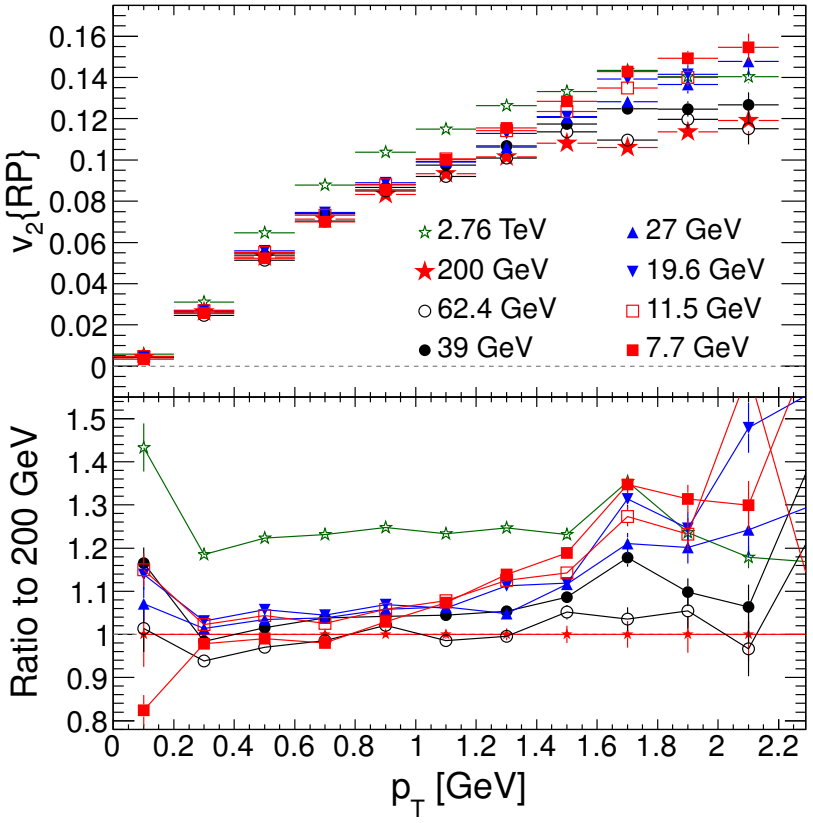

FIGURE 5.4: Top: $v_2(p_T)$ calculated with AMPT SM relative to the reaction plane ($v_2\{\mathrm{RP}\}$) for beam energies from 7.7 GeV to 2.76 TeV. Bottom: The $v_2\{\mathrm{RP}\}$ data at different energies are shown scaled by the results at 200 GeV.

change drastically. Since based on the AMPT model, we would not expect a large variation of $v_2\{\mathrm{RP}\}(p_T)$ with $\sqrt{s_{NN}}$, as long as one assumes that a string melting or QGP phase exists throughout the energy range under study, the fact that the data seem to change very little no longer appears to be so difficult to understand.

5.6 Comparison of v_3: AMPT and Data

Having shown that the parameter selection provides a good description of the charged particle multiplicity densities and the elliptic flow, it is worth investigating v_3 and its energy dependence.

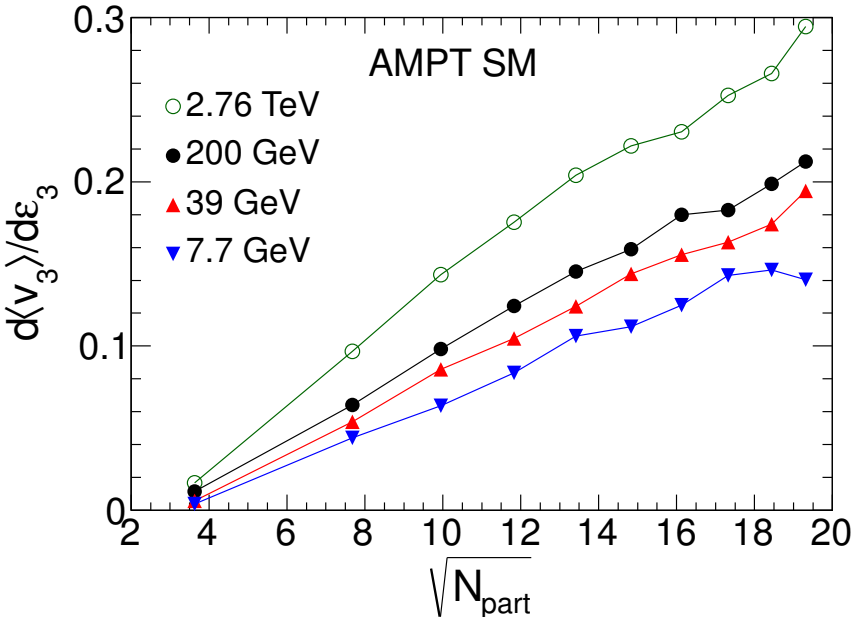

FIGURE 5.5: The slope of $\langle v_3 \rangle$ vs. ε_3 as a function of the square root of the number of participants for four different colliding energies.

The relationship of v_3 to the third harmonic participant eccentricity is studied. In Ref. [89] the AMPT model is used to show that v_2 and v_3 have a linear dependence on ε_2 and ε_3. Preleiminary results from STAR experiment have shown that v_3/ε_3 scales with $1/\sqrt{N_{\rm part}}$ [100]. It is interesting to check whether this phenomenological observation is also reproduced in the AMPT model. In Figure 5.5 the dependence of the slope of $\langle v_3 \rangle$ vs. ε_3 on $N_{\rm part}$ is investigated. The figure shows $d\langle v_3 \rangle/d\varepsilon_3$ vs. $\sqrt{N_{\rm part}}$ for $\sqrt{s_{_{NN}}}$ = 7.7 GeV, 39 GeV, 200 GeV, and 2.76 TeV. It is found that for all the energies investigated (including those not shown in the figure), $d\langle v_3 \rangle/d\varepsilon_3$ increases linearly with $\sqrt{N_{\rm part}}$. The AMPT model therefore correctly describes the phenomenological observation made by STAR. This also indicates that according to the string melting version of AMPT, even at energies as low as $\sqrt{s_{NN}}$=7.7 GeV, v_3 reflects the fluctuations in the initial geometry of the collisions and that the centrality dependence will remain similar at all energies although the magnitude will change. At the lowest energies investigated here, the contributions from jets and minijets should be negligible so they will not contribute significantly to the centrality dependence of v_3. The experimental observation of a similar centrality dependence for v_3 at 7.7 and 200 GeV [100], therefore strongly contradicts assertions that v_3 is dominated by jet-like correlations [101].

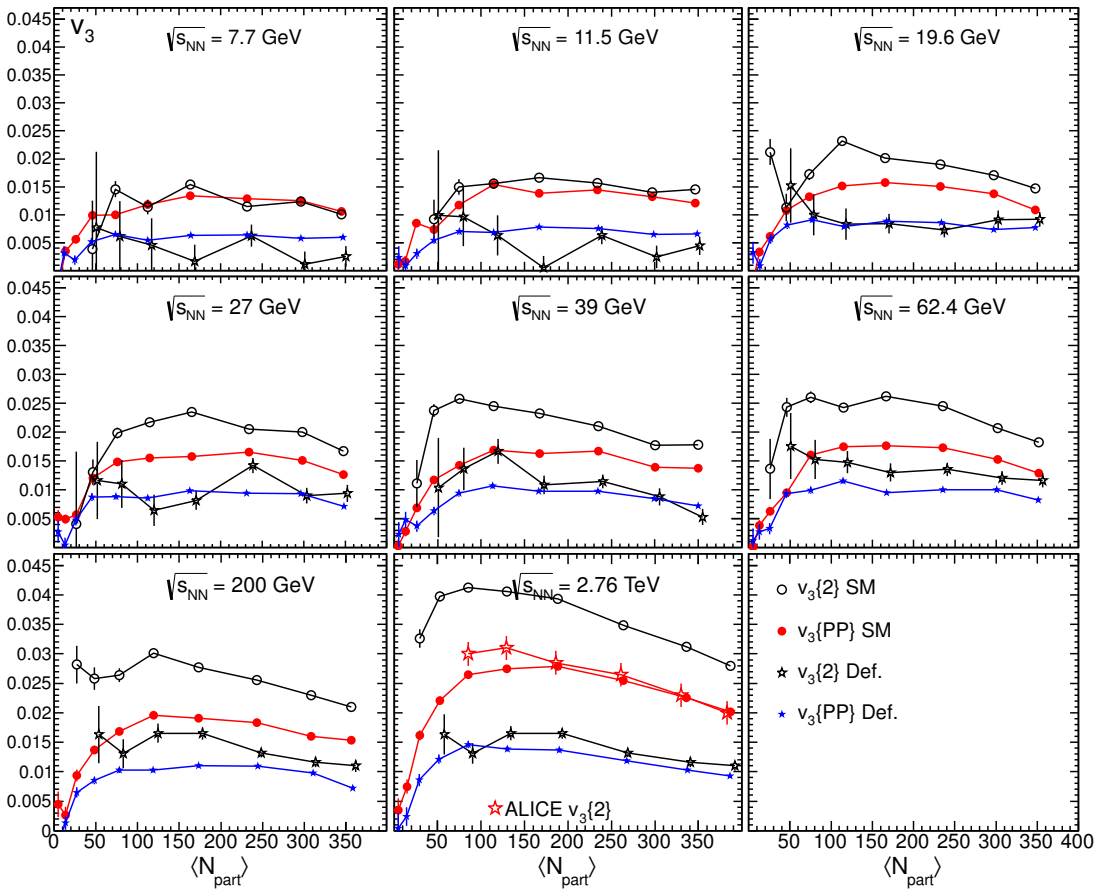

FIGURE 5.6: $v_3\{2\}$ and $v_3\{\mathrm{PP}\}$ from AMPT SM and Default calculations for $\sqrt{s_{NN}}$ = from 7.7 GeV to 2.76 TeV. Experimental results are shown at %200 GeV [100] and 2.76 TeV [102].

In Figure 5.6, AMPT SM and Default calculations of $v_3\{2\}$ and $v_3\{\mathrm{PP}\}$ are shown for 7.7, 11.5, 19.6, 27, 39, 62.4, 200 GeV and 2.76 TeV. While $v_3\{\mathrm{PP}\}$ reflects the true correlation of particles with the initial participant plane, $v_3\{2\}$ includes non-flow and fluctuation effects. The difference between $v_3\{2\}$ and $v_3\{\mathrm{PP}\}$ is large at 200 and 39 GeV while at 7.7 GeV $v_3\{2\}$ and $v_3\{\mathrm{PP}\}$ are equivalent. This indicates that indeed, according to AMPT SM, non-flow does not make an appreciable contribution to $v_3\{2\}$ at 7.7 GeV. The model results are compared to ALICE data at 2.76 TeV and it was found that $v_3\{\mathrm{PP}\}$ for AMPT SM matches the ALICE data on $v_3\{2\}$. The $v_3\{2\}$ AMPT SM results over predict the ALICE data and the $v_3\{\mathrm{PP}\}$ AMPT Default results underpredict the ALICE data. The $v_3\{2\}$ Default results also underpredict the ALICE data for $N_{\mathrm{part}} > 100$. The correspondence of $v_3\{\mathrm{PP}\}$ from AMPT SM with $v_3\{2\}$ from ALICE data means that either non-flow

and fluctuations are overpredicted in AMPT or v_3 is underpredicted. The 200 GeV data is also in good agreement with STAR data [100] (not shown) in the same centrality range. In more peripheral collisions, the STAR data in Ref. [100] tends to increase, as also seen with the AMPT $v_3\{2\}$ results. This suggests that while $v_3\{2\}$ measurements for $N_{\text{part}} > 100$ are dominated by the correlation of particles with the participant plane, in more peripheral collisions $v_3\{2\}$ begins to reflect correlations related to mini-jet structure similar to that in $p+p$ collisions.

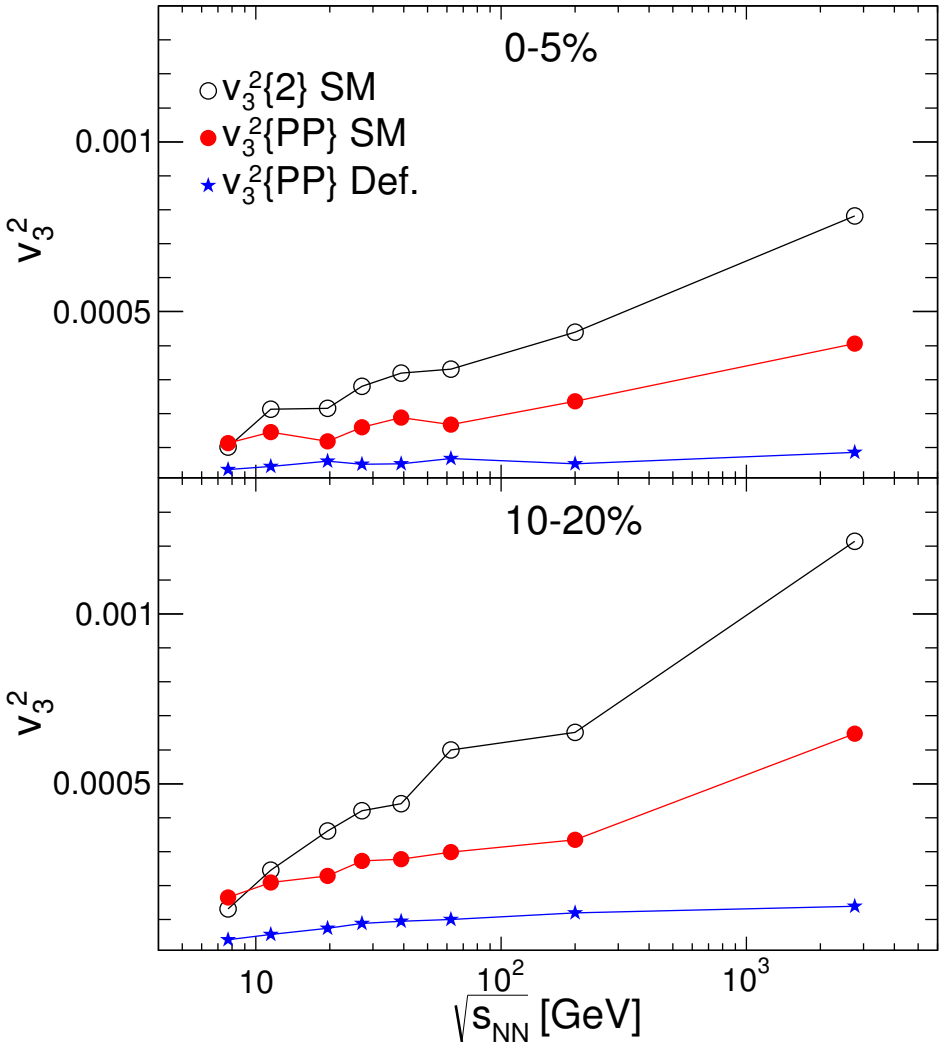

FIGURE 5.7: The $\sqrt{s_{NN}}$ dependence of $v_3^2\{2\}$ (SM), $v_3^2\{\text{PP}\}$ (SM), and $v_3^2\{\text{PP}\}$ (Default) for two different centrality intervals.

In figure 5.7 the AMPT results for the variation of $v_3^2\{2\}$ and $v_3^2\{\text{PP}\}$ with $\sqrt{s_{NN}}$ from 7.7 GeV to 2.76 TeV for two centrality intervals are shown. The results on

$v_3^2\{\mathrm{PP}\}$ using the default setting for AMPT are very small and well below the preliminary data presented by STAR. The $v_3^2\{\mathrm{PP}\}$ SM results decrease rather smoothly with decreasing energy but still have an appreciable value down to 7.7 GeV. The calculations for $v_3^2\{2\}$ SM have the same value as the $v_3^2\{\mathrm{PP}\}$ SM at 7.7 and 11.5 GeV. This again indicates that within this model, non-flow from minijets has a negligible impact on two-particle correlations at the lowest energies measured in the RHIC beam energy scan. Above those energies, the difference between $v_3^2\{2\}$ and $v_3^2\{\mathrm{PP}\}$ grows substantially. It will be interesting to see if the experimental data on v_3 follows the same trend as AMPT SM all the way down to 7.7 GeV where non-flow from minijets can be neglected. It will be most interesting to see if data eventually drops down to the values predicted by the AMPT Default model. Estimates of the Bjorken energy density [30] compared to the Lattice QCD estimates for the critical energy density suggest that this may not happen until below 7.7 GeV. The calculations presented in this paper provide a base-line with which to compare future experimental data.

5.7 Conclusion

In this chapter, results of v_2 and v_3 using AMPT SM and Default model have been presented. The primary purpose of these calculations is to provide a reference for measurements of the beam energy dependence of v_2 and v_3. The studies suggest that it was possible to describe RHIC and LHC data on multiplicity, v_2 and v_3 by turning off initial and final state radiation in HIJING (reducing the initial entropy) but keeping relatively large cross-sections in the QGP phase. The changes in $v_2(p_T)$ from 7.7 GeV to 2.76 TeV have also been studied, and the findings suggest that within this model, $v_2(p_T)$ changes very little across the whole energy range studied, consistent with what is observed in data. The AMPT reproduces the experimental observation that $v_3/\varepsilon_3 \propto \sqrt{N_{\mathrm{part}}}$. These experimental observations therefore seem to be understandable without major changes to our description of heavy-ion collisions and a subsequent nearly perfect liquid QGP phase. Our studies of the centrality and beam energy dependence of v_2 and v_3 with SM and Default settings provide a comparitive base-line for studies of v_2 and v_3 in the RHIC beam energy scan.

Chapter 6

Azimuthal Anisotropy in Inclusive Photons

Flow has been studied in STAR extensively at mid-rapidity. At forward rapidity, due to limited detection efficiency, STAR has studied only charge particle v_2 using FTPC. PMD provides a good opportunity to complement this measurement. PMD measures inclusive photons which are primarily produced by the decay of neutral pions and eta. The charge particles formed in the initial stages of matter would undergo final state interactions with the medium long after formation. Neutral pions do not undergo Coulomb interactions in the final state. The distributions of photons are governed by known kinematics of neutral pion decay, and is incorporated in most event generators.

6.1 Software for Flow

The flow in azimuthal distribution of photons is determined using a software chain with the following makers:

(i) **StFlowMaker :** This maker reads the STAR muDST.root files and selects events based on trigger, centrality and the quality of the event, e.g. event vertex. For each selected event, charged particle tracks are selected for construction of the event plane. The selected tracks have to fulfill the conditions

given in Table 6.1. Event plane angle for each harmonic is calculated using the equation :

$$\Psi_n = tan^{-1}\left(\frac{\sum_i w_i sin(n\phi_i)}{\sum_i w_i cos(n\phi_i)}\right)/n \tag{6.1}$$

where ϕ_i is the azimuthal angle of the i^{th} particle in an event and the w_i are the weights. Each event is divided into two subevents, and the event plane is obtained for each of them. The information of event, subevents for each harmonic and all selection criteria (different η gap between subevents, elaborated later in this chapter) can be shared with other Makers in the chain.

(ii) **StPmdFlowMaker :** This Maker reads the information from muDST after StFlowMaker. It obtains the value of different harmonics of event plane and subevent planes calculated in StFlowMaker. In addition, the information of PMD Clusters from StPmdClusterCollection is stored in a tree which is stored in a nanoDST.root file. The nanoDSTs are downloaded locally for further analysis.

	Track Cut
$\|\eta\|$	< 1.3
nHitFits	> 15
nHitFits / nHitsPoss	> 0.52
DCA-Global (cm)	< 2
p (GeV/c)	> 0.5

TABLE 6.1: Track cuts on TPC tracks used for flow analysis

Two passes of data are required for flow analysis. In the first pass, StFlowMaker fills the plots required to calculate the inverse azimuthal accceptance correction factors. The event plane calculated in the first pass, therefore, is the uncorrected event plane. During the second pass, StFlowMaker reads the acceptance plots, calculates the azimuthal acceptance correction factors and applies them when calculating the event plane. The event plane calculated in second pass is corrected for acceptance variation of TPC.

6.2 Event Plane and Resolution Using TPC

The event plane was measured using the charge particles tracks in Time Projection Chamber [69]. Since TPC takes data from $-1.3 \leq \eta \leq 1.3$ and PMD rapidity range is $-3.7 \leq \eta \leq -2.3$, there is a minimum of 1.0 unit of rapidity gap between any TPC track used for event plane calculation and any PMD cluster. This rapidity gap minimises any non-flow correlations in cluster distribution on PMD due to charged particles tracks in TPC.

The raw TPC event plane is obtained using the cuts on TPC tracks mentioned in Table 6.1. The event cuts are based on trigger, event centrality and vertex position. Any event showing large forward-backward asymmetry is also excluded, because these events were either at a v_z position far removed from the nominal center of STAR or some part of TPC was not working. A cut on minimum number of tracks in TPC was also applied since these are necessary to calculate the event plane.

A total of 337K events were used for analysis. Table 6.2 shows the number of events in each centrality. The data of day 101 of Au+Au 39 A GeV collisions during BES Run was used for this analysis.

Centrality (%)	No. of Events
0 - 5	21927
5 - 10	21724
10 - 20	44865
20 - 30	45344
30 - 40	44879
40 - 50	43192
50 - 60	43752
60 - 70	37380
70 - 80	35235

TABLE 6.2: This table shows number of events in each centrality bin.

6.2.1 Flattening TPC Event Plane

As mentioned earlier, the raw event plane from TPC was not isotropic in azimuthal plane as shown in Figure 6.1 by the solid line (in blue color). Each plot is for events

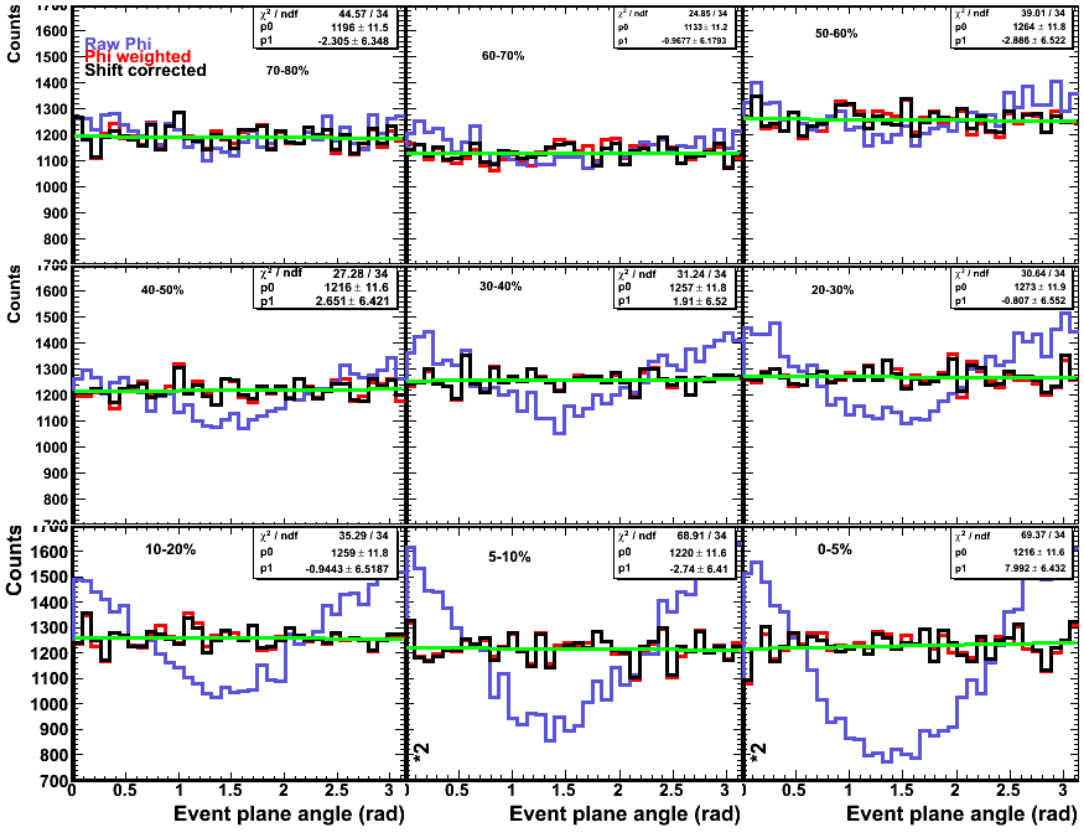

FIGURE 6.1: The distribution of event plane angle ψ_2 obtained from the charged particle in the TPC (i) uncorrected event plane (blue line) (ii) corrected by phi weights (red line) and (iii) shifting method (black line). The green line is a straight line fit to the data after shifting.

of different centralities, the plot in the right bottom box is for the most central and left top box is for the most peripheral events. A number of methods have been suggested in [48] to obtain a flat distribution of event plane angles. Inverse ϕ correction was employed to obtain a reasonable flattening. The results are shown in the Figure 6.1 by solid line (in red color). While this method removed most of the asymmetry of the event plane, the distribution was still not flat . This could be observed by fitting the event plane distribution to a first order polynomial, a straight line with a slope. A finite slope which was larger as compared to the error estimates on slope from fitting demonstrated that the event plane was not truly flat. An additional correction method of shifting the event planes was used to flatten the distribution.

In the first pass through the data locally, we calculated $< sin(in\psi_n) >$ and $<$

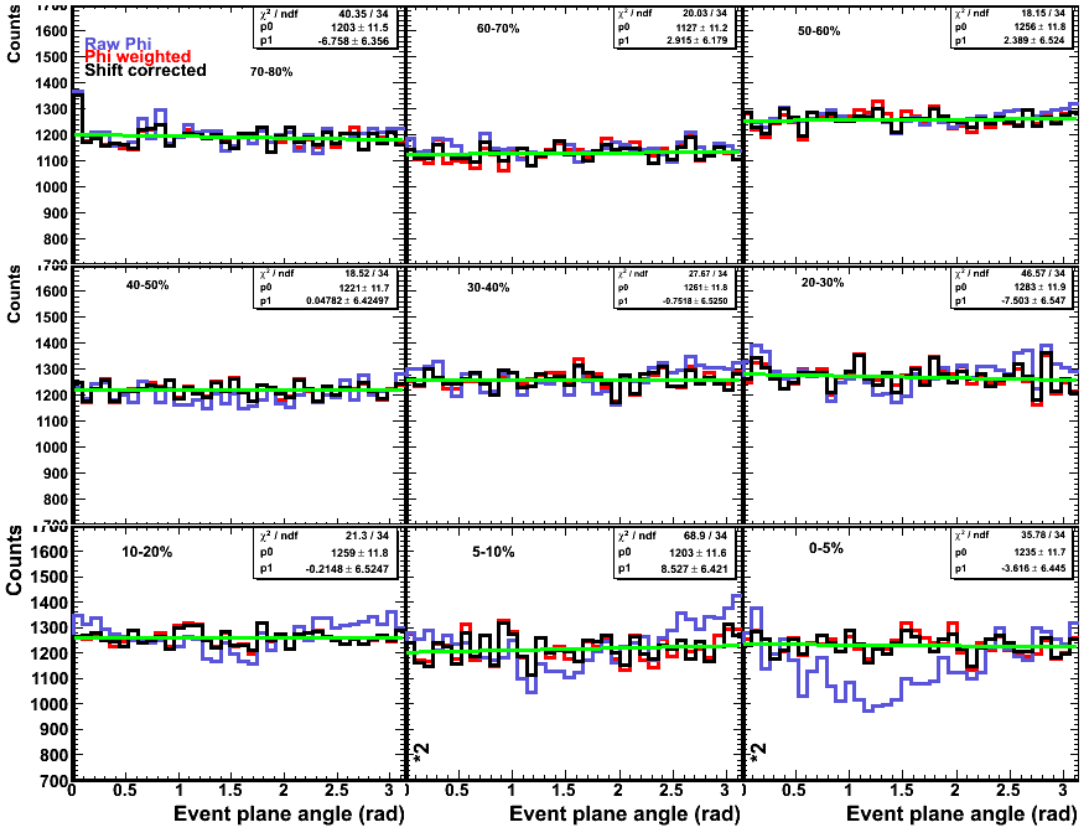

FIGURE 6.2: The distribution of event plane angle ψ_2 obtained from the charged particle in the positive rapidity region of TPC (i) uncorrected event plane (blue line) (ii) corrected by phi weights (red line) and (iii) shifting method (black line). The green line is a straight line fit to the data after shifting.

$cos(in\psi_n) >$ for different values of n (harmonics) and for i=$\sim$1 to $\sim$32 for the whole data set and stored it for further use. In the second pass through the data, for each event, the amount of shifting was calculated using Equation 6.2 as given in [48] :

$$n\Delta\Psi_n = \sum_{i=1}^{i_{max}} \frac{2}{i}(\langle sin(in\Psi_n)\rangle\, cos(in\Psi_n) + \langle cos(in\Psi_n)\rangle\, sin(in\Psi_n)) \tag{6.2}$$

Figure 6.1 shows the raw event plane (Blue solid ine), event plane after accpetance correction (Red line) as well as shifted event plane (Black line) for each centrality. The shifted event plane distributions given by the black line can be seen to fit nicely

to a straight line (green line) where the slope parameter is consistent with zero within the error estimates of this value.

The same procedure was also implemented for each subevent (see details of subevents in the next section). Figure 6.2 and Figure 6.3 also gives the subevent planes for the three cases mentioned above.

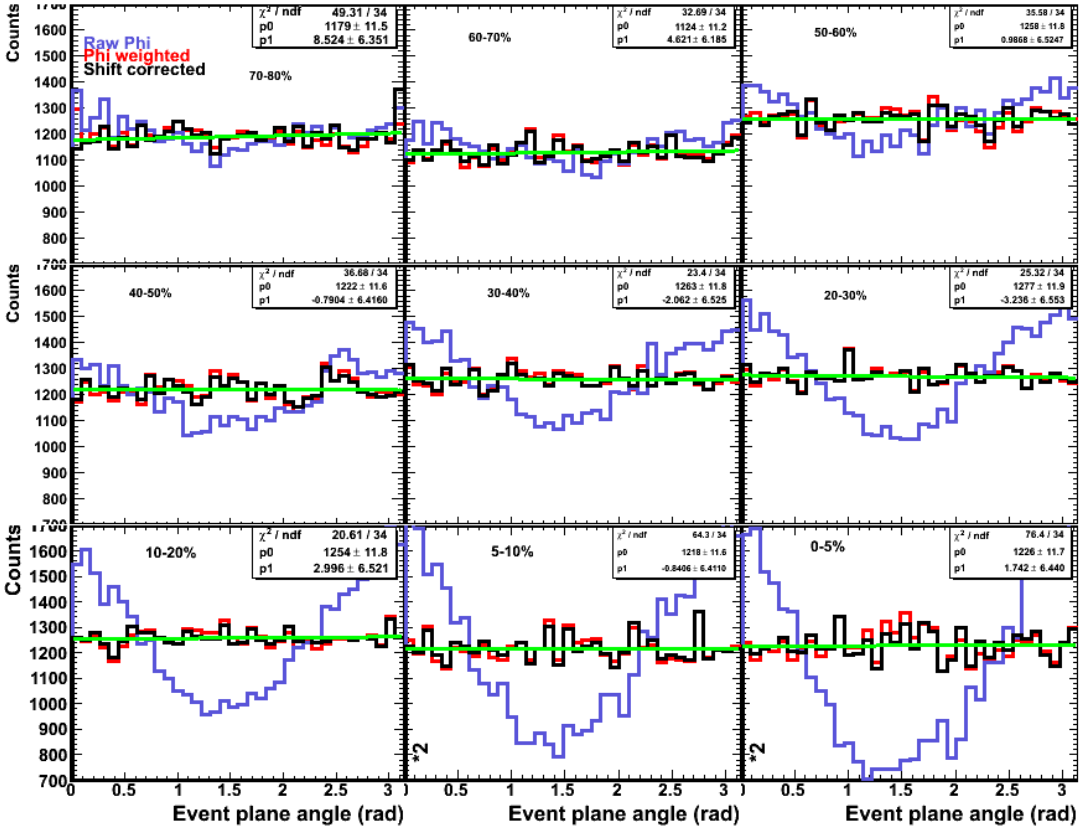

FIGURE 6.3: The distribution of event plane angle ψ_2 obtained from the charged particle in the negative rapidity region of TPC (i) uncorrected event plane (blue line) (ii) corrected by phi weights (red line) and (iii) shifting method (black line). The green line is a straight line fit to the data after shifting.

6.2.2 Event Plane Resolution Correction

The event plane reconstructed through the TPC tracks is an estimate of the actual reaction plane of that event. This estimate fluctuates about the reaction plane because the number of tracks used for event plane reconstruction is finite. The flow measured with respect to the estimated event plane would be less than the

flow with respect to the actual event plane. This uncorrected flow needs to be corrected for the event plane resolution. In order to estimate the flow correctly, it is important to estimate the resolution correction factor correctly.

For estimating the event plane resolution, two subevents were made out of each event. We used rapidity of the tracks to divide them into the subevents; all positive rapidity tracks make up one subevent and the negative tracks were the part of the other subevent. Event plane was estimated for each subevent and this event plane is also flattened using the same procedures used for full event plane and can be seen in above section. The correlation between the two subevent planes is a measure of the event plane resolution correction factor (RCF). The event plane resolution is determined from these subevent plane angle using the expression given below [48].

$$< cosn(\Psi_n - \Psi_r) >= \frac{\sqrt{\pi}}{2\sqrt{2}}\chi_n exp\left(\frac{-\chi_n^2}{4}\right)\left[I_{\frac{-1}{2}}\left(\frac{\chi_n^2}{4}\right) + I_{\frac{1}{2}}\left(\frac{\chi_n^2}{4}\right)\right] \tag{6.3}$$

where $\chi_n = v_n/\sigma$ and I_ν is the modified Bessel function of order ν.

To remove non-flow correlations, the two subevents were created with a rapidity gap between them, the gap removes short range correlations between tracks in the two subevents. The data was analysed using two values of the gaps: 0.2 and 0.4 units of rapidity. These were called Selection 1 and Selection 2 respectively. The resolution correction factors for all centralities are shown in Figure 6.4 for Au+Au collisions at 39 GeV. The resolution is maximum for semi-central collisions, and decreases on both sides. Increasing the gap between the subevents decreases non-flow correlations, causing the RCF to decrease.

Subevent plane angles can also be used for obtaining the flow in photons. Since the number of tracks in a subevent is half of the number of tracks in the full event, the subevent plane is expected to have larger fluctuations about the reaction plane. The RCF values for subevent are given in Figure 6.5.

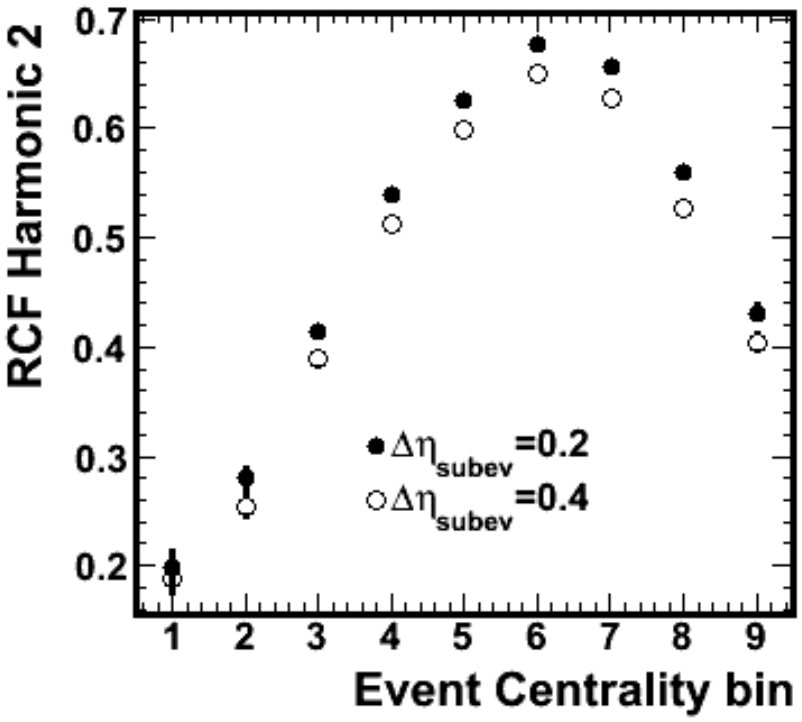

FIGURE 6.4: Centrality dependence of event plane resolution correction factor for full event. The numbers on the x-axis indicate the nine centrality intervals, 1 corresponding to most peripheral.

In the present study, besides the full event plane, the subevent plane on the west side TPC (away from PMD) has been used to further minimise non-flow correlation by increasing the gap between particles used to determine event plane and particles of interest. For this case, the RCF values will be lower, as seen in Figure 6.5. These are also obtained for two different $\Delta\eta$ and the value of RCF for larger rapidity gap is smaller, as expected.

6.3 Photon v_2 Using TPC Event Plane

The elliptic flow coefficient v_2 of photon like clusters in PMD is determined using the event plane from TPC. The event plane used is corrected for TPC acceptance and has also been shifted for additional flattening. Figure 6.6 shows the v_2 for

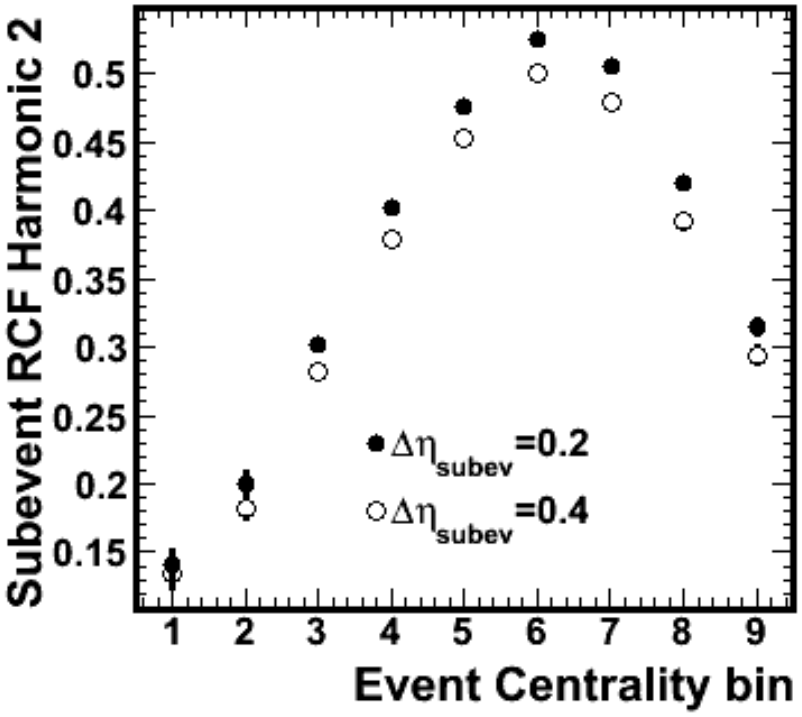

FIGURE 6.5: Centrality dependence of event plane resolution correction factor for subevents. The numbers on the x-axis indicate the nine centrality intervals, 1 corresponding to most peripheral.

different event centralities for different rapidity intervals for the following three cases.

(i) v_2 with respect to full event plane, without any weighting, corrected for full event plane resolution

(ii) v_2 with respect to subevent plane, without any weighting, corrected for subevent plane resolution

(iii) v_2 with respect to full event plane, weighted with acceptance of PMD and HLCF, corrected for full event plane resolution

Here HLCF is the hit loss correction Factor for each chain of PMD as discussed in Chapter 3.

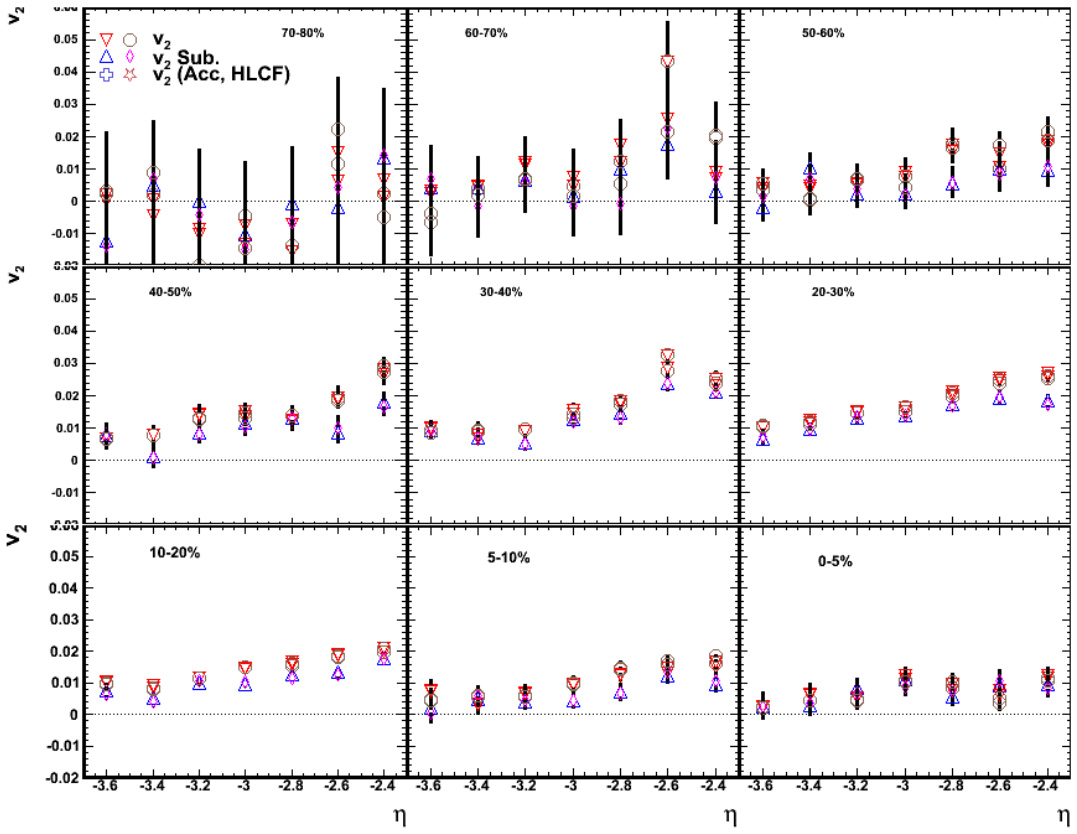

FIGURE 6.6: Pseudorapidity dependence of v_2 for different centralities in Au+Au collisions at 39 A GeV.

The above three cases are shown for two different rapidity gaps between the two subevents. The legend in the top left panel shows two sets of symbols; the first column refer to smaller rapidity gap (0.2 units) and the second column are for larger rapidity gap (0.4 units). The errors plotted in the figure are statistical. Large error bars for the peripheral events are because of the smaller number of tracks per event, even though the number of events is not so small and due to poor event plane resolution.

The data shows that the elliptic flow clearly increases towards mid-rapidity for centrality bins 0 to 60%. For most peripheral events the errors are too large to conclude anything from the data. The elliptic flow also shows an increase from most central to mid-central events and then decreases for more peripheral collisions. This is exactly what is expected from the eccentricity values which are small for near symmetric central events and large for highly asymmetric mid-central events. Small differences are observed for all the 6 cases shown for each

centrality in the Figure 6.6 and these are included as systematic errors.

Besides acceptance and HLCF, each photon like cluster is also weighted with either Cluster ADC or Cluster Size. While the reasons for weighting with acceptance and HLCF are self evident, weighting with Cluster ADC or Cluster Size and not so evident and are elaborated here.

6.3.1 Photon v_2 Weighted with Cluster Properties

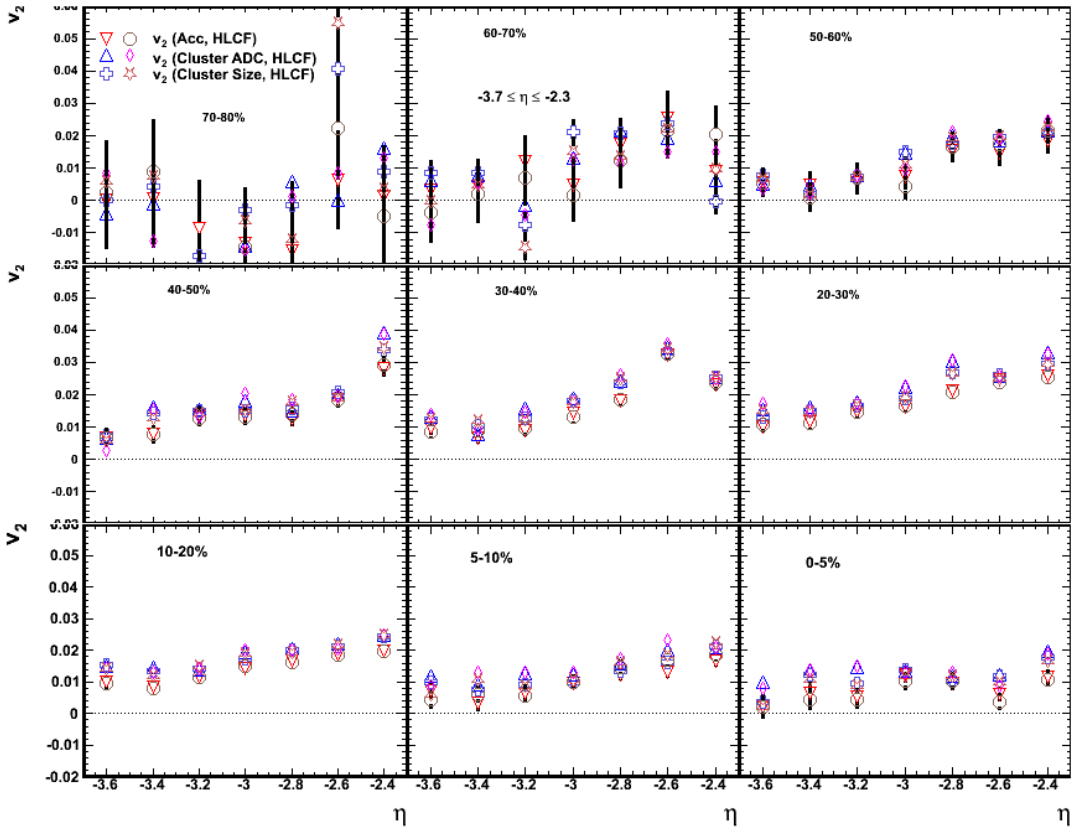

FIGURE 6.7: Pseudorapidity dependence of v_2 weighted by cluster adc and cluster size, for different centralities in Au+Au collisions at 39 A GeV.

It is now known that the efficiency and purity of photon sample measured in PMD depends on the occupancy of the detector. In an event, since particle density in-plane and out of plane is different, the occupancy in-plane and out of plane is different. This causes the efficiency and purity to change with azimuthal angle with respect to the event plane. The observed variation in efficiency and purity is because in a higher occupancy environment, clusters have a higher probability of

merging. This causes the mean cluster size to depend on occupancy. The bigger clusters have a higher probability of crossing the threshold conditions and resulting in higher efficiency as observed in previous chapters. If we only count the number of clusters, we are loosing part of the information, since due to possible merging of clusters, the clusters are fewer, but bigger. This loss of anisotropic signal is countered by weighting the clusters with ADC or Cluster size. This weighting also takes into account the of variation of efficiency and purity of $N_{\gamma-like}$ sample, with respect to the event plane.

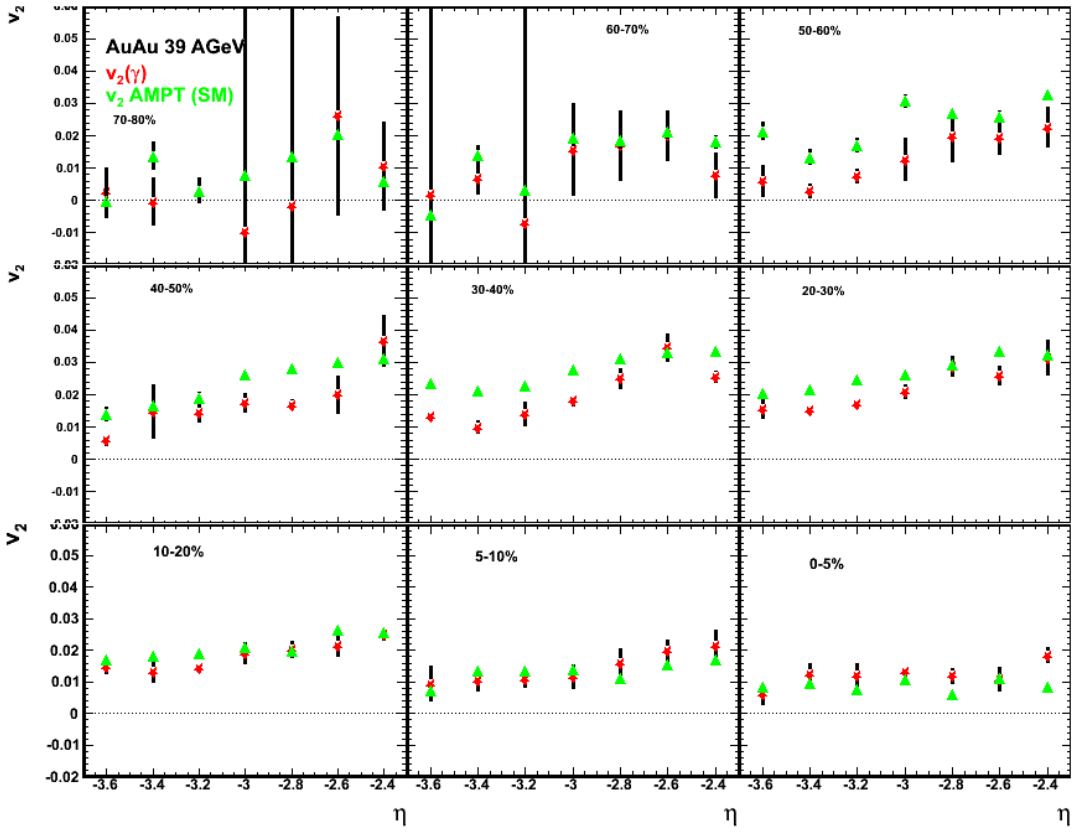

FIGURE 6.8: Pseudorapidity dependence of v_2 (mean of values obtained by weighting with cluster adc and cluster size) for different centralities in Au+Au collisions at 39 A GeV along with results of AMPT.

If there is a slight effect of merging, then we expect a slightly higher value of v_2 when we use the Cluster ADC weighting as compared to ClusterSize wieighting. This is because when two clusters merge due to their proximity, the resultant cluster size is smaller than than the size of the two unmerged clusters. On the other hand the ADC being additive, the ADC of the merged cluster is sum of the

ADC of the individual clusters and hence provides a higher weight. All the four estimates of v_2 (two different weights and two different event plane resolution) are plotted in Figure 6.7 which shows v_2 as a function of pseudorapidity for each centrality bin. The estimates of v_2 obtained without any weighting are also shown for comparison. The mean values of v_2 for all four estimates are shown Figure 6.8. The estimated values of v_2 from AMPT are also shown in the same figure and seem to be in reasonable agreement with the data.

6.4 Photon v_2: Data and AMPT

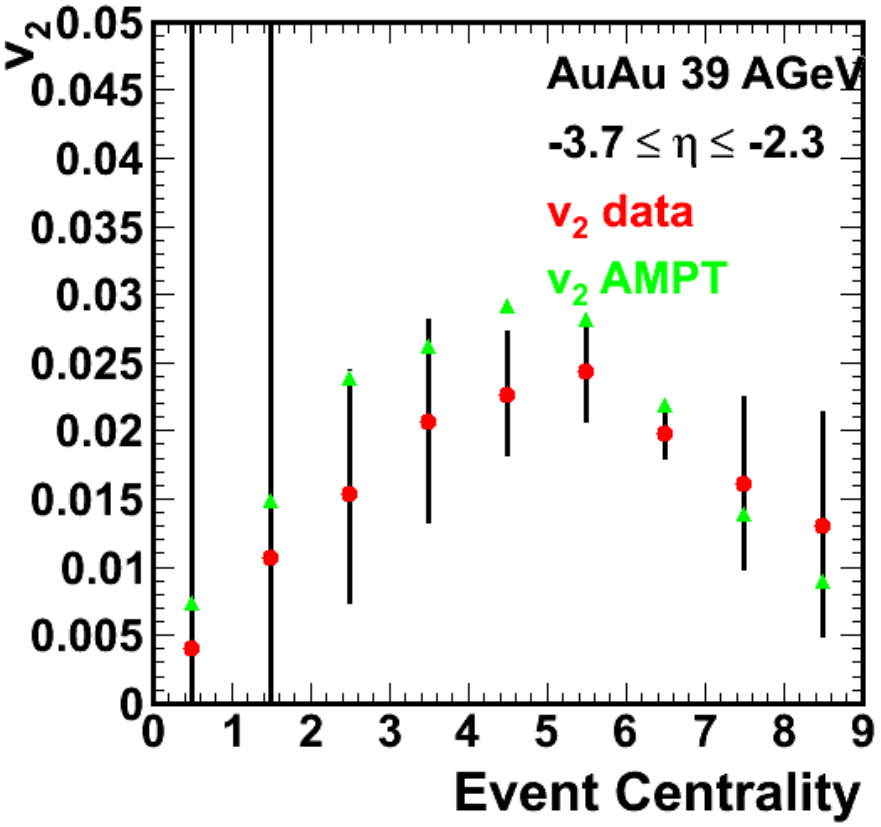

FIGURE 6.9: v_2 for photons at forward rapidity for different centrality bins in Au+Au collisions at 39 GeV. The results of AMPT are also shown.

The measurements of v_2 of photons in the forward rapidity are now compared with AMPT [80] results for Au+Au collisions at 39 A GeV. The parameters of AMPT

version used for this purpose were tuned to multiplicity as detailed in Chapter 5. v_2 has been measured with respect to the event plane determined from TPC tracks while the participant plane has been used for AMPT. The values in data are expected to be a little smaller that those from AMPT as argued in Chapter 5, and also observed in Figure 6.9. Elliptic flow of photons integrated over the rapidity range $-3.7 \leq \eta \leq -2.3$ was obtained for Au+Au collisions at 39 A GeV. The Figure 6.9 shows the v_2 obtained for data along with predictions from AMPT in the same rapidity window. The errors on the data points include the systematic error due to difference in event planes and different resolution correction factors due to the two subevent selections. The systematic errors also include variations in the values obtained by different weighting methods. The AMPT(SM) gives a good qualitative description of the elliptic flow observed in data, and is quantitatively consistent with the measured values and the systematic errors.

6.5 Summary

The elliptic flow of photons has been measured at forward rapidity in Au+Au collisions at 39 A GeV. The rapidity dependence of flow has been obtained for different centralities. Systematic errors due to different event planes and their corresponding resolutions, due to weighting of photon like clusters with cluster size and cluster ADC are estimated. This weighting with cluster parameters takes special significance because of the occupancy dependence of cluster profile, and the occupancy in-plane and out-of-plane being different because of flow.

The results for photons v_2 have been compared to the predictions from AMPT including string melting. We are grateful to the authors of AMPT for incorporating the decay of π^0 on our request which made this study possible.

The rapidity integrated values of v_2 of photons, within the systematic errors, compare well with predictions of AMPT.

Chapter 7

Conclusions and Outlook

The STAR experiment at RHIC was designed to study the relativistic heavy ion collisions at center-of-mass energies $\sqrt{s_{NN}}$ ranging from 7.7 GeV to 200 GeV. The present thesis dealt with investigation of scaling and limiting fragmentation in photons at forward rapidity region in the BES energies. The thesis also investigated the ability of AMPT event generator to explain the published results on v_2 and v_3 of charged particles from RHIC energies to LHC energies. The elliptic flow, v_2, of photons was measured at 39 A GeV and compared with AMPT predictions. The results discussed in the thesis are from Au+Au collisions at $\sqrt{s_{NN}}$ = 39, 27 and 19.6 GeV. The photons were measured using the Photon Multiplicity Detector in the STAR experiement at RHIC.

The above mentioned goal of this thesis were met using the data recorded in the PMD. Considering the non-uniformity of the response and gain in more than 40000 channels, it was necessary to clean the data by eliminating bad channels and normalise the measured gains. The variation in the cluster profiles and the variation in the incident particle density in different regions of the PMD required corrections to be made for different occupancies. Standard correction parameters like the efficiency and the purity of the detected sample were obtained for different occupancy bins, in addition to their estimation in bins corresponding to different centralities and rapidities. These studies required large statistics of simulated data and became possible by evolving methods to make association correspondence of clusters and the incident particle in the standard STAR simulated data.

The cleanup, normalisation and efficiency and purity estimation were detailed in Chapter 3 of this thesis. The detailed estimates of systematic errors due to various parameters affecting the PMD performance were also carried out. These details and the results on the pseudorapidity density distribution are in Chapter 3.

The measured values of pseudorapidity density of photons in the forward region were compared with predictions of HIJING and AMPT event generator. Whereas these event generators could explain the data at higher energies for all centralities, the data at BES energies was not in conformity with the predictions of the event generators, except for the most central collisions at all three energies. Earlier studies at 200 and 62.4 GeV had shown that the photon multiplicity per participating nucleon pair was observed to be independent of collision centrality indicating that photon production is dominated by soft processes. At lower energies, it was found that the scaled multiplicity is observed to increase with decreasing centrality. For central collisions the scaled multiplicity matches quite well with the predictions from AMPT and HIJING. Deviations from N_{part} scaling in peripheral collisions were significant, and beyond any systematic errors. This observation suggested a possible new source of photons on the PMD. The data further suggested that the yield from this source should increase with decreasing centrality, and decreasing energy of the beam. The event generators HIJING and AMPT do not incorporate fragmentation of the nuclear spectator and were not designed to predict the observed excess. The yield from such a source was parametrised without making any assumption about the dynamics or the physics of obtaining this extra yield. This parametrisation used two free parameters, values for both of which were obtained using data. Subsequently, the same parametrisation could explain the data at all 5 energies.

Data at 200 and 62.4 A GeV had also shown that photon production per unit rapidity per average number of participating nucleon pair vs. $\eta - y_{beam}$ demonstrated longitudinal scaling which is independent of collision energy, collision centrality as well as colliding system. This feature was also investigated at lower energies.

The photon pseudorapidity density normalized by the average number of participating nucleon pairs as a function of $\eta - y_{beam}$ for 10-20% centrality bin for collisions at 200, 62.4, 39, 27 and 19.6 AGeV demonstrated energy independent

limiting fragmentation behaviour. It was expected from observation at higher energies that the data for other centralities, normalised to the corresponding number of participating nucleons, would also show the same behaviour. However, the data at lower energies analysed and discussed in this thesis, showed significant deviations from such a scaling. The parametrisation used to understand the total multiplicity scaling was also applied to explore the limiting fragmentation behaviour. The rapidity density was now normalised to the total number of sources, participants and the ones obtained by the above mentioned parametrisation. Distributions normalised in this manner also demonstrated energy and centrality independent limiting fragmentation for production of photons at forward rapidities.

Considering the large number of measurement on v_2 and v_3 at RHIC and at LHC, it was important to have a reference from event generators to compare the experimental results. The simulated data from AMPT, both for the Default version and the String Melting version, were analysed to obtain the values of the coefficients, their p_T and centrality dependence for energies varying from BES at the RHIC to the LHC. The techniques to obtain the coefficients were also discussed briefly. The calculations show that the $v_2(p_T)$ changes very little across the whole energy range studied, consistent with what was observed in data. It was also observed that the AMPT can reproduce the experimental observation that $v_3/\varepsilon_3 \propto \sqrt{N_{\rm part}}$. Results on the centrality and beam energy dependence of v_2 and v_3 with SM and Default settings provide a comparative baseline for measurements of v_2 and v_3 in the RHIC beam energy scan.

The elliptic flow of photons was measured to complement results on charge particles. The v_2 results were compared to the predictions from AMPT (String Melting) and found to be in good agreement. The rapidity integrated values are also compared to AMPT and found to agree well within systematic errors.

Most of the discussions in the present thesis have focussed on results from the experiments at the Relativistic Heavy Ion Collider. In the recent years, results on Pb+Pb collisions at $\sqrt{s_{NN}} = 2.76$ TeV at the Large Hadron Collider at CERN have been available. The values of v_2 observed at LHC energies have been much greater than at the highest energies at RHIC. Further, many results on nuclear modification factor and jets have now demonstrated the existence of dense nuclear

matter and the current and future analyses is investigating the properties of this dense matter. Meanwhile, to explore the location of the critical point, the experiments at RHIC have the second phase of the BES program to scan the energy ranges close to the energies used in the first phase.

A photon multiplicity detector, similar to the one in STAR experiment, is also installed in the ALICE experiment at the LHC. Results similar to the present analyses can be carried out at the LHC energies, both to check participant scaling and limiting fragmentation. Further, the present thesis also provide important results that can be used by event generators while modelling fragmentation of nuclear spectators.

Bibliography

[1] S.A. Moszkowski and C.G. Kallman. Abnormal Neutron Star Matter at Ultrahigh Densities. *Nucl.Phys.*, A287:495–500, 1977. doi: 10.1016/0375-9474(77)90058-6.

[2] Thomas W. Ludlam. Relativistic Heavy Ions at Brookhaven: High-energy Nuclear Beams in the AGS and RHIC. *Nucl.Phys.*, A447:349C–369C, 1986. doi: 10.1016/0375-9474(86)90616-0.

[3] Edward V. Shuryak. Quark-Gluon Plasma and Hadronic Production of Leptons, Photons and Psions. *Phys.Lett.*, B78:150, 1978. doi: 10.1016/0370-2693(78)90370-2.

[4] M.M. Shapiho and R. Silberberg. Heavy cosmic ray nuclei. *Ann.Rev.Nucl.Part.Sci.*, 20:323–392, 1970. doi: 10.1146/annurev.ns.20.120170.001543.

[5] A.J. Baltz. Heavy ion transverse energy production at AGS energies: Single or multiple scattering? *Phys.Rev.*, C43:1420–1424, 1991. doi: 10.1103/PhysRevC.43.1420.

[6] J. Bartke et al. Neutral strange particle production in sulphur sulphur and proton sulphur collisions at 200-GeV/nucleon. *Z.Phys.*, C48:191–200, 1990. doi: 10.1007/BF01554465.

[7] M.M. Aggarwal et al. Azimuthal anisotropy of photon and charged particle emission in Pb-208 + Pb-208 collisions at 158-A-GeV/c. *Eur.Phys.J.*, C41:287–296, 2005. doi: 10.1140/epjc/s2005-02249-2.

[8] C. Alt et al. Centrality and system size dependence of multiplicity fluctuations in nuclear collisions at 158-A/GeV. *Phys.Rev.*, C75:064904, 2007. doi: 10.1103/PhysRevC.75.064904.

[9] John Adams et al. Experimental and theoretical challenges in the search for the quark gluon plasma: The STAR Collaboration's critical assessment of the evidence from RHIC collisions. *Nucl.Phys.*, A757:102–183, 2005. doi: 10.1016/j.nuclphysa.2005.03.085.

[10] K. Adcox et al. Formation of dense partonic matter in relativistic nucleus-nucleus collisions at RHIC: Experimental evaluation by the PHENIX collaboration. *Nucl.Phys.*, A757:184–283, 2005. doi: 10.1016/j.nuclphysa.2005.03.086.

[11] I. Arsene et al. Nuclear Modification Factor for Charged Pions and Protons at Forward Rapidity in Central Au+Au Collisions at 200-GeV. *Phys.Lett.*, B650:219–223, 2007. doi: 10.1016/j.physletb.2007.05.017.

[12] M.M. Aggarwal et al. An Experimental Exploration of the QCD Phase Diagram: The Search for the Critical Point and the Onset of De-confinement. *nucl-ex/1007.2613*, 2010.

[13] G. Odyniec. Beam energy scan program at RHIC: Experimental approach to the QCD phase diagram. *Phys.Atom.Nucl.*, 75:602–606, 2012. doi: 10.1134/S1063778812050183.

[14] B. Friman et al. *The CBM physics book: Compressed baryonic matter in laboratory experiments Lect.Notes Phys., vol. 814, pp. 1-980, 2011.* Springer Book, 2011.

[15] Mark G. Alford, Andreas Schmitt, Krishna Rajagopal, and Thomas SchÃďfer. Color superconductivity in dense quark matter. *Rev.Mod.Phys.*, 80:1455–1515, 2008. doi: 10.1103/RevModPhys.80.1455.

[16] J.P. Blaizot and Jean-Yves Ollitrault. Hydrodynamics of a Quark - Gluon Plasma Undergoing a Phase Transition. *Nucl.Phys.*, A458:745, 1986. doi: 10.1016/0375-9474(86)90198-3.

[17] Helmut Satz. The Transition From Hadron Matter to Quark - Gluon Plasma. *Ann.Rev.Nucl.Part.Sci.*, 35:245–270, 1985. doi: 10.1146/annurev.ns.35.120185.001333.

[18] Horst Stoecker and W. Greiner. High-Energy Heavy Ion Collisions: Probing the Equation of State of Highly Excited Hadronic Matter. *Phys.Rept.*, 137: 277–392, 1986. doi: 10.1016/0370-1573(86)90131-6.

[19] J. Kiskis, R. Narayanan, and H. Neuberger. Does the crossover from perturbative to nonperturbative physics in QCD become a phase transition at infinite N? *Phys.Lett.*, B574:65–74, 2003. doi: 10.1016/j.physletb.2003.08.070.

[20] Y. Aoki, G. Endrodi, Z. Fodor, S.D. Katz, and K.K. Szabo. The Order of the quantum chromodynamics transition predicted by the standard model of particle physics. *Nature*, 443:675–678, 2006. doi: 10.1038/nature05120.

[21] Y. Aoki, Szabolcs Borsanyi, Stephan Durr, Zoltan Fodor, Sandor D. Katz, et al. The QCD transition temperature: results with physical masses in the continuum limit II. *JHEP*, 0906:088, 2009. doi: 10.1088/1126-6708/2009/06/088.

[22] Misha A. Stephanov, K. Rajagopal, and Edward V. Shuryak. Signatures of the tricritical point in QCD. *Phys.Rev.Lett.*, 81:4816–4819, 1998. doi: 10.1103/PhysRevLett.81.4816.

[23] Misha A. Stephanov, K. Rajagopal, and Edward V. Shuryak. Event-by-event fluctuations in heavy ion collisions and the QCD critical point. *Phys.Rev.*, D60:114028, 1999. doi: 10.1103/PhysRevD.60.114028.

[24] R.V. Gavai and Sourendu Gupta. The Critical end point of QCD. *Phys.Rev.*, D71:114014, 2005. doi: 10.1103/PhysRevD.71.114014.

[25] J.T. Mitchell. The PHENIX potential in the search for the QCD critical point. *nucl-ex/0701079*, 2007.

[26] M Unger. Results from NA61/SHINE. *EPJ Web Conf.*, 52:01009, 2013. doi: 10.1051/epjconf/20125201009.

[27] Shine experiment. https://na61.web.cern.ch/.

[28] The nica collaboration. http://www.fair-center.eu/for-users/experiments/cbm.html.

[29] The nica collaboration. http://nica.jinr.ru/.

[30] J.D. Bjorken. Highly Relativistic Nucleus-Nucleus Collisions: The Central Rapidity Region. *Phys.Rev.*, D27:140–151, 1983. doi: 10.1103/PhysRevD.27.140.

[31] C. Y. Wong. *Introduction to High Energy Heavy Ion Collisions*. World Scientific, Singapore, 1994.

[32] B.B. Back et al. Charged particle pseudorapidity density distributions from Au+Au collisions at $\sqrt{s_{NN}}$ = 130-GeV. *Phys.Rev.Lett.*, 87:102303, 2001. doi: 10.1103/PhysRevLett.87.102303.

[33] J. Benecke, T.T. Chou, Chen-Ning Yang, and E. Yen. Hypothesis of Limiting Fragmentation in High-Energy Collisions. *Phys.Rev.*, 188:2159–2169, 1969. doi: 10.1103/PhysRev.188.2159.

[34] Dirk H. Rischke, Stefan Bernard, and Joachim A. Maruhn. Relativistic hydrodynamics for heavy ion collisions. 1. General aspects and expansion into vacuum. *Nucl.Phys.*, A595:346–382, 1995. doi: 10.1016/0375-9474(95)00355-1.

[35] Jean-Yves Ollitrault. Relativistic hydrodynamics for heavy-ion collisions. *Eur.J.Phys.*, 29:275–302, 2008. doi: 10.1088/0143-0807/29/2/010.

[36] Peter F. Kolb and Ulrich W. Heinz. Hydrodynamic description of ultrarelativistic heavy ion collisions. *nucl-th/0305084*, 2003.

[37] Jean-Yves Ollitrault. Anisotropy as a signature of transverse collective flow. *Phys.Rev.*, D46:229–245, 1992. doi: 10.1103/PhysRevD.46.229.

[38] Marcus Bleicher and Horst Stoecker. Anisotropic flow in ultrarelativistic heavy ion collisions. *Phys.Lett.*, B526:309–314, 2002. doi: 10.1016/S0370-2693(01)01495-2.

[39] Peter F. Kolb, Josef Sollfrank, and Ulrich W. Heinz. Anisotropic transverse flow and the quark hadron phase transition. *Phys.Rev.*, C62:054909, 2000. doi: 10.1103/PhysRevC.62.054909.

[40] P. Braun-Munzinger, J. Stachel, J.P. Wessels, and N. Xu. Thermal and hadrochemical equilibration in nucleus-nucleus collisions at the SPS. *Phys.Lett.*, B365:1–6, 1996. doi: 10.1016/0370-2693(95)01258-3.

[41] K. Adcox et al. Centrality dependence of charged particle multiplicity in Au - Au collisions at $\sqrt{s_{NN}}$ = 130-GeV. *Phys.Rev.Lett.*, 86:3500–3505, 2001. doi: 10.1103/PhysRevLett.86.3500.

[42] J. Adams et al. Multiplicity and pseudorapidity distributions of charged particles and photons at forward pseudorapidity in Au + Au collisions at $\sqrt{s_{NN}}$ = 62.4-GeV. *Phys.Rev.*, C73:034906, 2006. doi: 10.1103/PhysRevC.73.034906.

[43] B.I. Abelev et al. Center of mass energy and system-size dependence of photon production at forward rapidity at RHIC. *Nucl.Phys.*, A832:134–147, 2010. doi: 10.1016/j.nuclphysa.2009.11.011.

[44] Xin-Nian Wang and Miklos Gyulassy. HIJING: A Monte Carlo model for multiple jet production in p p, p A and A A collisions. *Phys.Rev.*, D44:3501–3516, 1991. doi: 10.1103/PhysRevD.44.3501.

[45] I.G. Bearden et al. Pseudorapidity distributions of charged particles from Au+Au collisions at the maximum RHIC energy. *Phys.Rev.Lett.*, 88:202301, 2002. doi: 10.1103/PhysRevLett.88.202301.

[46] I.G. Bearden et al. Charged particle densities from Au+Au collisions at $\sqrt{s_{NN}}$ = 130-GeV. *Phys.Lett.*, B523:227–233, 2001. doi: 10.1016/S0370-2693(01)01333-8.

[47] B.B. Back, M.D. Baker, D.S. Barton, R.R. Betts, M. Ballintijn, et al. The Significance of the fragmentation region in ultrarelativistic heavy ion collisions. *Phys.Rev.Lett.*, 91:052303, 2003. doi: 10.1103/PhysRevLett.91.052303.

[48] Arthur M. Poskanzer and S.A. Voloshin. Methods for analyzing anisotropic flow in relativistic nuclear collisions. *Phys.Rev.*, C58:1671–1678, 1998. doi: 10.1103/PhysRevC.58.1671.

[49] S. Voloshin and Y. Zhang. Flow study in relativistic nuclear collisions by Fourier expansion of Azimuthal particle distributions. *Z.Phys.*, C70:665–672, 1996. doi: 10.1007/s002880050141.

[50] J. Adams et al. Azimuthal anisotropy in Au+Au collisions at $\sqrt{s_{NN}}$ = 200-GeV. *Phys.Rev.*, C72:014904, 2005. doi: 10.1103/PhysRevC.72.014904.

[51] L. Adamczyk et al. Observation of an energy-dependent difference in elliptic flow between particles and anti-particles in relativistic heavy ion collisions. *Phys.Rev.Lett.*, 110:142301, 2013. doi: 10.1103/PhysRevLett.110.142301.

[52] L. Adamczyk et al. Elliptic flow of identified hadrons in Au+Au collisions at $\sqrt{s_{NN}}$ = 7.7-62.4 GeV. *Phys.Rev.*, C88(1):014902, 2013. doi: 10.1103/PhysRevC.88.014902.

[53] L. Adamczyk et al. Inclusive charged hadron elliptic flow in Au + Au collisions at $\sqrt{s_{NN}}$ = 7.7 - 39 GeV. *Phys.Rev.*, C86:054908, 2012. doi: 10.1103/PhysRevC.86.054908.

[54] Miklos Gyulassy, Ivan Vitev, Xin-Nian Wang, and Ben-Wei Zhang. Jet quenching and radiative energy loss in dense nuclear matter. *nucl-th/0302077*, 2003.

[55] Alexander Kovner and Urs Achim Wiedemann. Gluon radiation and parton energy loss. *hep-ph/0304151*, 2003.

[56] K. Adcox et al. Suppression of hadrons with large transverse momentum in central Au+Au collisions at $\sqrt{s_{NN}}$ = 130-GeV. *Phys.Rev.Lett.*, 88:022301, 2002. doi: 10.1103/PhysRevLett.88.022301.

[57] C. Adler et al. Disappearance of back-to-back high p_T hadron correlations in central Au+Au collisions at $\sqrt{s_{NN}}$ = 200-GeV. *Phys.Rev.Lett.*, 90:082302, 2003. doi: 10.1103/PhysRevLett.90.082302.

[58] Johann Rafelski and Berndt Muller. Strangeness Production in the Quark - Gluon Plasma. *Phys.Rev.Lett.*, 48:1066, 1982. doi: 10.1103/PhysRevLett.48.1066.

[59] G. Agakishiev et al. Strangeness Enhancement in Cu+Cu and Au+Au Collisions at $\sqrt{s_{NN}}$ = 200 GeV. *Phys.Rev.Lett.*, 108:072301, 2012. doi: 10.1103/PhysRevLett.108.072301.

[60] T. Matsui and H. Satz. J/ψ Suppression by Quark-Gluon Plasma Formation. *Phys.Lett.*, B178:416, 1986. doi: 10.1016/0370-2693(86)91404-8.

[61] M.C. Abreu et al. Evidence for deconfinement of quarks and gluons from the J/ψ suppression pattern measured in Pb + Pb collisions at the CERN SPS. *Phys.Lett.*, B477:28–36, 2000. doi: 10.1016/S0370-2693(00)00237-9.

[62] A. Adare et al. J/ψ Production vs Centrality, Transverse Momentum, and Rapidity in Au+Au Collisions at $\sqrt{s_{NN}}$ = 200 GeV. *Phys.Rev.Lett.*, 98: 232301, 2007. doi: 10.1103/PhysRevLett.98.232301.

[63] L. Adamczyk et al. Energy Dependence of Moments of Net-proton Multiplicity Distributions at RHIC. *nucl-ex/1309.5681*, 2013.

[64] M. Harrison, T. Ludlam, and S. Ozaki. RHIC project overview. *Nucl.Instrum.Meth.*, A499:235–244, 2003. doi: 10.1016/S0168-9002(02)01937-X.

[65] H. Hahn, E. Forsyth, H. Foelsche, M. Harrison, J. Kewisch, et al. The RHIC design overview. *Nucl.Instrum.Meth.*, A499:245–263, 2003. doi: 10.1016/S0168-9002(02)01938-1.

[66] K.H. Ackermann et al. STAR detector overview. *Nucl.Instrum.Meth.*, A499: 624–632, 2003. doi: 10.1016/S0168-9002(02)01960-5.

[67] K. Adcox et al. PHENIX detector overview. *Nucl.Instrum.Meth.*, A499: 469–479, 2003. doi: 10.1016/S0168-9002(02)01950-2.

[68] B.B. Back et al. The PHOBOS detector at RHIC. *Nucl.Instrum.Meth.*, A499:603–623, 2003. doi: 10.1016/S0168-9002(02)01959-9.

[69] M. Anderson, J. Berkovitz, W. Betts, R. Bossingham, F. Bieser, et al. The Star time projection chamber: A Unique tool for studying high multiplicity events at RHIC. *Nucl.Instrum.Meth.*, A499:659–678, 2003. doi: 10.1016/S0168-9002(02)01964-2.

[70] K.H. Ackermann, F. Bieser, F.P. Brady, D.A. Cebra, J.E. Draper, et al. The Forward time projection chamber (FTPC) in STAR. *Nucl.Instrum.Meth.*, A499:713–719, 2003. doi: 10.1016/S0168-9002(02)01968-X.

[71] B. Bonner, H. Chen, G. Eppley, F. Geurts, J. Lamas Valverde, et al. A single Time-of-Flight tray based on multigap resistive plate chambers for the STAR experiment at RHIC. *Nucl.Instrum.Meth.*, A508:181–184, 2003. doi: 10.1016/S0168-9002(03)01347-0.

[72] M.M. Aggarwal, S.K. Badyal, P. Bhaskar, V.S. Bhatia, S. Chattopadhyay, et al. The STAR photon multiplicity detector. *Nucl.Instrum.Meth.*, A499:751–761, 2003. doi: 10.1016/S0168-9002(02)01972-1.

[73] M. Beddo et al. The STAR barrel electromagnetic calorimeter. *Nucl.Instrum.Meth.*, A499:725–739, 2003. doi: 10.1016/S0168-9002(02)01970-8.

[74] C.E. Allgower et al. The STAR endcap electromagnetic calorimeter. *Nucl.Instrum.Meth.*, A499:740–750, 2003. doi: 10.1016/S0168-9002(02)01971-X.

[75] F.S. Bieser, H.J. Crawford, J. Engelage, G. Eppley, L.C. Greiner, et al. The STAR trigger. *Nucl.Instrum.Meth.*, A499:766–777, 2003. doi: 10.1016/S0168-9002(02)01974-5.

[76] Clemens Adler, Alexei Denisov, Edmundo Garcia, Michael J. Murray, Herbert Strobele, et al. The RHIC zero degree calorimeter. *Nucl.Instrum.Meth.*, A470:488–499, 2001. doi: 10.1016/S0168-9002(01)00627-1.

[77] Dmitri Kharzeev and Marzia Nardi. Hadron production in nuclear collisions at RHIC and high density QCD. *Phys.Lett.*, B507:121–128, 2001. doi: 10.1016/S0370-2693(01)00457-9.

[78] B.B. Back et al. Collision geometry scaling of Au+Au pseudorapidity density from $\sqrt{s_{NN}}$ = 19.6-GeV to 200-GeV. *Phys.Rev.*, C70:021902, 2004. doi: 10.1103/PhysRevC.70.021902.

[79] B.I. Abelev et al. Identified particle production, azimuthal anisotropy, and interferometry measurements in Au+Au collisions at $\sqrt{s_{NN}}$ = 9.2- GeV. *Phys.Rev.*, C81:024911, 2010. doi: 10.1103/PhysRevC.81.024911.

[80] Zi-Wei Lin, Che Ming Ko, Bao-An Li, Bin Zhang, and Subrata Pal. A Multi-phase transport model for relativistic heavy ion collisions. *Phys.Rev.*, C72: 064901, 2005. doi: 10.1103/PhysRevC.72.064901.

[81] M.M. Aggarwal, S.K. Badyal, V.S. Bhatia, S. Chattopadhyay, A.K. Dubey, et al. A Honeycomb proportional counter for photon multiplicity measurement in the ALICE experiment. *Nucl.Instrum.Meth.*, A488:131–143, 2002. doi: 10.1016/S0168-9002(02)00482-5.

[82] I. Arsene et al. Quark gluon plasma and color glass condensate at RHIC? The Perspective from the BRAHMS experiment. *Nucl.Phys.*, A757:1–27, 2005. doi: 10.1016/j.nuclphysa.2005.02.130.

[83] B.B. Back, M.D. Baker, M. Ballintijn, D.S. Barton, B. Becker, et al. The PHOBOS perspective on discoveries at RHIC. *Nucl.Phys.*, A757:28–101, 2005. doi: 10.1016/j.nuclphysa.2005.03.084.

[84] Pawan Kumar Netrakanti and Bedangadas Mohanty. The Width of the rapidity distribution in heavy ion collisions. *Phys.Rev.*, C71:047901, 2005. doi: 10.1103/PhysRevC.71.047901.

[85] Edwin Norbeck and Yasar Onel. Photons from spectators. 389:012041, 2012. doi: 10.1088/1742-6596/389/1/012041.

[86] W. Reisdorf and H.G. Ritter. Collective flow in heavy-ion collisions. *Ann.Rev.Nucl.Part.Sci.*, 47:663–709, 1997. doi: 10.1146/annurev.nucl.47.1.663.

[87] Sergei A. Voloshin, Arthur M. Poskanzer, and Raimond Snellings. Collective phenomena in non-central nuclear collisions. *nucl-ex/0809.2949*, 2008.

[88] Wojciech Broniowski, Piotr Bozek, and Maciej Rybczynski. Fluctuating initial conditions in heavy-ion collisions from the Glauber approach. *Phys.Rev.*, C76:054905, 2007. doi: 10.1103/PhysRevC.76.054905.

[89] B. Alver and G. Roland. Collision geometry fluctuations and triangular flow in heavy-ion collisions. *Phys.Rev.*, C81:054905, 2010. doi: 10.1103/PhysRevC.82.039903,10.1103/PhysRevC.81.054905.

[90] G.L. Ma, S. Zhang, Y.G. Ma, H.Z. Huang, X.Z. Cai, et al. Di-hadron azimuthal correlation and mach-like cone structure in parton/hadron transport model. *Phys.Lett.*, B641:362–367, 2006. doi: 10.1016/j.physletb.2006.09.001.

[91] Jun Xu and Che Ming Ko. Triangular flow in heavy ion collisions in a multiphase transport model. *Phys.Rev.*, C84:014903, 2011. doi: 10.1103/PhysRevC.84.014903.

[92] Dronika Solanki, Paul Sorensen, Sumit Basu, Rashmi Raniwala, and Tapan Kumar Nayak. Beam energy dependence of Elliptic and Triangular flow with the AMPT model. *Phys.Lett.*, B720:352–357, 2013. doi: 10.1016/j.physletb.2013.02.028.

[93] Nicolas Borghini, Phuong Mai Dinh, and Jean-Yves Ollitrault. Flow analysis from multiparticle azimuthal correlations. *Phys.Rev.*, C64:054901, 2001. doi: 10.1103/PhysRevC.64.054901.

[94] Nicolas Borghini, Phuong Mai Dinh, and Jean-Yves Ollitrault. A New method for measuring azimuthal distributions in nucleus-nucleus collisions. *Phys.Rev.*, C63:054906, 2001. doi: 10.1103/PhysRevC.63.054906.

[95] Nicolas Borghini, Phuong Mai Dinh, and Jean-Yves Ollitrault. Flow analysis from cumulants: A Practical guide. *nucl-ex/0110016*, 2001.

[96] K Aamodt et al. Charged-particle multiplicity density at mid-rapidity in central Pb-Pb collisions at $\sqrt{s_{NN}} = 2.76$ TeV. *Phys.Rev.Lett.*, 105:252301, 2010. doi: 10.1103/PhysRevLett.105.252301.

[97] Wei-Tian Deng, Xin-Nian Wang, and Rong Xu. Hadron production in p+p, p+Pb, and Pb+Pb collisions with the HIJING 2.0 model at energies available

at the CERN Large Hadron Collider. *Phys.Rev.*, C83:014915, 2011. doi: 10.1103/PhysRevC.83.014915.

[98] L. Adamczyk et al. Inclusive charged hadron elliptic flow in Au + Au collisions at $\sqrt{s_{NN}}$ = 7.7 - 39 GeV. *Phys.Rev.*, C86:054908, 2012. doi: 10.1103/PhysRevC.86.054908.

[99] Sergei A. Voloshin, Arthur M. Poskanzer, Aihong Tang, and Gang Wang. Elliptic flow in the Gaussian model of eccentricity fluctuations. *Phys.Lett.*, B659:537–541, 2008. doi: 10.1016/j.physletb.2007.11.043.

[100] Paul Sorensen. Higher Flow Harmonics in Heavy Ion Collisions from STAR. *J.Phys.*, G38:124029, 2011. doi: 10.1088/0954-3899/38/12/124029.

[101] Thomas A. Trainor, Duncan J. Prindle, and R.L. Ray. Challenging claims of nonjet 'higher harmonic' components in 2D angular correlations from high-energy heavy-ion collisions. *Phys.Rev.*, C86:064905, 2012. doi: 10.1103/PhysRevC.86.064905.

[102] K. Aamodt et al. Higher harmonic anisotropic flow measurements of charged particles in Pb-Pb collisions at $\sqrt{s_{NN}}$=2.76 TeV. *Phys.Rev.Lett.*, 107:032301, 2011. doi: 10.1103/PhysRevLett.107.032301.